



UNIVERSIDADE FEDERAL DE PERNAMBUCO
CENTRO DE TECNOLOGIA E GEOCIÊNCIAS
DEPARTAMENTO DE OCEANOGRAFIA
PROGRAMA DE PÓS-GRADUAÇÃO EM OCEANOGRAFIA

ALINA NATHANAEL DOSSA

**NEAR-SURFACE OCEAN DYNAMIC OFF NORTHEAST BRAZIL AND COASTAL
SEA SURFACE SALINITY GRADIENTS IN THE WORLD OCEAN**

Recife

2021

ALINA NATHANAEL DOSSA

**NEAR-SURFACE OCEAN DYNAMIC OFF NORTHEAST BRAZIL AND COASTAL
SEA SURFACE SALINITY GRADIENTS IN THE WORLD OCEAN**

Thesis presented to the Post-graduate program
in Oceanography at the Federal University of
Pernambuco, as a part of a requirement to
obtain a doctorate in Science, in the field of
Physical oceanography.

Supervisor: Prof. Dr. Alex Costa da Silva.

Co-supervisor: Prof. Dr. Arnaud Pierre Alexis Bertrand.

Recife

2021

Catálogo na fonte
Bibliotecária Margareth Malta, CRB-4 / 1198

D724n Dossa, Alina Nathanael.
Near-surface ocean dynamic off northeast Brazil and coastal sea surface
salinity gradients in the world ocean / Alina Nathanael Dossa. - 2021.
174 folhas, il., gráfs., tabs.

Orientador: Prof. Dr. Alex Costa da Silva.
Coorientador: Prof. Dr. Arnaud Pierre Alexis Bertrand.

Tese (Doutorado) – Universidade Federal de Pernambuco. CTG.
Programa de Pós-Graduação em Oceanografia, 2021.
Inclui Referências e Apêndices.
Resumo em francês.
Texto em Inglês.

1. Oceanografia. 2. Atlântico tropical ocidental. 3. Corrente Norte do
Brasil. 4. Subcorrente Norte do Brasil. 5. Atividade de mesoescala. 6.
Salinidade da superfície do mar. I. Silva, Alex Costa da (Orientador). II.
Bertrand, Arnaud Pierre Alexis (Coorientador). III. Título

UFPE

551.46 CDD (22. ed.)

BCTG/2021-184

ALINA NATHANAEL DOSSA

**NEAR-SURFACE OCEAN DYNAMIC OFF NORTHEAST BRAZIL AND COASTAL
SEA SURFACE SALINITY GRADIENTS IN THE WORLD OCEAN.**

Thesis presented to the Post-graduate program
in Oceanography at the Federal University of
Pernambuco, Center of Technology and
Geoscience, as a part of a requirement to obtain
a doctorate in Science, in the field of Physical
oceanography

Evaluated on: May 26, 2021.

EXAMINATION COMMISSION

Prof. Dr. Alex Costa da Silva (Supervisor)
Universidade Federal de Pernambuco

Prof. Dr. Moacyr Araujo de Cunha Filho (Internal examiner)
Universidade Federal de Pernambuco

Prof. Dr. Carmen Medeiros Limongi (Internal examiner)
Universidade Federal de Pernambuco

Prof. Dr. Fabrice Hernandez (External examiner)
Institute of Research for Development

Prof. Dr. Jacqueline Boutin (External examiner)
Sorbonne University

To my parents

Eugenie DJOSSOU and Dossou Thomas DOSSA

ACKNOWLEDGMENTS

I would particularly like to thank my supervisors, Alex Costa da Silva, Arnaud Bertrand and Gael Alory, for having been kind enough to share their expertise with me, for their patience, and especially for never having given up on me! I was extremely grateful for their human values, their attentiveness and understanding throughout this doctoral work.

I also thank Profs Moacyr Araujo, Alexis Chaigneau, Gérard Heldin and Fabrice Hernandez for their various collaborations.

I thank Bernard Bourlès, Casimir da Allada and Gaelle Herbert and Yves du Penhoat for their incentive and encouragement during this thesis.

I thank Armand Bahini for his incentive for the master.

I would also like to thank CAPES for financing my research in Brazil and CAPES PRINT for financing my 6-month stay at LEGOS (France).

I would also like to thank LEGOS for hosting me for my 6-month internship, but finally extended by 3 months due to the COVID19 pandemic.

I thank all the professors of DOCEAN for teaching me so much in their respective fields and for sharing their experiences with me.

I also thank my professors and colleagues from LOFEC Daniel Grados, Prof Doris Velede, Prof Marcus Silva, and Prof Carmen Medeiros Limongi and professors and colleagues of CEERMA with whom I have learned so much.

I would like to thank my office mates, Ramilla, Isabelle, Syumara, Suelen, Thayane, Minto, Pedro, Francis, Leonardo for the different exchanges and the conviviality.

I would also like to thank my brother and colleague Minto Dimoune with whom I learned and exchanged a lot.

Thanks to Ramilla for our constructive exchanges and for her availability.

I thank my roommates Thiago, Tulio, Ramon, and Wilmer who knew how to support my positive or negative moods with always a lot of understanding and humor during my first three years.

I also thank my parents and my brothers John, Sylvestre, Xavier, Romaric, Daniel, and my sisters Huguette, Justine, Georgette and Nicarette, for having supported and encouraged me until the end.

I also thank Bernice and Kèmi, for their support and availability.

I thank my friends and brothers Olivier, Benoit, Khalel, Faizath, Ezéchiél, Joel, Flamel that I met in Brazil and who gave me their support.

Thanks to Aubains and Karine for their welcome and support during this thesis.

I also thank Thiago Poletto's family and Ramon's mother for their kindness and love.

I cannot finish without thanking my colleagues Odilon and Micael for the different constructive exchanges.

I also thank Joseph for his welcome in France, and his support during this thesis.

I cannot finish without thanking my colleagues of the LMI TAPIOCA with whom I shared the TAPIOCA meeting, always very enriching.

This work is a contribution to the International Joint Laboratory TAPIOCA

At the end of this thesis, I would like to thank all those who have contributed to the realization of this work.

ABSTRACT

This study addresses near-surface western boundary circulation off northeast Brazil and the coastal gradient of sea surface salinity (SSS) in the world ocean. In this dissertation, we first, using conductivity temperature depth oxygen profiler (CTDO) measurements, ship-mounted acoustic Doppler current profiler (SADCP) measurements, altimetry data and numerical reanalysis products, examined the spatiotemporal variability of the North Brazil Undercurrent (NBUC) off northeast Brazil by providing an overview of the circulation, including the NBUC-NBC (North Brazil Current) transition and the potential impact of mesoscale activity. The NBUC originating south of 10S flows equatorward over the continental slope. The average NBUC velocity, transport, and vertical extent of the velocity core were higher in spring 2015 (0.81 m/s, 15.6 Sv, and >400 m) than in fall 2017 (0.65 m/s, 11.0 Sv, and ~300 m). The orographic effect shifts the flow from northeast to south by 7.5S to northwest to north by 7.5S, following the coastline. Furthermore, this flow may be locally influenced by mesoscale activity. Further north, at ~4.8S, in the fall of 2017, the central branch of the South Equatorial Current (cSEC) entered the western boundary system where it merged with the NBUC to form the NBC, flowing toward the Caribbean Sea. In fall, the NBUC retroflection does not feed the South Equatorial Undercurrent (SEUC), which instead originates from retroflections from the cSEC and the equatorial branch of the South Equatorial Current (eSEC). Second, the mesoscale activity off Northeast Brazil (37-25W; 13-1S) was investigated using altimetry data from 1993-2018. Approximately 1950 mesoscale eddy crossed the region, including 76% formed in the region, with amplitudes and radii ranging between 1 and 2 cm and 25 and 205 km, respectively. In the region around the Fernando de Noronha Archipelago (36-26W; 6-1S), the formation of cyclonic eddies is favored by the barotropic instability of surface currents and the wind stress curl. On the other hand, in the south of the region (36-26W; 12-8S), the formation of eddies is associated with the barotropic instability wind stress curl and surface currents meandering. Third, the analysis of coastal SSS gradients on a global scale was investigated. The objective was to assess the skills of four gridded products derived from the Soil Moisture Ocean Salinity (SMOS) and Soil Moisture Active Passive (SMAP) satellites, as well as the GLORYS global model reanalysis, to capture transboundary SSS gradients in coastal regions (300 km from the coast). These products were compared to thermosalinograph (TSG) measurements. The comparison shows various skills from one product to the other, decreasing as the coast gets closer. The satellite products generally agree better with the collocated TSG data than a global reanalysis, and show a wide range of coastal SSS gradients with different signs. In addition, the satellites reveal a global dominance of coastal cooling, mainly related to river runoff over shelves. This analysis shows a great potential of SSS remote sensing to monitor coastal processes, which would however require a jump in the resolution of future SSS satellite missions to be fully exploited.

Keywords: western tropical Atlantic; north Brazil current; north Brazil undercurrent; mesoscale activity; sea surface salinity.

RESUMO

Este estudo aborda a circulação na borda oeste do nordeste do Brasil e o gradiente costeiro da salinidade da superfície do mar (SSM) no oceano mundial. Para o desenvolvimento desta tese foram utilizados dados obtidos *in-situ* de CTDO, SADCP, dados de altimetria e produtos de reanálise numérica, com objetivo de melhor compreender a variabilidade espaço-temporal da Subcorrente Norte do Brasil (SCNB) ao largo do NE do Brasil, e o processo de transição da SCNB para a formação da CNB (Corrente Norte do Brasil). Através das análises apresentadas nesta tese foi possível caracterizar a variabilidade temporal das propriedades físicas da SCNB como velocidade média, transporte e extensão vertical do núcleo de máxima velocidade durante a primavera de 2015 (0,81 m/s, 15,6 Sv, e >400 m) e durante o outono de 2017 (0,65 m/s, 11,0 Sv, e ~300 m). Neste trabalho foram analisados a influência de outras correntes na região de estudo, em torno de 4,8S durante o outono de 2017 o ramo central da Corrente Sul Equatorial (CSEc) ao se aproximar da borda oeste influencia na SCNB para formar a CNB. Neste mesmo período, a retroflexão da SCNB não alimenta a Subcorrente Sul Equatorial (SCSE), que em vez disso sugere que a SCSE tem origem em retroflexões do ramo equatorial da Corrente Sul Equatorial (CSEe). Nesta tese, foram também investigadas atividades de mesoescala ao largo do Nordeste do Brasil (37 - 25W; 13-1S) usando dados de altimetria dos anos de 1993-2018. Aproximadamente 1950 vórtices de mesoescala foram observados nesta região do Atlântico, incluindo 76% formados na região de estudo, com amplitudes e raios variando entre 1 e 2 cm e 25 e 205 km, respectivamente. Na região entorno do Arquipélago de Fernando de Noronha (36-26W; 6 -1S), a formação de vórtices ciclônicos são favorecidas pela instabilidade barotrópica das correntes de superfície e pela ondulação da tensão do vento. Por outro lado, na região sul da zona de estudo (36 - 26W; 12-8S), a formação de vórtices estão associadas à instabilidade barotrópica das correntes de superfície combinada com a intensificação da tensão do vento e ao meandros das correntes de superfície. O terceiro e último objetivo de estudo desta tese, foram as análises dos gradientes de SSM em regiões próximas da costa em escala global. O objetivo era avaliar as capacidades de quatro produtos de malha derivados dos satélites SMOS (Soil Moisture Ocean Salinity) e SMAP (Soil Moisture Active Passive), bem como do modelo global GLORYS, para capturar gradientes SSM em regiões costeiras (300 km da costa). Estes produtos foram comparados as medidas obtidos *in-situ* de termossalinógrafo (TSG). Os produtos obtidos por satélites mostram uma ampla gama de gradientes de SSM costeiros com sinais diferentes. Além disso, os satélites revelam um domínio global do resfriamento costeiro, principalmente

relacionado ao escoamento de rios sobre plataformas. Esta análise mostra um grande potencial de detecção remota do SSM para monitorar os processos costeiros, o que exigiria, no entanto, um salto na resolução de futuras missões de satélites SSM a serem totalmente exploradas.

Palavras-chave: Atlântico tropical ocidental; corrente norte do Brasil; subcorrente norte do Brasil; atividade de mesoescala; salinidade da superfície do mar

RESUME

Cette étude porte sur la circulation de proche surface du bord ouest au large du nord-est du Brésil et sur le gradient côtier de la salinité de surface de la mer (SSS) à l'échelle globale. Dans cette thèse, nous avons tout d'abord examiné la variabilité spatio-temporelle du sous-courant nord-brésilien (NBUC) au large du nord-est du Brésil, en utilisant des mesures de CTDO, SADCP, des données altimétriques et des produits de réanalyse numérique. Le NBUC, qui prend naissance au sud de 10S, s'écoule vers l'équateur sur le talus continental. La vitesse moyenne du NBUC, son transport et l'étendue verticale du noyau de vitesse étaient plus élevés au printemps 2015 (0,81 m/s, 15,6 Sv et >400 m) qu'à l'automne 2017 (0,65 m/s, 11,0 Sv et ~300 m). L'effet orographique déplace le flux du nord-est au sud de 7,5S au nord-ouest à ~7,5S, en suivant l'orientation de la côte. De plus, ce flux peut être localement influencé par l'activité méso-échelle. Plus au nord, à ~4,8S, à l'automne 2017, la branche centrale du courant équatorial sud (cSEC) a pénétré dans le système de bord-ouest où elle a fusionné avec le NBUC pour former le NBC, se dirigeant vers la mer des Caraïbes. En automne, la rétroflexion du NBUC n'alimente pas le sous-courant équatorial sud (SEUC), qui provient plutôt des rétroflexions du cSEC et de la branche équatoriale du courant équatorial sud (eSEC). L'activité méso-échelle au large du nord-est du Brésil (37-25W ; 13 -1S) a été étudiée en utilisant les données altimétriques. Environ 1950 tourbillons de méso-échelle ont traversé la région, dont 76% se sont formés dans la région, avec des amplitudes et des rayons compris entre 1 et 2 cm et 25 et 205 km, respectivement. Autour de l'archipel de Fernando de Noronha (36-26W ; 6-1S), la formation de tourbillons cycloniques est favorisée par l'instabilité barotrope des courants de surface et le rotationnel de la tension du vent. Dans le sud de la région (36-26W ; 12-8S), la formation de tourbillons est associée à l'instabilité barotrope des courants de surface combinée au rotationnel de la tension du vent et au méandre de courants de surface. L'analyse des gradients côtiers de salinité de surface de la mer (SSS) à l'échelle mondiale a été étudiée. L'objectif était d'évaluer les performances de quatre produits grillés dérivés des satellites Soil Moisture Ocean Salinity (SMOS) et Soil Moisture Active Passive (SMAP), ainsi que de la réanalyse du modèle global GLORYS, afin de capter les gradients de SSS dans les régions côtières (300 km de la côte). Ces produits ont été comparés aux mesures du thermosalinographe (TSG). Les performances varient d'un produit à un autre, en diminuant lorsqu'on se rapprochant de la cote. Les produits satellitaires se rapprochent généralement mieux des données TSG colocalisées que le produit de réanalyse GLORYS, et montrent une large gamme de gradients SSS côtiers avec différents

signes. En outre, les satellites révèlent une dominance globale de dessalure côtier, principalement lié aux décharges des fleuves sur les plateaux.

Mots clés : bord ouest de l'Atlantique tropical; courant nord-Brazil; sous-courant nord-Brazil; activité méso-échelle; salinité de surface de la mer.

LIST OF FIGURES

INTRODUCTION

- Figure 1.** Mean (October 2015) Sea surface salinity (in color), superimposed with mean (October 2015) sea surface temperature (gray contours) and schematic representation of the tropical Atlantic circulation25
- Figure 2.** Temperature-salinity diagram in the NEB region from two ABRAÇOS cruises indicating the presence of tropical water (TW), the subtropical underwater (SUW), the south Atlantic central water (SACW) and the Antarctic Intermediate water (AAIW)30
- Figure 3.** Example of barotropic (left panel) and baroclinic Ocean (right panel). Black lines indicate isopycnals and green lines indicate isobars33
- Figure 4.** Local Rossby number superimposed to velocity field off Barreirinhas Bight at 25 m depth (left) and 125 m depth (right)34

ARTICLE 1

- Figure 1.** Schematic representation of mean currents and eddy generation along the Northeast Brazilian coast (lower panel) and a zoom (depicted by a grey rectangle) on the schematic circulation north of 5°S (upper panel). Surface currents in red and subsurface currents in blue. sSEC: southern branch of south equatorial current; BC: Brazil current; NBC: north Brazil current; SEUC: south equatorial undercurrent; NBUC: north Brazil undercurrent. The black rectangle indicates the NBUC-NBC transition zone. This figure summarizes the results of this study put into a wider context.63
- Figure 2.** Bathymetric maps of the study area with the SADCP ship tracks (black solid lines) obtained during surveys ABRAÇOS 1 in spring 2015 (a) and ABRAÇOS 2 in fall 2017 (b). Green circles indicate the positions of CTDO stations located off the shelf break and used in this work. Red circles indicate the CTDO stations used to discuss the current transition in the study area. The bold grey areas correspond to the shelf (<70 m).....64

Figure 4. Mean current velocity obtained from SADC profiles at 0-70 m (a, d) and 70-350 m (b, e). The red line depicts the bathymetric contour at 70 m. Meridional variation of the mean alongshore velocities at 0-70 m (blue line) and 70-350 m (black line) between the shelf break and 40 km offshore (c, f). Shaded grey and orange areas correspond to the standard deviation around the mean. The first row (a, b, c) corresponds to spring 2015, while the second row (d, e, f) corresponds to fall 2017.....66

Figure 5. 3D representations of the zonal (a, b) and meridional (c, d) flows during spring 2015 (a, c) and fall 2017 (b, d).67

Figure 6. Mean cross-shore sections (9°S - 6°S) of the alongshore velocity component and integrated transports. (a, d) Mean cross-shore section of alongshore velocity (in m s^{-1}) between the shelf break and 40 km offshore; the bold black solid line contours the core of the NBUC, i.e., the area where the alongshore velocity is greater than 70% of its maximum. (b, e) Mean vertical profile of alongshore transport integrated from the shelf break to 40 km offshore. The average total transport and associated deviation (in bold) were integrated from the shelf break to 40 km offshore and from the surface to 500 m depth. (c, f) Mean cross-shore distribution of the alongshore transport integrated between the surface and 500 m depth. Grey shaded areas correspond to the deviation around the mean. Panels (a), (b) and (c) correspond to spring 2015, while panels (d), (e) and (f) correspond to fall 2017.68

Figure 7. Mean cross-shore sections (from the shelf break) of the alongshore velocity (in m s^{-1}) by latitude bands during spring 2015 (a) and fall 2017 (b). The contour interval is 0.1 m s^{-1} . In each panel, the bold black solid line contours the core of the NBUC, i.e., the area where the alongshore velocity is greater than 70% of its maximum.69

Figure 8. Meridional variation of the alongshore transport (in Sv) integrated between the shelf break and 20 km offshore for three different layers: 0-70 m (black lines), 70-350 m (blue lines) and 0-500 m (green lines) depths. Grey shaded areas correspond to the standard deviations around the mean transports. Black, blue and green dots correspond to transport values obtained from previous observations during the same months of ABRAÇOS surveys (see Table 1)....69

Figure 9. (a) Transect positions superimposed on geostrophic currents. Mean zonal (U; upper panels) and meridional (V; lower panels) currents between: (b) 5°S and 3.3°S at $\sim 35^{\circ}\text{W}$ (green rectangle in (a)); (c) 5°S and 3.3°S (red rectangle in (a)); and (d) along six latitudinal transects (T1 to T6) between 34.7°W - 36.4°W (blue transects in (a)).70

Figure 10. SSH (in cm) superimposed on geostrophic current velocities. Climatologies for (a) spring (Sept. 29 - Oct. 21) and (d) fall (April 08 – May 09) periods, computed with data from January 1993 to December 2018. (b, e) SSH and geostrophic current velocities for spring 2015 and fall 2017 conditions. (c, f) Anomalies in SSH (in cm) and geostrophic current velocities (difference between mean and climatological conditions). The first row (a, b, c) corresponds to spring, while the second row (d, e, f) corresponds to fall. Shaded grey area correspond to the shelf. The fine black lines represent the isobaths 1000 m and 3000 m.71

Figure 11. Vertical profiles of temperature (red lines), salinity (blue lines) and oxygen (black lines) at (a) 8.9°S, 34.6°W; (b) 5°S, 35°W and (c) 3.8°S, 35°W in fall 2017.71

Figure 2. S 1. 2D representation of the latitudinal variation of the zonal (a,b) and meridional (c,d) flows in spring 2015 (a,c) and fall 2017 (b,d).72

Figure 2. S 2. SSH with superimposed geostrophic velocities (black arrows) over the period October 10-20, 2015. Green (black) contours and crosses represent contours and centres of cyclonic (anticyclonic) eddies. The white lines are the ship tracks corresponding to SSH dates.72

Figure 2. S 3. SSH with superimposed geostrophic velocities (black arrows) over the period April 10-19, 2017. Green (black) contours and crosses represent contours and centres of cyclonic (anticyclonic) eddies. The white lines are the ship tracks corresponding to SSH dates.73

Figure 2. S 4. Mean cross-shore sections (9°S-6°S) of the alongshore velocity component in Austral summer, fall, winter and spring seasons as estimated using the global reanalysis product GLORYS12V1.74

Figure 2. S 5. Mean cross-shore sections (9°S-6°S) of the alongshore velocity (in m s^{-1}) and integrated transports estimated using the global reanalysis product GLORYS12V1 in (a) spring 2015, (b) spring climatology 1993-2018, (c) difference between (a) and (b); (d) fall 2017, (e) fall climatology 1993-2018, (f) difference between (d) and (e). The transports are calculated between the surface and 500 m deep and from the shelf break to 40 km offshore (black solid line rectangle). The bold black solid line in (a), (b), (d) and (e) contours the core of the NBUC, i.e., the area where the alongshore velocity is greater than 70% of its maximum.75

Figure 2. S 6. Seasonal variation of sea surface high (in cm) superimposed on geostrophic current velocities.76

Figure 2. S 7. Geostrophic velocities magnitude (in m s^{-1}) (a, b) for spring 2015 and fall 2017 conditions. Climatologies for (c) spring (Sept. 29 - Oct. 21) and (d) fall (April 08 – May 09) periods, computed with data from January 1993 to December 2018. (c, f) Difference between spring and fall mean conditions of geostrophic velocities magnitude (in m s^{-1}). (g, h) difference between spring and fall climatologies of geostrophic velocities magnitude (in m s^{-1}). The fine black lines represent the isobaths 1000 m and 3000 m 77

ARTICLE 2

Figure 1. Snapshot of the SSH on October 11, 2015, with the results of the eddy-detection method with geostrophic velocities superimposed (black arrows). The white (black) contours indicate cyclonic (anticyclonic) eddy-detected edge, while the white (black) dots correspond to the cyclonic (anticyclonic) eddy center. (b) Zoom of a selected region with a cyclonic eddy. 81

Figure 2. Illustration of eddy tacking. The solid contours indicate eddy at the date t while dashed contours indicate eddies at date $t+dt$ (a) Black solid contours represent a given eddy edge (C_t) at time t whereas black dashed contours represent eddy edges (C_{t+dt}) at time $t+dt$; (b) no intersection between eddies at time $t+dt$ and C_t and the eddy tracking is stopped; (c) several eddies at $t+dt$ intersect C_t and the eddy-tracking algorithm uses a cost function to determine the one most similar to C_t ; (d) only one eddy at $t+dt$ intersects C_t ; (e) C_{t+dt} is included within C_t ; (f) C_t is included within C_{t+dt} . (based on Pegliasco et al., 2015). 82

Figure 3. Spatial distribution of mean annual number of detected eddies per degree square over 1993-2018 period: (a) all eddies, (b) eddy polarity. The dashed rectangles A and B indicate respectively northern part of NEB located around Atoll Rocas (AR) and Fernando de Noronha (FN) archipelago, and southern part of NEB. Black contour indicates the bathymetric contour at 70 m. 85

Figure 4. Spatial distribution of mean eddy characteristics per degree square over 1993 -2018 period: (a) eddy amplitude (cm), (b) eddy radius (km) and (c) eddy kinetic energy ($\text{cm}^2 \text{s}^{-2}$). 86

Figure 5. Trajectories of (a) cyclonic and (b) anticyclonic eddies which passed through Northeast Brazil between January 1993 and December 2018. Green dot indicate position where these eddies were first identified. Black box indicates the region off northeast Brazil while dashed boxes in (a) and (b) indicates respectively the region described figure 3b. 87

Figure 6. Spatial distribution per degree square over 1993-2018 period of (a) mean eddy speed of propagation and (b) mean eddy life time off northeast Brazil.	88
Figure 7. Seasonal cycle of number of eddies generated off Northeast Brazil.....	89
Figure 8. Seasonal cycle of (a) number of AE and CE (red and blue lines respectively) and wind stress curl (green line) within northern part of NEB (region A), (b) number of AE and CE (red and blue lines respectively) and wind stress curl (green line) within southern part of NEB (region B), and (c) wind stress magnitude in regions A (magenta line) and B (dashed magenta line).....	90
Figure 9. Monthly map of mean gradient of absolute vorticity of large-scale currents (color shading) superimposed with eddy location of long-lived eddies generated off northeast Brazil in August between 1993 and 2018 (blue and red circles for cyclonic and anticyclonic eddies respectively).....	92
Figure 10. Distribution of the number of detected cyclonic and anticyclonic eddies as function of the gradient of large-scale absolute vorticity C at eddy generation sites for all eddies generated between 1993 and 2018 within: (a) northern part of NEB (region A) and (b) southern part of NEB (region B). Green vertical in (a) and (b) indicate interval values C within $\pm 5 \times 10^{-10} \text{ m}^{-1} \text{ s}^{-1}$	93
Figure 11. Monthly map of surface currents from off NEB.	95

ARTICLE 3

Figure 1. Density of TSG data (in number of observations per 1° bins, logarithmic scale) from 1993 to 2019 in (a) the global Ocean Global and (b) the 0 - 300 km coastal band. Red boxes indicates the regions of interest: Amazon River plume (AMZ); northeast Brazil (NEB); Bay of Bengal (BOB); California (CAL) and Great Australian Bight (GAB).....	102
Figure 2. Illustration of the steps for extraction of cross-shore TSG transects: (a) Available TSG transects acquired during the ABRAÇOS cruise off Northeast Brazil in spring 2015. (b) Selection of coastal data within the 300 km from the coast. (c) Cross-shore transects selected for the SSS gradient estimation. Green contour in (b) shows the coastline nearest to selected coastal tracks and the thick black line corresponds to its linear fit. Blue transects in (c) show the selected cross-shore sections and pink lines show the local linear fits of the coastline of each individual section.....	106

Figure 3. Illustration of the steps for extraction of cross-shore SSS sections from gridded products off Northeast Brazil. (a) Grid points available in the 50-250 km coastal band. (b) Cross-shore axes computed every 25 km along the coast. Green dots indicate the coast points at which cross-shore axes are computed. The blue rectangle indicate the rectangle in which gridded data are interpolated on red dots along the cross-shore axes.	107
Figure 4. Overall coastal SSS statistics (April 2015- June 2019) of differences between gridded products and TSG observations, in terms of: (a) SSS bias (in pss); (b) standard deviation of differences; (c) number of pixels used for the comparison.	110
Figure 5. SSS off the Amazon River plume (6-9 march 2017) from (a) TSG; (b) SMOS LOCEAN ; (c) SMAP JPL ; (d) GLORYS; (e) SMOS BEC and (f) SMAP RSS. The TSG SSS from (a) is superimposed on satellite SSS maps (b-f).	112
Figure 6. SSS off Northeast Brazil (21 September - 28 October - 2015) from (a) TSG; (b) SMOS LOCEAN ; (c) SMAP JPL ; (d) GLORYS; (e) SMOS BEC and (f) SMAP RSS. The TSG SSS from (a) is superimposed on satellite SSS maps (b-f).	113
Figure 7. SSS in the Bay of Bengal (23-24 October 2015) from (a) TSG; (b) SMOS LOCEAN; (c) SMAP JPL; (d) GLORYS; (e) SMOS BEC and (f) SMAP RSS. The TSG SSS from (a) is superimposed on satellite SSS maps (b-f).	114
Figure 8. SSS off California (17-25 June 2019) from (a) TSG; (b) SMOS LOCEAN; (c) SMAP JPL; (d) GLORYS; (e) SMOS BEC and (f) SMAP RSS. The TSG SSS from (a) is superimposed on satellite SSS maps (b-f).	115
Figure 9. SSS in the Great Australian Bight (22 Oct-22 Nov 2015) from (a) TSG; (b) SMOS LOCEAN; (c) SMAP JPL; (d) GLORYS; (e) SMOS BEC and (f) SMAP RSS. The TSG SSS from (a) is superimposed on satellite SSS maps (b-f).	116
Figure 10. Global map of SSS gradients computed in the 50-250 km coastal band for the April 2015-June 2019 period from (a) TSG; (b) SMOS LOCEAN; (c) SMAP JPL; (d) GLORYS; (e) SMOS BEC and (f) SMAP RSS. Blue indicate negative SSS gradient while red indicate positive SSS gradient.	118
Figure 11. Global map of SSS gradients computed in the 50-250 km coastal band for the April 2015-June 2019 period from (a) TSG; (b) SMOS LOCEAN; (c) SMAP JPL; (d) GLORYS; (e) SMOS BEC and (f) SMAP RSS. Blue indicate negative SSS gradient while red indicate positive SSS gradient.	118

Figure 12. Distribution of SSS gradient computed in 50-250 km coastal band from (a) TSG along the cross-shore ship track on the available period (1993-2019); (b) SMOS LOCEAN; (c) SMAP JPL; (d) GLORYS12V1; (e) SMOS BEC and (f) SMAP RSS on the 2015-219 period. Values in the distribution and in the bracket correspond respectively to the mean and the standard deviation of the gradient of each dataset..... 120

Figure 13. Global map of SSS gradient computed in 50 km and 250 km coastal band. (a) Gradient computed from all TSG along the cross-shore ship track on the available period (1993-2019). (b-f) Mean (2015 -2019) gradient computed respectively from SMOS LOCEAN, SMAP JPL, GLORYS, SMOS BEC and SMAP RSS. Blue indicate negative SSS gradient while red indicate positive SSS gradient. 120

Figure 14. Overall statistics (April 2015- June 2019) of difference between the satellites, the reanalysis products and the TSG cross-shore SSS gradient computed in the 50-250 km coastal band. (a) percentage of pairs of same sign; (b) SSS gradient bias (in pss / 100 km); (c) standard deviation of the SSS gradient bias (in pss / 100 km); (d) number of cross-shore sections used for the comparison. 122

LIST OF TABLES

INTRODUCTION

Table 1 - Synthesis of transport (in Sv) estimations in the upper and lower layers (the precise depth range is provided in each case) across sections between 10°S and 3°S over the continental slope of the NEB from previous works..	28
---	----

ARTICLE 1

Table 1 Synthesis of transport (in Sv) estimations in the upper and lower layers (the precise depth range is provided in each case) across sections between 10°S and 3°S over the continental slope of the Northeast Brazil from this and previous works. The longitudinal extent of the sections is expressed in longitude or in distance from the shelf break. In some sections north of 5°S we observed both a westward zonal transport corresponding to the NBUC/NBC system and a zonal eastward transport corresponding to the SEUC. In this case we added, in bold, the transport calculation related to the SEUC. Note that in Stramma et al. (1995), the calculated transport corresponds to the geostrophic transport computed from CTD data.....	53
---	----

ARTICLE 2

Table 1 Mean (Standard deviation (STD)) properties and characteristics of AE and CE within NEB and northern part of NEB (A) and southern part of NEB (B).	88
--	----

ARTICLE 3

Table 1 Regions of interest (red boxes in Figure 1a).....	108
--	-----

LIST OF ABBREVIATIONS

SADCP	Ship-mounted acoustic Doppler current profiler
CTD	Conductivity-Temperature-Depth
NBC	North Brazil Current
NBUC	North Brazil Undercurrent
BC	Brazil Current
cSEC	Central South Equatorial Current
sSEC	Southern South Equatorial Current
eSEC	Equatorial South Equatorial Current
SECC	South Equatorial Countercurrent
SEUC	South Equatorial Undercurrent
NEUC	North Equatorial Undercurrent
EUC	Equatorial Undercurrent
NEC	North Equatorial Current
NECC	North Equatorial Countercurrent
AD	Angola Dome
GD	Guinea Dome
AAIW	Antarctic intermediate water
TW	Tropical Water
SACW	South Atlantic Central Water
SUW	Subtropical Underwater
SMOS	Soil Moisture Ocean Salinity
SMAP	Soil Moisture Active Passive
SSS	Sea Surface Salinity
SST	Sea Surface Temperature
GLORYS12V1	Global 1/12° Ocean Reanalysis version 1
TSG	Thermosalinographs
NEB	Northeast Brazil
ABRAÇOS	Acoustic along the Brazilian Coast
AMOC	Atlantic Meridional Overturning Circulation
CODAS	Common Ocean Data Access System
GPS	Global Positioning System

SSH	Sea Surface Height
DUACS	Data Unification and Altimeter Combination System
AE	Anticyclone Eddy
CE	Cyclone Eddy
TWI	Tropical Waves Instabilities
GDP	Global Drifter Program
EBUS	Eastern Benguela Upwelling System
RBC	Region of Brazil Current
C3S	Copernicus Climate Change Service
CMEMS	Copernicus Marine Environment Monitoring Service
EKE	Eddy Kinetic Energy
STD	Standard deviation
ITCZ	Intertropical Convergence Zone
STAO	South Tropical Atlantic Ocean
BoB	Bay of Bengal
GAB	Great Australian Bight
CAL	California upwelling system
AMZ	Amazon River plume
RV	Research vessel
TB	Brightness Temperature
BEC	Barcelona Expert Center
LOCEAN	Laboratoire d’Oceanographie et du Climat
RSS	Remote Sensing system
JPL	Jet Propulsion Laboratory
CATDS	Centre Aval de Traitements des Données SMOS
CEC-OS	Ocean Salinity Expertise Center

CONTENTS

1	INTRODUCTION AND OBJECTIVES	23
1.1	TROPICAL ATLANTIC CIRCULATION	23
1.1.1	Main currents of the tropical Atlantic.....	23
1.1.2	Description of the mains current of the northeast Brazil region	25
1.1.2.1	The south equatorial current.....	25
1.1.2.2	The north Brazil undercurrent	26
1.1.2.3	The north Brazil current	27
1.1.2.4	The south equatorial undercurrent.....	27
1.1.3	Transport and water masses	28
1.1.4	Sea surface salinity in coastal region with emphasis on the NBUC/NBC system	30
1.1.5	Mesoscale activity off northeast Brazil.....	32
1.2	THESIS OBJECTIVES	34
2	NEAR-SURFACE WESTERN BOUNDARY CIRCULATION OFF NORTHEAST BRAZIL	36
3	MESOSCALE EDDIES OCCURRENCE AND CHARACTERISTICS OFF NORTHEAST BRAZIL	78
4	GLOBAL ANALYSIS OF COASTAL GRADIENTS OF SEA SURFACE SALINITY.....	99
5	CONCLUSIONS AND PERSPECTIVES.....	134
5.1	CONCLUSIONS	134
5.2	PERSPECTIVES.....	136
	REFERENCES	138
	APENDIX A – SEASONAL CYCLE OF THE SALINITY BARRIER LAYER REVEALED IN THE NORTHEASTERN GULF OF GUINEA (14 PAGES).143	
	APENDIX B – SURFACE CIRCULATION AND VERTICAL STRUCTURE OF UPPER OCEAN VARIABILITY AROUND FERNANDO DE NORONHA ARCHIPELAGO AND ATOLL ROCAS DURING SPRING 2015 AND FALL 2017 (16 PAGES).....	158

1 INTRODUCTION AND OBJECTIVES

The present dissertation analyzes the near-surface circulation, the mesoscale eddies occurrence off northeast Brazil, as well as the coastal sea surface salinity gradients in the world ocean. In the following sections, we describe the main currents occurring off northeast Brazil and the physical processes driving the variability of the circulation in this region. Finally, we describe the main objectives of this work.

1.1 TROPICAL ATLANTIC CIRCULATION

Ocean circulation plays a major role in climate regulation. It transports and stores heat across the globe. Ocean currents, especially in the Atlantic Ocean, were primarily studied for commercial objectives. Indeed, in the 16th century, the marine had a good understanding of the ocean currents that were favorable to make their journey between Europe, Africa and America. Nevertheless, in recent decades, knowledge of ocean circulation has evolved considerably thanks to various scientific motivations that have promoted the observation of the ocean (*in situ* measurements, satellites) and thanks to the development of numerical modeling techniques. Ocean circulation is generally induced by wind, the effect of earth's rotation and changes in water density. Ocean circulation can be conceptualized in two components: the rapid surface circulation mainly due to the wind effect and confined to the first 1000 m, at most, of the ocean and the slow ocean circulation, below 1000 m, mainly related to density differences. In this section, we describe the tropical Atlantic circulation and more specifically in the western boundary region off Northeast Brazil.

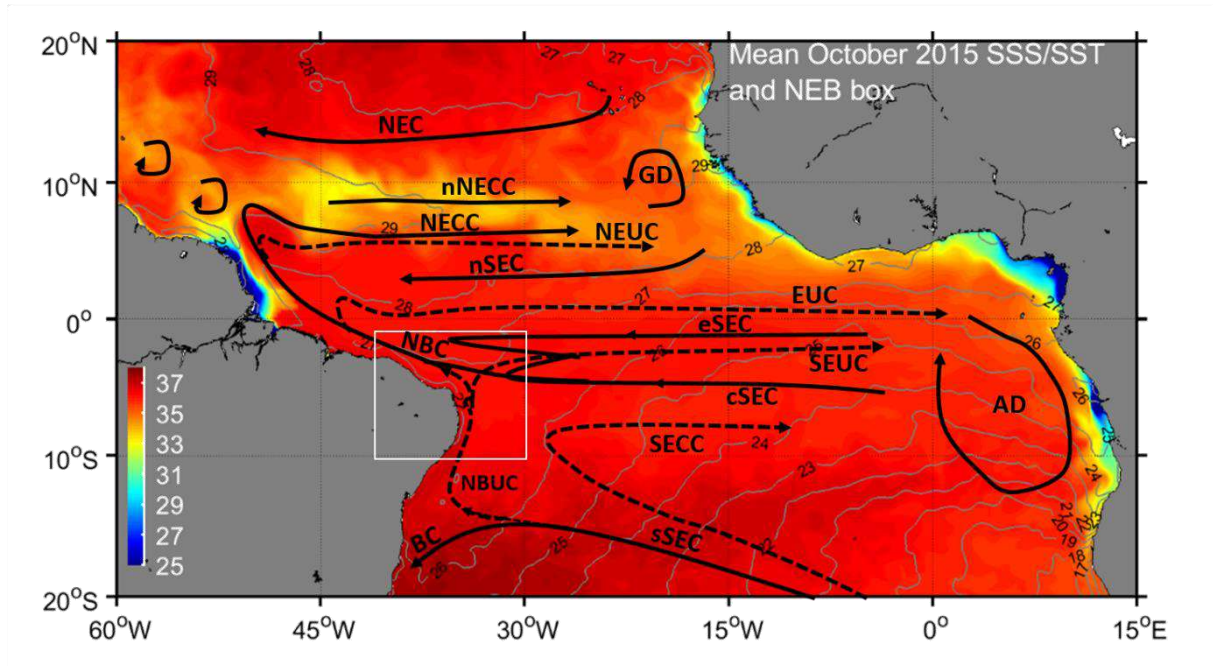
1.1.1 Main currents of the tropical Atlantic

The tropical Atlantic Ocean plays a key role in interhemispheric exchange of heat, salt and water mass (Gordon, 1986; Schmitz and McCartney, 1993). Therefore, the comprehension of its large-scale circulation is crucial for a better understanding of regional climate variability. In this region, ocean dynamic is very complex (Figure 1). Most currents flow in the zonal direction and can be classified into two groups: the westward and the eastward currents. In the surface layer, the dynamics is mainly led by the different branches of the south equatorial current (SEC)

and the North Equatorial current (NEC) that constitute the equatorial branches of the two subtropical gyres located on both sides of the equator. These main surface currents are directed towards the west. The currents directed towards the east are mostly subsurface except for the North equatorial countercurrent (NECC), which circulates in the surface layer. The main subsurface currents, namely the Equatorial Undercurrent (EUC), the North Equatorial Undercurrent (NEUC) and the South Equatorial Undercurrent (SEUC), separate the main zonal currents that flow westward. These eastward currents are mostly fed by the North Brazil current (NBC)-North Brazil undercurrent (NBUC) system. After crossing the equator, the NBC retroflects to feed the EUC, NEUC and NECC at different depths. In the south, the NBUC retroflection to feed the SEUC is questionable. From the retroflection of the NBC to feed the NECC, many circular structures shed and propagate toward Caribbean Sea. Other circular structures also occurs along African coast, the Guinea Dome (GD) and Angola Dome (AD) (e.g., Bourles et al., 1999a).

The two subtropical gyres of the tropical Atlantic have a much more intense termination in the west of the basin and a slightly different structure in the east, making the western boundary currents much more intense. These gyres are characterized by high salinity values due to the dominance of evaporation (Delcroix and Hénin, 1991; Gordon, 1986). The high salinity values of the South Atlantic subtropical gyre are transported to the western boundary of northeast Brazil, from the southern branch of the SEC (sSEC) (e.g., Stramma and England, 1999). Northwest of the basin, the largest Amazon River flows into the basin, creating low-salinity at the coast (e.g., Silva et al., 2005). In the following section, we describe the main characteristics of the currents controlling the ocean dynamics off Northeast Brazil (NEB) (white box in Figure 1).

Figure 1. Mean (October 2015) Sea surface salinity (in color), superimposed with mean (October 2015) sea surface temperature (gray contours) and schematic representation of the tropical Atlantic circulation



Source: The Author (2021).

Solid lines represent surface-intensified currents, and dashed lines, subsurface currents. The currents shown, are the south, central, equatorial and north branches of the South Equatorial Current (sSEC, cSEC, eSEC and nSEC, respectively), North Brazil undercurrent (NBUC), North Brazil current (NBC), South Equatorial Undercurrent (SEUC), Equatorial Undercurrent (EUC), North Equatorial Undercurrent (NEUC), North Equatorial Countercurrent (NECC), north branch of North equatorial countercurrent (nNECC), North Equatorial current (NEC), South equatorial countercurrent (SECC), Angola dome (AD) and Guinea dome (GD). Based on (Bourles et al., 1999b; Goes et al., 2005; Friedrich A. Schott et al., 2004; Stramma and England, 1999). The white box indicates the northeast Brazil (NEB) region.

1.1.2 Description of the mains current of the northeast Brazil region

1.1.2.1 The south equatorial current

In the Atlantic Ocean, the south equatorial current (SEC) constitutes the northern part of the subtropical gyre of south Atlantic flowing from the Benguela current region toward the Brazilian coast. It flows westward between 20°S and 4°N and transport the South Atlantic central water toward the south America coasts (Lumpkin and Garzoli, 2005). Because of its extension, it is divided into three branches separated by the South equatorial undercurrent (SEUC) and the south equatorial countercurrent (SECC), according to (Molinari, 1982) and into 4 branches according to (Peterson and Stramma, 1991; Stramma and Schott, 1999). Here after we describe the four branches of the SEC found by (Peterson & Stramma, 1991; Stramma & Schott, 1999).

- The southern branch of the SEC (sSEC) is a part of SEC located at the south of the south equatorial countercurrent (SECC). It can extend between 20°S and 8°S (Lumpkin & Garzoli, 2005). Its transport above 500 m is of ~20 Sv with surface velocity up to 10 cm s⁻¹ (Stramma, 2008). The sSEC bifurcates at about 10-20°S, from where originates the North Brazil undercurrent (NBUC) towards the north and the Brazil current (BC) towards the south (Rodrigues et al., 2007; M. Silva et al., 2009; da Silveira et al., 1994; Stramma et al., 1995). This bifurcation has been observed at different latitude and different depth. Using observational analysis, it was suggested to occur at 14-16°S in the upper layer (0-100 m) and at 20-24°S in the thermocline layer (400-500 m) (Boebel et al., 1999; Stramma and England, 1999). Using numerical model the bifurcation of the sSEC was observed in the near-surface layer close Brazil coast at 17-18°S (Harper, 2000; Malanotte-Rizzoli et al., 2000). Other modelling results suggest that the bifurcation occurs above 200 m depth and its latitude reaches its northernmost position (~13°S) in November and the southernmost position (~17°S) in July (Rodrigues et al., 2007)
- The central branch of the SEC (cSEC) is located between the SECC and the south equatorial undercurrent (SEUC) (Stramma and Schott, 1999). It is mostly centered at ~4°S with velocity up to 0.34 m s⁻¹ and transports 29 Sv at 30°W (Lumpkin and Garzoli, 2005). The intrusion of the cSEC to the western boundary circulation at ~5°S, contributes to the formation of the NBC.
- The equatorial branch of the SEC (eSEC) is located south of the equatorial undercurrent (EUC) and north of the SEUC (Peterson and Stramma, 1991; Stramma and England, 1999).
- The northern SEC (nSEC) is the only portion of the SEC located in the northern hemisphere. It flows between the north equatorial undercurrents (NEUC) and south of the EUC. The nSEC was observed at 2-3°N, 45-46°W with velocity up to 0.9 m s⁻¹ (Lumpkin and Garzoli, 2005). The surface expression of the SEC branches is mostly weak because undercurrents separate them.

1.1.2.2 The north Brazil undercurrent

The north Brazil undercurrent (NBUC) is the main current of the near-surface western boundary circulation. It originates from the bifurcation of the sSEC from where it flows equatorward. It carries high-salinity and high-oxygen waters of the South Central Atlantic Water (SCAW), along the Brazilian coast (e.g., Arhan et al., 1998; Schott et al., 1995). Despite the surface expression of the sSEC, the southward Ekman drift induces a weak surface expression of the NBUC (Stramma et al., 1995). At 11°S, the NBUC is well developed and transports

equatorward ~ 25.4 Sv above 1100 m of depth (Schott et al., 2005). Between 10°S and 5°S , its core is on average centered at 200 m depth with a mean velocity up to 0.9 m s^{-1} (Ilson C. A. da Silveira et al., 1994). In austral fall, at 5°S , its core is located at 150-300 m depth with velocity up to 1.2 m s^{-1} (Bourlès et al., 1999a). At this latitude, its transport is ~ 10.6 -11 Sv (Bourlès et al., 1999a; Schott et al., 1995; Schott et al., 1998). The NBUC exhibits a seasonal variation at 11°S with an amplitude of 2.5 Sv, with its maximum occurring in July and its minimum in October-November (Schott et al., 2005). This seasonal variation has been related to the north-south variation of the latitude of the bifurcation of the sSEC (Rodrigues et al., 2007). Furthermore, Veleda et al. (2012) found that the NBUC displays an intraseasonal fluctuation at 11°S , due to the propagation of coastal trapped waves along the Brazilian coast. The NBUC encompasses four water masses (see section 1.2.5): tropical water (TW), the subtropical underwater (SUW), the south Atlantic central water (SACW) and the Antarctic Intermediate water (AAIW).

1.1.2.3 The north Brazil current

The NBC originates from the overriding of the cSEC on the NBUC at approximately 5°S around 35°W (Bourles et al., 1999a; Bourlès et al., 1999b; Schott et al., 1998; Stramma et al., 1995). North of this latitude, the NBC flows northwestward along the Brazil coast above ~ 70 m depth with velocity up to 0.9 m s^{-1} . At 35°W , its transport varies according to the season and its vertical extension. It exhibits minimum transport (8.6 Sv) when it is located above 60 m depth in April, while in February its transport can reach 12.1 Sv when it extends from the surface to about ~ 100 m depth (Bourlès et al., 1999a). The NBC continues flowing northwestward along the Brazil coast. After crossing the equator, it separates from the coast at 6 - 8°N , 45°W and retroflects southeastward to feed the north equatorial countercurrent (NECC) (e.g., Garzoli et al., 2003; Johns et al., 1990). Results based on satellite images and *in situ* observations demonstrate that several rings break away from the retroflection and move northwestward along the coast of Guyana, representing an important mechanism for transporting waters from both equatorial and South Atlantic to the Northern Hemisphere (Garzoli et al., 2003).

1.1.2.4 The south equatorial undercurrent

The SEUC is an eastward strong subsurface flow ranged in the latitude band 5-3°S (Bourlès et al., 1999b; Molinari, 1982; Schott et al., 2005). In austral fall the SEUC ranges across 35°W between 4-3°S with velocity up to 0.3 m s⁻¹ and a transport of ~1.7-2.2 Sv at 24.5-26.8 isopycnals (Bourles et al., 1999a; Schott et al., 1995; Schott et al., 1998). At 30°W, it is centered at 4°S with velocity up to 0.2 m s⁻¹. However, its supply is still controversial. While first studies on the SEUC indicate that it is enriched-oxygen from the NBUC retroflection (e.g., Bourles et al., 1999a), others studies suggested, on the contrary, that the low-oxygen water from the SEC supplies the SEUC (e.g., Schott et al., 1998). Goes et al. (2005) indicated that apart from the later supply, the SEUC receives a minor supply from the NBUC retroflection. Using a numerical model, Jochum & Malanotte-Rizzoli (2004) suggested that the SEUC is maintained in the central equatorial Atlantic by eddy fluxes induced by tropical instability waves. Further, Hüttl-Kabus and Böning (2008) applied a high resolution numerical model and suggested that the SEUC is predominantly fed through the recirculation in the ocean interior.

1.1.3 Transport and water masses

In this section, we summarize information about (i) the transport of the main currents of the Western boundary off Northeast Brazil region, and (ii) water masses carried by the different current of the region.

As above described, NBC, sSEC and cSEC flow in the surface layer while the NBUC and the SEUC lay in subsurface. Therefore, most previous studies based the transport on the surface layer bounded by the surface and the isopycnal 24.5 (~70 m depth) and on the subsurface layer bounded by the isopycnals 24.5 and 26.76 (~350 m depth) (e.g., Bourles et al., 1999a; Stramma et al., 1995). The transports estimated at different sections of the NEB are summarized in Table 1.

Table 1. Synthesis of transport (in Sv) estimations in the upper and lower layers (the precise depth range is provided in each case) across sections between 10°S and 3°S over the continental slope of the NEB from previous works.

Reference	Sections	Upper layer	Lower layer	Total transport	Date
Silveira et al., (1994)	7°S, 34.5°W-32°W	9.1 (0-150 m)	-	17.3 (0-500 m)	May-July 1986
	8.5°S, 34.6°W-33°W	8.3 (0-150 m)	-	20.4 (0-500 m)	May-July 1986
Schott et al., (1998)	5°S, 35°W-32.5°W	1.8 (0-70 m)	11.7 (70-350 m)	-	Oct. 1990

	5°S, 35°W-32°W	2.1 (0-70 m)	11.1 (70-350 m)	-	March 1994
	5°S, 35°W-32.5°W	2.6 (0-70 m)	8.2 (70-350 m)	-	Oct. 1992
	10°S, 35°W-32.5°W	0.8 (0-70 m)	11.7 (70-350 m)	-	Oct. 1992
	10°S, 35°W-32°W	0.6 (0-70 m)	9 (70-350 m)	-	March 1994
Schott et al., (2002)	5°S, 35°W-33°W	2.7±1.8 (0-70 m)	13.4±2.7 (70-350 m)	-	Mean of 6 sections (1990 & 2000)
Goes et al., (2005)	5°S, 35°W-34°W	2.3 (0-70 m)	12.3 (70-350 m)	-	Feb. 2002
	35°W, 5.2°S-3.8°S	6.5 (0-70 m)	16.9 (70-350 m)	-	Feb. 2002
	35°W, 4°S-2°S	-	3.3 (120 – 405 m)	-	Feb. 2002
Stramma et al., (1995)	5.5°S, 35°W-33.5°W	2.9 (0-100 m)	-	19.3 (0-500 m)	Oct. 1990
	5.5°S, 35°W-32.46°W	2.9 (0-100 m)	-	19.3 (0-500 m)	Nov. 1992
	10°S, 35.5°W-34.25°W	2.5 (0-100 m)	-	16.0 (0-500 m)	Nov. 1992
Bourlès et al., (1999b)	5°S, 35°W-34°W	3.8 (0-70 m)	10.6 (70-350 m)	-	Feb. 1993
Bourlès et al., (1999b)	35°W, 4°S-3°S	-	3.1 (70 -350 m)	-	Feb. 1993
Bourlès et al., (1999b)	35°W, 5°S-2°S	8.6 (0-70 m)	15.6 (70-350 m)	-	April 1996
Bourlès et al., (1999b)	35°W, 4°S-3°S	-	2.1 (70 -350 m)	-	April 1996
Schott et al., (1995)	35°W, 5°S-3.2°S	5.1 (0-70 m)	13.1 (70-350 m)	-	March 1994
Schott et al., (2005)	5°S, 35°W-32°W	3.8 (0-70 m)	14.2 (70-350 m)	-	Mean of 9 sections (2000-2004)

Source: The Author (2021).

The longitudinal extent of the sections is expressed in longitude or in distance from the shelf break. In some sections north of 5°S we observed both a westward zonal transport corresponding to the NBUC/NBC system and a zonal eastward transport corresponding to the SEUC. In this case we added, in bold, the transport calculation related to the SEUC. Note that in Stramma et al. (1999), the calculated transport corresponds to the geostrophic transport computed.

Along the coast of Western boundary off Northeast Brazil region, four waters masses could be identified (Figure 2): the Tropical Water (TW), the Subtropical Underwater (SUW), the South Atlantic Central Water (SACW) and the Antarctic Intermediate Water (AAIW).

- The TW is formed in equatorial regions and lays above the 24.5 kg m^{-3} isopycnal (Bourlès et al., 1999b; Stramma and England, 1999). Due to the intense solar radiation at the equator and excess evaporation relative to the precipitations, the TW is characterized by high salinity (> 37) and temperature ($> 25^\circ\text{C}$).

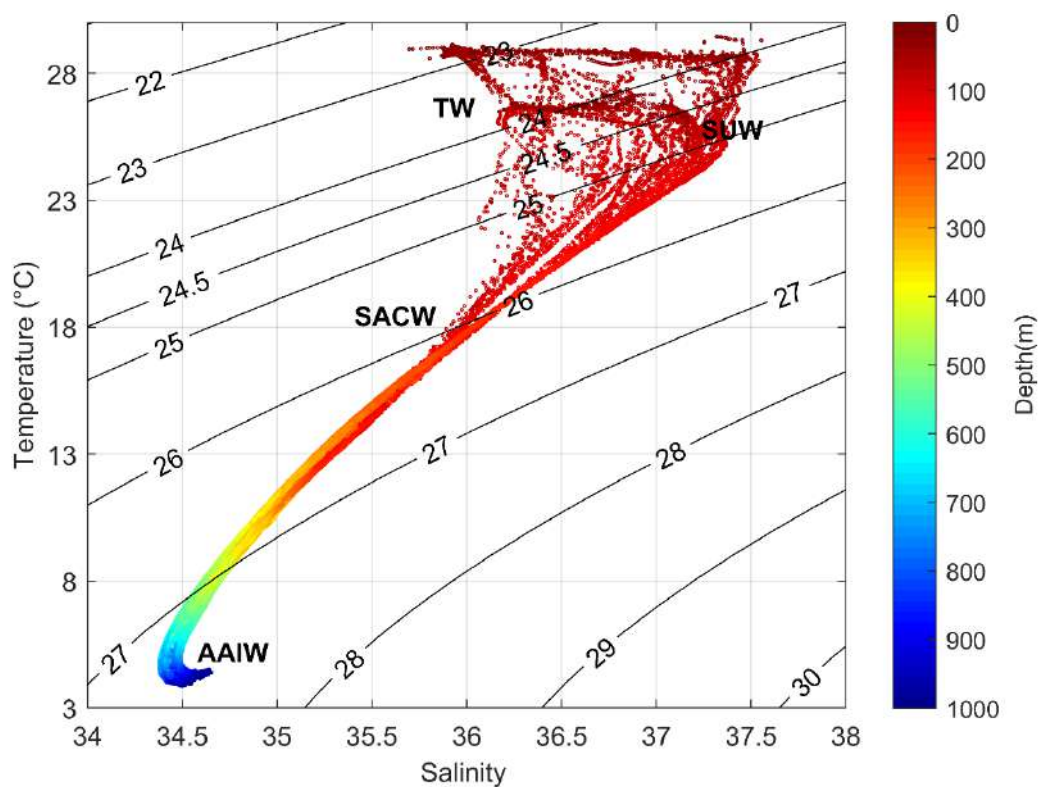
- The SUW is formed in the tropic-subtropics transition region by subduction. This water lays above the thermocline and is embedded to the TW. It is characterized by maximum salinity

(>36.5) and densities slightly below 25 kg m^{-3} .

- The SACW originates in the South Atlantic and is mainly encountered in the subtropical gyre. It is carried toward the eastern Brazil coasts within the sSEC and the eSEC. From the eastern Brazil coast, it is transported equatorward by the NBUC-NBC system. The SACW lays between 24.5 and 26.8 isopycnals and is characterized by temperatures ranging from 10°C to 23°C and salinities >35 (Stramma and England, 1999).

- The AAIW originates from a surface region of circumpolar layer and from the Indian Ocean. It lays between 27 and 32.15 kg m^{-3} and is characterized by subsurface maximum oxygen and minimum salinity. In the NEB region, this water mass is encountered below ~ 500 m depth.

Figure 2. Temperature-salinity diagram in the NEB region from two ABRAÇOS cruises indicating the presence of tropical water (TW), the subtropical underwter (SUW), the south Atlantic central water (SACW) and the Antarctic Intermediate water (AAIW)



Source: The Author (2021).

1.1.4 Sea surface salinity in coastal region with emphasis on the NBUC/NBC system

The sea surface salinity (SSS) is a key parameter for the understanding of ocean-atmosphere interactions, climate variability and the water cycle. At global scale, SSS spatial distribution is mainly controlled by ocean dynamics, surface forcing such evaporation, precipitation and ice freezing. High SSS values are found in regions where evaporation dominates while low SSS values are found in intertropical convergence zones where precipitation dominates (Delcroix & Hénin, 1991; Gordon, 1986). Through the transport of water properties, ocean circulation and mesoscale eddies contribute to the spatial distribution of SSS (e.g., Hénin et al., 1998). At high latitude, SSS is affected by the formation or melting of sea ice (Alexander Haumann et al., 2016).

The salinity controls with the temperature the seawater density and therefore plays a key role in thermohaline circulation. In region where precipitation or river runoff is associated with the salinity stratification within a deeper isothermal layer, barrier layer can occur between the base of the isothermal layer and the top of the mixed layer (Lukas and Lindstrom, 1991; Sprintall and Tomczak, 1992). When it occurs, it reduces the mixed layer thickness and modify heat exchange between the mixed layer and the ocean interior. For instance, in the work I recently published, we emphasized the impacts of the barrier layer on the mixed layer depth and the sea surface temperature off northeastern Gulf of Guinea (Dossa et al., 2019) (see appendix).

In coastal regions, many physicals processes can induce SSS variation. Rivers discharges induces salinity decrease. At high latitudes, continental ice melting can also induce strong salinity decrease. In addition, topical rainfall concentrated in coastal belt can also induce salinity decrease comparable to that of rivers (Ogino et al., 2017). Through alongshore currents, these coastal SSS anomalies are redistributed.

In the western boundary region off northeast Brazil, the SSS distribution is affect by the NBUC, which carry salty water from subtropical south Atlantic gyre. This salty was observed at 100 m depth near the coast (da Silveira et al., 1994). From vertical mixing induced by wind shear or friction with the continental slope, the salty water could be transported to the surface. At $\sim 5^{\circ}\text{S}$, the Ekman drift weakens and favors the rising of the salty core of the NBUC (Stramma et al., 1995) therefore inducing salinity increase at the coast. In addition, evaporation occurring in the region may also favor the salinity increase at the coast.

The salty water of the region are transported northwestward by the NBC. At $0-5^{\circ}\text{N}$, a salinity contrast is observed between the salty water from the South and the low-salinity water induced by the Amazon River plume. When the trade winds (south-west wind) are intense, the NBC is

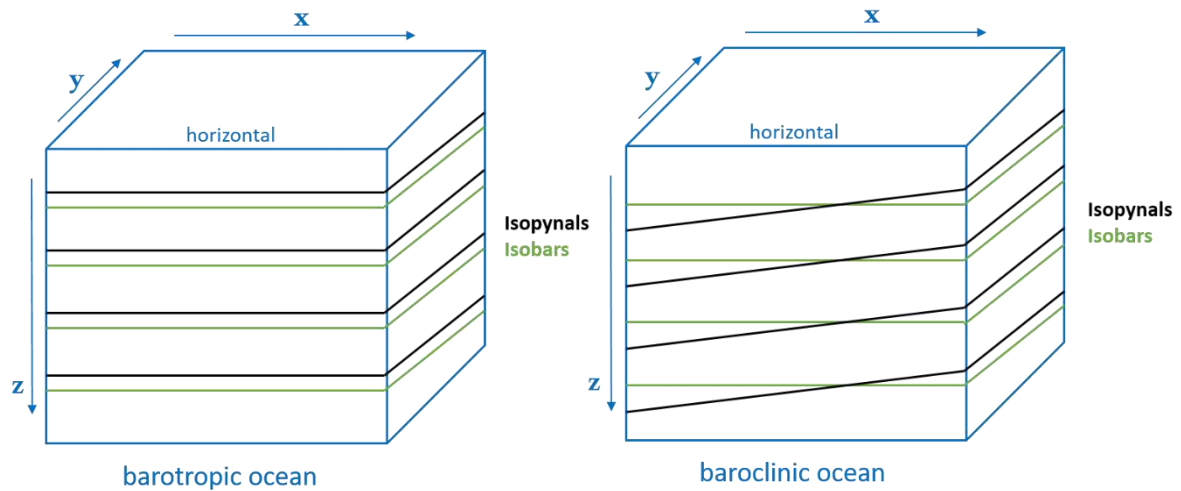
attached to the coast and transports northwestward, along the coast of Brazil, waters of low salinity of the Amazon (Field, 2005; Johns et al., 1990; Silva et al., 2009). At 6-8 ° N, the NBC separates from the coast and retroflects towards the east of the basin to feed the NECC with low salinity waters (Deremble et al., 2017; Garzoli, 2004; Varona et al., 2019). The rings generated during the retroflection of the NBC trap the low salinity water and transport it to the Caribbean Sea.

1.1.5 Mesoscale activity off northeast Brazil

Mesoscale variability is a dominant signal of ocean circulation with scales of 50 to 500 km in space and 10 to 100 days in time (Morrow and Le Traon, 2006). The emergence of satellites and drifting buoys for ocean observation has revealed the presence of oceanic circular structures throughout the ocean. The mesoscale activity is much more intense in the Antarctic Circumpolar Current and the major western boundary currents (Gulf Stream, Kuroshio and the Brazil-Malvinas confluence region) where the mean sea surface anomaly can reach 20 cm (Pascual et al., 2006). Mesoscale eddies have a spatial scale ranging from tens of km to hundreds of km. They have lifetimes ranging from days to months and can travel hundreds of km before dissipating (Fu et al., 2010). There are two types of eddies, cyclones and anticyclones, which differ in their rotation direction. In the southern hemisphere, cyclonic (anticyclonic) eddies have a clockwise (counterclockwise) direction of rotation and inversely in the northern hemisphere.

The formation of eddies is due to several physical processes. In general, eddies are formed by horizontal and vertical shearing of major currents (Stammer, 1997) as well as barotropic and or baroclinic instabilities (Figure 3). They can also form downstream of obstacles such as islands (Aristegui et al., 1997; Barton and Mitchelson-jacob, 2000) or by cape effects (e.g., Djakouré et al., 2014; Doglioli et al., 2004; Magaldi et al., 2010). In equatorial regions, eddy formation is favored by the presence of tropical instability waves (Caltabiano et al., 2005). Local variations in wind stress or wind direction variability are processes that also favor eddy formation (Dickey et al., 2008).

Figure 3. Example of barotropic (left panel) and baroclinic Ocean (right panel). Black lines indicate isopycnals and green lines indicate isobars



Source: The authors (2021)

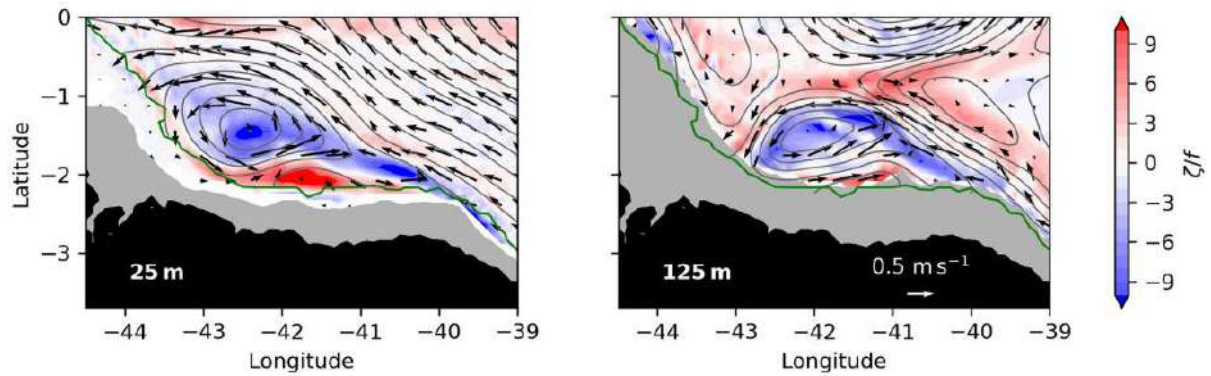
Eddies propagation, is related to the variation of the Coriolis force as a function of latitude variation. Nevertheless, their displacement can be influenced by the presence of topography or strong large-scale currents. In the northern hemisphere, anticyclonic (cyclonic) eddies propagate in the southwest (northwest) direction while southern hemisphere, anticyclonic (cyclonic) eddies propagate in the northwest (southwest) direction (e.g., Chelton et al., 2011; Morrow et al., 2004) due to beta-effect.

Eddies play an important role in ocean-atmosphere exchanges and the distribution of biogeochemical and physical properties in the ocean. When they form, they can trap water mass properties and heat from their region of formation, and transport them along their path to their region of dissipation. In this way, they generate mass and heat anomalies that can influence ocean-atmosphere exchanges (e.g., Frenger et al., 2013; Villas Bôas et al., 2015).

In the tropical Atlantic, the activities of mesoscale eddies have been the subject of several studies. Eddies are frequently observed in the Canary and Benguela eastern edge upwelling systems (e.g., Chaigneau et al., 2009; Chelton et al., 2011; Pegliasco et al., 2015), the formation region of the Brazil Current (10-20 ° S) (e.g., Arruda et al., 2013; Campos, 2006), the NBC retroflection region (Aguedjou et al., 2019; Aroucha et al., 2020; Johns et al., 1990; Ilson Carlos Almeida da Silveira et al., 2000). The region of the western boundary of the tropical Atlantic off Northeast Brazil remains poorly documented in terms of mesoscale activity. Silveira et al. (1994) was the first to observe a clockwise recirculation of the cSEC at the surface as it

approaches the northeast coast of Brazil at $\sim 33^\circ$ W. Nevertheless, the authors suggest that it could be occasional and seasonal. Then, based on numerical simulations, Silva et al. (2009) highlighted the high surface mesoscale activity along the cSEC patches near the northeast Brazil region. More recently, mesoscale activity observed in the region based on altimetry data at specific times (Dossa et al., 2021; Silva et al., 2021). Furthermore, Simoes-Sousa et al. (2021) have shown the formation of anticyclonic eddies off Barreirinhas Bight (44° - 39° W; 4° - 0° S), based on a combination of observational and reanalysis data (Figure 4). The latter suggest that eddies are formed by the interaction of the NBC with the topography.

Figure 4. Local Rossby number superimposed to velocity field off Barreirinhas Bight at 25 m depth (left) and 125 m depth (right)



Source: Simoes-Sousa *et al.* (2021)

1.2 THESIS OBJECTIVES

As mentioned in previous sections, the ocean dynamics of the western boundary system off northeast Brazil remains poorly documented. It is mainly described at 5° S and 11° S where the cSEC and sSEC arrive into the region (e.g., Bourles et al., 1999; Schott et al., 1998). Between these two latitudes, little is known about ocean dynamics along the coast due to lack of *in situ* data. Furthermore, the retroflection of the NBUC to feed the SEUC is still under discussion. In addition, mesoscale activities that play important role in the ocean dynamics is less documented within the region. On other hand, the variability of the alongshore currents plays important role in the distribution of SSS through out the region. It is also known that at global scale, specific processes like, ice melt in high latitudes; coastal upwelling could induce change in coastal SSS distribution. However, very little is known about coastal SSS patterns and gradient world ocean. In the above presented context, the present dissertation aims at characterizing the near-surface western boundary circulation off northeast Brazil and to investigating mesoscale eddy

occurrence and characteristics within the region and their influence on the western boundary circulation. The dissertation also aims at analyzing the global coastal sea surface salinity with a zoom on five regions of interest, including the NEB. To achieve this goal, we analyze *in situ* hydrographic and current data, reanalysis data and SSS data from thermosalinographs (TSG) and two satellites.

In particular, the specific objectives of the dissertation are:

1. Describe the seasonal and inter-annual ocean circulation in the near-surface layer in the NEB region;
2. Analyze the spatial and temporal variability of the NBC-NBUC currents system in the NEB region and adjacent ocean region, through in situ observations and reanalysis;
3. Analyze possible mesoscale eddies activities within NEB;
4. Analyze the spatial and temporal variability of the SSS in the world ocean including NEB through in situ observations ,and analysis of satellites and reanalysis data;
5. Analyze the relationship of the a possible coastal SSS gradient and physical processes acting in the world ocean including NEB

This manuscript is organized as follows. Chapter 2 is devoted to the near-surface circulation off northeast Brazil. In Chapter 3, we describe the mesoscale eddies occurrence in our region of study. In Chapter 4, we analyze the coastal sea surface salinity gradient in the World ocean, including the NEB. The manuscript concludes with Chapter 5, where we provide final remarks on the major results we obtained and some perspectives aiming at signposting possible future work.

2 NEAR-SURFACE WESTERN BOUNDARY CIRCULATION OFF NORTHEAST BRAZIL

In this chapter, we describe the near-surface dynamics off the northeast Brazil. Our analysis are based on conductivity temperature depth oxygen probe and ship-mounted acoustic Doppler current profiler measurements acquired during two ABRAÇOS surveys along Northeast Brazil coast, altimetry data, and numerical reanalysis products.

This work was published as scientific paper in "Progress in Oceanography" and is described the section below. Doi: 10.1016/j.pocean.2020.102475

Alina N. Dossa^{1*}, Alex Costa da Silva¹, Alexis Chaigneau^{2,3,4}, Gérard Eldin², Moacyr Araujo^{1,5} and Arnaud Bertrand^{6,1,7}

¹Laboratório de Oceanografia Física Estuarina e Costeira, Depto. Oceanografia, UFPE, Recife-PE, Brazil

²Laboratoire d'Études en Géophysique et Océanographie Spatiale (LEGOS), Université de Toulouse, CNES, CNRD, IRD, UPS, Toulouse, France

³Institut de Recherches Halieutiques et Océanologiques du Bénin (IRHOB), Cotonou, Benin,

⁴International Chair in Mathematical Physics and Applications (ICMPA–UNESCO Chair), University of Abomey-Calavi, Cotonou, Benin

⁵Brazilian Research Network on Global Climate Change, São José dos Campos, SP, Brazil

⁶Institut de Recherche pour le Développement (IRD), MARBEC, Univ Montpellier, CNRS, Ifremer, IRD, Sète, France.

⁷Universidade Federal Rural de Pernambuco, Recife, Brazil

*Corresponding author: Alina N. Dossa, nath2dossa@gmail.com

Abstract

In the tropical Atlantic Ocean, the North Brazil Undercurrent (NBUC) and the North Brazil Current (NBC) play important roles as near-surface northward paths for the Atlantic meridional overturning circulation. To investigate the meridional evolution of the near-surface western boundary circulation in that region, two surveys were carried out off Northeast Brazil during austral spring 2015 and fall 2017, periods that we show to be representative of typical conditions for the spring and fall seasons. Using conductivity temperature depth oxygen probe and ship-mounted acoustic Doppler current profiler measurements, altimetry data, and numerical

reanalysis products, we examine the spatiotemporal variability of the NBUC, providing a comprehensive view of the circulation, including NBUC-NBC transition and the potential impact of mesoscale eddies. The NBUC originating south of 10°S flows equatorward over the continental slope. NBUC mean velocity, transport and vertical extent of the velocity core were higher in spring 2015 (0.81 m s^{-1} , 15.6 Sv, and >400 m) than in fall 2017 (0.65 m s^{-1} , 11.0 Sv, and ~300 m). The upper limit of the NBUC velocity core rose slightly from 160 m at 9°S to 105 m depth at 6°S. This pattern is associated with a northward increase in current velocity from 0.7 m s^{-1} at 9°S to 1 m s^{-1} at 5°S. The orographic effect shifts the flow from northeastward south of 7.5°S to northwestward north of 7.5°S, following the shoreline. Besides, altimetry data show that this flow can be locally influenced by mesoscale activity. Farther north, at ~4.8°S, data obtained in fall 2017 show that the central branch of the South Equatorial Current (cSEC) enters into the western boundary system where it coalesces with the NBUC to form the NBC, flowing toward the Caribbean Sea. Finally, the NBUC retroflection does not feed the South Equatorial Undercurrent (SEUC), which, instead originates from retroflections of the cSEC and the equatorial branch of the South Equatorial Current (eSEC).

Keywords

Western Tropical Atlantic; North Brazil Undercurrent; North Brazil Current; Flow-topography interaction; Mesoscale activity, ADCP.

1. INTRODUCTION

The western tropical Atlantic Ocean is a critical region for the interhemispheric exchange of heat, salt and water mass (Gordon, 1986; Schmitz and McCartney, 1993). In this region, near-surface western boundary currents play major roles in the equatorward patch of the Atlantic Meridional Overturning Circulation (AMOC) (Garzoli, 2004; Schott et al., 2002; Zhang et al., 2011). In particular, the North Brazil Undercurrent (NBUC) and the North Brazil Current (NBC) act as an AMOC channel for the mean northward return flow (Rühs et al., 2015). The NBUC originates from the bifurcation of the southern South Equatorial Current (sSEC) (Figure 1) and controls the northward transport along the eastern portion of the Northeastern Brazilian coast (Peterson and Stramma, 1991; Stramma and Schott, 1999; Lumpkin and Garzoli, 2005;

Rodrigues et al., 2007; Silva et al., 2009). The sSEC arises from the westward deflection of the Benguela Current in the southeast Atlantic. During its journey, the sSEC progressively warms and thus carries relatively warm and salty water from the southeast and central South Atlantic northwestward. The sSEC reaches the Brazilian coast at approximately 10-20°S, where it bifurcates into two branches (Stramma and England, 1999; Rodrigues et al., 2007; Silva et al., 2009; Soutelino et al., 2011). A small part of the sSEC feeds the surface Brazil Current (BC) that flows southward along the Brazilian continental shelf, whereas the main part of the sSEC feeds the subsurface NBUC flowing northward (da Silveira et al., 1994; Stramma et al., 1995; Schott et al., 2005). Although the sSEC is a nearly westward surface current flowing in the first hundreds of meters of the ocean, the NBUC has a weak surface expression and flows predominantly in the subsurface due to the southward wind-driven surface drift in the region (Stramma et al., 1995). Between 10°S and 5°S, along the Brazilian coast, the core of the NBUC transports a South Atlantic water mass characterized by a high oxygen content and high salinity (Arhan et al., 1998; Schott et al., 1998). At ~5°S, the NBUC is reinforced by the central SEC (cSEC) that enters the western boundary system. The equatorward transport is thus increased, and the NBUC forms the NBC in the near-surface layer.

The above-described large-scale picture of the nearshore circulation off Northeast Brazil (NEB) has mostly been derived from geostrophic and hydrographic data (da Silveira et al., 1994; Schott et al., 1995; Stramma et al., 1995), which do not have the resolution and precision of shipboard acoustic Doppler current profiler (SADCP) data. Some studies, have used SADCP data to investigate the regional circulation (Stramma et al., 1995; Schott et al., 1995, 2003; Bourlès et al., 2002; Goes et al., 2005; Neto and Da Silva, 2014), but they were mostly limited to sections at 5°S and 11°S and did not provide comprehensive coverage of the NEB region. The general patterns of the NBUC/NBC transition, for example, have been previously examined (da Silveira et al., 1994; Stramma et al., 1995; Bourlès et al., 1999; Schott et al., 2003), but a more detailed description of the connection between these western boundary currents is still needed. Indeed, Bourlès et al. (1999) showed along of the 44°W section that in the region where the NBC forms, the NBUC weakens and retroflects to feed the eastward South Equatorial Undercurrent (SEUC). Conversely, Schott et al. (1998) suggested that the SEUC is not fed by the NBUC but rather by the large-scale recirculation of the tropical gyre (the equatorial branch of the south equatorial current, eSEC). Furthermore, Goes et al. (2005) found that apart from the gyre recirculation, there is a minor contribution from the NBUC to the SEUC. This still controversial debate will be investigated in the present study.

In addition to the need to understand the processes in this transition zone, the potential impact of mesoscale eddies on the NBUC/NBC system is not yet documented. Although mesoscale eddies are known to impact ocean boundary flows (Chelton et al., 2007, 2011; McWilliams, 2008), as far as we know this has not been previously investigated along the eastern NEB.

In this context, the objective of this work is to fill gaps on existing knowledge to provide a more comprehensive and updated description of near-surface western boundary circulation off Northeast Brazil (Figure 1). All previous NBUC/NBC observing works come from cross-shelf transects and mooring array measurements at 5°S and 11°S (Veleda et al., 2011, 2012; Hummels et al., 2015; Herrford et al., 2020). We aim at describing the spatial variability of the NBUC/NBC system along Northeast Brazil for two different periods of the year. To achieve this goal and to construct a comprehensive picture, two surveys were carried out along the NEB shoreline in austral spring 2015 and fall 2017 (Bertrand, 2015, 2017), when systematic cross-shore sections of conductivity-temperature-depth-oxygen (CTDO) were obtained and underway SADCP measurements were performed. Using such a dataset and altimetry information, we examined the spatial variability of the NBUC/NBC system during both periods. Although synoptic, those measurements appear to be representative of spring and fall canonical conditions and allow a detailed analysis of the equatorward evolution of the NBUC, its interaction with shelf topography, and its transition from under to surface current (NBUC/NBC). Finally, we show how mesoscale activity can impact the near-surface circulation.

2. Material and methods

2.1. *In situ* measurements

Data were collected during two multidisciplinary ‘Acoustic along the Brazilian Coast’ (ABRAÇOS) surveys performed along the continental slope of the NEB (Figure 2) onboard the R/V Antea in austral spring 2015 (September 28 - October 21, 2015) and fall 2017 (April 9 - May 8, 2017) (Bertrand, 2015; 2017). The survey pattern consisted of systematic cross-shore sections (Figure 2). An ‘Ocean Surveyor’ ship-mounted acoustic Doppler current profiler (SADCP) operating at a frequency of 75 kHz with a depth range of 15-700 m was used to measure the zonal and meridional components of the currents in the upper water column. Raw SADCP data were acquired every 3 s in deep water (>150 m bottom depth) and every 1 s in

shallow water (<150 m bottom depth) using a vertical bin length of 8 m. Velocities estimated from each ping were vector-averaged in each vertical bin into 10 min ensembles.

SADCP data were processed and edited using the Common Ocean Data Access System (CODAS) software package developed at the University of Hawaii. The relative velocities were rotated from the transducer to the Earth reference frame using the ship gyrocompass. The global positioning system (GPS) was used to retrieve the absolute current velocities. The orientation of the transducer relative to the gyroscopic compass and an amplitude correction factor for the ADCP were determined by standard calibration procedures (Joyce, 1989; Pollard and Read, 1989). Finally, velocity profiles were averaged hourly, providing profiles in the 19-600 m depth range. SADCP data located over the shelf (bathymetry shallower than 70 m) were often affected by spurious reflections on the bottom, so the data coverage was only partial in these shallow areas.

To describe the main currents, we divided the data into two layers: the upper layer (0-70 m) and the subsurface layer (70-350 m). These limits of 70 m and 350 m depth correspond to the relative depths where $\sigma_\theta = 24.5 \text{ kg m}^{-3}$ and $\sigma_\theta = 26.8 \text{ kg m}^{-3}$, respectively. These isopycnals were defined in previous studies on the basis of the current distribution associated with the density structures (Bourles et al., 2002; Goes et al., 2005; Schott et al., 2005). Indeed, these isopycnals also correspond to the limits of the current and water mass cores of the region. The NBC core is located above $\sigma_\theta = 24.5 \text{ kg m}^{-3}$, while the NBUC core and the thermocline are located between $\sigma_\theta = 24.5 \text{ kg m}^{-3}$ and 26.8 kg m^{-3} (Bourlès et al., 1999a; Goes et al., 2005). Note that for the mean circulation in the upper layer (0-19 m), the current velocity was set equal to the first level of the ADCP data (i.e., 19 m) because the mixed-layer depth is deeper than 19 m throughout the region (Araujo et al., 2011; Assunção et al., 2020). This step may induce a slight bias due to the Ekman ageostrophic circulation, which is maximum at the sea surface and decreases with depth.

We estimated alongshore velocities between the shelf break (isobath 70 m) and 60 km offshore (or to the transect limit when shorter than 60 km from the shelf break). To represent the average velocities between 9°S and 6°S, we horizontally interpolated SADCP velocity data into 5 km bins from the shelf break to the outermost limit of each cross-shore transect. To better depict the latitudinal variations, we interpolated alongshore and cross-shore velocity data by latitude bins of 1°. We defined the NBUC core as the area where the alongshore velocities were greater than 70% of its maximum. This criterion, chosen after sensitivity tests permits to capture the core of the NBUC in the subsurface layer, as observed in previous studies where the NBUC

core was centred at 150-300 m (e.g., Bourlès et al. 1999b; Velede et al., 2011, 2012; Hummels et al., 2015; Herrford et al., 2020).

Mean transports (in Sv) and the associated standard deviations around the mean were calculated within the two layers described above (0-70 m and 70-350 m) and also in the range 0-500 m. Alongshore transports between 9.4°S and 5°S were computed between the shelf break and 20 km offshore (i.e., the offshore extent of the shortest transect).

Vertical profiles of physical and biogeochemical parameters were collected from the surface to 1000 m depth using a Seabird SBE911+ conductivity temperature depth (CTD) probe equipped with a dissolved oxygen sensor (CTDO). The temperature and conductivity sensors were laboratory-calibrated before and after each cruise. In total, 47 and 49 profiles were acquired during the cruises performed in austral spring 2015 and austral fall 2017, respectively. Conductivity, temperature and pressure accuracies were estimated to be 3 mS m⁻¹, 10-3°C and 0.7 dbar, respectively. Here, we considered only the profiles obtained off the shelf break (Figure 2). Following previous studies (Schott et al., 1995; Goes et al., 2005; Urbano et al., 2008), we selected data at distinct locations as reference sources for South Atlantic water (SAW) for austral spring and austral fall. The data sources used as reference sources for the SAW were acquired from the ETAMBOT cruise (Gouriou, 1995) at 4°S, 35°W (September 1995, austral spring) and from the World Ocean Atlas data set (<http://www.nodc.noaa.gov/OC5/WOD>) at 16°S, 24°W (May 1994, austral fall).

2.2 Altimetry and reanalysis data

To investigate mesoscale activity in the nearshore NEB region, we analysed satellite altimeter data of sea surface height (SSH) from the Data Unification and Altimeter Combination System (DUACS) multimission product. This dataset spans from January 1993 to the present and is mapped daily onto a 0.25° x 0.25° latitude/longitude grid (Ablain et al., 2015; Dupuy et al., 2016). This SSH product is based on measurements from several altimeter missions (Jason-3, Sentinel-3A, HY-2A, Saral/AltiKa, Cryosat-2, Jason-2, Jason-1, T/P, ENVISAT, GFO, and ERS1/2). The processing and distribution of the product is provided by the Copernicus Marine Environment Monitoring Service (CMEMS: <http://marine.copernicus.eu>).

SSH and geostrophic current conditions in spring 2015 and fall 2017 were used to identify the possible presence of mesoscale eddies and to investigate their impact on the nearshore circulation.

This dataset was also used to determine whether the conditions observed in spring 2015 and fall 2017 during the ABRAÇOS cruises are representative of the mean states for spring and fall or, in contrast, if these conditions differ from the mean climatological states. For this purpose, we constructed the climatology of SSH and geostrophic currents using data from January 1993 to December 2018 for all four seasons and more specifically for the two climatological periods corresponding to the ABRAÇOS surveys: spring (September 29 – October 21) and fall (April 8 – May 9). These climatologies were then compared to the SSH and geostrophic current conditions observed during spring 2015 and fall 2017. To facilitate the comparison, we also computed a map of SSH and geostrophic current anomalies between the climatology and survey conditions.

In addition, to compare our observations and replace them within a broader seasonal and interannual perspective we used the global ocean reanalysis product GLORYS12V1 that assimilates vertical profile and satellite data. This product is based on the current real-time global forecasting CMEMS system (<http://marine.copernicus.eu>). The ocean model component is the NEMO platform forced at the surface by ECMWF ERA-Interim reanalysis. Observations are assimilated by means of a reduced-order Kalman filter. This product is distributed on a standard regular grid at 1/12 degree and on 50 standard levels and consists on daily fields from 1993 to 2018.

3. Results

3.1 Water masses

TS diagrams and oxygen-salinity curves confirmed the dominance of South Atlantic water masses in the NEB region (Figure 3). Four water masses could be identified. In the surface layer (~0-100 m), lays the Tropical Atlantic water (TW) characterised by temperature $>25^{\circ}\text{C}$ and isopycnals σ_{θ} between 23 and 24.5 kg m^{-3} . Below, between ~80-150 m lays the Subtropical Underwater (SUW), characterized by maximum salinity (core salinity >36.5) and densities slightly below $\sigma_{\theta} 25 \text{ kg m}^{-3}$. Then, down to 500 m, lays the South Atlantic central water (SACW) characterised by temperatures ranging from 10°C to 23°C and salinities >35 ($24.5 < \sigma_{\theta} < 27 \text{ kg m}^{-3}$, Stramma and England, 1999). Finally, at greater depths, with $\sigma_{\theta} > 27 \text{ kg}$

m^{-3} , we observed the presence of Antarctic intermediate water (AAIW) characterized by low salinity (da Silveira et al., 1994; Stramma and England, 1999).

In the TW level, the temperature was $\sim 2^{\circ}\text{C}$ warmer in fall 2017 than spring 2015 (Figure 3a, b). The vertical extent of the maximal salinity core (SUW) was however greater in fall, especially towards the surface. This was consistent with the trend observed for the mixed layer depth and the upper thermocline and halocline depths that were shallower in fall than in spring (Figure 3; Assunção et al., 2020). The dissolved oxygen concentration was overall higher than $140 \mu\text{mol l}^{-1}$ along the water column except for two profiles in fall 2017, where a clear oxycline occurred with the dissolved oxygen concentration decreasing to $100 \mu\text{mol l}^{-1}$ in the depth range $\sim 150\text{--}400 \text{ m}$. These two profiles were located north of 4°S at 35°W and 34.5°W , where Eastern Atlantic Water, characterized by a low oxygen content, is transported by the equatorial branches of the south equatorial current (eSEC and cSEC).

3.2 Meridional variability of the NBUC/NBC currents and transport

In spring 2015 and fall 2017, the circulation along the northeastern Brazilian coast was predominantly equatorward between 9.4°S and 4.2°S , both in the upper (0–70 m) and subsurface (70–350 m) layers (Figure 4). However, in spring 2015, the upper layer equatorward flow weakened between 7.8°S and 8.3°S with even a southward flow occurring ($\sim -0.1 \text{ m s}^{-1}$). This pattern was also evidenced by the upper alongshore velocity that almost vanished at approximately 8.2°S (Figure 4c, blue line). This weakening was further observed in the subsurface circulation (Figure 4b, c), although to a lesser extent. Overall, the subsurface flow was consistently equatorward, which is characteristic of the NBUC, with an intensification between 8°S and 7°S (mean velocity reaching 1 m s^{-1}).

Contrary to spring 2015, during fall 2017, we did not observe any clear signal of weakening of the upper layer equatorward flow at $\sim 8^{\circ}\text{S}$ but a small flow reduction near 8.5°S (Figure 4d, e, f). Both surface and subsurface flows increased between 8°S and 7°S and at $\sim 5.5^{\circ}\text{S}$, with the mean velocities reaching 0.7 m s^{-1} and $\sim 1 \text{ m s}^{-1}$ in the upper and subsurface layers, respectively. In fall 2017, north of 5°S (no data were acquired north of 5°S in spring 2015), where the coastal orientation changes, the circulation was consistently northwestward in both layers but was comparatively weaker in the subsurface layer, especially at $4.2\text{--}5^{\circ}\text{S}$, $36\text{--}35.5^{\circ}\text{W}$. North of 4°S , the upper layer flow was greater than the subsurface flow between 35.5°W and 34.5°W . The 3D representations of the flow over the continental slope (Figure 5) provide a more

comprehensive view of the current dynamics (see Figure 2.S1 for 2D corresponding 2D section). During both seasons, the zonal flow was mainly eastward between 9°S and 7.5°S, with velocities up to 0.3 m s^{-1} . North of 7.5°S, this flow suddenly shifted westward with velocities reaching 0.3 m s^{-1} . In fall 2017, north of 5.7°S (no data for spring 2015), the westward strength of the zonal flow (Figure 5b) increased in the upper layer. However, the zonal flow was eastward in the subsurface layer over the region 5-4.8°S, 36-35.5°W. The meridional flow (Figure 5c, d) was dominantly equatorward along the coast at approximately 100-500 m depth with a clear intensification north of 8°S in spring 2015 and north of 6°S in fall 2017. In fall 2017, nevertheless, the flow strength decreased between 36°W and 35.5°W.

The alongshore velocity averaged between 9°S and 6°S revealed dominance of the NBUC with strong positive equatorward flow during both seasons (Figure 6). In spring 2015, the core of the NBUC (area where the alongshore velocity is greater than 70% of its maximum) extended from 105 m to more than 500 m depth and between 2 and 40 km from the shelf break, with velocities reaching 0.9 m s^{-1} (mean: 0.81 m s^{-1}) (Figure 6a). At depths less than ~100 m, the equatorward flow strongly weakened. The average total transport integrated between the shelf break and 40 km offshore and between the surface and 500 m depth was $15.6 \pm 4.3 \text{ Sv}$ (Figure 6b). The alongshore transport integrated between the shelf break and 40 km offshore was maximum ($> \sim 0.04 \text{ Sv m}^{-1}$) between 135 m and 450 m depth (Figure 6b), which corresponded to the NBUC core. Horizontally, the vertically integrated transport between the surface and 500 m depth was maximum ($> 0.8 \text{ km}^{-1}$) between 5 and 25 km from the shelf break (Figure 6c). In fall 2017 (Figure 6d, e, f), the NBUC velocity core was less intense and shallower but extended farther offshore than in spring 2015. Its velocity core ranged between ~80 m and 390 m depth and extended between 3 km and more than 40 km from the shelf break, with velocities reaching 0.7 m s^{-1} (mean: 0.65 m s^{-1}) (Figure 6d). Surface velocities were higher than in spring 2015 (Figure 6d), as also seen in Figure 5. With $11.0 \pm 2.6 \text{ Sv}$, the average total transport integrated between the shelf break and 40 km offshore and between the surface and 500 m depth was ~4.6 Sv weaker than in spring 2015. The mean alongshore transport integrated between the shelf break and 40 km offshore was maximum ($> \sim 0.03 \times 10^{-1} \text{ Sv m}^{-1}$) between 100 and 330 m depth (Figure 6e), which corresponded to the centre of the NBUC core. Horizontally, the integrated transport between the surface and 500 m depth was maximum ($> \sim 0.6 \text{ Sv km}^{-1}$) between 5 and 30 km from the shelf break (Figure 6f), similar to what was observed in spring 2015.

To better describe the meridional variation of the nearshore circulation and transport in the NEB region, we averaged the cross-shore sections by latitude bands of 1° between 9°S and 5°S (Figure 7; Table 1).

In spring 2015 (Figure 7a), between 9°S and 8°S , the NBUC velocity core was located between 160 m and 550 m depth and extended between the shelf break and 40 km offshore, with velocities up to 0.8 m s^{-1} . Above 100 m depth, the alongshore velocity was very weak with velocity values of less than 0.2 m s^{-1} . Between 8°S and 7°S , the cross-shore sections were shorter, hampering a robust estimate of the extent of the NBUC. The NBUC velocity core extended from ~ 120 m to more than 600 m depth and extended from the shelf break to the length of the cross-shore section (20 km). The velocity was higher than that farther south, reaching values up to 1.2 m s^{-1} (Figure 7a). Between 7°S and 6°S , the NBUC velocity core extended from 105 m to ~ 600 m depth and from ~ 5 km from the shelf break to the length of the section (30 km). Velocities were lower (up to 0.9 m s^{-1}) than those observed between 8°S and 7°S . Overall, in spring 2015, the NBUC velocity core increased from 0.8 m s^{-1} at 9°S to 1.2 m s^{-1} at 7°S and then decreased to 0.9 m s^{-1} , and its upper limit shallowed from 160 m at 9°S to 105 m at 6°S due to the strong vertical shear.

In fall 2017 (Figure 7b), between 9°S and 8°S , the NBUC velocity core was centred at 70-440 m depth and extended between the shelf break and 30 km offshore with velocity up to 0.7 m s^{-1} . Above 100 m depth, consistent velocity values ($> 0.3\text{ m s}^{-1}$) were observed. As in spring 2015, the NBUC velocity intensified north of 8°S . From 8°S to 5°S , the velocity core was rather consistent with the velocity reaching 1 m s^{-1} at 5°S . However, its vertical range and width varied according to the latitude bands. Between 8°S and 7°S , it was vertically extended to 50-350 m depth and located between the shelf break and ~ 40 km offshore, with velocity up to 0.9 m s^{-1} . In the latitude band 7°S - 6°S , the NBUC velocity core extended vertically from 80-380 m depth and horizontally between ~ 5 and 50 km from the shelf break, with velocity reaching 0.8 m s^{-1} . Between 6°S and 5°S , the NBUC velocity core was located at 50-340 m depth and ~ 5 and 50 km from the shelf break. Overall, in fall 2017, the NBUC velocity core increased from 0.7 m s^{-1} at 9°S to 1 m s^{-1} at 5°S , and its core shallowed from 70-440 m depth at 9°S to 50-350 m depth at 5°S . Note that in both spring 2015 and fall 2017, strong velocity shears were observed in the upper layer between the surface and 100 m depth or at the base of the NBUC core. These vertically sheared currents, characterized by vertical velocity gradients of $6.10^{-3}\text{ m s}^{-1}$ per m, might be baroclinically unstable, providing a mechanism of formation for mesoscale eddies (Bourlès et al. 1999b).

To estimate the whole transport of the NBUC, we also calculated the alongshore transport integrated between the shelf break and 20 km between 0 and 500 m (Figure 8). In addition, for comparison with earlier studies (Table 1), we estimated the transports between 0 and 70 m, and in the range 70-350 m, corresponding to the isopycnals $\sigma\theta = 24.5 \text{ kg m}^{-3}$ and $\sigma\theta = 26.8 \text{ kg m}^{-3}$.

In the upper layer (0-70 m), the transport was relatively weak ($\sim 0.4\text{-}2 \text{ Sv}$) and mainly northward between 9.2°S and 6°S during both periods (Figure 8). However, the transport was null or slightly southwards at $\sim 8^\circ\text{S}$ in spring 2015 (Figure 8). Due to the shallowing of the NBUC, the surface equatorward transport slightly increased northward from 0.7 Sv at 9°S to 1.2 Sv at 6°S . Surface transport was slightly stronger in fall 2017, particularly between 8.5°S and 7°S . In the subsurface layer (70-350 m), the alongshore transport associated with the equatorward-flowing NBUC varied between 4.5 and 11 Sv in both periods (Figure 8). The meridional variations were similar in both periods, with an overall increase from south (6.1 Sv at 8.5°S) to the north (9.4 Sv at 6.2°S), except at $9.2\text{-}8.5^\circ\text{S}$ and $7.1\text{-}7.6^\circ\text{S}$, where the transport was higher in spring 2015 than in fall 2017 ($\sim 2.9 \text{ Sv}$ difference).

The total alongshore transport calculated above 500 m depth varied between 6.2 Sv and 16.9 Sv in spring 2015 and between 7.2 Sv and 17.2 Sv in fall 2017 (Figure 8). Its meridional variations were similar in both periods. However, it was higher in spring 2015 than in fall 2017 at $9.2^\circ\text{S}\text{-}8.5^\circ\text{S}$ ($\sim 5.4 \text{ Sv}$ difference) and at $7.1^\circ\text{S}\text{-}6.5^\circ\text{S}$ ($\sim 6.5 \text{ Sv}$ difference). At $\sim 8.1^\circ\text{S}$, it weakened (6.2 Sv) in spring 2015.

3.3 NBUC/NBC transition

North of 5°S , the coastal orientation changes. In this region, the transition between the NBUC and the NBC has been previously reported (e.g., Schott et al., 1998; Bourlès et al., 1999a). To provide a comprehensive view of the current dynamics in this transitional region, we describe the circulation pattern between 5°S and 3°S during fall 2017 (Figure 9). The longitudinal (36.3°W - 34.7°W) variation of latitudinal transects ($4.1^\circ\text{S}\text{-}3.3^\circ\text{S}$) revealed the presence of a variety of features in this transitional area (Figure 9d). Between the surface and 70 m we observed a consistent westward transport (see Table 1 for transport calculations). This transport increased from east to west from -1.9 ± 0.1 at 34.7°W to $5.6 \pm 0.1 \text{ Sv}$ at 35.4°W and $6.3 \pm 0.1 \text{ Sv}$ at 36°W and 36.4°W (Table 1). According to previous works (e.g., Stramma et al., 1995;

Bourlès et al., 1999b), this flow can be related to the cSEC in the east and to the NBC west of 35.5°W with no clear limits (see also the geostrophic currents in Figure 9a). Below, we observed two main patterns. In the eastern transects (34.7°W - 36°W), a southeastward subsurface flow, characteristic of the SEUC, occurred. This southeastward flow observed north of 3.8°S had velocities of $\sim 0.1 \text{ m s}^{-1}$, a narrow vertical range ~ 250 - 350 m and a transport of 0.2 Sv in western transects. It increased to reach velocity up to 0.3 m s^{-1} , a vertical extension ranging from ~ 150 to 570 m and a transport up to 3.4 Sv in eastern transects (35°W - 34.7°W) (Figure 9d, Table 1 in bold). South of 3.8°S , between 36.3°W and 35°W , we observed a consistent northwestward flow over 0 - 500 m , associated with the NBUC/NBC, with a stronger zonal intensity (at 36.4°W the maximum speed and transport were of 1.4 m s^{-1} and $39.5 \pm 3.2 \text{ Sv}$, respectively) (Figure 9d).

Now, we describe the current dynamics latitudinally (5°S - 3.2°S) by two meridional bands (from east to west, Figure 9b and Figure 9c, as indicated in Figure 9a by green and red rectangles, respectively). First, in the region 34.7°W - 35.4°W (green rectangle), we observed a consistent northwestward surface flow, the NBC-cSEC (above $\sim 100 \text{ m}$), along 5°S - 3.3°S , with no clear limit between the NBC and the cSEC (Figure, 2.9a, b). The westward transport estimated between the surface and 70 m depth was $7.6 \pm 0.8 \text{ Sv}$ i.e., much higher than the transport arriving from the south (2.1 Sv ; Table 1) illustrating the role of the cSEC. Below this depth, the flow was consistently northwestward south of $\sim 3.8^{\circ}\text{S}$ with velocities up to 1 m s^{-1} (characteristic of the NBUC) (Figure 9b). The westward transport crossing the section 35°W at 70 - 350 m depth was $15.8 \pm 4.6 \text{ Sv}$. Finally, north of $\sim 3.8^{\circ}\text{S}$, the flow was mainly southeastward (characteristic of the SEUC) in the depth range of ~ 120 - 330 m , with velocity up to 0.2 m s^{-1} and was associated with eastward transport up to $2.6 \pm 1.2 \text{ Sv}$.

Second, in the region 35.3°W - 36°W (red rectangle), we observed a surface northwestward flow along 5°S - 3.3°S with velocity up to 1 m s^{-1} (Figure 9c). The westward transport crossing the section at 35.8°W , estimated between the surface and 70 m depth, was $8.7 \pm 1.1 \text{ Sv}$. In the subsurface layer, the patterns varied with latitude. South of 4.8°S we observed a northwestward pattern consistent with the NBUC. Between 4.8°S and $\sim 4.4^{\circ}\text{S}$, the subsurface flow was mainly positive (eastward) with no clear meridional pattern. We cannot propose a clear diagnosis for this region that is likely affected by complex orographic processes. Between $\sim 4.4^{\circ}\text{S}$ and 3.7°S , the flow was consistently northwestward over the water column but stronger (characteristic of the NBC) in the surface layer (above $\sim 150 \text{ m}$). In the depth range of 70 - 350 m depth, the westward transport crossing the section 5°S - 3.3°S , 35.3°W - 36°W increased to $14.2 \pm 4.2 \text{ Sv}$. Finally, north of 3.7°S , we observed a northwestward flow above $\sim 150 \text{ m}$, an eastward flow

between ~150 m and 300 m with 0.6 Sv as eastward transport, and a weak southwestern flow in the range of ~300-600 m.

3.4. Mesoscale activity and representativeness of spring 2015 and fall 2017 conditions

When comparing the SSH and surface geostrophic currents between the seasonal climatologies and the conditions observed during the surveys (Figure 10) in the slope region, we observe similar patterns with, however, some differences. Indeed, the SSH was higher overall during spring 2015 and fall 2017 when compared with climatological conditions. However, although the SSH was higher, geostrophic currents were overall similar in the study area ($\sim 0.3\text{-}0.4\text{ m s}^{-1}$) when comparing the survey periods to climatological conditions (maximal difference in current velocity $< 0.1\text{ m s}^{-1}$). Differences in geostrophic currents are notable only in regions where mesoscale eddies occurred during the survey periods. Indeed, mesoscale activity is flattened in climatological pictures but clear when considering the survey periods, which explains these eddy-related differences.

The nearshore geostrophic circulation was mainly equatorward in the NEB region during spring 2015 (Figure 10). However, as indicated above, we observed an area between 7.8°S and 8.3°S with weak surface currents and even the occurrence of southward flow (Figure 10a, c). This area matches the presence of an anticyclonic eddy with a radius of $\sim 50\text{ km}$ that locally impacted the surface circulation (Figure 10b; Supplementary material Figure 2.S2). The impact of this eddy was, to a lesser extent, also observable in the subsurface (Figure 4b, c). The coastal eddy observed in our data evolved slightly during the survey period. On October 10, 2015, it extended longitudinally over $35\text{-}34^{\circ}\text{W}$, with its core located at 8.9°S , 34.1°W . Then, it moved slightly around its origin position and disappeared 10 days later.

In fall 2017, the nearshore geostrophic circulation was also mainly equatorward (Figure 10). Several eddies were detected (Supplementary material Figure 2.S3). For instance, between $6\text{-}7^{\circ}\text{S}$ and $34.5\text{-}33.5^{\circ}\text{W}$, a cyclonic eddy with a radius of $\sim 55\text{ km}$ was observed offshore on April 13, 2017, but it disappeared two days later. Another cyclonic eddy was detected offshore in the southern part of the study area ($34^{\circ}\text{W}\text{-}32^{\circ}\text{W}$, $10^{\circ}\text{S}\text{-}8^{\circ}\text{S}$). This eddy originated at 33°W , 8.8°S on April 13, 2017, and disappeared on April 30, 2017, with a constant position (Supplementary material Figure 2.S3). This eddy occurred oceanward of the survey area. We could not observe any clear impact of this eddy on the nearshore circulation except in the extreme southern survey area where surface equatorward circulation seemed enhanced (Figures 2.4, 10).

Another important question is the extent to which the features we described for spring 2015 and fall 2017 are representative of canonical spring and fall conditions and these conditions ranges within the overall seasonal maximum and minimum.

For this purpose, we considered the use of GLORYS12V1 reanalysis products for the period 1993-2018. The climatological seasonal variability reproduced by GLORYS for the 6°-9°S latitudinal band between the shelf-break and 150 km offshore is weak (Supplementary material Figure 2.S4). More specifically, if we compare the GLORYS climatologies for the fall and spring seasons with the GLORYS product corresponding to the periods of the two ABRAÇOS surveys (Supplementary material Figure 2.S5) we notice several limitations. First, the position of the NBUC core is shifted offshore by about 15 km with respect to our observations. Moreover, if GLORYS12V1 represents the upward extent of the core in austral autumn, the seasonality of the transport is reversed with respect to our observations. Thus, current GLORYS products therefore seem to have drawback in this near-coastal zone that prevent the use of this product as a reliable baseline.

As previously indicated, we observed similar patterns of SSH and surface geostrophic currents between the seasonal climatologies and the conditions observed during the surveys in the slope region (Figure 10). If we put the spring and fall conditions in perspective within the total seasonal cycle, we can see that these two seasons do correspond to contrasted states (Supplementary material Figure 2.S6). We prepared maps of interpolated geostrophic current for spring 2015, fall 2017 and the climatology for spring and fall for the period 1993-2018 (Supplementary material Figure 2.S7). On this basis, we first compared the seasonal differences (spring minus fall) for the periods of the two surveys and for the 1993-2018 climatologies. In the study area, the patterns are remarkably similar although, quite logically, the differences are a slightly more marked in the case of the spring 2015 - fall 2017 comparison than in that of the climatologies. Now if we compare the geostrophic currents of spring 2015 to the spring climatology and fall 2017 to the fall climatology, we also observe small differences in the study area.

4. Discussion

In this study, we used SADCP, CTDO and altimetry data to portray the ocean circulation over the continental slope of the NEB in austral spring 2015 and fall 2017. Our study is based on synoptic observations. Before discussing the results, it is important to investigate the representativeness of our data. Since re-analysis products (GLORYS12V1) showed to have limitations in this near-shore region, we could only base our comparison on geostrophic

currents. The differences between the conditions observed in spring 2015 and fall 2017 with the climatological conditions for these seasons are small (Figure 10; Supplementary material Figure 2.S7). In addition, using both direct observations and numerical simulations, Hummels et al. (2015) showed that the average transport of the North Brazil Undercurrent at 11°S did not change between 2000–2004 and 2013–2014. Moreover, Assunção et al. (2020) did not observe any significant differences in the thermohaline structure of the region during spring 2015 and fall 2017 when compared with the same periods from other years. For all these reasons we can reasonably consider that the conditions observed during the ABRAÇOS surveys in spring 2015 and fall 2017 are representative of the canonical conditions of spring and fall, which allows us to address seasonal changes to a certain extent. Using these data, we provide a high-resolution description of the NBUC characteristics in the two seasons and a comprehensive picture of the NBUC/NBC transition in fall.

4.1. NBUC features and variability

Current measurements acquired during surveys display the NBUC trapped along the NEB coast between 9°S and 5°S (Figures 2.6 and 7). Its maximum velocity is on average centred at approximately 200–300 m depth with velocity that can locally reach 1.2 m s^{-1} in spring 2015, in accordance with Silveira et al. (1994). The NBUC carries equatorward high-salinity and oxygen-enriched South Atlantic Water (Bourlès et al. 1999a) (Figure 3) within its core and exhibits higher transport in spring than fall (Figures 4–9; Table 1). In the surface layer, transport was slightly higher in fall 2017 than in spring 2015 (Figure 8; Table 1) due to an observed shallower NBUC core in the fall. It is difficult to directly compare our results with previous studies since they were mostly performed at a specific latitude and period and with a variety of methods. In Table 1, we provide a synthesis of current transport from this and other studies. It shows that our results fall within previous measurements but provide a more detailed picture.

Between 9°S and 6°S, the NBUC mean velocity and transport (Figures 2.4 to 7) were higher in spring 2015 than in fall 2017 (difference of 0.2 m s^{-1} in velocity and 5 Sv in transport). In addition, the vertical extent of the NBUC velocity core was higher in spring 2015 (110 m to more than 500 m depth) than in fall 2017 (50–410 m). These results bring additional information to previous studies based on both in situ data (Stramma et al., 1995; Schott et al., 2005; Veleda et al., 2012; Hummels et al., 2015; Herrford et al., 2020) and numerical simulations (Rodrigues et al., 2007; Silva et al., 2009; Veleda et al., 2011; Herrford et al., 2020). These studies reported

a seasonal variability of the near surface sSEC-NBUC-BC (BC for Brazil Current) system transports associated with changes in the local wind stress curl due to the annual north–south excursion of the Inter Tropical Convergence Zone. Indeed, in austral winter, the sSEC bifurcation latitude reaches its southernmost position, the NBUC transport is higher and BC transport is lower (e.g., Rodrigues et al., 2007; Silva et al., 2009). In contrast, the near surface sSEC bifurcation latitude is located at the northernmost position during summer, when the NBUC transport is seasonally lower and the BC transport is higher. The wind velocity follows this pattern with highest values ($>9 \text{ m s}^{-1}$) between August and December and lowest velocities ($<8 \text{ m s}^{-1}$) in April-May (Domingues et al., 2017).

The equatorward increase in NBUC strength was accompanied by an increase in its core (Figure 7a, b). As previously described (e.g., Schott et al., 1998), this upward pattern is attributed to the Ekman drift, which is less intense north of the area (Stramma et al., 1995). Indeed, the westerly-driven Ekman drift is southwestward in the region, constraining the equatorward flow to the subsurface from its origin to approximately 5°S , from where it decreases.

Another reason for the latitudinal variation in the NBUC along the NEB continental slope is the orography effect. Whatever the season, we observed a change in the zonal flow, shifting from eastward south of 7.5°S to westward farther north (Figure 5a, b), and the intensification of the equatorward flow between 8°S and 7°S (Figures 2.4c, f and 2.5). This consistency suggests that the coastal curvature affects the mean nearshore circulation characteristics. In fact, using a two-layer model, Ou and De Ruijter (1986) pointed out that boundary currents are subjected to a separation where a positive coastal curvature occurs. Their calculation showed that the separation is dominantly controlled by inertial and beta effects.

4.2. NBUC/NBC transition

The region located north of 5°S , between 36.5°W and 34.5°W , is a crucial transition area where the SEUC and the NBC (Schott et al., 1998; Bourlès et al., 1999a, b; Goes et al., 2005) originate. Here, we provide a comprehensive description of the NBUC/NBC transition, its interaction with the cSEC, and further evidences about the origin of the SEUC. The image we propose is based on fall 2017 data only, but the feature and position of this transition should not significantly vary according to the season. Indeed, surface currents are stronger in this transitional area during fall than spring, but the position where the geostrophic current increases is alike (Supplementary material, Figures 2.S5 and 2.S6). In this area, the NBUC and the cSEC

coalesce to form the NBC (Figure 9) as already depicted by previous works (Stramma et al., 1995; Bourlès et al., 1999b; Schott et al., 1995, 1998). Moving to the west, a clear distinction between the NBC and the cSEC is no longer possible in the upper layer.

More precisely, the mean NBUC inflow crossing 5°S in the surface layer (0-70 m) was up to 1.8 Sv (Figure 8). North of this latitude (5°S - 3.3°S), at 35°W , this upper layer transport increased to 7.6 ± 0.8 Sv. The observed rapid increase in surface transport at 5°S is due to the cSEC input, that overlies the NBUC (Figure 9a, b). Thus, the net contribution of the cSEC to the surface western boundary flow is the difference between the upper layer transports observed at 5°S (1.8 Sv) and 35°W (7.6 Sv). Therefore, this contribution is 5.8 Sv. These results agree with previous studies (Table 1). In particular, Schott et al. (2003) estimated the cSEC transport between 4°S and 2.5°S up to 7 Sv above the $\sigma_{\theta} = 24.5$ isopycnal (70 m).

Table 1. Synthesis of transport (in Sv) estimations in the upper and lower layers (the precise depth range is provided in each case) across sections between 10°S and 3°S over the continental slope of the Northeast Brazil from this and previous works. The longitudinal extent of the sections is expressed in longitude or in distance from the shelf break. In some sections, north of 5°S we observed both a westward zonal transport corresponding to the NBUC/NBC system and a zonal eastward transport corresponding to the SEUC. In this case we added, in bold, the transport calculation related to the SEUC. Note that in Stramma et al. (1995), the calculated transport corresponds to the geostrophic transport computed from CTD data.

Reference	Sections	Upper layer	Lower layer	Total transport	Period
This study	9°S-6°S, 0-40 km	0.8±0.4 (0-70 m)	9.4±2.3 (70-350 m)	15.6±4.3 (0-500 m)	Spring (Sept. –Oct.) 2015
This study	9°S-8°S, 0-55 km	0.8±0.3 (0-70 m)	8.7±2.2 (70-350 m)	14.9±4.8 (0-500 m)	Spring (Sept. –Oct.) 2015
This study	8°S-7°S, 0-20 km	0.5±0.2 (0-70 m)	8.1±0.9 (70-350 m)	12.8±1.7 (0-500 m)	Spring (Sept. –Oct.) 2015
This study	7°S-6°S, 0-30 km	0.8±0.3 (0-70 m)	7.8±1.4 (70-350 m)	12.9±2.5 (0-500 m)	Spring (Sept. –Oct.) 2015
This study	9°S-6°S, 0-40 km	1.3±0.4 (0-70 m)	8.0±1.8 (70-350 m)	11.0±2.6 (0-500 m)	Fall (April- May) 2017
This study	9°S-8°S, 0-35 km	0.8±0.4 (0-70 m)	5.8±1.2 (70-350 m)	9.2± 2.0 (0-500 m)	Fall (April- May) 2017
This study	8°S-7°S, 0-50 km	1.7±0.3 (0-70 m)	10.5±1.3 (70-350 m)	15.3±2.5 (0-500 m)	Fall (April- May) 2017
This study	7°S-6°S, 0-50 km	1.8±0.3 (0-70 m)	10.4± 1.2 (70-350 m)	15.6±2.4 (0-500 m)	Fall (April- May) 2017
This study	6°S-5°S, 0-35 km	2.1±0.4 (0-70 m)	11.4± 1.6 (0-350 m)	16.8±1.7 (0-500 m)	Fall (April- May) 2017
This study	5°S-3.3°S, 34.7°W-35.3°W	7.6±0.8 (0-70 m)	15.8±4.6 (70-350 m)	-	Fall (April- May) 2017
This study	3.8°S-3.3°S, 34.7°W- 35.3°W	-	2.6±1.2 (120- 330 m)	-	Fall (April- May) 2017
This study	5°S-3.3°S, 35.3°W-36°W	8.7±1.1 (0-70 m)	14.2±4.2 (70-350 m)	-	Fall (April- May) 2017
This study	5°S-3.3°S, 35.3°W-36°W	-	0.6 ±0.1 (150- 300 m)	-	Fall (April- May) 2017
This study	34.7°W, 3.3°S-3.8°S	1.9 ± 0.1 (0- 70 m)	0.7±0.0 (70-350 m)	2.8±0.2 (0 -600 m)	Fall (April- May) 2017
This study	34.7°W, 3.3°S-3.8°S	-	2.1±0.1 (140 - 600 m)	-	Fall (April- May) 2017
This study	35°W, 3.3°S-4.1°S	4.5±0.1 (0 – 70 m)	1.7 ± 0.4 (70-350 m)	7.9 ±0.9 (0-600 m)	Fall (April- May) 2017

This study	35°W, 3.3°S-4.1°S	-	3.4±0.7 (120 – 570 m)	-	Fall (April- May) 2017
This study	35.4°W, 3.3°S-4.1°S	5.6± 0.1(0-70 m)	13.9 ± 0.5 (70-350 m)	21.6±1.2 (0-600)	Fall (April- May) 2017
This study	35.4°W, 3.3°S-4.1°S	-	0.4±0.1 (100 – 350 m)	-	Fall (April- May) 2017
This study	35.7°W, 3.3°S-4.1°S	6.1 ±0.3 (0-70 m)	12.4± 0.8(70 -350 m)	23.6 ± 2.1 (0-600 m)	Fall (April- May) 2017
This study	35.7°W, 3.3°S-4.1°S	-	0.2±0.0 (150 – 400 m)	-	Fall (April- May) 2017
This study	36°W, 3.3°S-4.1°S	6.3 ± 0.1 (0-70 m)	18.5 ±1.2 (70-350 m)	32.1 ± 2.7 (0-600 m)	Fall (April- May) 2017
This study	36.4°W, 3.3°S-4.1°S	6.3±0.1 (0-70 m)	22.8 ± 1.1	39.5 ± 3.2 (0- 600 m)	Fall (April- May) 2017
Silveira et al. (1994)	7°S, 34.5°W-32°W	9.1 (0-150 m)	-	17.3 (0-500 m)	May-July 1986
	8.5°S, 34.6°W-33°W	8.3 (0-150 m)	-	20.4 (0-500 m)	May-July 1986
Schott et al. (1998)	5°S, 35°W-32.5°W	1.8 (0-70 m)	11.7 (70-350 m)	-	Oct. 1990
	5°S, 35°W-32°W	2.1 (0-70 m)	11.1 (70-350 m)	-	March 1994
	5°S, 35°W-32.5°W	2.6 (0-70 m)	8.2 (70-350 m)	-	Oct. 1992
	10°S, 35°W-32.5°W	0.8 (0-70 m)	11.7 (70-350 m)	-	Oct. 1992
	10°S, 35°W-32°W	0.6 (0-70 m)	9 (70-350 m)	-	March 1994
Schott et al. (2002)	5°S, 35°W-33°W	2.7±1.8 (0-70 m)	13.4±2.7 (70-350 m)	-	Mean of 6 sections (1990 & 2000)
Goes et al. (2005)	5°S, 35°W-34°W	2.3 (0-70 m)	12.3 (70-350 m)	-	Feb. 2002
	35°W, 5.2°S-3.8°S	6.5 (0-70 m)	16.9 (70-350 m)	-	Feb. 2002
	35°W, 4°S-2°S	-	3.3 (120 – 405 m)	-	Feb. 2002
Stramma et al. (1995)	5.5°S, 35°W-33.5°W	2.9 (0-100 m)	-	19.3 (0-500 m)	Oct. 1990
	5.5°S, 35°W-32.46°W	2.9 (0-100 m)	-	19.3 (0-500 m)	Nov. 1992
	10°S, 35.5°W-34.25°W	2.5 (0-100 m)	-	16.0 (0-500 m)	Nov. 1992
Bourlès et al. (1999b)	5°S, 35°W-34°W	3.8 (0-70 m)	10.6 (70-350 m)	-	Feb. 1993
Bourlès et al. (1999b)	35°W,4°S-3°S	-	3.1 (70 -350 m)	-	Feb. 1993
Bourlès et al. (1999b)	35°W, 5°S-2°S	8.6 (0-70 m)	15.6 (70-350 m)	-	April 1996
Bourlès et al. (1999b)	35°W,4°S-3°S	-	2.1 (70 -350 m)	-	April 1996

Schott et al. (1995)	35°W, 5°S-3.2°S	5.1 (0-70 m)	13.1 (70-350 m)	-	March 1994
Schott et al. (2005)	5°S, 35°W-32°W	3.8 (0-70 m)	14.2 (70-350 m)	-	Mean of 9 sections (2000-2004)
Reference	Sections	Upper layer	Lower layer	Total transport	Period
This study	9°S-6°S, 0-40 km	0.8±0.4 (0-70 m)	19.4±2.3 (70-350 m)	115.6±4.3 (0-500 m)	Spring (Sept. –Oct.) 2015
This study	9°S-8°S, 0-55 km	0.8±0.3 (0-70 m)	8.7±2.2 (70-350 m)	14.9±4.8 (0-500 m)	Spring (Sept. –Oct.) 2015
This study	8°S-7°S, 0-20 km	0.5±0.2 (0-70 m)	8.1±0.9 (70-350 m)	112.8±1.7 (0-500 m)	Spring (Sept. –Oct.) 2015
This study	7°S-6°S, 0-30 km	0.8±0.3 (0-70 m)	7.8±1.4 (70-350 m)	112.9±2.5 (0-500 m)	Spring (Sept. –Oct.) 2015
This study	9°S-6°S, 0-40 km	1.3±0.4 (0-70 m)	8.0±1.8 (70-350 m)	11.0±2.6 (0-500 m)	Fall (April- May) 2017
This study	9°S-8°S, 0-35 km	0.8±0.4 (0-70 m)	5.8±1.2 (70-350 m)	19.2± 2.0 (0-500 m)	Fall (April- May) 2017
This study	8°S-7°S, 0-50 km	1.7±0.3 (0-70 m)	10.5±1.3 (70-350 m)	15.3±2.5 (0-500 m)	Fall (April- May) 2017
This study	7°S-6°S, 0-50 km	1.8±0.3 (0-70 m)	10.4± 1.2 (70-350 m)	15.6±2.4 (0-500 m)	Fall (April- May) 2017
This study	6°S-5°S, 0-35 km	2.1±0.4 (0-70 m)	11.4± 1.6 (0-350 m)	16.8±1.7 (0-500 m)	Fall (April- May) 2017
This study	5°S-3.3°S, 34.7°W-35.3°W	7.6±0.8 (0-70 m)	15.8±4.6 (70-350 m)	-	Fall (April- May) 2017
This study	3.8°S-3.3°S, 34.7°W-35.3°W	-	2.6±1.2 (120- 330 m)	-	Fall (April- May) 2017
This study	5°S-3.3°S, 35.3°W-36°W	8.7±1.1 (0-70 m)	14.2±4.2 (70-350 m)	-	Fall (April- May) 2017
This study	5°S-3.3°S, 35.3°W-36°W	-	0.6 ±0.1 (150- 300 m)	-	Fall (April- May) 2017
This study	34.7°W, 3.3°S-3.8°S	1.9 ± 0.1 (0- 70 m)	0.7±0.0 (70-350 m)	2.8±0.2 (0 -600 m)	Fall (April- May) 2017
This study	34.7°W, 3.3°S-3.8°S	-	2.1±0.1 (140 - 600 m)	-	Fall (April- May) 2017
This study	35°W, 3.3°S-4.1°S	4.5±0.1 (0 – 70 m)	1.7 ± 0.4 (70-350 m)	7.9 ±0.9 (0-600 m)	Fall (April- May) 2017
This study	35°W, 3.3°S-4.1°S	-	3.4±0.7 (120 – 570 m)	-	Fall (April- May) 2017
This study	35.4°W, 3.3°S-4.1°S	5.6± 0.1(0-70 m)	13.9 ± 0.5 (70-350 m)	21.6±1.2 (0-600)	Fall (April- May) 2017
This study	35.4°W, 3.3°S-4.1°S	-	0.4±0.1 (100 – 350 m)	-	Fall (April- May) 2017

One overarching question in the literature is the development of the NBUC after crossing 5°S. It is known that after the generation of the NBC in the upper layer, a subsurface part of the NBUC continues flowing in the same direction as the NBC (e.g., Bourlès et al., 1999b). The increase in NBUC transport from 6.1-11.5 Sv (Figure 8) south of 5°S to 15.8 ± 4.6 Sv north of this latitude at 35°W (Table 1, this study) implies that the contribution of the cSEC to the western boundary equatorward flow is not restricted to the upper layer. The subsurface cSEC contribution maintains the NBUC flow northwestward after the formation of the NBC in the upper layer (Bourlès et al., 1999b; Goes et al., 2005).

On the other hand, there is still no consensus on the origins of the SEUC. Schott et al. (2002) found that high oxygen values in the SEUC suggest a western boundary origin, while Schott et al. (1995, 1998) did not observe any contribution of the NBUC to the SEUC and rather suggested that the SEUC originates from the SEC recirculation. Our results help to settle the debate. North of 3.8°S, at 35°W, the core of the SEUC extends from 120-330 m depth with velocity up to 0.2 m s^{-1} and transports 2.6 ± 1.2 Sv (Figure 9b), also in accordance with previous studies (e.g., Bourlès et al., 1999b; Schott et al., 2003; Goes et al., 2005). Our hydrographic data show that the water mass at 3.8°S, 35°W (Figure 11c), corresponding to SEUC, is oxygen-depleted in the subsurface, contrary to the NBUC, which is characterized by a high oxygen content (Figure 11a, b). This illustrates that the SEUC is actually supplied by interior recirculation of the near-equator cSEC, and eSEC waters from the east, as proposed by Schott et al. (1995, 1998, 2002), and not by the NBUC. On the other hand, the eastward flow observed at 35.8°W, south of 4.4°S at ~100-600 m (Figure 9c), is not well documented, probably because of a lack of data close to the coast. This flow pattern may be due to the topographic effect on the large-scale circulation.

4.3. Impact of Mesoscale activity

We also report the impact of mesoscale activity on the mean nearshore circulation of the NEB region. In spring 2015, an anticyclonic eddy centred at 8.5°S between 35°S and 34°W (Figure 10b, Supplementary material Figure 2.S2) locally weakened the nearshore circulation in the NEB area (Figure 4c). In fall 2017, a cyclonic eddy centred at 33°W, 8.8°S slightly enhanced the nearshore surface circulation in the extreme southern part of the survey area (Figures 2.10, Supplementary material Figure 2.S3). Such mesoscale eddy impacts on large-scale circulation with weakening or intensification of local circulation have already been evidenced in western

(Ma et al., 2016) and eastern (Chaigneau et al., 2013; Czeschel et al., 2011) boundary systems in the Pacific Ocean, but never in the western boundary along the NEB.

5. Summary and Conclusion

The western boundary currents offshore Brazil are a key region of wind and thermohaline-induced circulation in the Atlantic Ocean. This part of the ocean works as a kind of "highway", where important components of the Atlantic meridional overturning circulation (AMOC) and the Atlantic subtropical cell meet. Direct observations along the Northeast Brazil shoreline confirm the southward transport of cold deep waters associated with the northward transport of warm and intermediate waters through the Northern Brazilian Undercurrent. Considering this geophysical situation important scientific efforts have been achieved (Schott et al., 2003, 2005; Hummels et al., 2015; Herrford et al., 2020; Bourlès et al., 2019; Foltz et al., 2019). Although all these efforts have been notable, there were still a lack of information about the spatial variability of the western boundary circulation along the Northeast Brazilian coast.

This study complement the understanding of the dynamics of the western boundary currents in the south tropical Atlantic, including the NBUC/NBC system in two seasons. By continuous coverage along the NEB continental slope (9.4°S-3.4°S), we fill the gap left by previous works that mostly focused on few specific latitudes, as above discussed. We describe the seasonal and spatial variations in NBUC characteristics resulting from ocean-atmosphere processes, orographic effects, and mesoscale activity. In addition, we describe in detail the NBUC/NBC transition and settle the debate about the origin of the SEUC. From these results, we propose an updated description of the shallow western boundary circulation along the NEB (Figure 1). The NBUC originating south of 10°S flows equatorward over the continental slope in the NEB region. This equatorward flow is locally influenced by mesoscale activity. The orographic effect shifts the zonal flow from eastward south of 7.5°S to westward north of 7.5°S. At ~4.8°S, the cSEC enters the equatorward flow system where it coalesces with the NBUC to form the NBC, which flows northwestward toward the Caribbean Sea. In the subsurface layer, the NBUC continues flowing together with NBC, after receiving the cSEC contribution in the subsurface. Finally, contrary to what had been proposed by some authors (e.g., Bourlès et al., 1999) the NBUC retroflection does not aliment the SEUC, which, instead, is originated by retroflections of the eSEC and the cSEC.

Recently, a decadal increase in salinity in the central waters at 11°S off Brazil has been detected (Hummels et al., 2015). In addition, different numerical experiments suggested a trend to an increase in Agulhas leakage (Chang et al., 2008; Biastoch et al., 2009; Zhang et al., 2011). In this context of changing ocean, the more comprehensive description of the western boundary circulation off Northeast Brazil presented herein will also certainly serve as a reference for diagnosing future variations in the upper/warm tropical branch of the Atlantic Meridional Overturning Circulation - AMOC.

Acknowledgments

We acknowledge the French oceanographic fleet for funding ABRAÇOS 1 and 2 ship-time and the officers and crew of the R/V Antea for their contribution to the success of the operations. Pierre Lopez (IRD, MARBEC) is thanked for editing Figure 1. This work was supported by the CAPES (Coordenação de Aperfeiçoamento de Pessoal de Nível Superior) through a PhD scholarship grant for A.N.D. M.A. appreciates the support of the Brazilian Research Network on Global Climate Changes – Rede CLIMA (FINEP-CNPq 437167/2016-0) and the Brazilian National Institute of Science and Technology for Tropical Marine Environments - INCT AmbTropic (CNPq/FAPESB 565054/2010-4 and 8936/2011). This work is a contribution to the International Joint Laboratory TAPIOCA (www.tapioca.ird.fr), to the SMAC project (CAPES/COFECUB n° 88881.142689/2017–01), the PADDLE project (funding by the European Union’s Horizon 2020 research and innovation programme - grant agreement No. 73427), and to the TRIATLAS project, which has also received funding from the European Union’s Horizon 2020 research and innovation program under grant agreement No 817578.

References

- Ablain, M., Cazenave, A., Larnicol, G., Balmaseda, M., Cipollini, P., Faugère, Y., Fernandes, M.J., Henry, O., Johannessen, J.A., Knudsen, P., Andersen, O., Legeais, J., Meyssignac, B., Picot, N., Roca, M., Rudenko, S., Scharffenberg, M.G., Stammer, D., Timms, G., Benveniste, J., 2015. Improved sea level record over the satellite altimetry era (1993-2010) from the Climate Change Initiative project. *Ocean Science* 11, 67–82. <https://doi.org/10.5194/os-11-67-2015>
- Arhan, M., Mercier, H., Bourlès, B., Gouriou, Y., 1998. Hydrographic sections across the Atlantic at 7°30N and 4°30S. *Deep-Sea Research Part I: Oceanographic Research Papers* 45, 829–872. [https://doi.org/10.1016/S0967-0637\(98\)00001-6](https://doi.org/10.1016/S0967-0637(98)00001-6)

- Assunção, R.V., Costa da Silva, A., Roy, A., Bourlès, B., Silva, C.H., TERNON, J.F., Araujo, M., Bertrand A., 2020. 3D characterisation of the thermohaline structure in the southwestern tropical Atlantic derived from functional data analysis of in situ profiles. *Progress in Oceanography*, 187: 102399. <https://doi.org/10.1016/j.pocean.2020.102399>.
- Bertrand A. 2015. ABRACOS Cruise, RV Antea, <https://doi.org/10.17600/15005600>.
- Bertrand A. 2017. ABRACOS 2 Cruise, RV Antea, <https://doi.org/10.17600/17004100>.
- Biaostoch, A., Böning, C.W., Schwarzkopf, F.U., Lutjeharms, J.R.E., 2009. Increase in Agulhas leakage due to poleward shift of Southern Hemisphere westerlies. *Nature* 462, 495–498. <https://doi.org/10.1038/nature08519>
- Bourlès, B., D’Orgeville, M., Eldin, G., Gouriou, Y., Chuchla, R., DuPenhoat, Y., Arnault, S., 2002. On the evolution of the thermocline and subthermocline eastward currents in the Equatorial Atlantic. *Geophysical Research Letters* 29, 32-1-32-4. <https://doi.org/10.1029/2002GL015098>
- Bourlès, B., Gouriou, Y., Chuchla, R., 1999a. On the circulation in the upper layer of the western equatorial Atlantic. *Journal of Geophysical Research: Oceans* 104, 21151–21170. <https://doi.org/10.1029/1999JC900058>
- Bourlès, B., Molinari, R.L., Johns, E., Wilson, W.D., 1999b. Upper layer currents in the western tropical North Atlantic (1989-1991). *Journal of Geophysical Research* 104, 1361–1375.
- Bourles, B., Molinari, R.L., Johns, E., Wilson, W.D., Leaman, K.D., 2002. Upper layer currents in the western tropical North Atlantic (1989-1991). *Journal of Geophysical Research: Oceans* 104, 1361–1375. <https://doi.org/10.1029/1998jc900025>
- Bourlès, B., Araujo, M., McPhaden, M. J., Brandt, P., Foltz, G. R., Lumpkin, R., Giordani, H., Hernandez, F., Lefèvre, N., Nobre, P., Campos, E. Saravanan, R., Trotte-Duhà, J., Dengler, M., Hahn, J., Hummels, R., Lübbecke, J.F., Rouaut, M., Citrim, L., Sutton, A., Jochum, M., Perez, R.C., 2019. PIRATA: A sustained observing system for tropical Atlantic climate research and forecasting. *Earth and Space Science*, 6(4), 577-616. <https://doi.org/10.1029/2018EA000428>
- Chaigneau, A., Dominguez, N., Eldin, G., Vasquez, L., Flores, R., Grados, C., Echevin, V., 2013. Near-coastal circulation in the Northern Humboldt Current System from shipboard ADCP data. *Journal of Geophysical Research: Oceans* 118, 5251–5266. <https://doi.org/10.1002/jgrc.20328>
- Chang, P., Zhang, R., Hazeleger, W., Wen, C., Wan, X., Ji, L., Haarsma, R.J., Breugem, W.P., Seidel, H., 2008. Oceanic link between abrupt changes in the north Atlantic ocean and the African monsoon. *Nature Geoscience* 1, 444–448. <https://doi.org/10.1038/ngeo218>
- Chelton, D.B., Schlax, M.G., Samelson, R.M., 2011. Global observations of nonlinear mesoscale eddies. *Progress in Oceanography* 91, 167–216. <https://doi.org/10.1016/j.pocean.2011.01.002>

- Chelton, D.B., Schlax, M.G., Samelson, R.M., de Szoeke, R.A., 2007. Global observations of large oceanic eddies. *Geophysical Research Letters* 34, 1–5. <https://doi.org/10.1029/2007GL030812>
- Czeschel, R., Stramma, L., Schwarzkopf, F.U., Giese, B.S., Funk, A., Karstensen, J., 2011. Middepth circulation of the eastern tropical South Pacific and its link to the oxygen minimum zone. *Journal of Geophysical Research: Oceans* 116, 1–13. <https://doi.org/10.1029/2010JC006565>
- da Silveira, I.C.A., de Miranda, L.B., Brown, W.S., 1994. On the origins of the North Brazil Current. *Journal of Geophysical Research* 99, 22501. <https://doi.org/10.1029/94JC01776>
- Domingues, E. de C., Schettini, C.A.F., Truccolo, E.C., Oliveira Filho, J.C. de, 2017. Hydrography and currents on the Pernambuco Continental Shelf. *Rbrh* 22. <https://doi.org/10.1590/2318-0331.0217170027>
- Dupuy, S., Pujol, M.-I., Picot, N., Ablain, M., Faugère, Y., Taburet, G., Pelloquin, C., 2016. DUACS DT2014: the new multi-mission altimeter data set reprocessed over 20 years. *Ocean Science* 12, 1067–1090. <https://doi.org/10.5194/os-12-1067-2016>
- Foltz, G.R., Brandt, P., Richter, I., Rodriguez-Fonseca, B., Hernandez, F., Dengler, M., Rodrigues, R.R., ..., Reul, N., 2019. The tropical Atlantic observing system. *Frontiers in Marine Science*, 6, 206. <https://doi.org/10.3389/fmars.2019.00206>
- Garzoli, S.L., 2004. North Brazil Current retroflection and transports. *Journal of Geophysical Research* 109, C01013. <https://doi.org/10.1029/2003JC001775>
- Goes, M., Molinari, R., Da Silveira, I., Wainer, I., 2005. Retroflections of the North Brazil Current during February 2002. *Deep-Sea Research Part I: Oceanographic Research Papers* 52, 647–667. <https://doi.org/10.1016/j.dsr.2004.10.010>
- Gouriou, Y., 1995. ETAMBOT 1 cruise, RV Le Noroit, <https://doi.org/10.17600/95030010>
- Gordon, A.L., 1986. Interocean exchange of thermocline water. *Journal of Geophysical Research* 91, 5037. <https://doi.org/10.1029/JC091iC04p05037>
- Herrford, J., Brandt, P., Kanzow, T., Hummels, R., Araujo, M., Durgadoo, J.V., 2020. Seasonal variability of the Atlantic Meridional Overturning Circulation at 11° S inferred from bottom pressure measurements. *Ocean Science Discussions*, 1-37. <https://doi.org/10.5194/os-2020-55>
- Hummels, R., Brandt, P., Dengler, M., Fischer, J., Araujo, M., Veleza, D., Durgadoo, J. V., 2015. Interannual to decadal changes in the western boundary circulation in the Atlantic at 11°S. *Geophysical Research Letters* 42, 7615–7622. <https://doi.org/10.1002/2015GL065254>
- Lumpkin, R., Garzoli, S.L., 2005. Near-surface circulation in the Tropical Atlantic Ocean. *Deep-Sea Research Part I: Oceanographic Research Papers* 52, 495–518. <https://doi.org/10.1016/j.dsr.2004.09.001>
- Ma, X., Jing, Z., Chang, P., Liu, X., Montuoro, R., Small, R.J., Bryan, F.O., Greatbatch, R.J., Brandt, P., Wu, D., Lin, X., Wu, L., 2016. Western boundary currents regulated by interaction

between ocean eddies and the atmosphere. *Nature* 535, 533–537. <https://doi.org/10.1038/nature18640>

McWilliams, J.C., 2008. The nature and consequences of oceanic eddies, in: *Geophysical Monograph Series*. pp. 5–15. <https://doi.org/10.1029/177GM03>

Neto, A.V.N., Da Silva, A.C., 2014. Seawater temperature changes associated with the North Brazil current dynamics. *Ocean Dynamics* 64, 13–27. <https://doi.org/10.1007/s10236-013-0667-4>

Ou, H.W., De Ruijter, W.P.M., 1986. Separation of an Inertial Boundary Current from a Curved Coastline. *Journal of Physical Oceanography* 16, 280–289. [https://doi.org/10.1175/1520-0485\(1986\)016<0280:SOAIBC>2.0.CO;2](https://doi.org/10.1175/1520-0485(1986)016<0280:SOAIBC>2.0.CO;2)

Peterson, R.G., Stramma, L., 1991. Upper-level circulation in the South Atlantic Ocean. *Progress in Oceanography* 26, 1–73. [https://doi.org/10.1016/0079-6611\(91\)90006-8](https://doi.org/10.1016/0079-6611(91)90006-8)

Rodrigues, R.R., Rothstein, L.M., Wimbush, M., 2007. Seasonal Variability of the South Equatorial Current Bifurcation in the Atlantic Ocean: A Numerical Study. *Journal of Physical Oceanography* 37, 16–30. <https://doi.org/10.1175/JPO2983.1>

Rühs, S., Getzlaff, K., Durgadoo, J. V., Biastoch, A., Böning, C.W., 2015. On the suitability of North Brazil Current transport estimates for monitoring basin-scale AMOC changes. *Geophysical Research Letters* 42, 8072–8080. <https://doi.org/10.1002/2015GL065695>

Schmitz, W.J., McCartney, M.S., 1993. On the North Atlantic Circulation. *Reviews of Geophysics* 31, 29–49. <https://doi.org/10.1029/92RG02583>

Schott, F. a., Dengler, M., Zantopp, R., Stramma, L., Fischer, J., Brandt, P., 2005. The Shallow and Deep Western Boundary Circulation of the South Atlantic at 5°–11°S. *Journal of Physical Oceanography* 35, 2031–2053. <https://doi.org/10.1175/JPO2813.1>

Schott, F.A., Brandt, P., Hamann, M., Fischer, J., Stramma, L., 2002. On the boundary flow off Brazil at 5–10°S and its connection to the interior tropical Atlantic. *Geophysical Research Letters* 29, 21-1-21–4. <https://doi.org/10.1029/2002GL014786>

Schott, F.A., Dengler, M., Brandt, P., Affler, K., Fischer, J., Bourlès, B., Gouriou, Y., Molinari, R.L., Rhein, M., 2003. The zonal currents and transports at 35°W in the tropical Atlantic. *Geophysical Research Letters* 30, 35–38. <https://doi.org/10.1029/2002GL016849>

Schott, F.A., Fischer, J., Stramma, L., 1998. Transports and Pathways of the Upper-Layer Circulation in the Western Tropical Atlantic. *Journal of Physical Oceanography* 28, 1904–1928. [https://doi.org/10.1175/1520-0485\(1998\)028<1904:TAPOTU>2.0.CO;2](https://doi.org/10.1175/1520-0485(1998)028<1904:TAPOTU>2.0.CO;2)

Schott, F.A., Stramma, L., Fischer, J., 1995. The warm water inflow into the western tropical Atlantic boundary regime, spring 1994. *Journal of Geophysical Research* 100, 24745. <https://doi.org/10.1029/95JC02803>

- Silva, M., Araujo, M., Servain, J., Penven, P., Lentini, C.A.D., 2009. High-resolution regional ocean dynamics simulation in the southwestern tropical Atlantic. *Ocean Modelling* 30, 256–269. <https://doi.org/10.1016/j.ocemod.2009.07.002>
- Soutelino, R.G., Da Silveira, I.C.A., Gangopadhyay, A., Miranda, J.A., 2011. Is the Brazil Current eddy-dominated to the north of 20°S? *Geophysical Research Letters* 38, 1–5. <https://doi.org/10.1029/2010GL046276>
- Stramma, L., England, M., 1999. On the water masses and mean circulation of the South Atlantic Ocean. *Journal of Geophysical Research: Oceans* 104, 20863–20883. <https://doi.org/10.1029/1999JC900139>
- Stramma, L., Fischer, J., Reppin, J., 1995. The North Brazil Undercurrent. *Deep-Sea Research Part I* 42, 773–795. [https://doi.org/10.1016/0967-0637\(95\)00014-W](https://doi.org/10.1016/0967-0637(95)00014-W)
- Stramma, L., Schott, F., 1999. The mean flow field of the tropical Atlantic Ocean. *Deep Sea Research Part II: Topical Studies in Oceanography* 46, 279–303. [https://doi.org/10.1016/S0967-0645\(98\)00109-X](https://doi.org/10.1016/S0967-0645(98)00109-X)
- Urbano, D.F., De Almeida, R.A.F., Nobre, P., 2008. Equatorial undercurrent and North equatorial countercurrent at 38°W: A new perspective from direct velocity data. *Journal of Geophysical Research: Oceans* 113, 1–16. <https://doi.org/10.1029/2007JC004215>
- Veleda, D.R.A., Araujo, M., Silva, M., Montagne, R., Araújo, R., 2011. Seasonal and interannual variability of the southern south equatorial current bifurcation and meridional transport along the eastern Brazilian edge. *Tropical Oceanography*, 39(1), 27-59.
- Veleda, D., Araujo, M., Zantopp, R., Montagne, R., 2012. Intraseasonal variability of the North Brazil Undercurrent forced by remote winds. *Journal of Geophysical Research: Oceans*, 117(C11). <https://doi.org/10.1029/2012JC008392>
- Zhang, D., Msadek, R., McPhaden, M.J., Delworth, T., 2011. Multidecadal variability of the North Brazil Current and its connection to the Atlantic meridional overturning circulation. *Journal of Geophysical Research* 116, C04012. <https://doi.org/10.1029/2010JC006812>

Figures and Captions

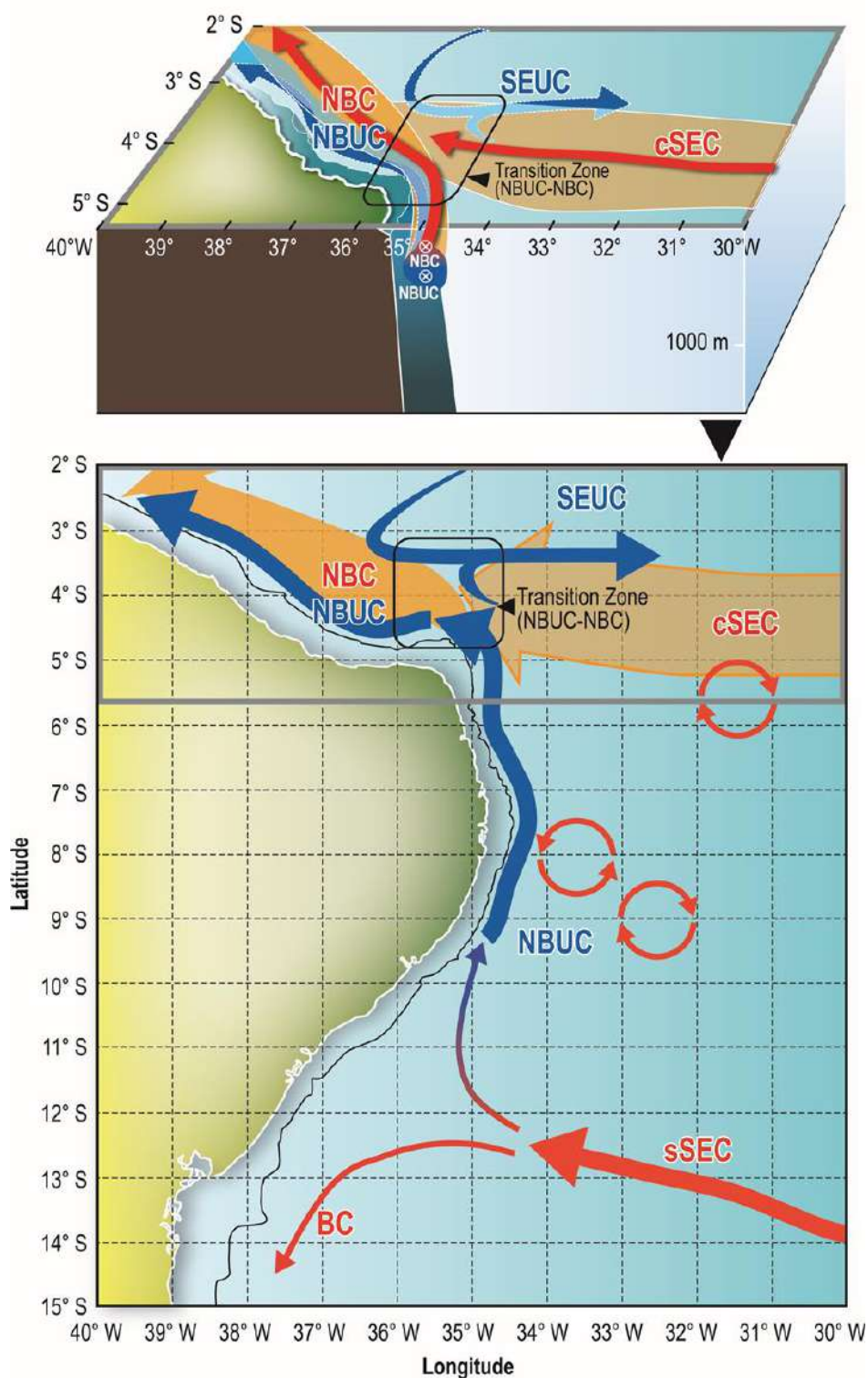


Figure 1. Schematic representation of mean currents and eddy generation along the Northeast Brazilian coast (lower panel) and a zoom (depicted by a grey rectangle) on the schematic circulation north of 5°S (upper panel). Surface currents in red and subsurface currents in blue. sSEC: southern branch of south equatorial current; BC: Brazil current; NBC: north Brazil current; SEUC: south equatorial undercurrent; NBUC: north Brazil undercurrent. The black

rectangle indicates the NBUC-NBC transition zone. This figure summarizes the results of this study put into a wider context.

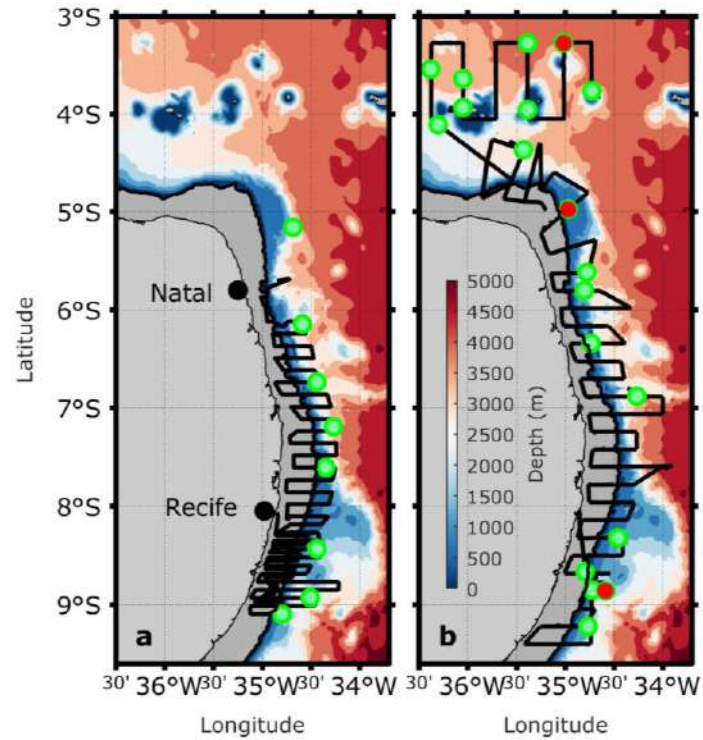


Figure 2. Bathymetric maps of the study area with the SADCP ship tracks (black solid lines) obtained during surveys ABRAÇOS 1 in spring 2015 (a) and ABRAÇOS 2 in fall 2017 (b). Green circles indicate the positions of CTDO stations located off the shelf break and used in this work. Red circles indicate the CTDO stations used to discuss the current transition in the study area. The bold grey areas correspond to the shelf (<70 m).

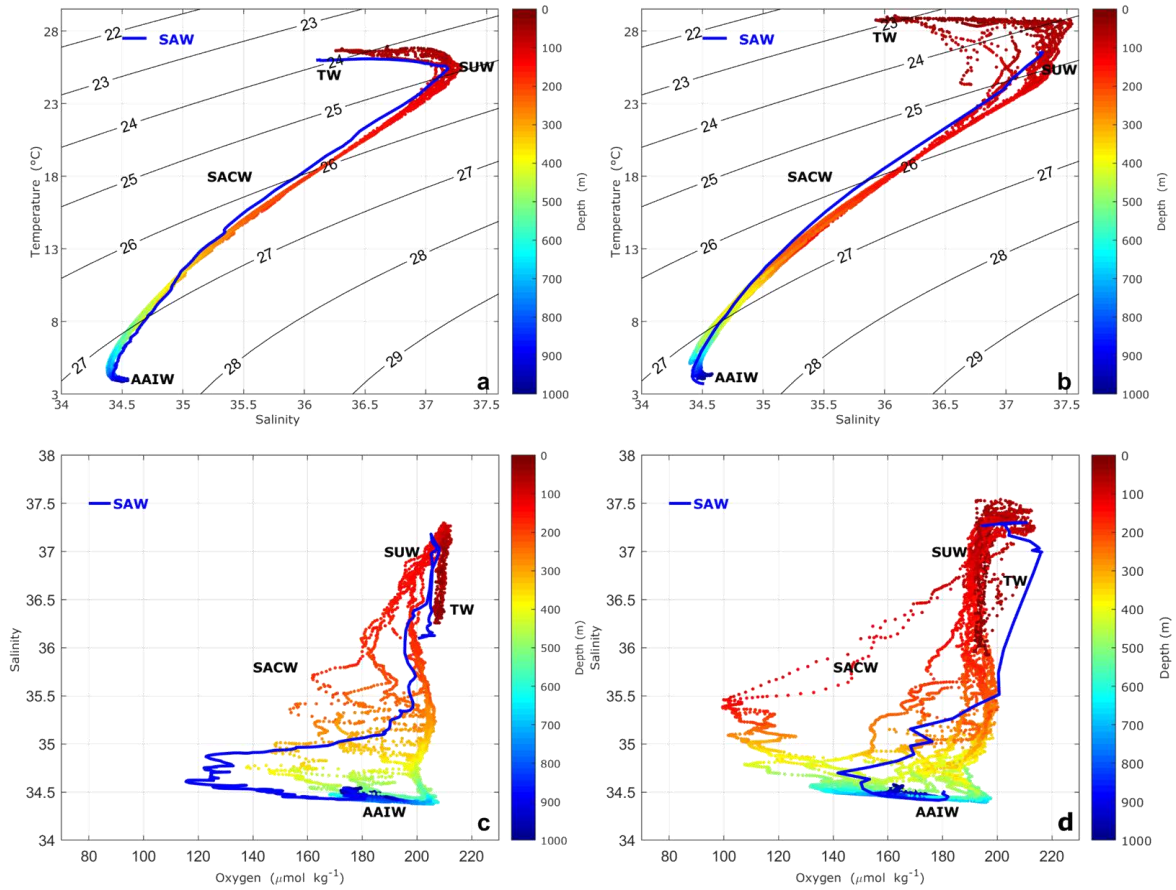


Figure 2. Temperature-salinity diagrams (a, b) and salinity-oxygen curves (c, d) from CTDO profiles obtained during the ABRAÇOS surveys in spring 2015 and fall 2017. The blue line represents typical South Atlantic water (SAW) profiles. Panels (a) and (c) correspond to spring 2015, while panels (c) and (d) correspond to fall 2017. TW: Tropical water; SUW: Subtropical Underwater; SACW: South Atlantic central water; AAIW: Antarctic intermediate water.

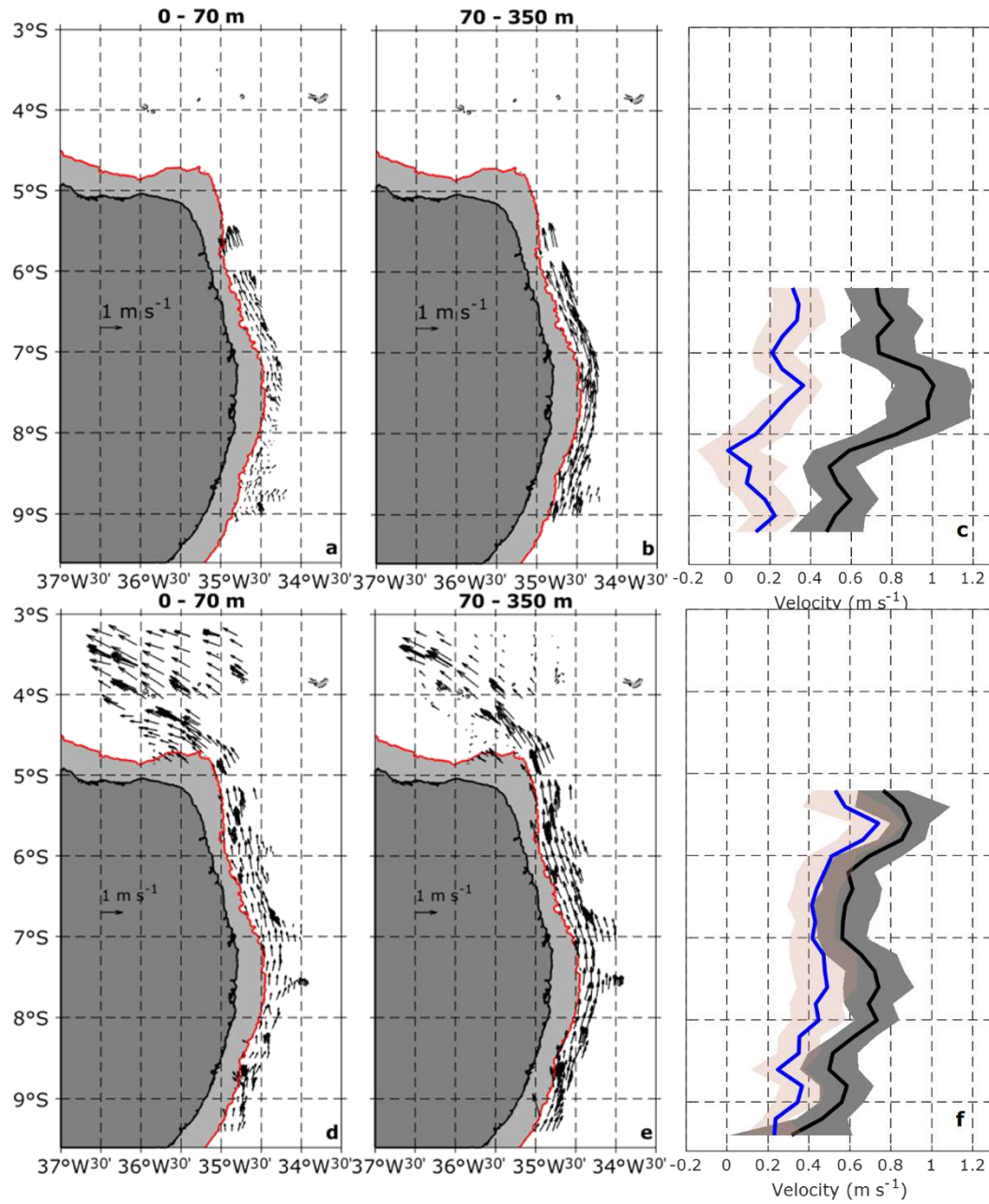


Figure 3. Mean current velocity obtained from SADC profiles at 0-70 m (a, d) and 70-350 m (b, e). The red line depicts the bathymetric contour at 70 m. Meridional variation of the mean alongshore velocities at 0-70 m (blue line) and 70-350 m (black line) between the shelf break and 40 km offshore (c, f). Shaded grey and orange areas correspond to the standard deviation around the mean. The first row (a, b, c) corresponds to spring 2015, while the second row (d, e, f) corresponds to fall 2017.

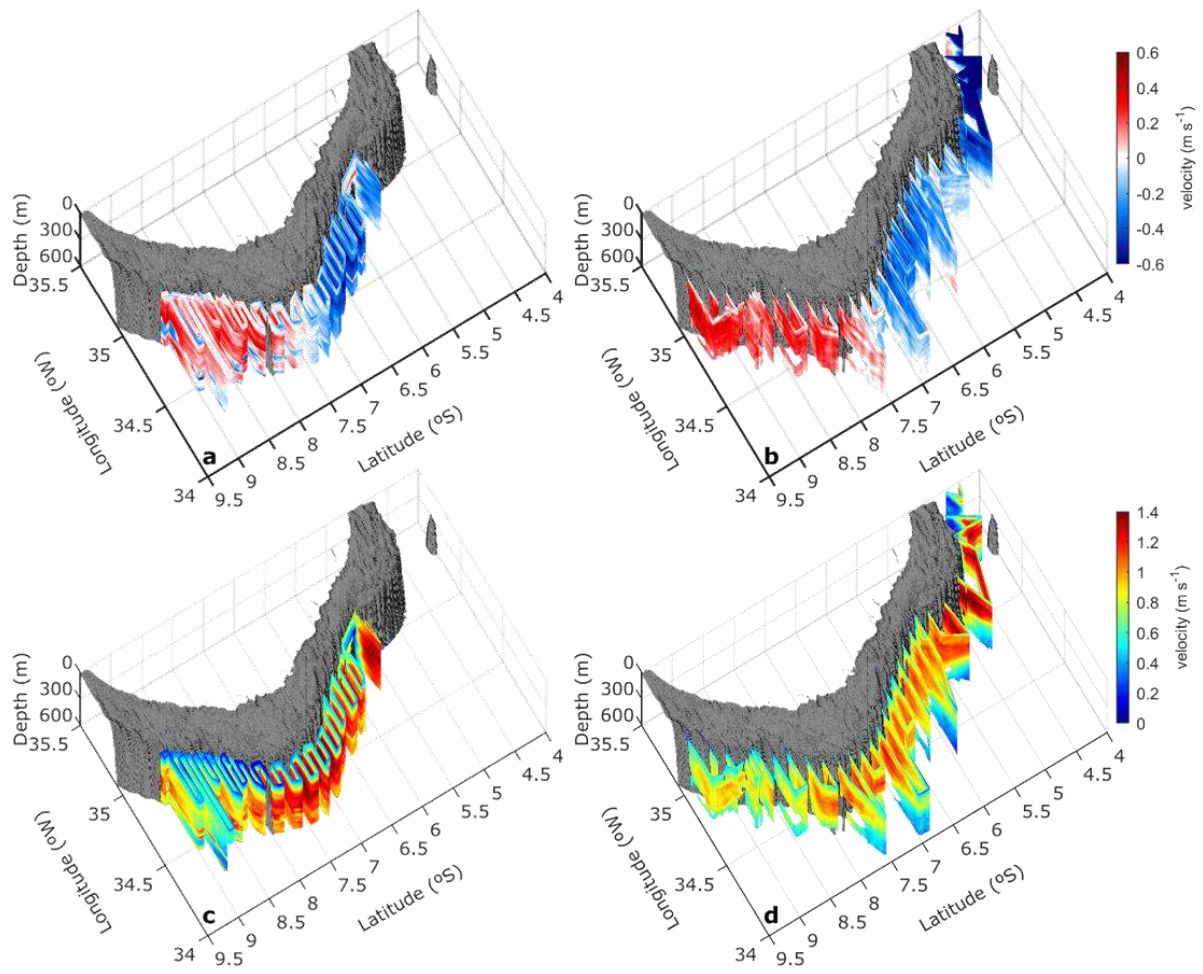


Figure 4. 3D representations of the zonal (a, b) and meridional (c, d) flows during spring 2015 (a, c) and fall 2017 (b, d).

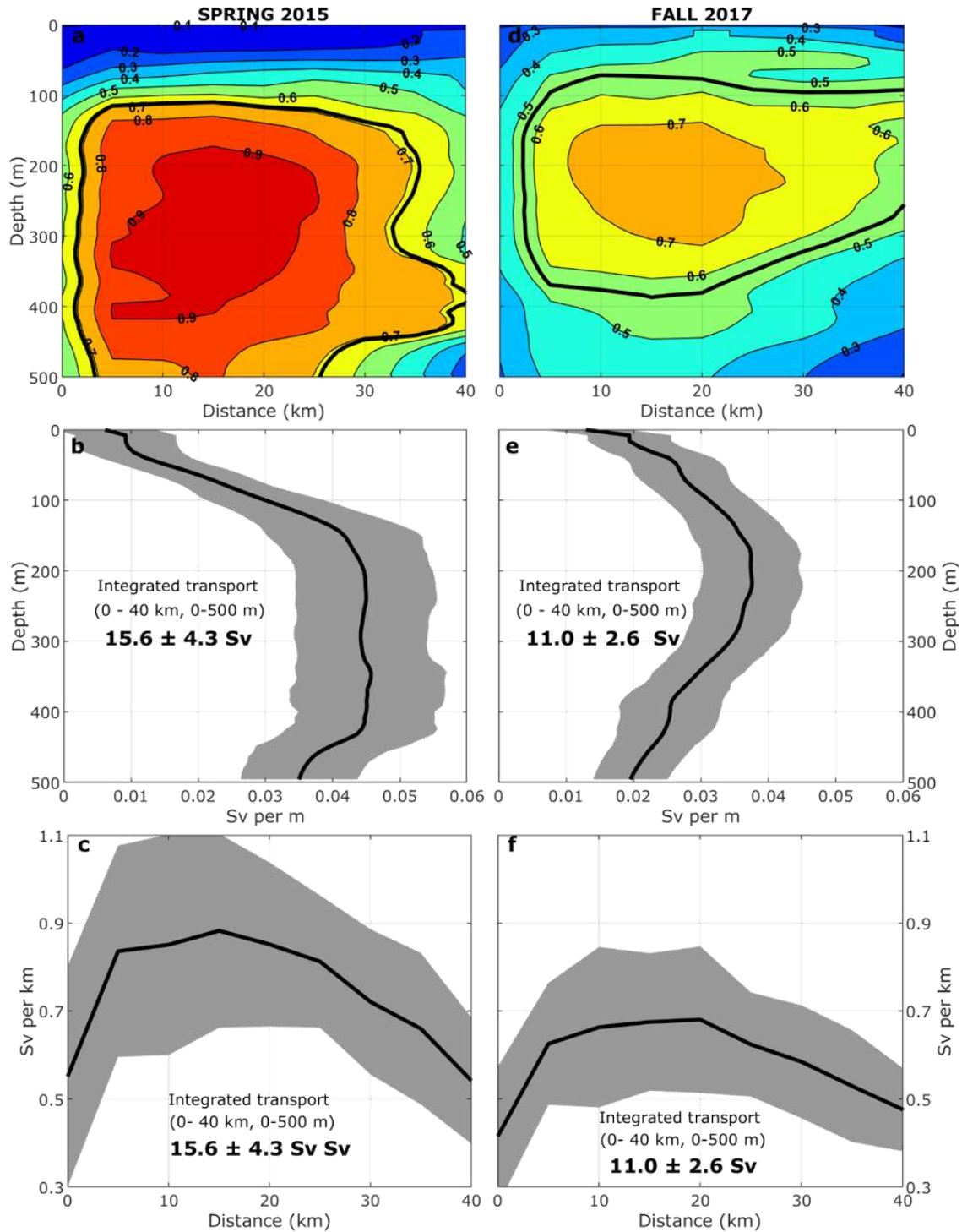


Figure 5. Mean cross-shore sections (9°S-6°S) of the alongshore velocity component and integrated transports. (a, d) Mean cross-shore section of alongshore velocity (in m s⁻¹) between the shelf break and 40 km offshore; the bold black solid line contours the core of the NBUC, i.e., the area where the alongshore velocity is greater than 70% of its maximum. (b, e) Mean vertical profile of alongshore transport integrated from the shelf break to 40 km offshore. The average total transport and associated deviation (in bold) were integrated from the shelf break to 40 km offshore and from the surface to 500 m depth. (c, f) Mean cross-shore distribution of the alongshore transport integrated between the surface and 500 m depth. Grey shaded areas

correspond to the deviation around the mean. Panels (a), (b) and (c) correspond to spring 2015, while panels (d), (e) and (f) correspond to fall 2017.

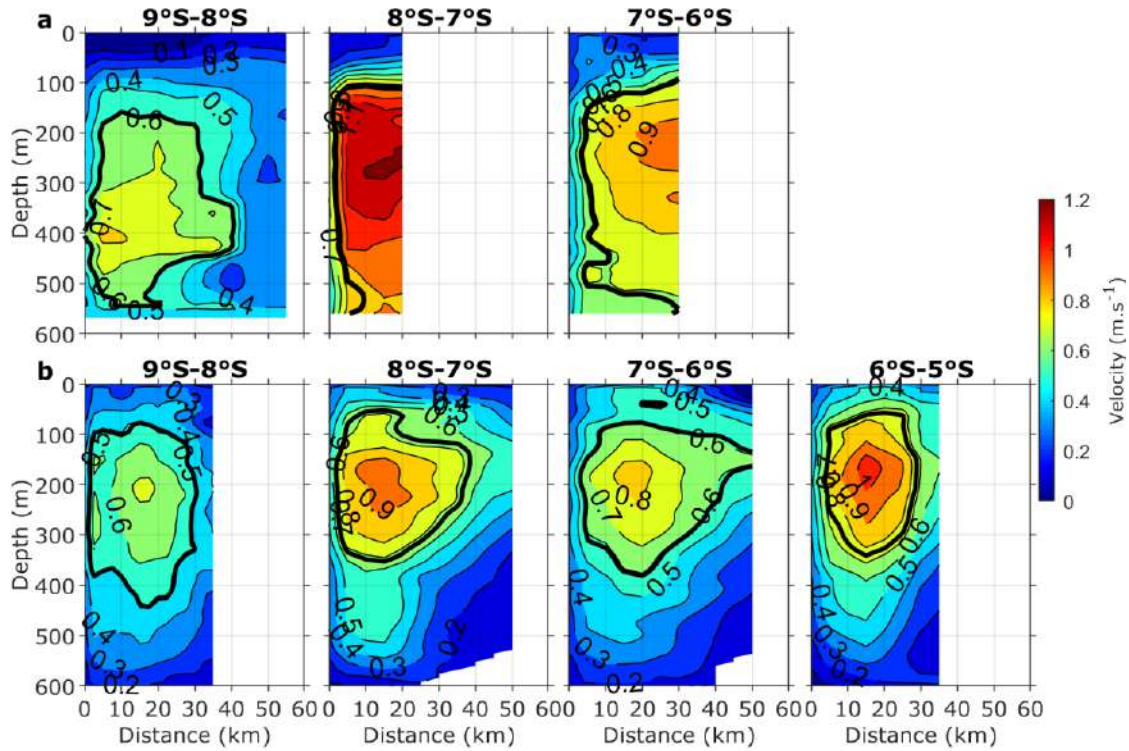


Figure 6. Mean cross-shore sections (from the shelf break) of the alongshore velocity (in m s^{-1}) by latitude bands during spring 2015 (a) and fall 2017 (b). The contour interval is 0.1 m s^{-1} . In each panel, the bold black solid line contours the core of the NBUC, i.e., the area where the alongshore velocity is greater than 70% of its maximum.

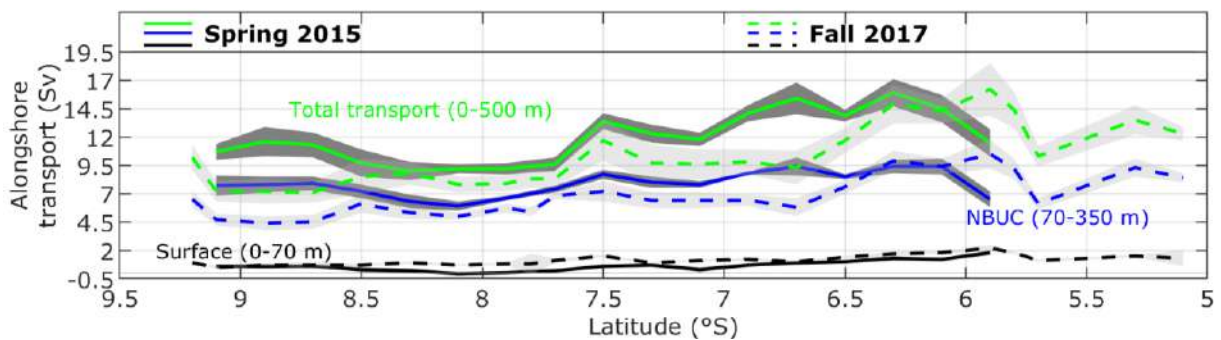


Figure 7. Meridional variation of the alongshore transport (in Sv) integrated between the shelf break and 20 km offshore for three different layers: 0-70 m (black lines), 70-350 m (blue lines) and 0-500 m (green lines) depths. Grey shaded areas correspond to the standard deviations around the mean transports. Black, blue and green dots correspond to transport values obtained from previous observations during the same months of ABRAÇOS surveys (see Table 1).

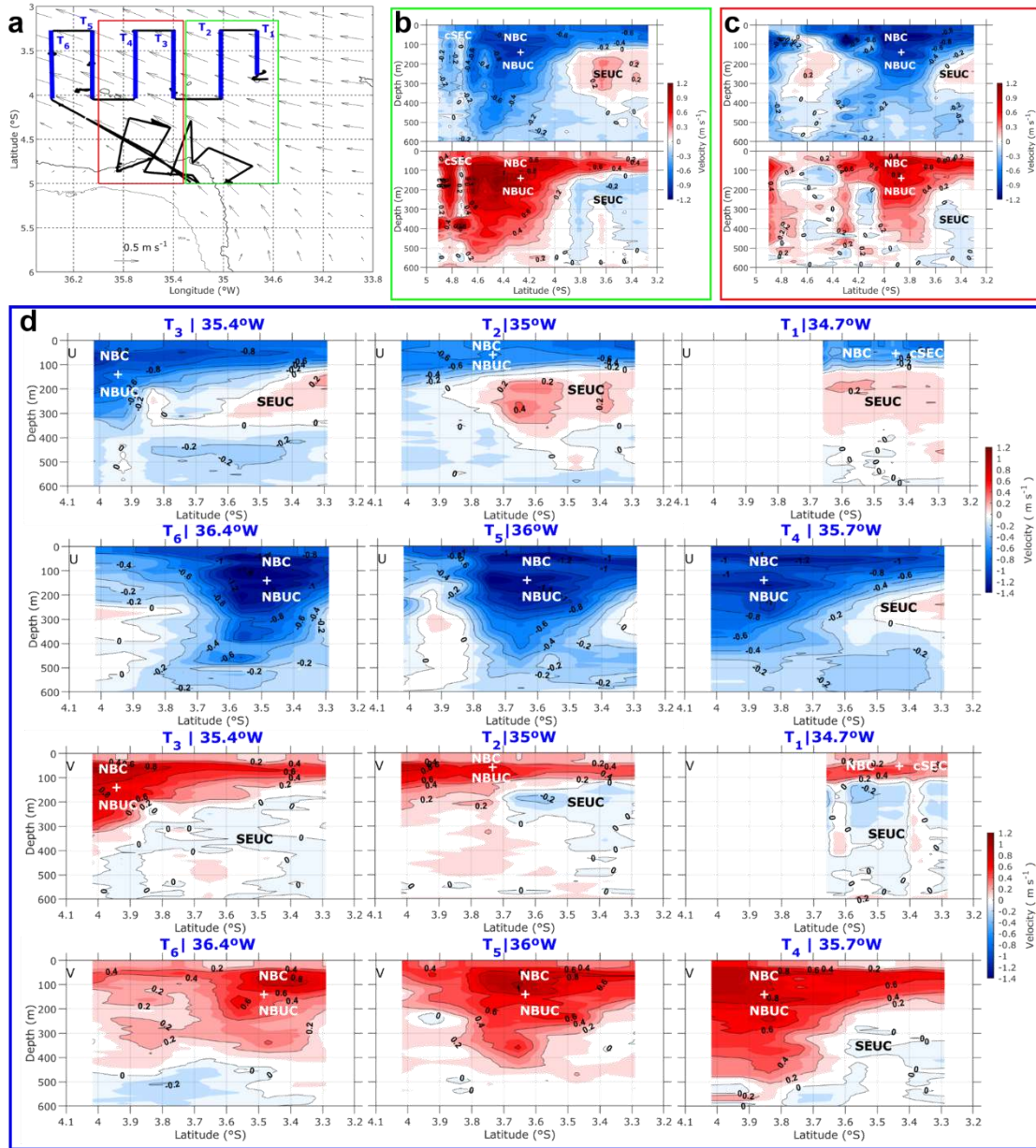


Figure 8. (a) Transect positions superimposed on geostrophic currents. Mean zonal (U; upper panels) and meridional (V; lower panels) currents between: (b) 5°S and 3.3°S at ~35°W (green rectangle in (a)); (c) 5°S and 3.3°S (red rectangle in (a)); and (d) along six latitudinal transects (T1 to T6) between 34.7°W-36.4°W (blue transects in (a)).

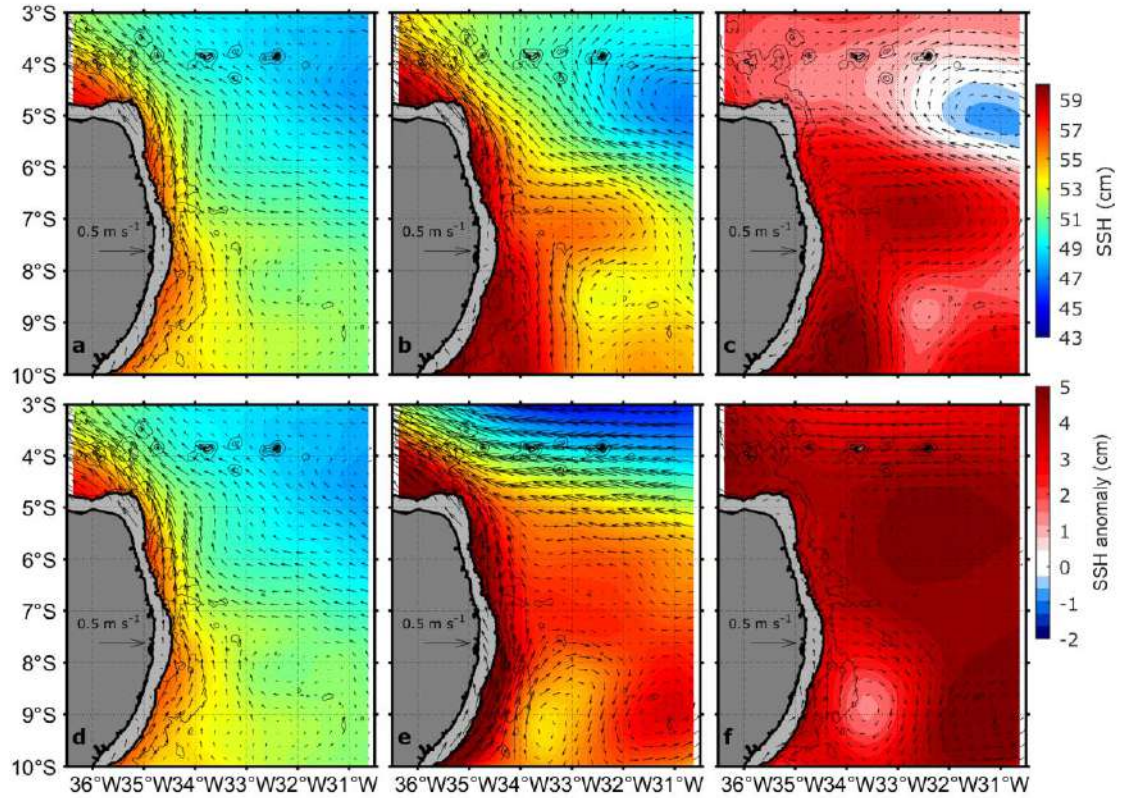


Figure 9. SSH (in cm) superimposed on geostrophic current velocities. Climatologies for (a) spring (Sept. 29 - Oct. 21) and (d) fall (April 08 – May 09) periods, computed with data from January 1993 to December 2018. (b, e) SSH and geostrophic current velocities for spring 2015 and fall 2017 conditions. (c, f) Anomalies in SSH (in cm) and geostrophic current velocities (difference between mean and climatological conditions). The first row (a, b, c) corresponds to spring, while the second row (d, e, f) corresponds to fall. Shaded grey area correspond to the shelf. The fine black lines represent the isobaths 1000 m and 3000 m.

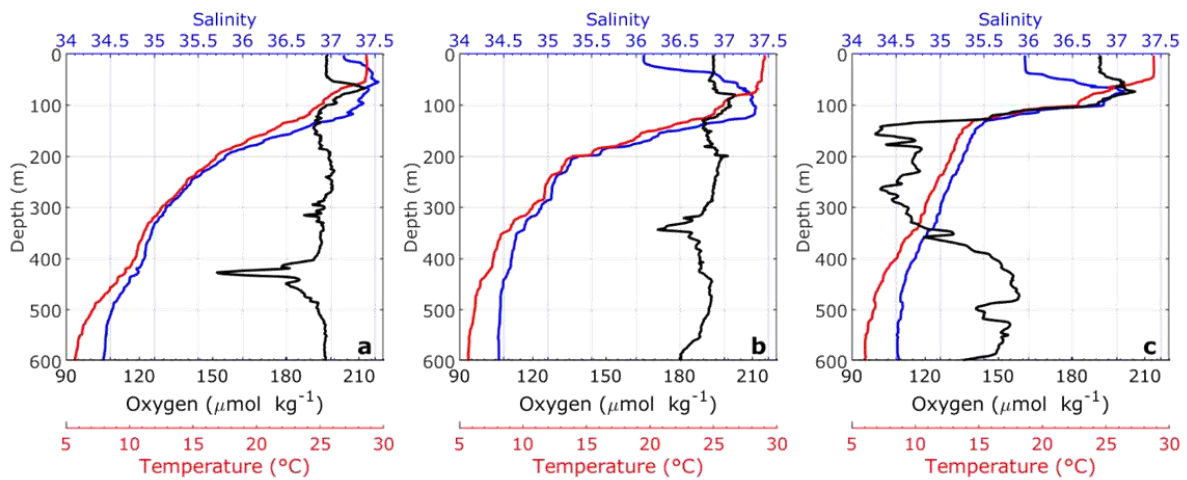


Figure 10. Vertical profiles of temperature (red lines), salinity (blue lines) and oxygen (black lines) at (a) 8.9°S, 34.6°W; (b) 5°S, 35°W and (c) 3.8°S, 35°W in fall 2017.

Supplementary material

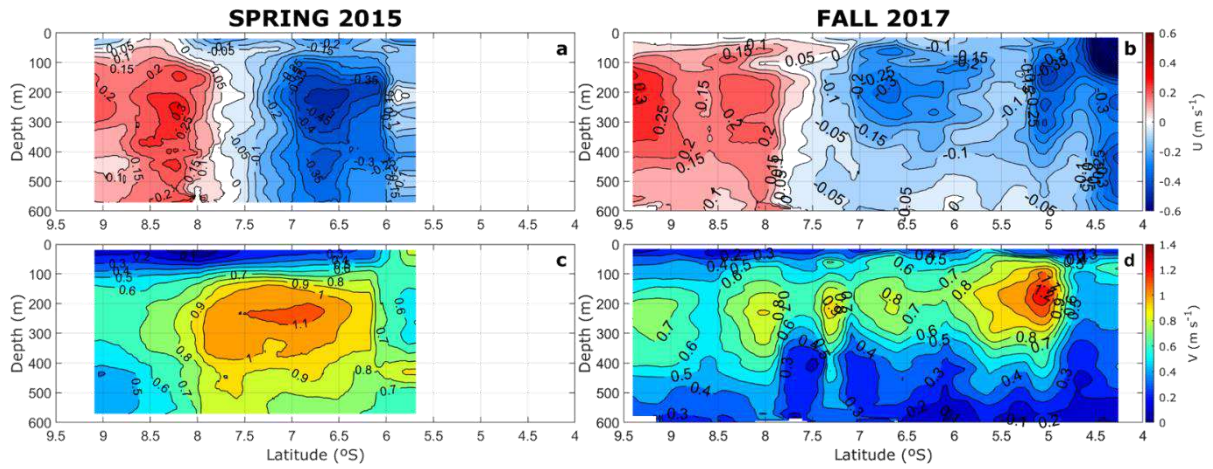


Figure 2. S 1. 2D representation of the latitudinal variation of the zonal (a,b) and meridional (c,d) flows in spring 2015 (a,c) and fall 2017 (b,d).

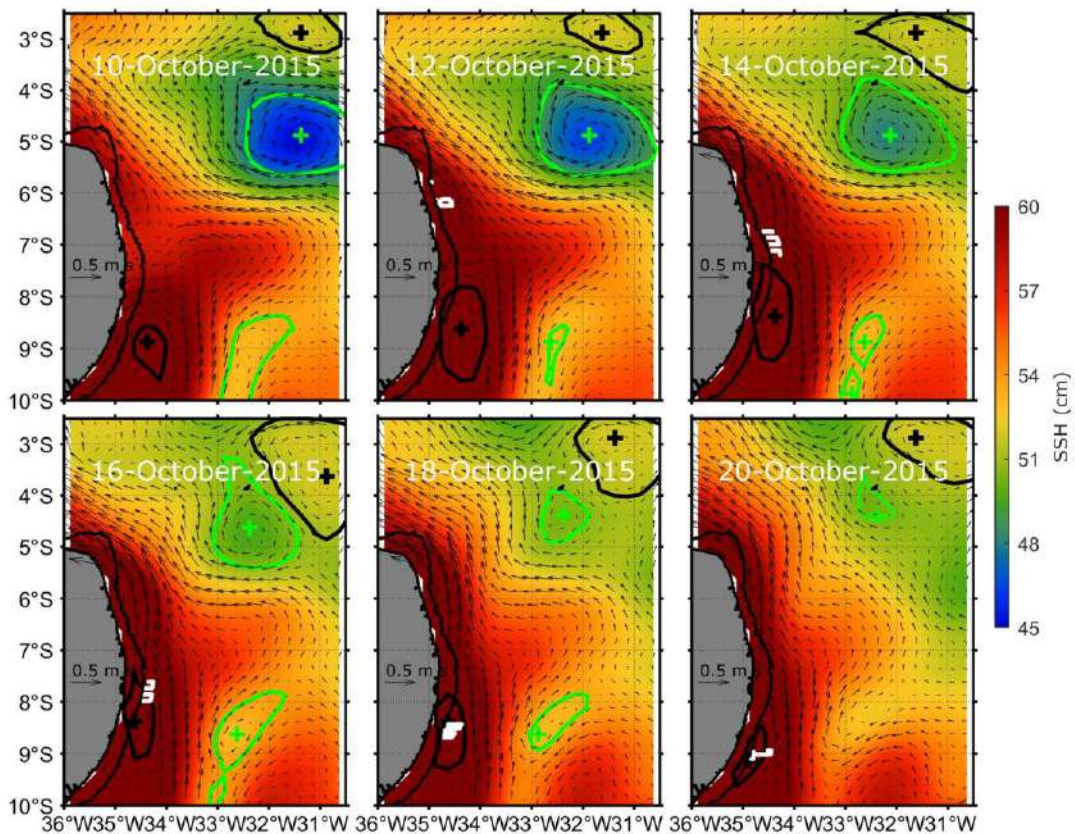


Figure 2. S 2. SSH with superimposed geostrophic velocities (black arrows) over the period October 10-20, 2015. Green (black) contours and crosses represent contours and centres of cyclonic (anticyclonic) eddies. The white lines are the ship tracks corresponding to SSH dates.

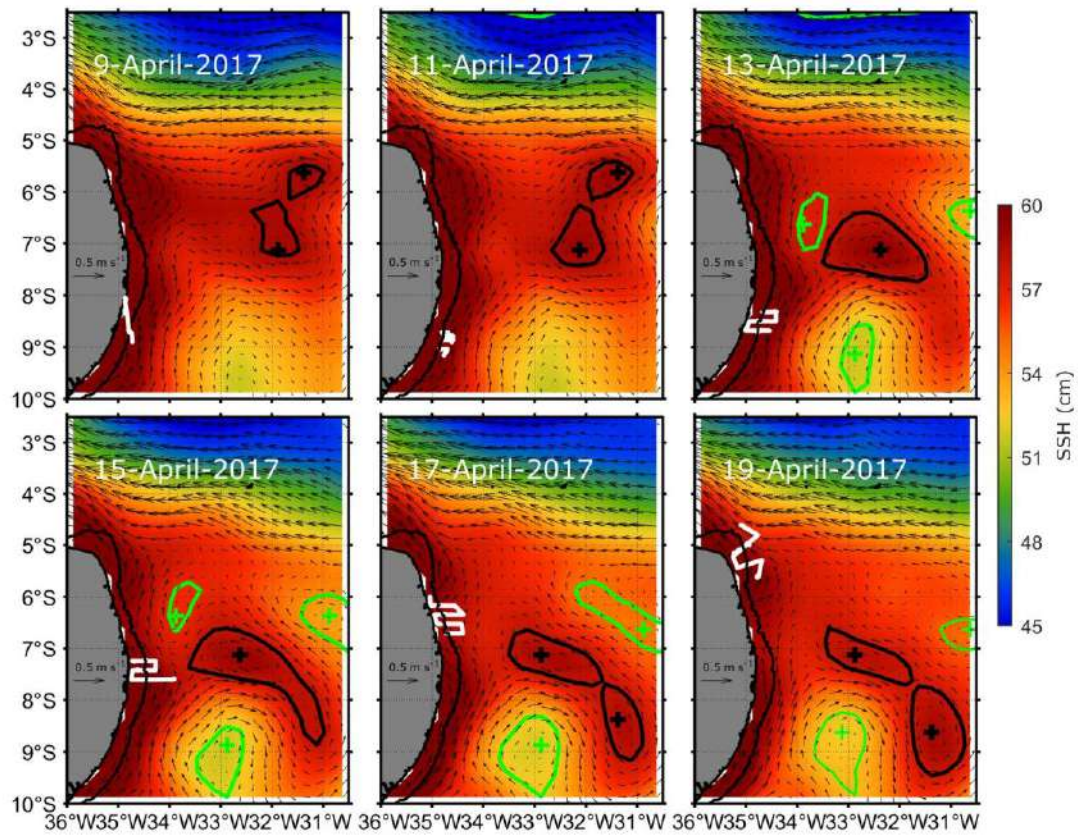


Figure 2. S 3. SSH with superimposed geostrophic velocities (black arrows) over the period April 10-19, 2017. Green (black) contours and crosses represent contours and centres of cyclonic (anticyclonic) eddies. The white lines are the ship tracks corresponding to SSH dates.

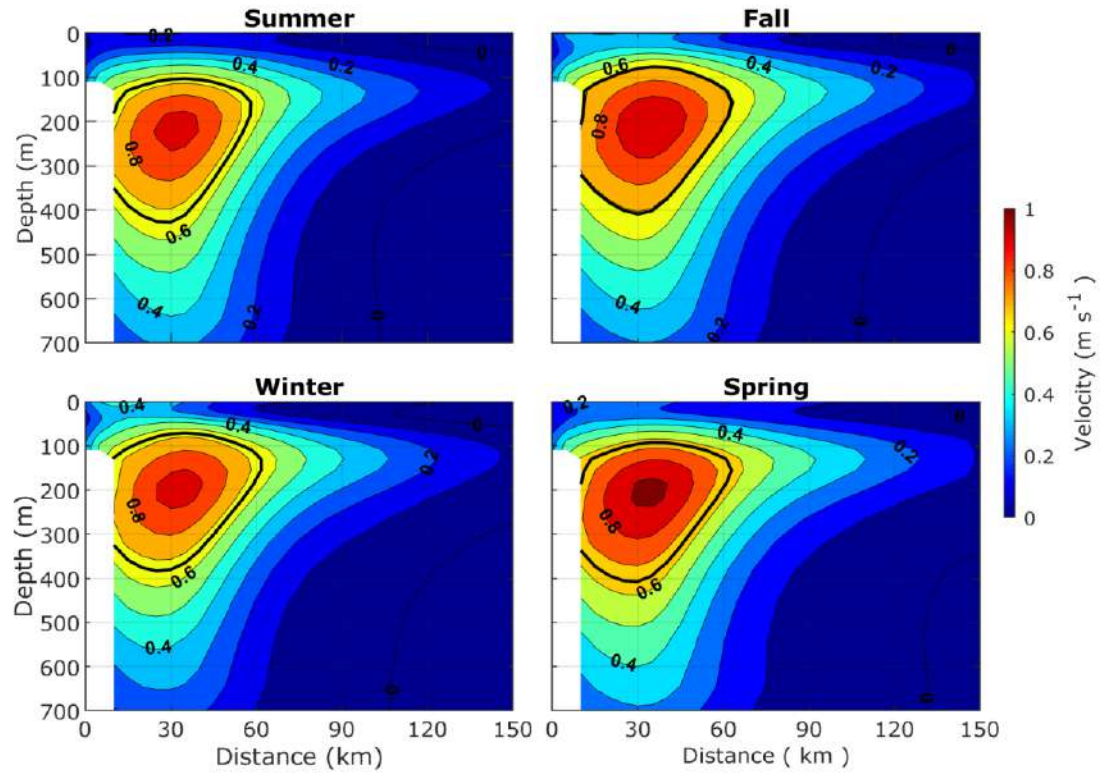


Figure 2. S 4. Mean cross-shore sections (9°S - 6°S) of the alongshore velocity component in Austral summer, fall, winter and spring seasons as estimated using the global reanalysis product GLORYS12V1.

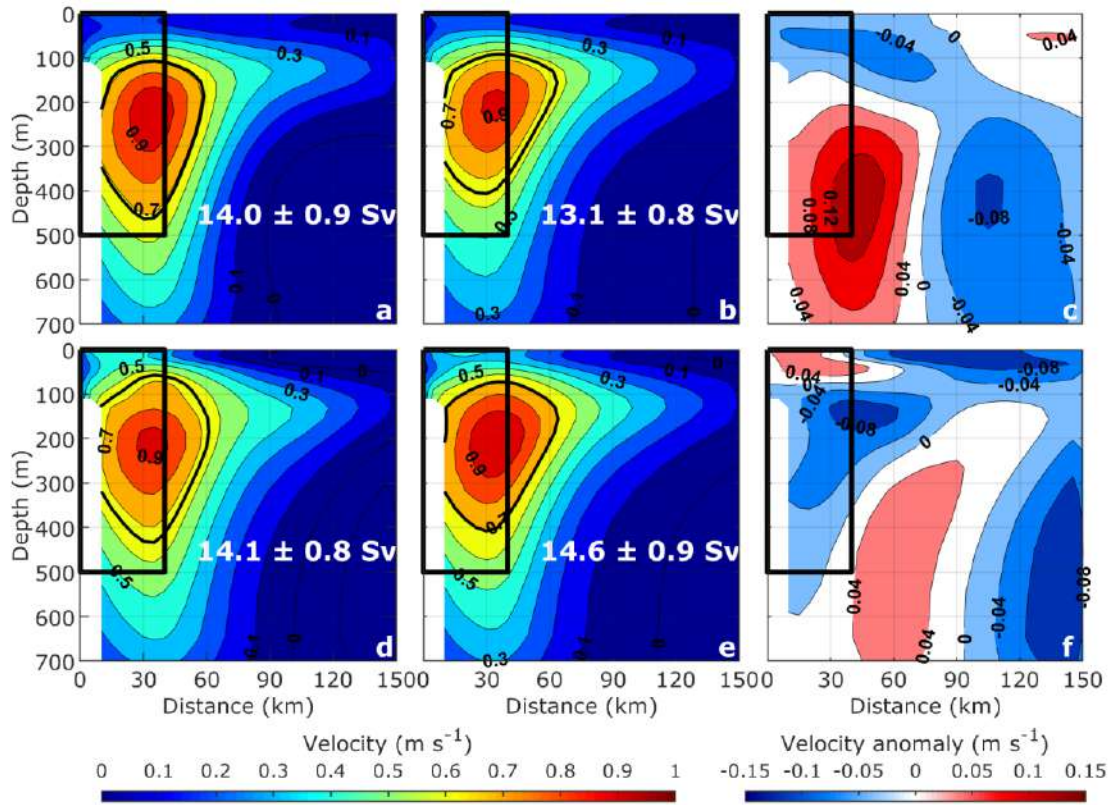


Figure 2. S 5. Mean cross-shore sections (9°S - 6°S) of the alongshore velocity (in m s^{-1}) and integrated transports estimated using the global reanalysis product GLORYS12V1 in (a) spring 2015, (b) spring climatology 1993-2018, (c) difference between (a) and (b); (d) fall 2017, (e) fall climatology 1993-2018, (f) difference between (d) and (e). The transports are calculated between the surface and 500 m deep and from the shelf break to 40 km offshore (black solid line rectangle). The bold black solid line in (a), (b), (d) and (e) contours the core of the NBUC, i.e., the area where the alongshore velocity is greater than 70% of its maximum.

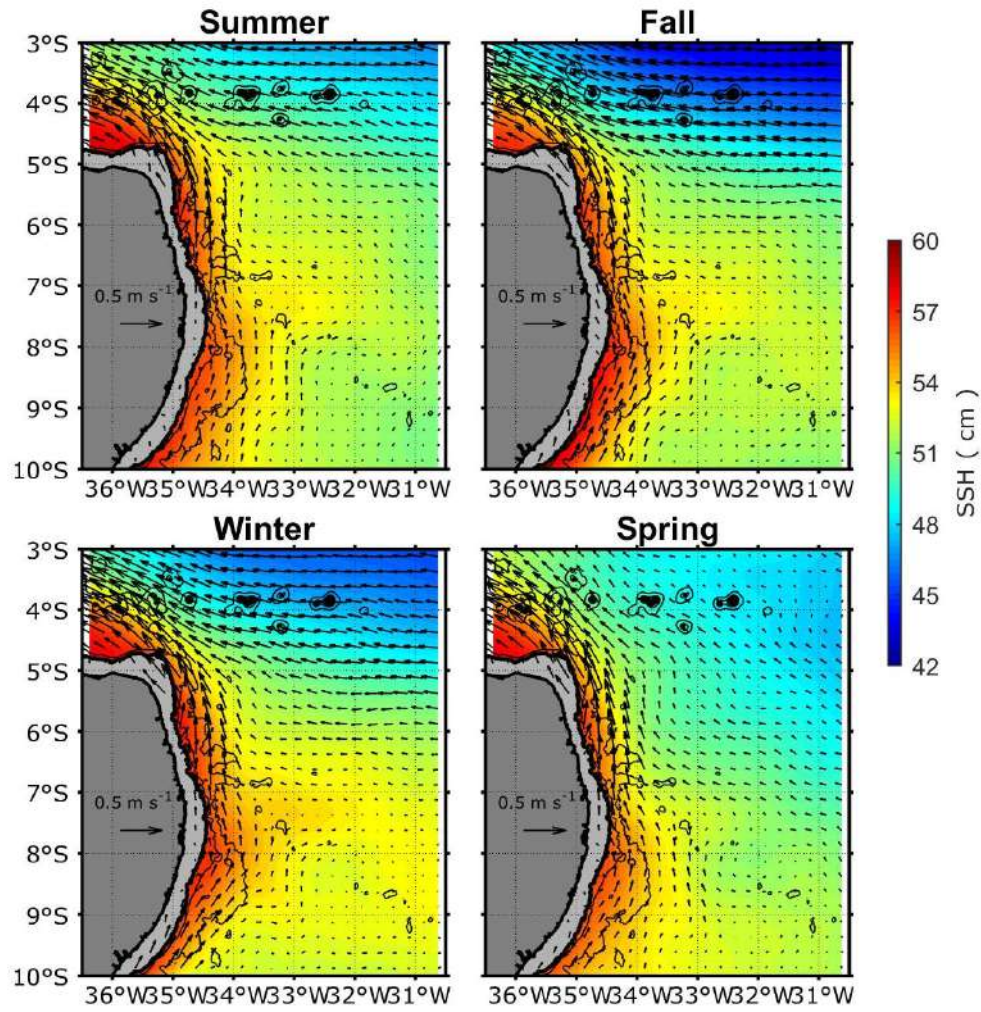


Figure 2. S 6. Seasonal variation of sea surface high (in cm) superimposed on geostrophic current velocities.

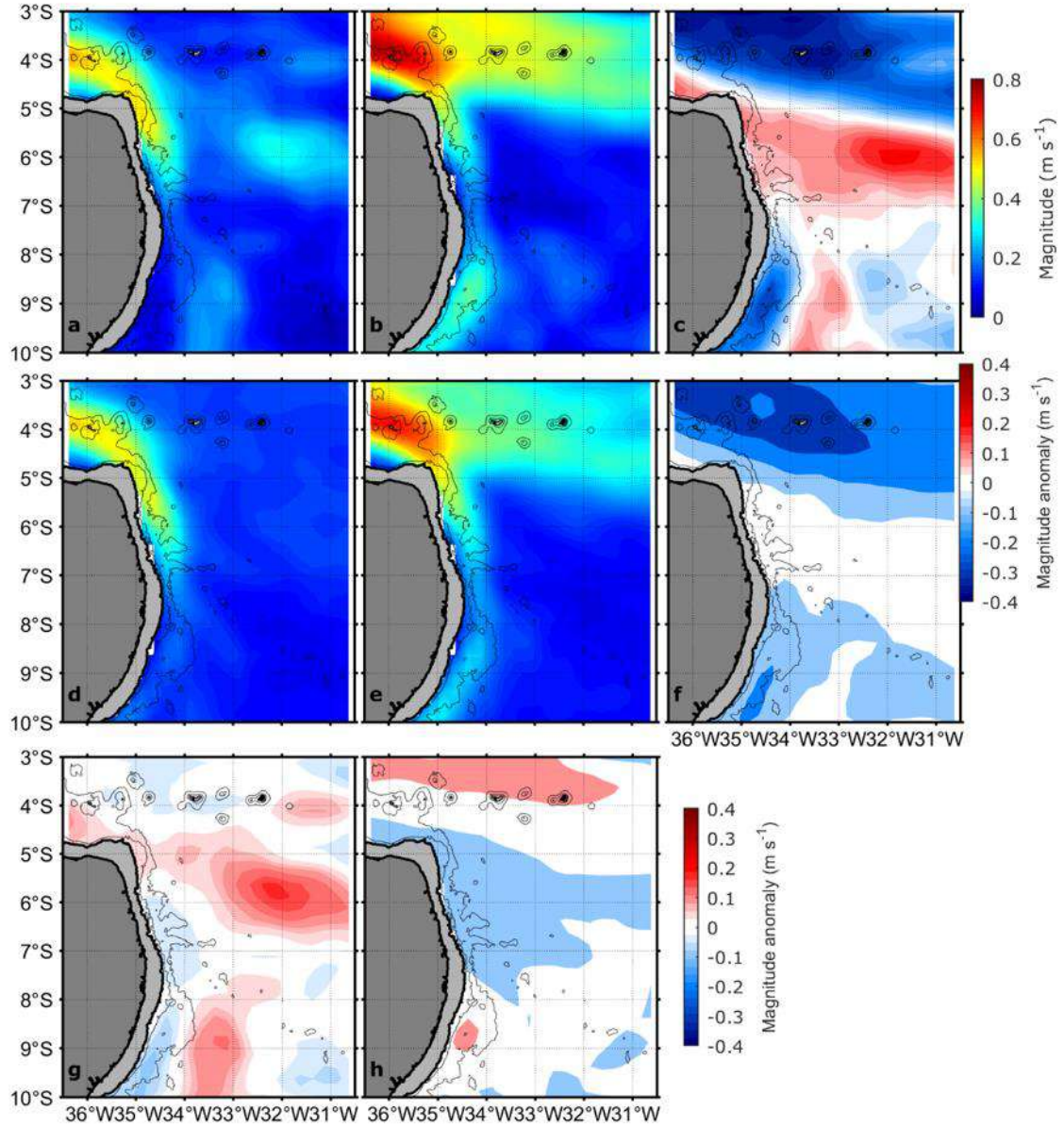


Figure 2. S 7. Geostrophic velocities magnitude (in m s^{-1}) (a, b) for spring 2015 and fall 2017 conditions. Climatologies for (c) spring (Sept. 29 - Oct. 21) and (d) fall (April 08 – May 09) periods, computed with data from January 1993 to December 2018. (e, f) Difference between spring and fall mean conditions of geostrophic velocities magnitude (in m s^{-1}). (g, h) difference between spring and fall climatologies of geostrophic velocities magnitude (in m s^{-1}). The fine black lines represent the isobaths 1000 m and 3000 m

3 MESOSCALE EDDIES OCCURRENCE AND CHARACTERISTICS OFF NORTHEAST BRAZIL

In this chapter, we investigate the mesoscale activity off Northeast Brazil. Our analysis are based on 26 years altimetry data, surface velocities from DRIFTER and wind velocity speed from ERA5. This work is an article in preparation.

Abstract

The region off northeast Brazil a region of complex ocean dynamic where originate the strong western boundary current system North Brazil current – North Brazil undercurrent (NBC-NBUC). The region includes archipelago of Fernando de Noronha and Atoll das Rocas. Such features are favorable for mesoscales eddies occurrence within the region. However, not a lot is known about mesoscales eddies activities in the region. Using satellites altimetry data from 1993 to 2018 off Northeast Brazil (37-25°W; 13-1°S), we analyze eddy characteristics, polarity, spatial and temporal distribution, trajectories. Approximately 1950 mesoscale eddy crossed the region, including 76% formed in the region, with amplitudes and radii ranging between 1 and 2 cm and 25 and 205 km, respectively. In the region around the Fernando de Noronha Archipelago (36-26°W; 6-1°S), the formation of cyclonic eddies is favored by the barotropic instability of surface currents and the wind stress curl. On the other hand, in the south of the region (36-26°W; 12-8°S), the formation of eddies is associated with the barotropic instability wind stress curl and surface currents meandering.

1. INTRODUCTION

Eddy generation is a common feature of the World Ocean. They constitute one of the main contributors to oceanic variability. When formed, eddies can trap local water of their region of formation and transport its properties toward another region. Therefore, they contribute significantly to the transport of heat, salt, nutrients and other chemicals (Chelton et al., 2011; Wunsch, 1999). Moreover, on their pathway, they influence ocean- atmosphere exchanges by affecting the heat at air-sea interface, winds, cloud cover and precipitations (e.g., Frenger et al., 2013; Villas Bôas et al., 2015). They can also affect temperature, salinity and velocities from the sea surface to ~1000 m depth (Keppler et al., 2018).

In the south tropical Atlantic Ocean (STAO), mesoscale eddies are frequently formed in the Benguela eastern boundary upwelling system (EBUS) (10-30°S; 0-30°E) (e.g., Chaigneau et al., 2009; Chelton et al., 2011; Pegliasco et al., 2015) and the region of the Brazil current (RBC) (10-20°S) (e.g., Arruda et al., 2013; Campos, 2006; Soutelino et al., 2011, 2013). In the Benguela EBUS, mesoscale eddies are generated from baroclinic/barotropic instability, topographic features, strong wind shear, large-scale currents interaction with the shelf (e.g., Pegliasco et al., 2015), while in the RBC, mesoscale eddies generation is due to the BC meandering along the shelf break, topographic and baroclinicity effect (e.g., Campos, 2006; Schmid et al., 1995). However, others mechanisms such as wind stress curl and wind stress can favor eddy generation (e.g., Dandapat and Chakraborty, 2016).

The western part of the STAO, the region enclosing the concave coastline between Maceio and Fortaleza (Northeast Brazil, 10-3°S; 37-30°W), constitutes the pathway of two major western boundary currents, the North Brazil undercurrent (NBUC) and the North Brazil current (NBC). It is also a region of complex bathymetry, with the presence of Islands (Fernando de Noronha and Rocas Atoll) and seamounts (along the Fernando de Noronha ridge) acting as an obstacle for large-scale circulation (Silva et al., 2021). In the near-shore region, the main northward undercurrent, the NBUC, shifts from northeastward to northwestward at about 7.5°S as the coast orientation change (Dossa et al., 2021). Moreover, the central branch of the south equatorial current (cSEC) coalesces with the NBUC at about 4.8°S, to form the NBC (e.g., Dossa et al., 2021; Schott et al., 1995, 1998).

In this region, very few studies emphasized the mesoscale activities. Silveira et al. (1994) was the first to observe a clockwise recirculation of the cSEC at the surface, when it approaches the northeast Brazil coast at ~33°W. However, the authors suggested that it might be occasional and seasonal. Then, based on numerical simulations, Silva et al. (2009) pointed out the high surface mesoscale activity along the cSEC patches close the northeast Brazil region. More recently, mesoscale activities was observed in the region based on altimetry data at specific periods (Dossa et al., 2021; Silva et al., 2021). However, no study provided a general vision of the characteristics of mesoscale activities and their seasonal variation in northeast Brazil (NEB). This is the objective of the present study taking advantage of 26 years of altimetric observations.

3.1 2. DATA AND METHODS

2.1 Data

Altimetry data

To investigate mesoscale activity and describe the geostrophic circulation off northeast Brazil, we used altimetric observations available from January 1993 to December 2018. Data were produced by Ssalto/DUACS multi-mission products with support from Cnes (<http://www.AVISO.altimetry.fr/duacs/>). Multi-mission products refer to the combination of all satellites data available at one time: Jason-3, Sentinel-3A, HY-2A, Saral/AltiKa, Cryosat-2, Jason-2, Jason-1, T/P, ENVISAT, GFO, and ERS1/2. This dataset includes sea surface height (SSH) and geostrophic velocities component and is mapped daily onto a $0.25^\circ \times 0.25^\circ$ latitude/longitude grid (ABLAIN, M. *et al.*, 2015; DUPUY *et al.*, 2016). The Copernicus Marine Environment Monitoring Service (CMEMS: <http://marine.copernicus.eu>) provides the processing and distribution of the product.

Geostrophic velocities included in the product are obtained from first derivatives of the sea surface height SSH:

$$u = -\frac{g}{f} \frac{\partial(SSH)}{\partial y} \quad (1)$$

$$v = \frac{g}{f} \frac{\partial(SSH)}{\partial x} \quad (2)$$

where u is the zonal velocity (velocity in the east–west direction, with eastward velocities being positive), v is the meridional velocity (velocity in the north–south direction, with northward velocities being positive), g is the gravitational acceleration, f is the Coriolis parameter, x is the zonal spatial and y is the meridional spatial coordinate.

Surface current data

The drifter data used in the present study is the near-surface velocities climatology from the Global Drifter Program (GDP). The velocities are obtained from satellite-tracked drifting buoys, which are drogued at 15 m depth. The climatology is built from dataset spanning from 1979 to 2015. The data were low passed at 1.5 times, the local inertial period or at 5 days if that is smaller with a floor of 1 day. The data is monthly available on the grid $0.25^\circ \times 0.25^\circ$. This climatology is an update version of the older version described in Lauindo *et al.* (2017) (https://www.aoml.noaa.gov/phod/gdp/mean_velocity.php).

Wind data

The wind dataset used in the present study is the quality-assured monthly update of ERA5 available from 1979 to the present. The dataset includes zonal and meridional wind component estimated at 10 m above sea level. The data available is produced by Copernicus Climate Change Service (C3S) and is available at <https://www.ecmwf.int/en/forecasts/datasets/reanalysis-datasets/era5>. In the present study, we used zonal and meridional component of the wind to estimate the wind stress and the wind stress curl within the NEB.

2.2 Methods

Eddy identification and tracking

The mesoscale eddies identification is based on SSH map, using the eddy detection algorithm from Chaigneau et al. (2008, 2009). This algorithm finds the eddy center corresponding to the local extrema of SSH (maxima for anticyclone eddy (AE), minima for cyclonic eddy (CE)), and defines the outermost closed contour around these extrema as the eddy edge (Figure 1).

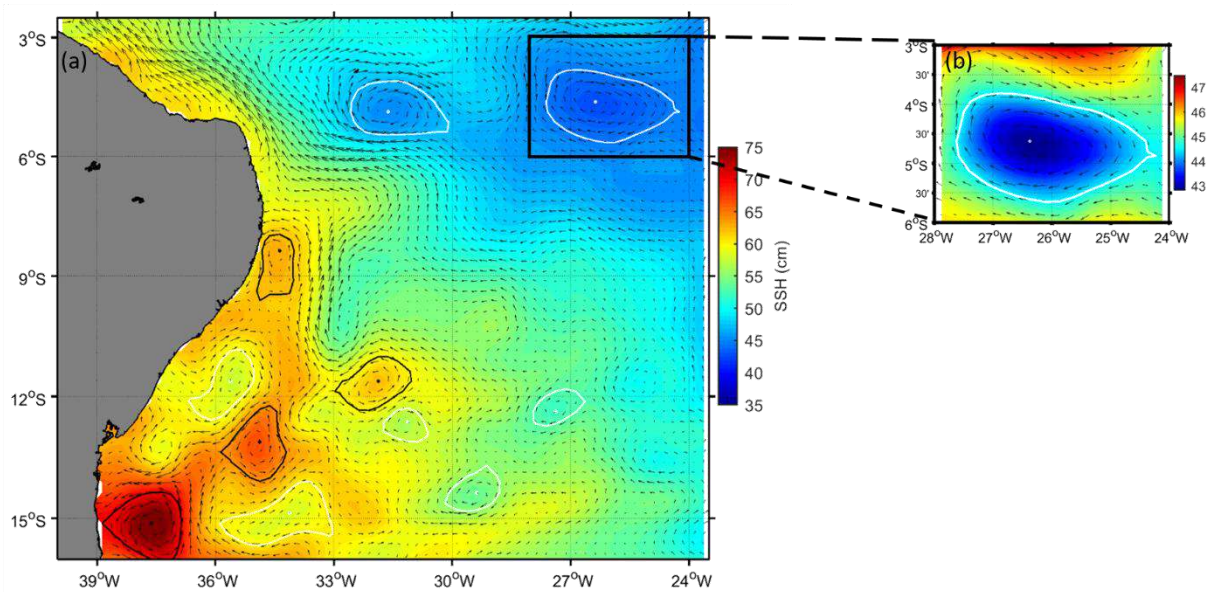


Figure 1. Snapshot of the SSH on October 11, 2015, with the results of the eddy-detection method with geostrophic velocities superimposed (black arrows). The white (black) contours indicate cyclonic (anticyclonic) eddy-detected edge, while the white (black) dots correspond to the cyclonic (anticyclonic) eddy center. (b) Zoom of a selected region with a cyclonic eddy.

Further steps consist of eddies tracking from their genesis to their dissipation. This tracking method is based on the algorithm developed by Pegliasco et al. (2015a). This algorithm first separates all detected eddies into AE and CE. Second, for each eddy detected at time t and delimited by contour C_t (Figure 2a), the algorithm searches at time $t+dt$ ($dt = 1$ day), any eddy edge C_{t+dt} (contour of any eddy edge detected at time $t+dt$ ($dt=1$ day) intersecting with C_t . Several scenarios are possible (Figure 2b-f). If none contour C_t intersect with the contour C_{t+dt} (Figure 2b), the eddy detected at time t is considered to have disappeared. If only one contour C_{t+dt} intersects with contour C_t , the eddy at time $t+dt$ is considered to be the same from time t to $t+dt$ (Figure 2d). However, between t and $t+dt$, the eddy can display two different patterns: a translation induced by contour intersections (Figure 2d) or not (Figure 2b); eddy size decay (Figure 2e) or growth (Figure 2f) without any translation. If several contours C_{t+dt} intersect with contour C_t (Figure 2c), a cost function is calculated. The algorithm searches among the contours C_{t+dt} intersecting with C_t , the one for that the cost function is minimized and depicts no clear change in amplitude, Eddy Kinetic Energy (EKE) and radius. In our study, we only retained eddies with a minimum lifetime of 14 days.

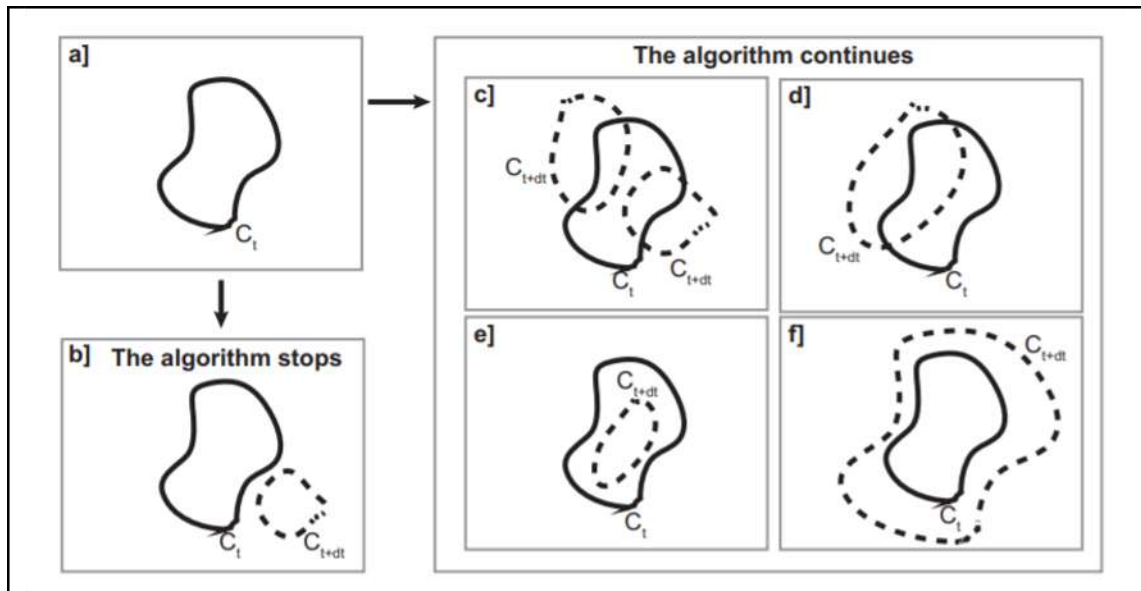


Figure 2. Illustration of eddy tracking. The solid contours indicate eddy at the date t while dashed contours indicate eddies at date $t+dt$ (a) Black solid contours represent a given eddy edge (C_t) at time t whereas black dashed contours represent eddy edges (C_{t+dt}) at time $t+dt$; (b) no intersection between eddies at time $t+dt$ and C_t and the eddy tracking is stopped; (c) several eddies at $t+dt$ intersect C_t and the eddy-tracking algorithm uses a cost function to determine the one most similar to C_t ; (d) only one eddy at $t+dt$ intersects C_t ; (e) C_{t+dt} is included within C_t ; (f) C_t is included within C_{t+dt} . (based on Pegliasco et al., 2015).

To investigate mechanisms driving eddy generation, we computed the relative vorticity of large-scale currents from both geostrophic and surface total currents as follow:

$$\zeta = \frac{\partial v}{\partial x} - \frac{\partial u}{\partial y} \quad (3)$$

As described above, barotropic instability, associated with the change of sign of the gradient of absolute vorticity, could drive eddy generation (e.g., Aguedjou et al., 2019; Johns et al., 1990). Indeed, it occurs in the region with weak value of C . In this regard, we also computed the gradient of absolute vorticity as follow:

$$C = \vec{\nabla} (f + \zeta) \cdot \vec{n} \quad (4)$$

where $\vec{n} = \frac{\vec{\nabla}(\psi)}{(\|\vec{\nabla}(\psi)\|)}$ is the unit vector perpendicular to geostrophic streamlines,

$\psi = -\frac{g}{f}SSH$ is the stream function, f is the Coriolis parameter.

Eddies properties

For each detected eddy, several properties are assessed. A center, an amplitude, a radius and a kinetic energy that it transports characterize an eddy. In the present study, the eddy center corresponds to the point where the SSH extremum (minimum for CE and maximum for AE) is observed (white dot in Figure 1b). The amplitude of the eddy corresponds to the absolute value of the difference between the SSH at the eddy center SSH_{center} and the averaged SSH along the eddy edge (SSH_{edge}). In our study, only eddies with amplitude higher than 1 cm were retained. The eddy radius corresponds to the radius of a disk delimited by the eddy edge (Figure 1b). Only eddies with radius larger than 25 km were retained. The eddy kinetic energy (EKE) was computed as averaged EKE inside the eddy, based on the velocity components.

$$Amplitude = |SSH_{center} - SSH_{edge}|$$

Assuming that the area of the disk delimited by the eddy edge is A , then the radius is defined as follow:

$$Radius = \sqrt{\frac{A}{\pi}}$$

$$EKE = \frac{1}{2}(u^2 + v^2)$$

3.2 3 MAPS OF EDDY PROPERTIES

In order to investigate eddy occurrence off Northeast Brazil (NEB) (37°-25°W;13°-1°S), we first build maps of spatial distribution of the number of detected eddies, eddy polarity, eddy properties (radius, amplitude), EKE, as well eddy speed of propagation and eddy life time.

Eddy mean properties are accessed after gridding the region onto on 1° × 1° cells. The mean eddy properties correspond to the mean of all eddy-like features with lifetime > 14 days that occur in each cell. The analysis is performed over the period of study (January-1993-December 2018).

Eddy number maps are built by considering the number of eddies with lifetime > 14 days within each cell. These maps show individual observations of eddies. For instance, if an eddy is stationary within a cell for 4 days, it will count as four observations within that cell. The eddy polarity is the probability for an eddy to be a cyclone (polarity < 0) or an anticyclone (polarity >0) and is defined as follow:

$$P = \frac{N_{AE} - N_{CE}}{N_{AE} + N_{CE}}$$

where N_{AE} is the number of AE while N_{CE} correspond to the number of CE.

Mean EKE maps correspond to the average mean EKE of eddy detected in each cell over the period of study.

Eddy mean propagation maps are built by considering the mean propagation speed of eddies with lifetime > 14 days within each cell. The eddy speed within each grid cell corresponds to the mean propagation speed of all eddy detected in each grid cell. Note that the eddy speed is the speed of a detected eddy from its location at time t to its next location at time $t+1$.

3.3 4 RESULTS AND DISCUSSION

4.1 Eddy density and mean properties off northeast Brazil.

In oceanic region off NEB, about 1500 eddies with radius larger than 25 km, amplitude larger than 1 cm and lifespan longer than 14 days were identified including 40% (60%) of AE (CE). Figure 3 shown the spatial distribution of mean annual number of detected eddies by 1° x 1°

cell off NEB from 1993 to 2018. The number of eddies was higher south of 8°S where up to 50 eddies per square degree per year were identified (Figure 3a). Actually, the northern and southern part of the study area presented overall differences in eddy numbers of characteristics. We thus defined two regions, one to the north named region A ($36^{\circ}\text{-}26^{\circ}\text{W}$; $6^{\circ}\text{S-}2^{\circ}\text{S}$) and one to the south named region B ($36^{\circ}\text{-}26^{\circ}\text{W}$; $8^{\circ}\text{-}12^{\circ}\text{S}$) (dashed rectangles in Figure 3a), to study the statistics of the different eddy properties and the likely processes responsible for their formation in these two regions. In the north lies the Fernando de Noronha ridge encompassing seamounts and islands. It is also the region where the central branch of south equatorial current (cSEC) transits to enter into the system of the western boundary and form the NBC. On the other hand, the southern part is associated with the bifurcation of the southern branch of south equatorial current (sSEC) from where originate the NBUC that flows northward and the BC that flows southward.

In the region A, CE eddies dominate with a mean polarity that can reach -1 (Figure 3b). However, AE can dominate in some areas. In region B, AE and CE were alike with the polarity that can locally reach 1 or -1 in some cells. Overall there is no clear geophysical pattern for CE and AE in the NEB, as observed in the global oceans (Chelton et al., 2011) and in the tropical Atlantic ocean (Aguedjou et al., 2019).

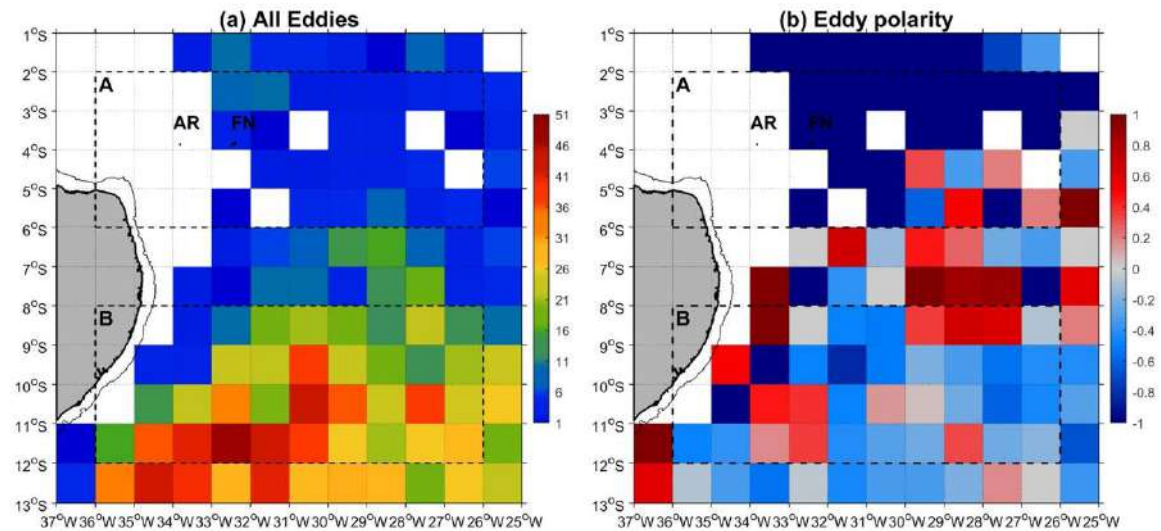


Figure 3. Spatial distribution of mean annual number of detected eddies per degree square over 1993-2018 period: (a) all eddies, (b) eddy polarity. The dashed rectangles A and B indicate respectively northern part of NEB located around Atoll Rocas (AR) and Fernando de Noronha (FN) archipelago, and southern part of NEB. Black contour indicates the bathymetric contour at 70 m.

Eddy amplitude globally ranged between 1 and 2 cm with no clear spatial pattern (Figure 4a). Eddy radii ranged between 25 and 205 km with radii decreasing from the north (> 110 km) to the south (Figure 4b) in accordance to the baroclinic Rossby radius deformation (e.g., Chaigneau et al., 2009) and tropical wave's instabilities (TWIs) in the near equatorial regions (e.g., Athie & Marin, 2008). Eddies with higher EKE values were dominantly observed in the equatorial region, north of 5°S , where EKE values reach $210 \text{ cm}^2 \text{ s}^{-2}$. In the southern part of NEB, region B the EKE was dominantly weak ($< 70 \text{ cm}^2 \text{ s}^{-2}$).

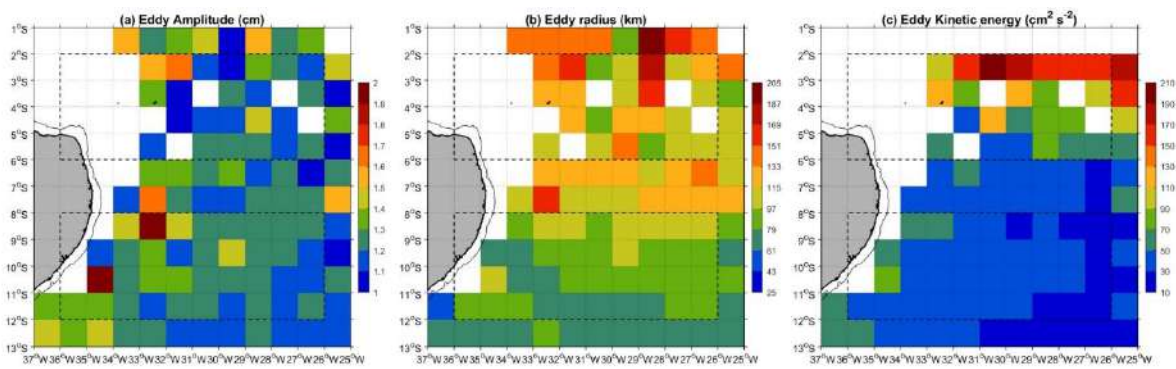


Figure 4. Spatial distribution of mean eddy characteristics per degree square over 1993–2018 period: (a) eddy amplitude (cm), (b) eddy radius (km) and (c) eddy kinetic energy ($\text{cm}^2 \text{ s}^{-2}$).

4.2 Eddy genesis and propagation off northeast of Brazil

To investigate eddy genesis location and their propagation within and beyond the NEB, we look at individual eddy trajectories from their formation until their dissipation (Figure 5) and at maps of spatial distribution mean eddy speed and lifetime (Figure 6). While, the individual trajectories give insight into eddy's genesis distribution within each regions, mean eddy speed and lifetime distribution show overview on eddy stationarity.

We detected and analyzed the trajectories of 1950 CE (40%) and AE (60%) eddies with amplitude and radius greater than 1 cm and 25 km, respectively, and a lifespan longer than 14 days. 25% of these eddies were formed outside the region mainly to the east from where they propagated westward into the region, due to the beta effect.

Most of eddies formed in the region are concentrated in the southern part, in region B. In region A tracked eddies are mostly CE (85%). No AE were identified within 1° around Atoll Rocas and the Fernando de Noronha archipelago. In region B the proportion between tracked CE and

AE was more homogeneous (58%/42%). However, in the most coastal zone, from the shelf-break to about 30 km offshore, only AE were tracked.

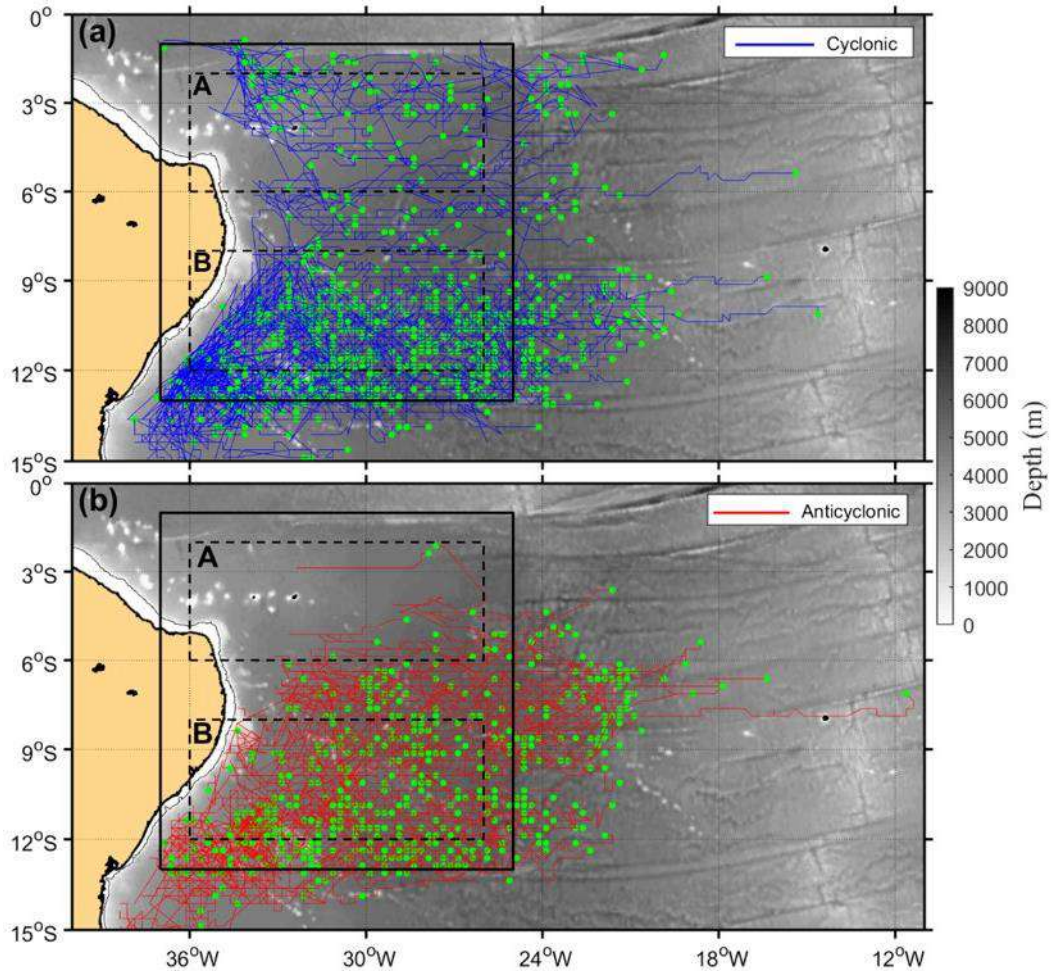


Figure 5. Trajectories of (a) cyclonic and (b) anticyclonic eddies which passed through Northeast Brazil between January 1993 and December 2018. Green dot indicate position where these eddies were first identified. Black box indicates the region off northeast Brazil while dashed boxes in (a) and (b) indicates respectively the region described figure 3b.

Eddies with higher speed (> 10 cm s) are located within region A (Figure 6a) and are mostly associated with short lifetimes (< 30 days) (Figure 6b). On the other hand, low velocity eddies (< 10 cm s) are dominant in region B (Figure 6a) with relatively large lifetimes (> 30 days). The eddies formed near the shelf-break west of 33°W have relatively low velocities and short lifetimes. Eddies within NEB last more when they have weak speed of propagation.

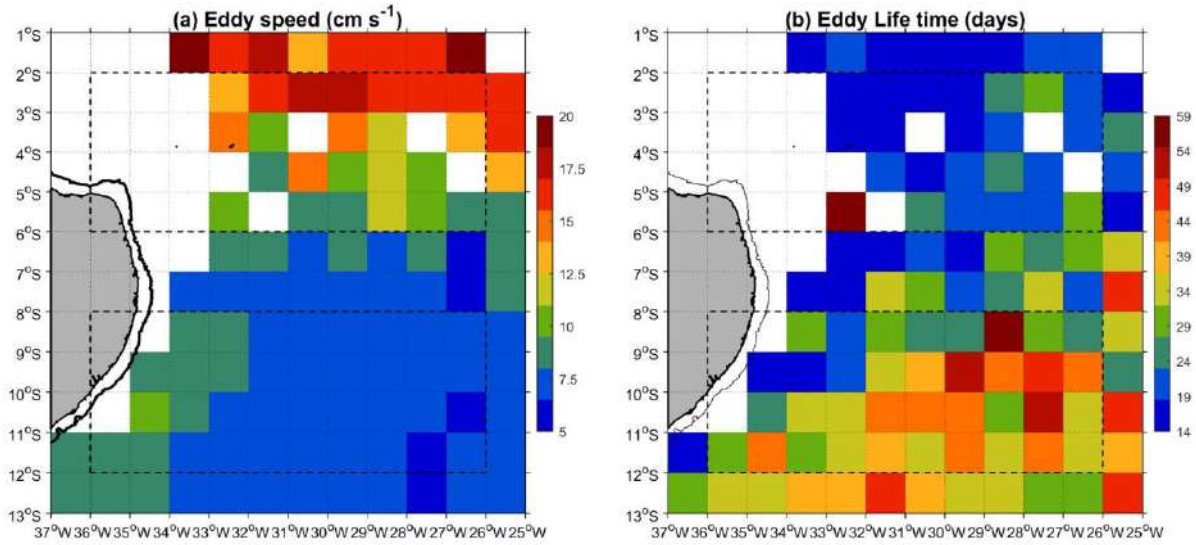


Figure 6. Spatial distribution per degree square over 1993-2018 period of (a) mean eddy speed of propagation and (b) mean eddy life time off northeast Brazil.

Eddies properties within NEB, A and B are summarized in Table 1. In the three regions, the mean amplitudes of the AE and CE were alike (Table 1). The average radius of the AE was larger than the average radius of the CE in the NEB and B, whereas in the region A, the average radius of the CE was larger than that of the AE. On the other hand, for the other properties, a difference between the AE and CE varied from one region to another (with STD values more or less close to the average values of the properties). The CE had a higher mean properties (EKE, speed and lifetime) than the AE in the three regions except for the lifetime of eddies in region A where it is the same for both types of eddies. In addition, CE eddies have a higher mean speed than AE and are associated with higher lifetimes.

Table 1 Mean (Standard deviation (STD)) properties and characteristics of AE and CE within NEB and northern part of NEB (A) and southern part of NEB (B).

	Mean (STD)					
	NEB		A		B	
	AE	CE	AE	CE	AE	CE
Number of trajectories crossing	775	1173	41	134	448	666
Number of eddies generated within	583	887	14	80	326	442
Amplitude (cm)	1.2 (0.3)	1.3 (0.3)	1.2 (0.2)	1.3 (0.3)	1.2 (0.3)	1.3 (0.5)
Radius (km)	94.7 (23.8)	90.3 (26.2)	121.5 (18.1)	130.0 (46.3)	91.4 (29.1)	86.2 (29.0)

EKE ($\text{cm}^2 \text{s}^{-2}$)	35.0 (14.0)	51.0 (32.0)	79.0 (4.1)	132.0 (32.1)	32.0 (12.0)	38.0 (21.0)
Speed (cm s^{-1})	7.4 (1.6)	8.6 (3.2)	11.0 (2.3)	14.3 (3.4)	7.2 (1.3)	7.7 (1.8)
Lifetime (days)	32 (24)	35 (26)	21 (5)	21 (8)	33 (22)	41 (29)

4.3 Eddy seasonal variability and mechanisms behind its formation off northeast Brazil

In the NEB region, there is more CE than AE throughout the year except in June when the numbers are alike (Figure 7). However, the number of both types of eddies shows a similar pronounced seasonal cycle. More eddies occur in August-September-October for both types of eddies with a maximum in October. The lower number of eddies is observed in February-March, with however a minimum in June for CE.

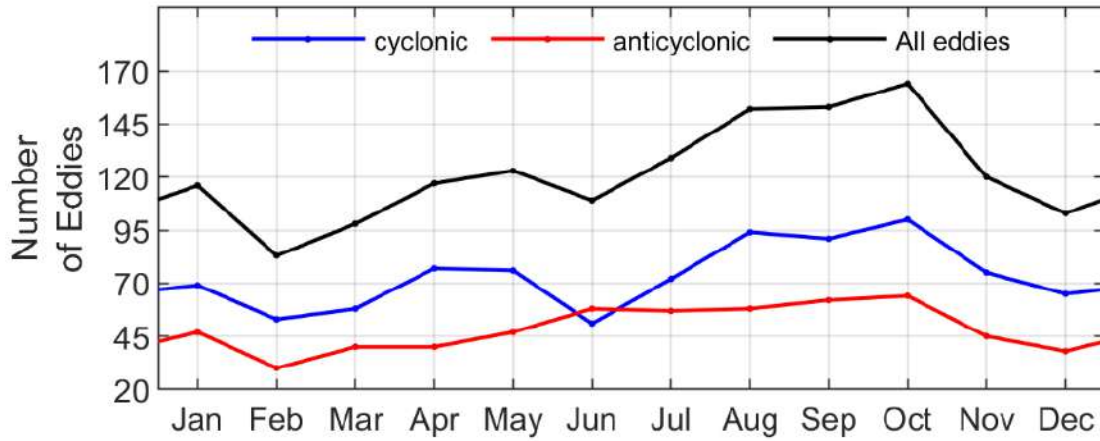


Figure 7. Seasonal cycle of number of eddies generated off Northeast Brazil.

We further estimated the seasonal variation of the number of AE and CE eddies as well as the wind stress curl and wind stress magnitude in regions A and B. In each region, the number of each type of eddies show a different seasonal variation (Figure 8a,b). In region A, the number of CE is much larger than the number of AE between March and December with a larger difference in October. From December to March, the number of AE and CE is almost the same. However, there is a pronounced seasonal cycle for CE, with a maximum number of eddies in August-September. This seasonal variation in the number of CE in this region seems related to the seasonal variation in the wind stress curl. In addition, the wind stress curl is negative throughout the year indicating that CE within region A are mostly induced by negative wind stress curl resulting from cyclonic circulation (e.g., Rodrigues et al., 2007).

On other side, less seasonal variation was observed in region B. However, AE and CE were respectively minimum in April and June and maximum in August and October. The averaged wind stress curl within the region shows similar seasonal variation as the CE. It reaches its minimum value ($-1.8 \cdot 10^{-8} \text{ N}$) in July and maximum ($0.7 \cdot 10^{-8} \text{ N}$) value in November, consistent

with the observation Rodrigues et al (2007). The wind stress curl was positive when the CE was higher (> 35 / per month). When it reached its minimum value in June, the number of CE was at its minimum value. Therefore, the occurrence of CE seems to be favored by seasonal variation of the wind stress curl. On other side, wind stress variation and AE variation are alike. The increase of wind stress induce the increase in AE while its decrease induce AE decrease. The intensification of the wind stress seems to favor the formation of AE within region B. Overall, CE formation within region is favored by wind stress curl while AE are favored by intensification of wind stress magnitude. However, it is necessary to verify the existence of other mechanisms that could induce eddy formation in the region.

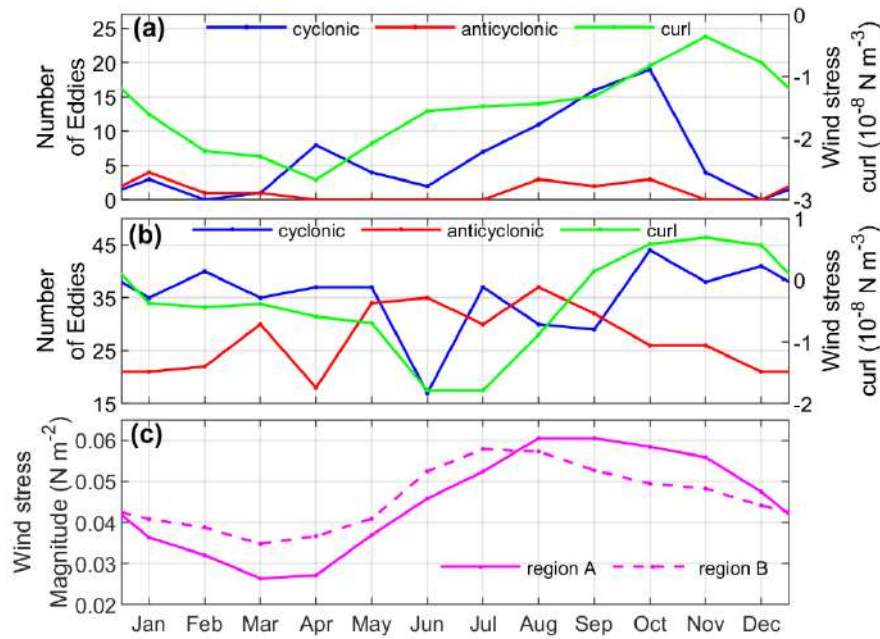


Figure 8. Seasonal cycle of (a) number of AE and CE (red and blue lines respectively) and wind stress curl (green line) within northern part of NEB (region A), (b) number of AE and CE (red and blue lines respectively) and wind stress curl (green line) within southern part of NEB (region B), and (c) wind stress magnitude in regions A (magenta line) and B (dashed magenta line).

Indeed, several other mechanisms such as the topographic effect, barotropic and baroclinic instabilities are susceptible to promote the formation of eddies in the world ocean. According to the Rayleigh (1880) criterion extended to nonparallel steady currents and applied in the geostrophic context, barotropic instabilities increase in regions where the gradient of the absolute vorticity (C) of large-scale currents is small by changing sign. This criterion was recently applied in the region of the NECC retroflection in the tropical Atlantic (Aguedjou et al., 2019) where more than 55% of eddies are formed in areas of low vorticity gradient. In the same context, we first estimated the seasonal variability of the gradient of absolute vorticity gradient superimposed on the formation position of each eddy detected in regions A and B,

each month, between 1993 and 2018 (Figure 9). In a second step, we assessed the variation of the number of eddies formed in each region as a function of the absolute vorticity gradient (Figure 10).

The spatial map of the gradient of absolute vorticity within NEB does not show clear seasonal patterns within NEB (Figure 9). The position of eddy formed within region A shown that none AE are formed within area where the gradient of absolute velocity is weak. Nevertheless, four CE were observed in the weak gradient of absolute vorticity. The four CE occurs respectively in January, March, July and August. These observation are also underlined in Figure 10a, where only 4 CE within $\pm 5 \times 10^{-10}$.

In region B, the spatial distribution of gradient of the absolute vorticity shown weaker value than the region A. However, it was possible to distinguish eddies occurring within region of weak gradient of absolute vorticity. Overall, at least 3 eddies of each type are formed per month within the region weak gradient of absolute (Figure 9). This is highlighted on figure 10b, which shown occurrence of 87 (105) AE (CE) within $\pm 5 \times 10^{-10}$. This number of eddies occurring within region of weak gradient of absolute vorticity indicate that apart from wind stress curl and barotropic instabilities others mechanisms may favor eddies occurs within both region. In this regard, we investigated the seasonal variation of large scale surface currents.

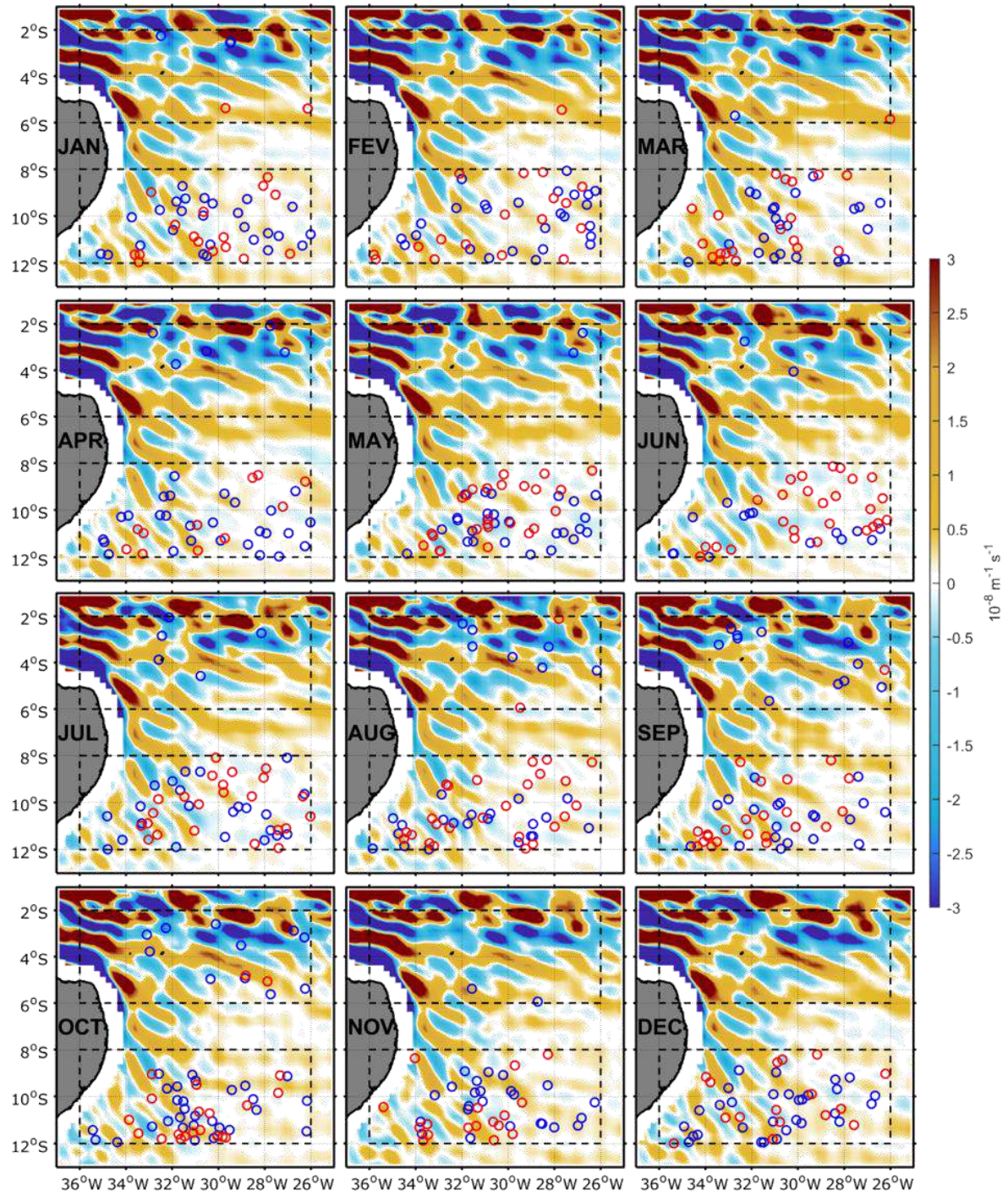


Figure 9. Monthly map of mean gradient of absolute vorticity of large-scale currents (color shading) superimposed with eddy location of long-lived eddies generated off northeast Brazil in August between 1993 and 2018 (blue and red circles for cyclonic and anticyclonic eddies respectively).

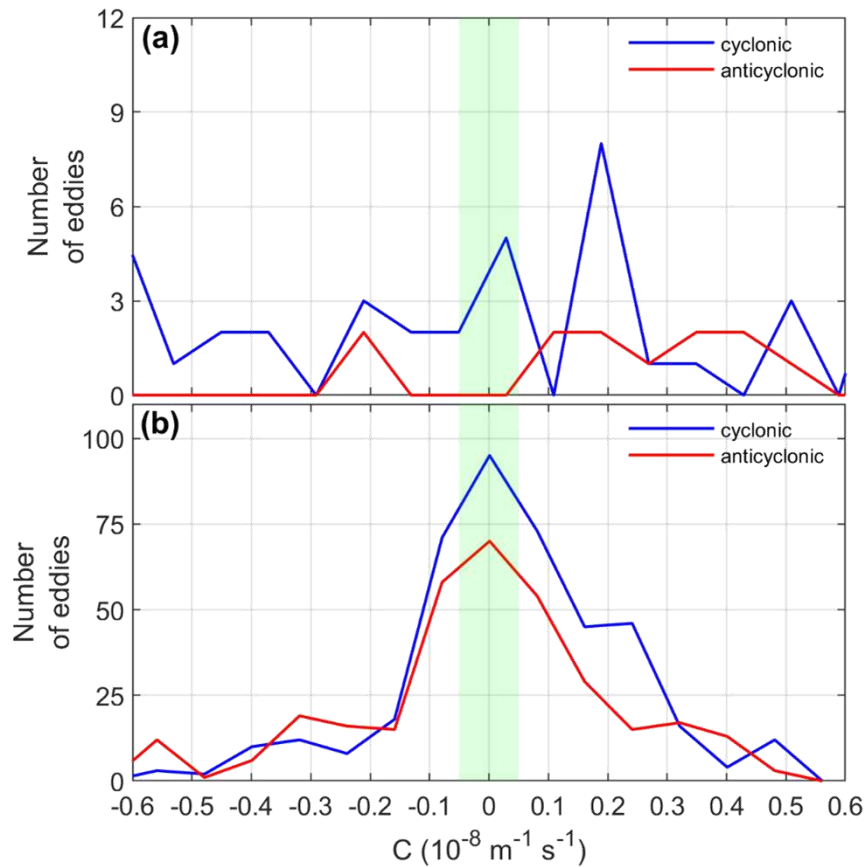


Figure 10. Distribution of the number of detected cyclonic and anticyclonic eddies as function of the gradient of large-scale absolute vorticity C at eddy generation sites for all eddies generated between 1993 and 2018 within: (a) northern part of NEB (region A) and (b) southern part of NEB (region B). Green vertical in (a) and (b) indicate interval values C within $\pm 5 \times 10^{-10} \text{ m}^{-1} \text{ s}^{-1}$.

Surface current velocities along the coast exhibited a seasonal variability (Figure 11). They intensify progressively from January to July with the occurrence of strong values in May-June when the speed can reach 1 m s^{-1} north of 5°S and 0.8 m s^{-1} south of 8°S . In the second half of the year, from July to December, the velocities along the coast weaken relatively compared to the first half of the year.

In region A, the circulation is mainly westward (characteristic of the cSEC) at the beginning of the year (January-February-March). In April, the current velocities strengthen ($>0.8 \text{ m s}^{-1}$). During this month, a cyclonic recirculation around 2°S between 26° - 30°W is noted, which remains permanent until May, when it gradually disappears. This cyclonic recirculation at the northern limit of region A would contribute to the little peak in the number of CE observed in the region in April. From May onward, the circulation changes direction slightly and progressively shifts to the southwest around 3°S east of 28°W . This orientation becomes noticeable in most of the region until August. However, from this month, the strength of the current weakens in the region and becomes westward until the end of the year.

On the other hand, the current velocities in region B are weaker than those in region A, throughout the year. Moreover, the circulation is not as organized as in region A. Early in the year, cyclonic structures are noted around 28°W between 10° - 8°S . Moreover, around 10°S to about 34°W , there is a retroflection of a zonal flow from the east, remarkable from February. During the retroflection, the zonal flow splits in two, one is directed to the north and the other to the south. This southward flow seems recirculates further south and enter into the northward coastal flow. In April, we notice that the retroflection occurs a little further north around 8°S , while the recirculation of the southward flow occurs around 10°S . This retroflection remains permanent around 8°S throughout the year. On the other hand, the cyclonic recirculation of the southward flow occurs progressively further south. In July-August, it is quite remarkable around 12°S to $\sim 36^{\circ}\text{W}$. Between September and December, it seems to occur much more to the south. In addition, east of the region at 10° - 8°S ; 30 - 28°W , a meander of the surface current is present between August and September. The different processes observed in the B region explained better the formation of a large number of eddies in region B compared to region A.

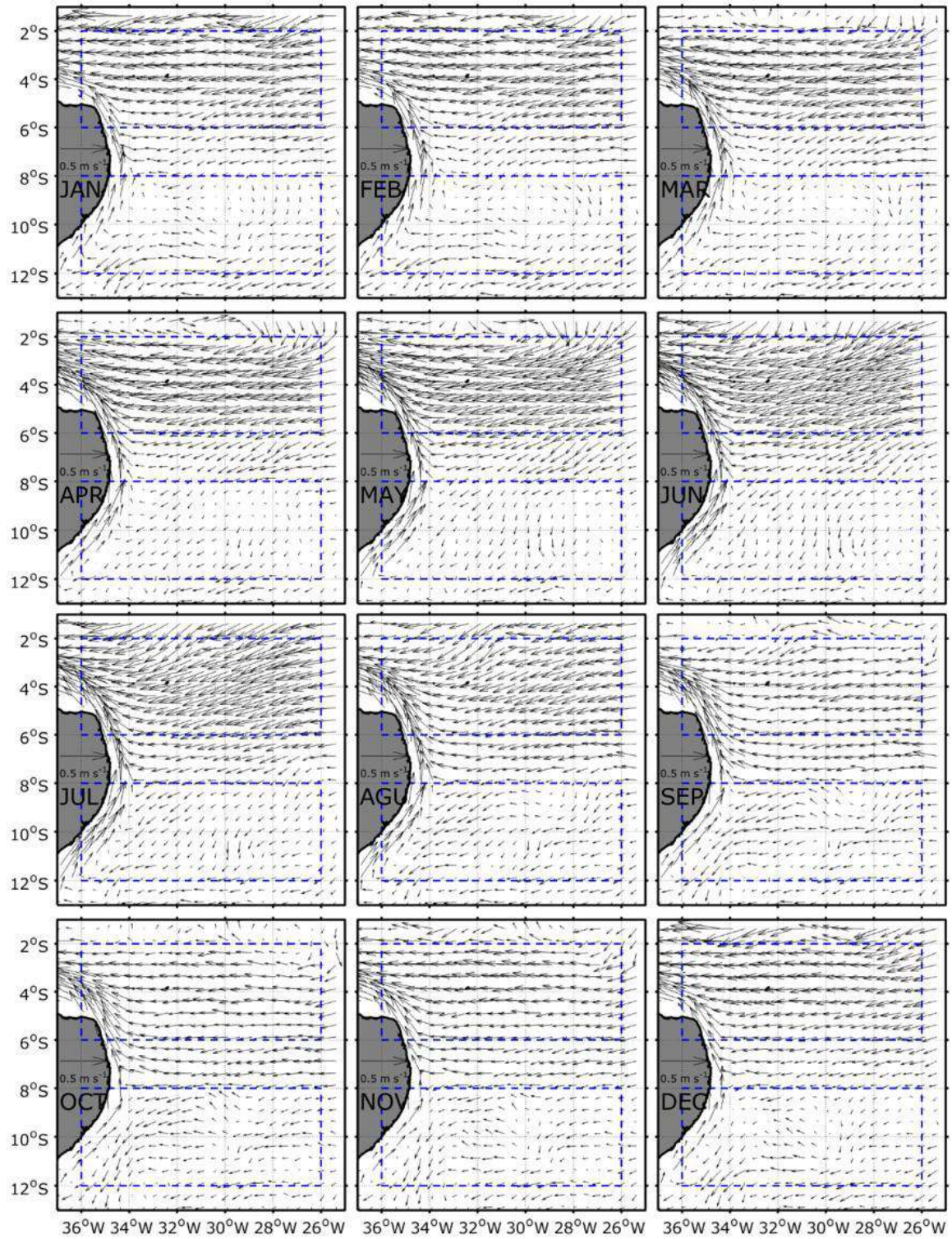


Figure 11. Monthly map of surface currents from off NEB.

5 Conclusion

In the present chapter, by applying the automatic eddy, detection and tracking algorithm on 26 years of daily SSH, we described the main properties of mesoscale eddies activities off northeast Brazil. In this region, about 1950 eddies trajectories were identified. Among the trajectories crossing the region, only 76% are formed within the region. These eddies show amplitudes, radii and EKE, ranged at 1-2 cm, 25-205 km, and $10\text{-}210\text{ cm}^2\text{ s}^{-2}$ respectively. Eddies with high mean EKE mostly occur north of 5°S .

Seasonally, the highest number of eddies occurs in August-September-October with the maximum in October, while a small number of eddies occur in February-March. CE are almost more abundant than AE throughout the year except in June. To investigate the different mechanisms that can favor the formation of eddies in the region; we have defined two key regions characterized by a somewhat different physical process. A region A ($36\text{-}26^\circ\text{S}$; $2^\circ\text{-}6^\circ\text{S}$) was defined in the northern part and included Rocas Atoll and Fernando de Noronha archipelago. A second region B ($36^\circ\text{-}26^\circ$; $8\text{-}12^\circ\text{S}$) has been defined in the southern part and takes into account part of the sSEC retroflection area.

In both regions, the number of formed CE is higher than the number of formed AE. As in the large NEB region, the largest number of eddies in both regions are formed in October. In the A region, several mechanisms are favorable for eddy formation. The formation of CE is partly related to barotropic instabilities due to the shearing of zonal currents and wind stress curl. On the other hand, the formation of AE in the region A is partly related to the wind stress curl. In region B, about 25% of both types of eddies are formed by barotropic instabilities. Other mechanisms such as wind stress curl, meandering of surface currents are also responsible for the formation of eddies in the region. Others physical mechanisms related to vertical structures may also be responsible for the eddy generation in the region. Nevertheless, this investigation will require long-term hydrographic data at fine temporal and spatial resolution.

References

- Aguedjou, H. M. A., Dadou, I., Chaigneau, A., Morel, Y., & Alory, G. (2019). Eddies in the Tropical Atlantic Ocean and Their Seasonal Variability. *Geophysical Research Letters*, 156–164. <https://doi.org/10.1029/2019GL083925>
- Arruda, W. Z., Campos, E. J. D., Zharkov, V., Soutelino, R. G., & da Silveira, I. C. A. (2013). Events of equatorward translation of the Vitoria Eddy. *Continental Shelf Research*, 70, 61–73. <https://doi.org/10.1016/j.csr.2013.05.004>
- Athie, G., & Marin, F. (2008). Cross-equatorial structure and temporal modulation of intraseasonal variability at the surface of the Tropical Atlantic Ocean. *Journal of Geophysical Research: Oceans*, 113(8), 1–17. <https://doi.org/10.1029/2007JC004332>

- Campos, E. J. D. (2006). Equatorward translation of the Vitoria Eddy in a numerical simulation. *Geophysical Research Letters*, 33(22), 1–5. <https://doi.org/10.1029/2006GL026997>
- Chaigneau, A., Gizolme, A., & Grados, C. (2008). Mesoscale eddies off Peru in altimeter records: Identification algorithms and eddy spatio-temporal patterns. *Progress in Oceanography*, 79(2–4), 106–119. <https://doi.org/10.1016/j.pocean.2008.10.013>
- Chaigneau, A., Eldin, G., & Dewitte, B. (2009). Eddy activity in the four major upwelling systems from satellite altimetry (1992–2007). *Progress in Oceanography*, 83(1–4), 117–123. <https://doi.org/10.1016/j.pocean.2009.07.012>
- Chelton, D. B., Schlax, M. G., & Samelson, R. M. (2011). Global observations of nonlinear mesoscale eddies. *Progress in Oceanography*, 91(2), 167–216. <https://doi.org/10.1016/j.pocean.2011.01.002>
- Dandapat, S., & Chakraborty, A. (2016). Mesoscale Eddies in the Western Bay of Bengal as Observed from Satellite Altimetry in 1993–2014: Statistical Characteristics, Variability and Three-Dimensional Properties. *IEEE Journal of Selected Topics in Applied Earth Observations and Remote Sensing*, 9(11), 5044–5054. <https://doi.org/10.1109/JSTARS.2016.2585179>
- Dossa, A. N., Silva, A. C., Chaigneau, A., Eldin, G., Araujo, M., & Bertrand, A. (2021). Near-surface western boundary circulation off Northeast Brazil. *Progress in Oceanography*, 190(January 2020), 102475. <https://doi.org/10.1016/j.pocean.2020.102475>
- Frenger, I., Gruber, N., Knutti, R., & Münnich, M. (2013). Imprint of Southern Ocean eddies on winds, clouds and rainfall. *Nature Geoscience*, 6(8), 608–612. <https://doi.org/10.1038/ngeo1863>
- Johns, W. E., Lee, T. N., Schott, F. A., Zantopp, R. J., & Evans, R. H. (1990). • EQUATORIAL, 95, 103–120.
- Keppler, L., Cravatte, S., Chaigneau, A., Pegliasco, C., Gourdeau, L., & Singh, A. (2018). Observed Characteristics and Vertical Structure of Mesoscale Eddies in the Southwest Tropical Pacific. *Journal of Geophysical Research: Oceans*, 123(4), 2731–2756. <https://doi.org/10.1002/2017JC013712>
- Pegliasco, C., Chaigneau, A., & Morrow, R. (2015). Main eddy vertical structures observed in the four major Eastern Boundary Upwelling Systems. *Journal of Geophysical Research: Oceans*, 120(9), 6008–6033. <https://doi.org/10.1002/2015JC010950>
- Schmid, C., Schafer, H., Podesta, G., & Zenk, W. (1995). The Vitoria eddy and its relation to the Brazil Current. *Journal of Physical Oceanography*. [https://doi.org/10.1175/1520-0485\(1995\)025<2532:tveair>2.0.co;2](https://doi.org/10.1175/1520-0485(1995)025<2532:tveair>2.0.co;2)
- Schott, F. A., Stramma, L., & Fischer, J. (1995). The warm water inflow into the western tropical Atlantic boundary regime, spring 1994. *Journal of Geophysical Research*, 100(C12), 24745. <https://doi.org/10.1029/95JC02803>

- Schott, F. A., Fischer, J., & Stramma, L. (1998). Transports and Pathways of the Upper-Layer Circulation in the Western Tropical Atlantic. *Journal of Physical Oceanography*, 28(10), 1904–1928. [https://doi.org/10.1175/1520-0485\(1998\)028<1904:TAPOTU>2.0.CO;2](https://doi.org/10.1175/1520-0485(1998)028<1904:TAPOTU>2.0.CO;2)
- Soutelino, R. G., Da Silveira, I. C. A., Gangopadhyay, A., & Miranda, J. A. (2011). Is the Brazil Current eddy-dominated to the north of 20°S? *Geophysical Research Letters*, 38(3), 1–5. <https://doi.org/10.1029/2010GL046276>
- Soutelino, R. G., Gangopadhyay, A., & da Silveira, I. C. A. (2013). The roles of vertical shear and topography on the eddy formation near the site of origin of the Brazil Current. *Continental Shelf Research*, 70, 46–60. <https://doi.org/10.1016/j.csr.2013.10.001>
- Villas Bôas, A. B., Sato, O. T., Chaigneau, A., & Castelão, G. P. (2015). The signature of mesoscale eddies on the air-sea turbulent heat fluxes in the South Atlantic Ocean. *Geophysical Research Letters*, 42(6), 1856–1862. <https://doi.org/10.1002/2015GL063105>
- Wunsch, C. (1999). Where do ocean eddy heat fluxes matter? *Journal of Geophysical Research: Oceans*, 104(C6), 13235–13249. <https://doi.org/10.1029/1999jc900062>
- Berrisford, P., Dee, D., Poli, P., Brugge, R., Fielding, K., Fuentes, M., ... & Simmons, A. (2011). The ERA-Interim archive, version 2.0.

4 GLOBAL ANALYSIS OF COASTAL GRADIENTS OF SEA SURFACE SALINITY

In this chapter, we analysis the coastal gradients of sea surface salinity, based on two satellites products, model reanalysis and in situ observations. This work was published in “Remote Sensing” journal as original Research and is described in the section below.

Doi:10.3390/rs13132507

Alina N. Dossa^{1,2*}, Gaël Alory², Alex Silva¹, Adeola M. Dahunsi³ and Arnaud Bertrand^{4,1,5}

¹Laboratório de Oceanografia Física Estuarina e Costeira, Depto. Oceanografia, UFPE, Recife-PE, Brazil

²Laboratoire d'Études en Géophysique et Océanographie Spatiale (LEGOS), Université de Toulouse, CNES/CNRS/IRD/UPS, Toulouse, France

³International Chair in Mathematical Physics and Applications (ICMPA), Université d'Abomey-Calavi, Cotonou, Benin

⁴Institut de Recherche pour le Développement, MARBEC, Univ Montpellier, CNRS, Ifremer, IRD, Sète, France.

⁵Universidade Federal Rural de Pernambuco (UFRPE), Recife, Brazil

*Corresponding author: Dossa Alina Nathanaël, nath2dossa@gmail.com

Abstract

Sea surface salinity (SSS) is a key variable for ocean-atmosphere interactions and the water cycle. Due to its climatic importance, increasing efforts have been made for its global *in situ* observation, and dedicated satellite missions have been launched more recently to allow homogeneous coverage at higher resolution. Cross-shore SSS gradients can bear the signature of different coastal processes such as river plumes, upwelling or boundary currents, as we illustrate in a few regions. However, satellites performances are questionable in coastal regions. Here, we assess the skill of four gridded products derived from the Soil Moisture Ocean Salinity (SMOS) and Soil Moisture Active Passive (SMAP) satellites, and the GLORYS global model reanalysis, at capturing cross-shore SSS gradients in coastal bands up to 300 km wide. These products are compared with thermosalinographs (TSG) measurements, which provide continuous data from the open ocean to the coast along ship tracks. The comparison shows various skills from one product to the other, decreasing as the coast gets closer. The bias in reproducing coastal SSS gradients is unrelated to how the SSS biases evolve with the distance

to the coast. Despite limited skill, satellite products generally agree better with collocated TSG data than a global reanalysis, and show a large range of coastal SSS gradients with different signs. Moreover, satellites reveal a global dominance of coastal freshening, primarily related to river runoff over shelves. This work shows a great potential of SSS remote sensing to monitor coastal processes, which would however require a jump in the resolution of future SSS satellite missions to be fully exploited.

Keywords: SSS; thermosalinograph; SMOS; SMAP; GLORYS; Amazon River plume; northeast Brazil; Bay of Bengal; California Current system; Great Australian Bight

1. INTRODUCTION

Sea surface salinity (SSS) is an essential climate variable that bears the signature of the water cycle at the ocean-atmosphere interface, where most water fluxes occur [1]. The large-scale spatial patterns of SSS mostly result from the balance between evaporation and precipitation. High SSS is found in the subtropical gyres, where evaporation dominates [2,3], while lower SSS is found around the intertropical convergence zones and at high latitudes, where precipitation dominates. SSS is also affected at high latitudes by the formation or melting of sea ice, which has much smaller salt content than seawater [4]. Ocean circulation and mesoscale eddies also contribute to the transport of water properties and thus to the spatial distribution of SSS (e.g., [5]).

On the other hand, with temperature, salinity controls seawater density. SSS increase under freezing sea ice plays a key role in the deep convection that controls the thermohaline ocean circulation [2,6][6]. Low SSS due to precipitation or river runoff is associated with strong stratification, which often leads to the formation of a barrier layer within the near isothermal layer (e.g., [7,8]). Barrier layers reduce the mixed layer thickness, lessen vertical exchanges with the deep ocean and enhance ocean-atmosphere interactions (e.g., [9,10]).

In coastal regions, some specific processes affect SSS. Runoff from large rivers, which create plumes extending offshore, or from smaller rivers decreases SSS (e.g., [11]). This effect can be amplified at high latitudes by continental ice melt [12]. Recent studies suggest that in the tropics, rainfall is mostly concentrated in a coastal belt of around 100 km each side of the coastline, which would result in a freshwater supply comparable to that of rivers, also reducing coastal SSS [13]. These coastal anomalies can be redistributed along-shore by currents, which

are particularly strong at ocean western boundaries [14,15]. Coastal upwelling can also generate SSS anomalies, in the presence of a vertical salinity gradient, which would typically extend offshore up to 10s to a few 100s km, following the local Rossby radius of deformation [16].

To better describe and understand SSS spatio-temporal variations, as well as their role on Earth climate, increasing efforts have been made in recent decades to monitor the SSS, or more generally salinity, globally. In addition to the classic methods (CTD, bottle sampling), thermosalinographs (TSG) were installed on Voluntary Observing Ships (VOS) that cross the global ocean [17,18]. ARGO floats were deployed to automatically collect temperature and salinity profiles of the global ocean. In addition, more recently, satellites missions were launched to monitor SSS remotely. Soil Moisture Ocean Salinity (SMOS) was first launched in 2009 [19], followed by the Aquarius satellite in 2011 [20]. Soil Moisture Active Passive (SMAP) replaced Aquarius in 2015. The combination of these data with numerical models has greatly enhanced our understanding of the patterns of SSS variability and distribution at different spatial and temporal scales in the Pacific (e.g., [5,21,22]), Atlantic (e.g., [23–25]) and Indian [26–28] oceans. In situ SSS measurements are the foundation of this knowledge as they are also necessary to validate and improve the accuracy of numerical models [29,30], and to calibrate/validate satellite SSS measurements [31].

In spite of a high number of studies focusing on SSS variability and distribution, coastal SSS patterns and gradients remain poorly documented globally for at least three main reasons. First, in situ SSS measurements are relatively sparse in both space and time in coastal regions. Second, the knowledge of continental freshwater forcing and its introduction as a boundary condition need improvement in numerical models [32]. Third, satellites skill in coastal regions are subject to flaws due to land shadowing in the sensor footprint (e.g., [33,34]). However, coastal bias corrections have been introduced in satellite products (e.g., [35,36]), but their skills have not been compared against each other to ground truth.

In this context, we take advantage of SSS measurements from TSG, which, despite their relatively sparse coverage, extend continuously from the open ocean to the coast, to estimate the skill of different gridded SMOS and SMAP satellite SSS products and a model reanalysis in capturing coastal SSS gradients. Data and methods are presented in the next section. It is followed by a global statistical analysis of coastal SSS gradients, illustrated with a selection of case studies: Amazon River plume, northeast Brazil, Bay of Bengal, California Current system

and the Great Australian Bight. We finally discuss the results and present the conclusions of the study.

2. DATA AND METHODS

2.1. Data

2.1.1 *In situ* data

In situ SSS data used in the present study come from underway TSG measurements available in the global Ocean from 1993 to the present (Figure 1a). The main source is the French TSG database, including measurements from VOS, managed by the SSS Observation Service [17], from research vessels (RV)[37] and sailing ships [38], representing together about half of the global TSG network [39]. Other sources include TSG data from the US-managed Shipboard Automated Meteorological and Oceanographic System initiative [40], VOS managed by the US National Oceanic and Atmospheric Administration (NOAA), by the Japanese National Institute for Environmental Studies and VOS Nippon organization, RV operated by NOAA, the Australian Commonwealth Scientific and Industrial Research Organization and the Japan Agency for Marine-Earth Science and Technology.

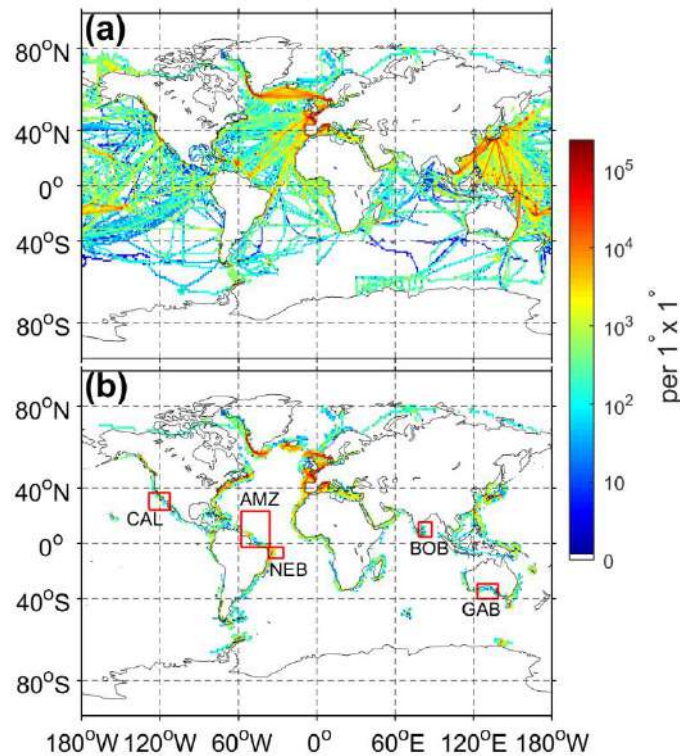


Figure 1. Density of TSG data (in number of observations per 1° bins, logarithmic scale) from 1993 to 2019 in (a) the global Ocean Global and (b) the 0 - 300 km coastal band. Red boxes

indicates the regions of interest: Amazon River plume (AMZ); northeast Brazil (NEB); Bay of Bengal (BOB); California (CAL) and Great Australian Bight (GAB).

These measurements are mostly collected from the SBE-21 TSG manufactured by Seabird Electronics. The TSG is generally installed in the engine room of VOS. The depth at which the seawater is collected depends on the ship and its load but is around 5-10 m for VOS, a bit shallower for RV. The temporal resolution is 1 or 5 minutes for RV and VOS, respectively, which corresponds roughly to a 2-3 km along-track resolution for VOS typically cruising at 15 knots and even finer for RV. TSG data density is high in the north Atlantic and western Pacific, and relatively low in the southern hemisphere (Figure 1a). The present study is based on TSG data available in the nearest 300 km from the coast, with a focus on a selection of five coastal regions: Amazon River plume, northeast Brazil, Bay of Bengal, California upwelling system and Great Australian Bight (Figure 1b; Table 1).

2.1.2 Satellites SSS products

2.1.2.1. SMOS satellite products

The Soil Moisture and Ocean Salinity mission is conducted by the European Space Agency (ESA) in collaboration with the Centre National d'Etudes Spatiales (CNES) in France and the Centro para el Desarrollo Tecnoligica Industrial (CDTI) in Spain [19]. The satellite is equipped with a radiometer that measures the microwaves of electromagnetic radiation emitted by the Earth's surface at L-band (1.4 GHz) using an interferometric radiometer called Microwave Image Radiometer using Aperture Synthesis (MIRAS) designed by ESA. MIRAS measures the brightness temperature (TB) for the recovery of SSS over the oceans and soil moisture on land. SMOS satellite follows the sun-synchronous polar orbit at an altitude of 763 km. The satellite achieves global coverage every three days with an incidence range of 0-60° and a swath of ~1000 km at full polarization.

In this study, we used two SMOS SSS products. The first is the de-biased SMOS Level 3 (L3) gridded product version 5 made by the Laboratoire d'Océanographie et du Climat (LOCEAN) and the Ocean Salinity Expertise Center (CEC-OS) of Centre Aval de Traitements des Données SMOS (CATDS). Compared to previous versions, this product uses an improved adjustment of land-sea biases close to the coast and ice filtering at high latitudes [35]. The 9-day running maps are available on a $0.25^\circ \times 0.25^\circ$ grid at 4-day time scale on the 2010-2020 period. This product is referred as SMOS LOCEAN hereafter. The second SMOS product is the so-called L3 version 2 product from Barcelona Expert Center (BEC)[41]. This product was derived from the debiased non-Bayesian retrieval that reduces the spatial biases induced by land-sea and radio

frequency interference contamination close to the coast. The 9-day running maps, the so-called L3 product are daily produced and are available on a $0.25^\circ \times 0.25^\circ$ grid at daily time scale on the 2011- 2019 period. This product is referred as SMOS BEC hereafter.

2.1.2.1 SMAP satellite products

The National Aeronautics and Space Administration (NASA) leads the Soil Moisture Active Passive (SMAP) mission that also monitor the SSS. The SMAP satellite is in a near-polar orbit, sun-synchronous, at an inclination of 98° and an altitude of 685 km. With its swath (~ 1000 km), the satellite reaches its global coverage in approximatively 3 days with a spatial resolution approximatively 40 km. The sensors onboard the mission are passive microwave radiometers operating at 1.4 GHz (L-band). SSS is retrieved from the TB measurement.

Here, we used two SMAP SSS maps produced by different centers. One was the SMAP L3 version 4.3 product developed by Jet Propulsion Laboratory (JPL). This product is based on the retrieval algorithm that was developed in the context of the previous Aquarius mission and updated to SMAP. It has an inherent feature resolution of 60 km and is mapped on a $0.25^\circ \times 0.25^\circ$ grid, at 8-day resolution (based on temporal running means). This product includes land-sea bias corrections [42]. It is referred hereafter as SMAP JPL. The other product is the SMAP L3 version 4.0 product developed by Remote Sensing system (RSS, www.remss.com/missions/smap). The product is derived from a 40-km spatial resolution product using Backus Gilbert Optimum Interpolation (OI). It was then smoothed with approximatively 70-km spatial resolution using simple next neighbor averaging at each grid cell that allows noise reduction. It is available on a $0.25^\circ \times 0.25^\circ$, 8-day grid. This product includes land correction with retrieval of salinity within 30-40 km off the coast. It is referred hereafter as SMAP RSS. These two SMAP SSS product are available from April 1, 2015 to the present and are distributed by the NASA Physical Oceanography Distributed Active Archive Center (PO.DAAC).

2.1.3 Reanalysis product

The Global $1/12^\circ$ Ocean Reanalysis version 1 (GLORYS12V1) developed by Mercator and distributed by the European Copernicus Marine Environment Monitoring Service (CMEMS) aims at producing state of the art eddy resolving ocean simulations constrained by oceanic observations by means of data assimilation [43]. The ocean model component is NEMO, forced at the surface by ECMWF-ERA interim reanalysis including precipitation and radiative fluxes corrections. The assimilation scheme is 3D-VAR providing a correction for the slowly evolving

large-scale biases in temperature and salinity. The assimilated observations are Reynolds 0.25 AVHRR-only SST, delayed time SLA from the satellites, *in situ* T/S profiles from the Coriolis Ocean dataset for Reanalysis version 4.1 (CORAV4.1) database [44]. The ETOPO1 Earth topography at 1 arc-minute resolution was used for the deep ocean topography while the Global Earth Bathymetric Chart of the Oceans (GEBCO) 1-resolution dataset was used for the coast and continental shelf topography. The GLORYS12V1 product includes daily and monthly outputs of salinity, temperature, currents, sea level, mixed layer depth and ice parameters available on a regular grid at $1/12^\circ$ and 50 standard vertical levels. The product spans from January 1993 to June 2019. In this study, we used the daily salinity outputs estimated at the ocean surface (~ 0.5 m depth). This product is referred as GLORYS hereafter.

2.2 Methods

The computation of coastal SSS gradients from TSG, satellite and reanalysis data is based on a linear least square fit method. Gradient were estimated in bands ranging from 50 to 150, 200 and 250 km from the coast, along cross-shore sections. Data in the first 50 km from the coast were excluded because of the poor skill of satellite data in this band. Due to the spatial scales considered here, coastal data around islands smaller than 150 km in diameter were excluded from the present study.

2.2.1 SSS Gradient calculation from TSG data

SSS gradient from TSG data were calculated along cross-shore ship tracks data available in coastal regions (Figure 2). The extractions of cross-shore ship tracks works as follow. For a given ship trip (Figure 2a), tracks are first extracted in each coastal region whatever their orientation to the coast (red ship tracks in Figure 2b). To estimate the orientation of the tracks we use the nearest coastline (green contour in Figure 2b). As a first step, a track section is considered as cross-shore when the angle between the ship trajectory and the coastline, linearized by a least square fit in a large box enclosing the whole coastal part of the track (black thick line in Figure 2b), is in a $90^\circ \pm 40^\circ$ range. As a second step, after excluding other parts of the track, for each individual cross-shore section, the coastline is linearized in a smaller box enclosing the section (Figure 2c) and only sections with angle of $90^\circ \pm 20^\circ$ relative to the coastline are kept. Sections with length less than 25 km are excluded. Finally, the SSS cross-shore gradient is estimated by linear least square fit applied on the SSS data collected along each selected cross-shore section.

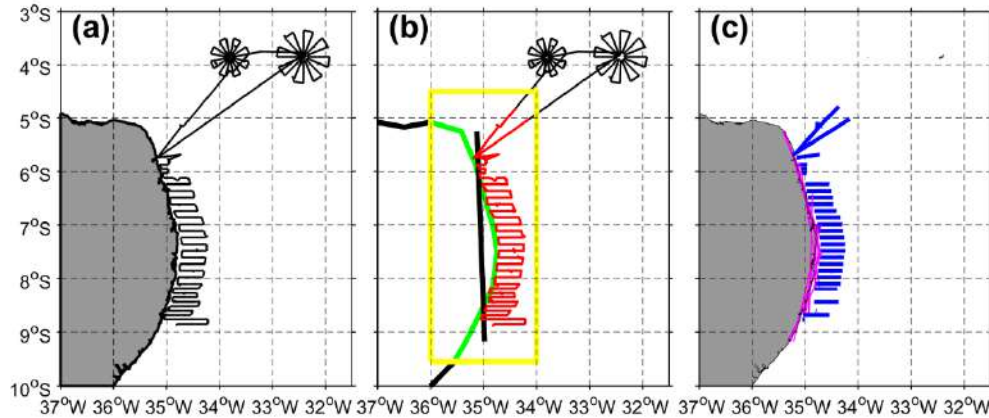


Figure 2. Illustration of the steps for extraction of cross-shore TSG transects: (a) Available TSG transects acquired during the ABRACOS cruise off Northeast Brazil in spring 2015. (b) Selection of coastal data within the 300 km from the coast. (c) Cross-shore transects selected for the SSS gradient estimation. Green contour in (b) shows the coastline nearest to selected coastal tracks and the thick black line corresponds to its linear fit. Blue transects in (c) show the selected cross-shore sections and pink lines show the local linear fits of the coastline of each individual section.

2.2.2 SSS Gradient calculation from gridded products

Reanalysis and satellites products are available on a global regular grid. Therefore, the estimation of SSS gradients is different from the TSG. First, every 25 km along the global coastline, we compute cross-shore axes, which local direction is estimated relatively to a linear least-square fit of the local coastline (within a 200 km radius of the coastal point considered, Figure 3b). Second, for each gridded product, coastal SSS data are selected (Figure 3a) and those found in a 50-km wide swath following each cross-shore axis (blue rectangle in Figure 3b) are interpolated at points every 25 km along this axis. Third, SSS cross-shore gradients are estimated at each time step by a linear least-square fit of these interpolated data. A minimum of three data points available on each cross-shore axis is required to estimate the gradient. The number of gradients computed with this method varies from one product to another because they have different coverage in coastal regions.

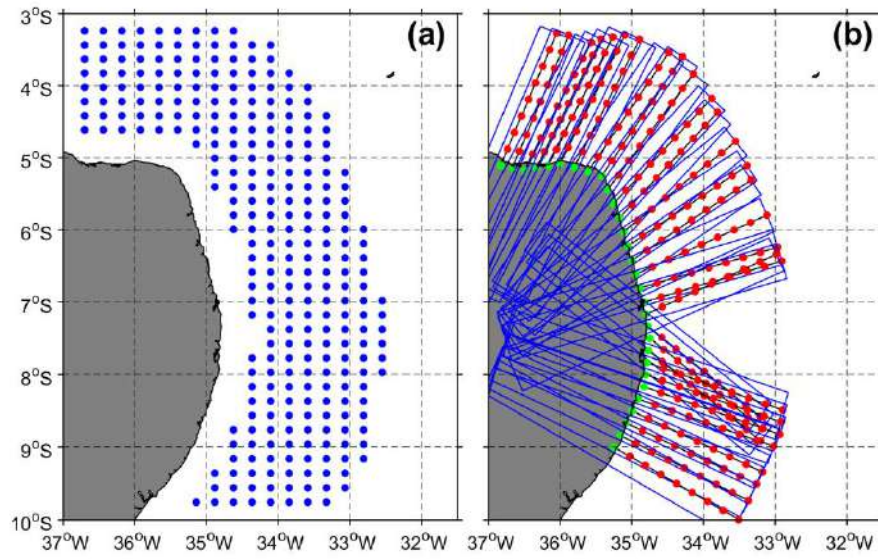


Figure 3. Illustration of the steps for extraction of cross-shore SSS sections from gridded products off Northeast Brazil. (a) Grid points available in the 50-250 km coastal band. (b) Cross-shore axes computed every 25 km along the coast. Green dots indicate the coast points at which cross-shore axes are computed. The blue rectangle indicate the rectangle in which gridded data are interpolated on red dots along the cross-shore axes.

2.2.3 Global statistics on coastal SSS and SSS gradient

Besides computing the SSS gradients, we evaluated the difference between SSS measurements from TSG and estimation from satellites and reanalysis products in the nearest 300 km from the coast, divided in 50 km width coastal bands. SSS from TSG and from gridded products were co-located in time and space for the common period April 2015-June 2019. Each TSG measurement was associated with SSS from a given product at the nearest grid point, and then all TSG measurements associated with the same grid point were averaged to create pairs of TSG and product SSS values. Based on these pairs, global statistics of differences between the SSS from TSG and from each gridded product can be quantified. We computed the bias and standard deviation of the differences (STD) as follows:

$$Bias(product - TSG) = \frac{\sum(SSS_{product} - SSS_{TSG})}{N},$$

$$std(product - TSG) = \sqrt{\frac{\sum(SSS_{product} - mean(SSS_{TSG}))^2}{N}}$$

where SSS_{product} corresponds to the SSS from a satellite or reanalysis product, SSS_{TSG} corresponds to the SSS from TSG measurements, and N corresponds to the total number of co-located pairs (number of pixels).

The same methodology was applied to investigate satellites and reanalysis performance in SSS gradient estimation. In this case, we first evaluated if the gradients were of the same sign. Then for the gradients of the same sign, each TSG SSS gradient was associated with the nearest gradient estimated from a given product, if any available within a radius of 50 km and 4 days. Bias and STD were computed by replacing SSS with SSS gradient in the formulas above.

Table 1 Regions of interest (red boxes in Figure 1a)

Regions name	Amazon River plume (AMZ)	Northeast Brazil (NEB)	Bay of Bengal (BOB)	California upwelling system (CAL)	Great Australian Bight (GAB)
Regions location	64-35°W; 4-24°N	37-31.5°W; 9.2-3°S	78-86.5°E; 10-16.5°N	123.5-119.5°W; 25-37°N	140-122°E; 40-30°S
Data period	6-9 March 2017	28 Sept-21 Oct 2015	23-24 Oct 2015	17-25 June 2019	28 Oct- 27 Nov 2015
Ship name	Toucan	RV Antea	Onyx	RV Bell Shimada	RV Investigator

4.1 3. RESULTS

3.1 Comparison of SSS from TSG measurement and satellites and reanalysis products

When comparing satellite and reanalysis SSS products with TSG measurements, we first investigated the global statistics. Then, we focused on five regions of interest (Table 1, Figure 1b) selected based on their particular strong or remarkable coastal SSS gradients observed with TSG data and the different driving physical processes.

3.1.1 Global statistics in coastal SSS

Differences between coastal TSG measurements and satellite or reanalysis SSS products vary according to the product (Figure 4). They are relatively small between 100 and 300 km from the coast. In this band, SMOS LOCEAN, SMOS BEC and SMAP RSS show a generally positive mean bias of 0.09 pss (0.07 to 0.14 pss), 0.08 pss (0.01 to 0.12 pss) and 0.15 pss (-0.02

to 0.25 pss), respectively. It is smaller and negative for SMAP JPL and GLORYS with values of -0.07 pss (-0.09 to -0.03 pss) and -0.02 pss (-0.03 to 0.03 pss), respectively. In terms of STD, farther than 100 km from the coast, ranking model skill is very dependent on the 50-km wide band considered. However, SMOS BEC shows overall the largest STD, ranging from 0.76 to 1.32 pss, and GLORYS the smallest STD, ranging from 0.38 to 0.85 pss, with other products in-between. Except for the bias of SMAP RSS and the STD of SMOS LOCEAN, there is no obvious loss in data quality when approaching the coast, farther than 100 km offshore.

In the nearest 100 km from the coast, differences with TSG data increase for all products. The bias jumps over 1 pss for SMAP RSS. For SMOS BEC and GLORYS, it rises up to 0.28 and 0.24 pss in the 50-100 km band and 0.86 and 0.51 pss in the 0-50 km band, respectively. It only increases in the 0-50 km band for SMOS LOCEAN, where it reaches 0.38 pss, while it is still only 0.08 pss for SMAP JPL. The STD also jumps over 2.5 and up to 4 pss for SMAP RSS, SMOS BEC and GLORYS in the 0-100 km coastal band. The increase is less pronounced for SMOS LOCEAN and SMAP JPL with STD of 1.60 and 0.81 pss in the 50-100 km band, 1.80 and 1.62 pss in the 0-50 km band, respectively. It must be noted that for all products, the number of pixels steadily increases from 300 km to 100 km off the coast, which reflects more collocated TSG data available due to the increasing density of ship traffic, but decreases in the last 50 km in all products but GLORYS due to less satellite data available. The number of pixels also varies from one satellite product to another, reflecting more or less data availability. We could have selected only grid points where all satellite products are available for the statistical comparison with TSG data but we adopted the point of view of the coastal data user, exploiting all the data available in the product distribution. In addition, GLORYS has one order of magnitude more pixels than satellites products, even relatively far from the coast.

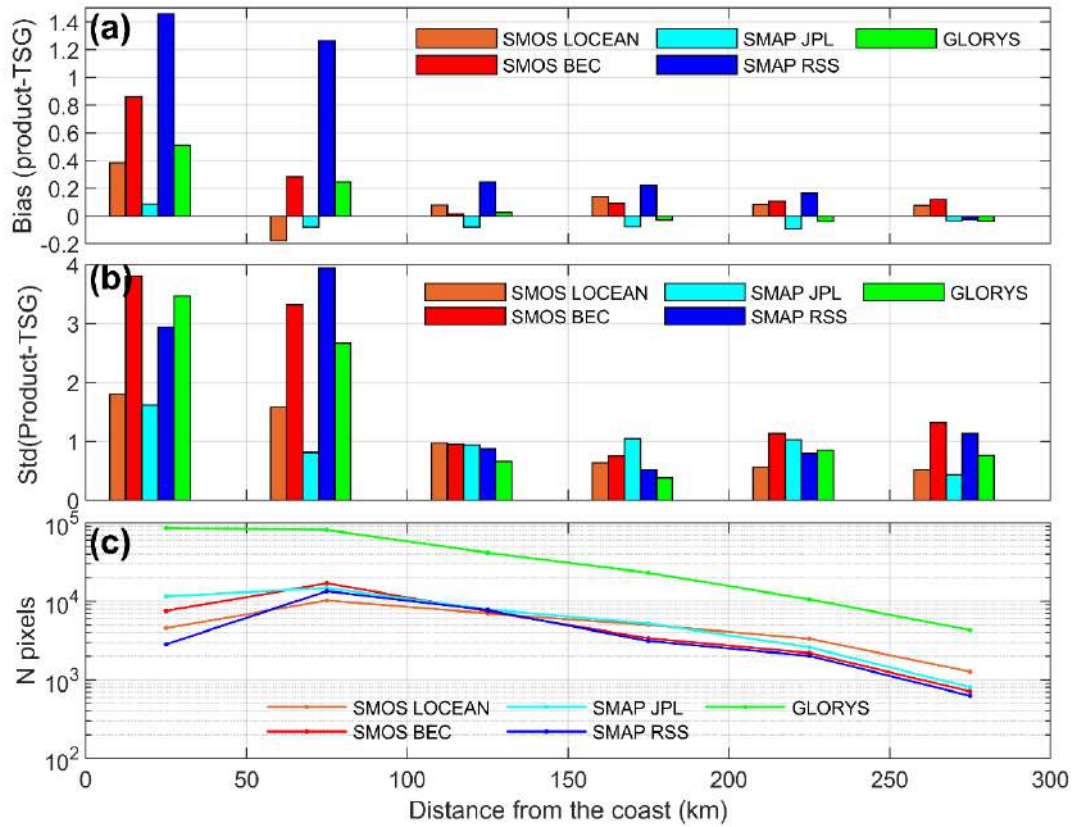


Figure 4. Overall coastal SSS statistics (April 2015- June 2019) of differences between gridded products and TSG observations, in terms of: (a) SSS bias (in pss); (b) standard deviation of differences; (c) number of pixels used for the comparison.

3.1.2 Regions of interest

In order to validate the accuracy of the satellites and reanalysis products, we selected five regions of interest due to their strong or remarkable, coastal SSS gradients observed with TSG data, representative of specific physical processes. We provide a qualitative comparison of gridded products with ship TSG sections to illustrate regional mesoscale features. The selected regions are the Amazon River plume (AMZ), Northeast Brazil (NEB), Bay of Bengal (BoB), California coast (CAL) and Great Australian Bight (GAB) (Figure 1b; Table 1).

Amazon River plume

The AMZ region is an area where significant surface freshening takes place due to the discharge of the Amazon River [45–47]. Moreover, it is a region where the North Brazil Current (NBC), a strong western boundary surface current, flows in a northwestern direction along the Brazilian coast [48]. The NBC brings salty waters, with a maximum salinity core located around 100 m depth that can be traced back to the SSS maximum in the South Atlantic subtropical gyre in

boreal winter, which creates a SSS contrast with the low salinity of the Amazon river plume [49–51]. At about 6–8°N, 48–50°W, the NBC separates from the coast and partly retroflects eastward to connect with the North Equatorial Counter-Current (NECC), generating large anticyclonic rings that can reach the Caribbean Sea [e.g., 52,53]. The upper NBC transport low-salinity waters from the Amazon plume along the coast, which can later feed the NECC or swirl around NBC rings [54,55].

In this region, all tested products reproduce the alongshore extension of the Amazon water lens at about 54°W (Figure 5). In addition, Amazon water lens were also observed in all products extending along the continental shelf. GLORYS, which provides the finest resolution, shows a ring centered at 10°N, 57°W that is not represented on satellites maps, probably due to modelling artifact. Differences in coastal flagging from one product to another can be seen and correspond to the different number of pixels available in the 0–50 km coastal band (Figure 4c). All products represent well the strong cross-shore salinity gradient observed in the TSG transect with SSS increasing from more than 37 pss offshore to less than 32 pss at the coast. However, the distance from the coast of the haline front (around 300 km) is underestimated in all products, which are also too salty until 48°W along the TSG track. The different vertical sampling of salinity at 0–10 m in TSG data *vs* 5 m in GLORYS *vs* skin layer in satellite products [17,34], potentially important in this highly stratified region [56], cannot explain these differences. Temporal sampling (8-day running mean *vs* 3-day transect) may contribute to them.

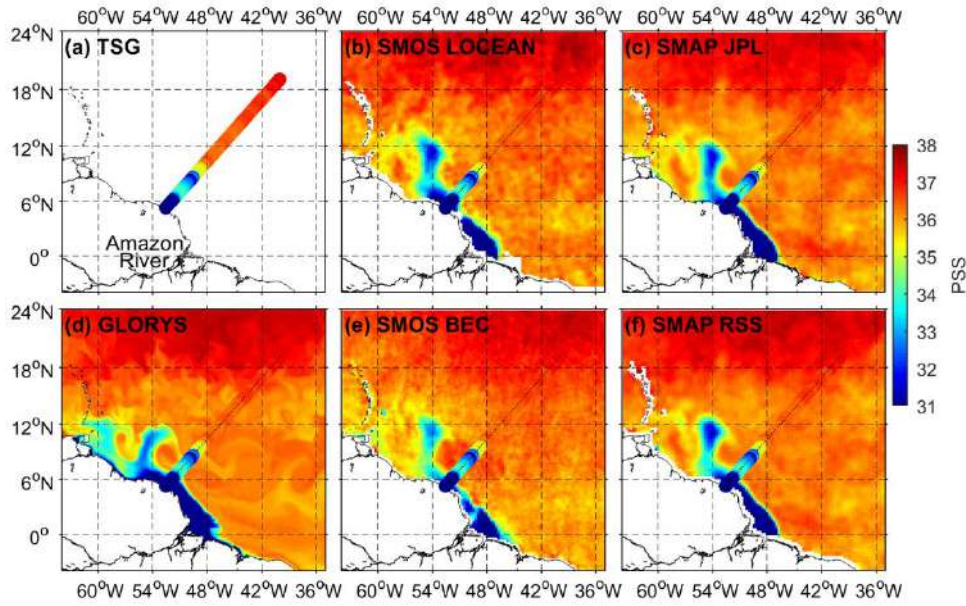


Figure 5. SSS off the Amazon River plume (6-9 march 2017) from (a) TSG; (b) SMOS LOCEAN ; (c) SMAP JPL ; (d) GLORYS; (e) SMOS BEC and (f) SMAP RSS. The TSG SSS from (a) is superimposed on satellite SSS maps (b-f).

Northeast Brazil

Northeast Brazil, located 500-1000 km south of the Amazon River mouth, is the source region for the NBC. Between 10°S and 5°S, the North Brazil Undercurrent (NBUC) flows equatorward along the coast [57–59]. This western boundary current originates from the northward bifurcation of the westward southern South Equatorial Current (sSEC) at the Brazilian coast further south. As the coast orientation changes at around 5°S, it is joined by the central South Equatorial Current (cSEC) to form the NBC. The NBUC has a weak surface expression due to the southward wind-driven surface drift in this region [60]. It transports salty waters from subtropical origin with maximum salinity found around 100 m depth close to the coast [57].

It is obvious from SSS maps that the NBUC salty core has also a surface signature [61], with SSS increasing over 36.5 pss toward the coast (Figure 6). This may be favored by vertical mixing due to the wind-induced shear stress or friction with the shelf slope. SSS is particularly high over the narrow shelf, possibly due to evaporation, as seen in TSG and GLORYS data that extend closer to the coast than satellite data. A direct comparison with TSG data is difficult for SMAP RSS between 6°S and 8°S due to the coastal flagging, while SMOS BEC seems particularly noisy. However, all products represent well the high salinity extending farther offshore south of 7.5°S, although it is too high in GLORYS and SMAP products. This pattern

is probably associated with the orographic effect here that shifted the path of the NBUC away from the coast [58]. From the coast to the islands located around 4°S, GLORYS reproduces better the TSG observations than the satellites products.

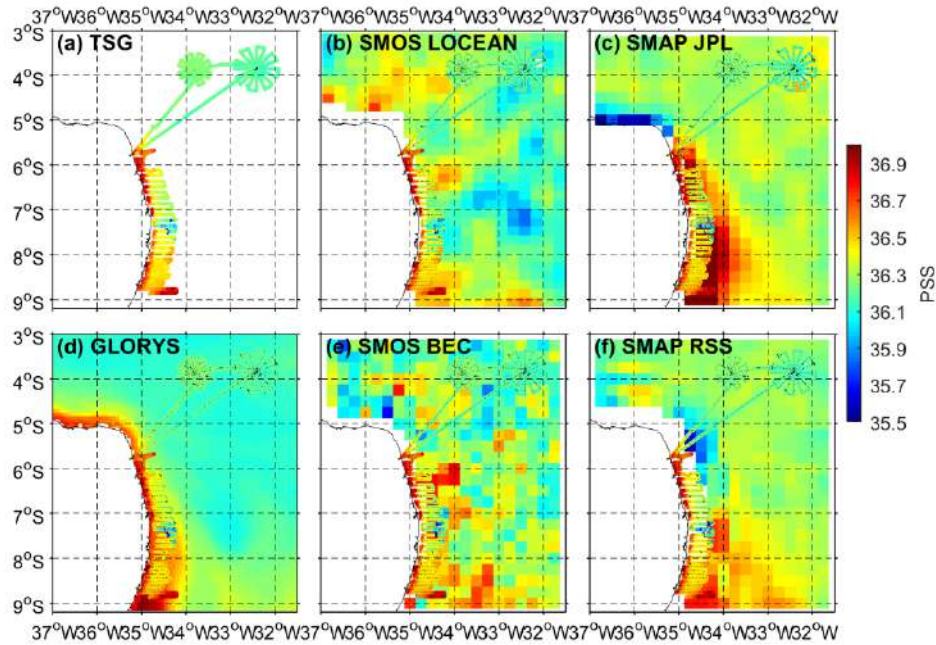


Figure 6. SSS off Northeast Brazil (21 September - 28 October - 2015) from (a) TSG; (b) SMOS LOCEAN ; (c) SMAP JPL ; (d) GLORYS; (e) SMOS BEC and (f) SMAP RSS. The TSG SSS from (a) is superimposed on satellite SSS maps (b-f).

Bay of Bengal

The Bay of Bengal (BoB) is a region of high SSS contrasts due to strong seasonal freshwater inputs by summer monsoon rains, which feed large rivers. Oceanic rainfall and river discharge contribute equally to freshwater inputs in the northern BoB, while the Ganga-Brahmaputra River located at its the northern end represents more than 60% of total discharge in the BoB [15,62–64]. After the monsoon, the East Indian Coastal Current (EICC) reverses and flows southward, transporting this freshwater along what has been called a River in the Sea (RIS), which is about 100 km wide and can extend up to 3000 km from the main river mouth [15,65,66].

Some satellite SSS products have been tested in the BoB, with available in situ data. The semi-enclosed configuration of the BoB induces strong land-sea contamination and early SMOS products had very limited skill in this region [67] but improved versions perform much better and allow to study interannual SSS variations thanks to the decade-long record [68]. SMAP would even work better. It compares well with in situ SSS cross-shore sections in the BoB, and reproduces a large part of seasonal SSS variations measured at coastal stations along the RIS

[18,66,69]. In October 2015 (Figure 7), SMOS LOCEAN, SMAP JPL and GLORYS capture the coastal freshening (SSS < 32 pss) seen by TSG data at 13°N, clearly associated with the northern BoB freshening transported southward by the RIS. SMOS BEC and SMAP RSS lack coastal data to enable the comparison. The RIS southward extension is impacted by interannual and intraseasonal anomalies [69]. It was relatively limited in 2015 due to a negative Indian Ocean Dipole and, according to GLORYS, by a mesoscale cyclonic eddy that diverts its path [66–69].

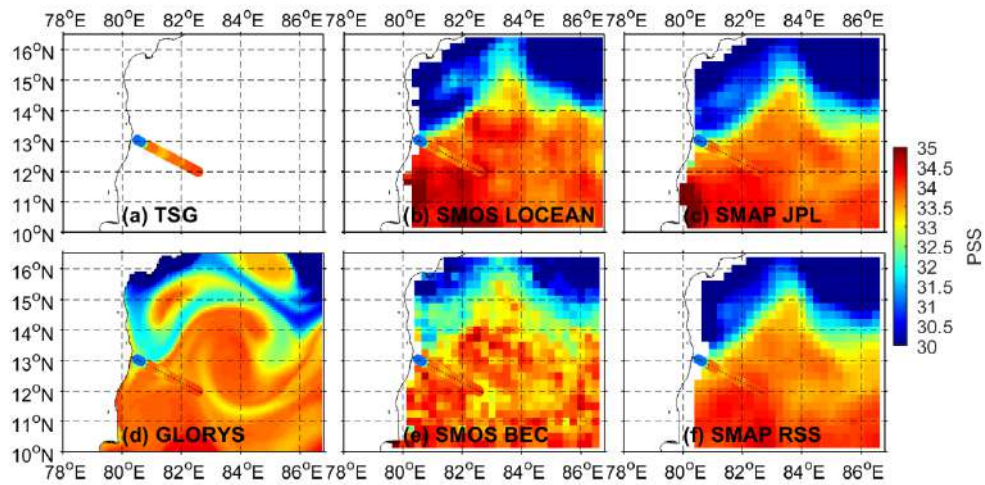


Figure 7 SSS in the Bay of Bengal (23–24 October 2015) from (a) TSG; (b) SMOS LOCEAN; (c) SMAP JPL; (d) GLORYS; (e) SMOS BEC and (f) SMAP RSS. The TSG SSS from (a) is superimposed on satellite SSS maps (b–f).

California upwelling system

One of the major Eastern Boundary Upwelling Systems (EBUS) takes place along the California coast. This wind-driven upwelling generally uplifts salty subsurface waters to the surface, while the California Current, farther offshore, transports relative fresh waters equatorward, which creates a cross-shore SSS gradient [70–73].

The upwelling is particularly strong along the central California coast in summer (Figure 8). TSG data show a SSS contrast of about 1 pss with SSS over 33 pss in a coastal band that gets wider (around 100 km) towards the south. GLORYS reproduces remarkably well this cross-shore SSS gradient. Among satellite products, only SMOS BEC reproduces this gradient, except for a few grid points around 36°N. It is also the satellite product with the best coastal coverage in this region. Other satellite products do not capture the coastal SSS increase. On the opposite, SMAP JPL shows a strong contrast between a relatively high SSS (> 34) offshore and low SSS (< 32.5) at the coast, south of 36°N. This product however reproduced much better in situ SSS gradients at monthly to yearly timescales in this region [74]. For SMAP RSS, which

has a data gap at the time of TSG observations (17-25 June 2019), we instead show data from 14-15 June 2019, which may partly explain the differences.

Note that, while some upwelling regions are associated with coastal SSS increase [75,76], others are associated with coastal freshening (e.g., [74]). Mean vertical salinity gradients are indeed different and can be of opposite sign in the four major EBUS [78]. This depends on the upwelled subsurface water masses, that can vary locally within the same upwelling system, at seasonal or interannual timescale, and can be influenced by other processes such as river plumes [79–81].

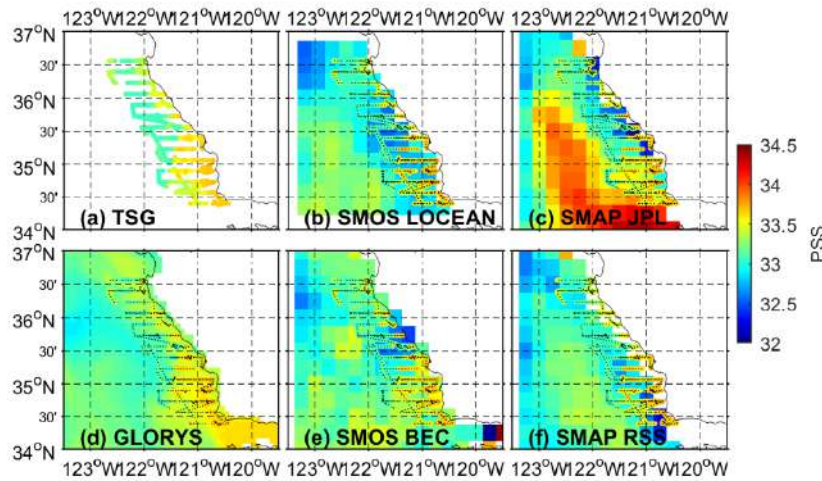


Figure 8. SSS off California (17-25 June 2019) from (a) TSG; (b) SMOS LOCEAN; (c) SMAP JPL; (d) GLORYS; (e) SMOS BEC and (f) SMAP RSS. The TSG SSS from (a) is superimposed on satellite SSS maps (b-f).

Great Australian Bight

In the Great Australian Bight (GAB), the Spencer Gulf is a remarkable inverse estuary, where strong evaporation over shallowing waters produces a year-round meridional SSS gradient, with maximum SSS at its head [82]. This phenomenon occurs in other hot and dry regions of the world [83–85]. The salinity increase is particularly strong during summer and followed by winter cooling. This results in a density increase that generates gravity currents out of the gulf mouth and along the shelf slope, compensated by a surface in-flow of fresher waters [86,87]. It was later found that this process occurs at larger scale in the whole GAB that has been called a mega inverse estuary [87,88].

Available TSG observations do not penetrate far inside the GAB but clearly show the SSS increase toward the entrance of the Spencer Gulf, where it already reaches 36 pss compared to values lower than 35.5 pss farther offshore (Figure 9). SMAP JPL is too fresh compared to the TSG data south of 36°S and shows a large scale SSS increase in the GAB, less pronounced than

in other products. Moreover, the SMAP JPL coastal freshening is unexpected in this dry region with very little freshwater runoff. SMOS LOCEAN is generally too salty north of 36°S while the few grid points in the Spencer Gulf do not capture the expected local SSS maximum. On the contrary, GLORYS, SMOS BEC and SMAP RSS re-produce well the SSS along the ship track. The SSS increase in the Spencer Gulf captured by GLORYS is consistent with the few grid points available here for the latter satellite products. Except for probably spurious local freshening at a few points along the coast in SMAP RSS, SMOS BEC and SMAP RSS largely agree with GLORYS on the large-scale meridional gradient between 40°S and 32°S.

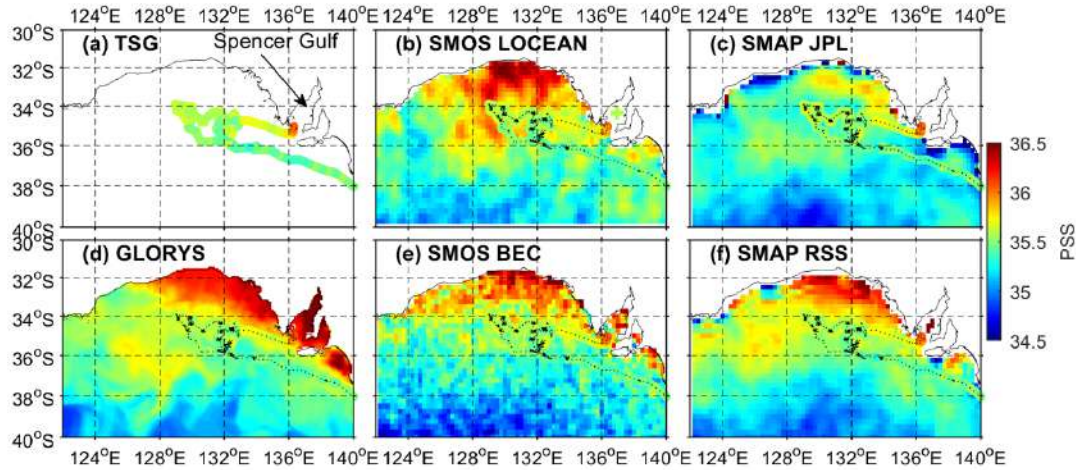


Figure 9. SSS in the Great Australian Bight (22 Oct-22 Nov 2015) from (a) TSG; (b) SMOS LOCEAN; (c) SMAP JPL; (d) GLORYS; (e) SMOS BEC and (f) SMAP RSS. The TSG SSS from (a) is superimposed on satellite SSS maps (b-f).

3.2 Comparison of SSS gradient from TSG measurement and satellites and reanalysis products

In this section, we examine the satellites and reanalysis skill at reproducing the observed SSS gradients computed from TSG. We first present the global distribution of the SSS gradients computed from TSG, satellites and reanalysis. Then, we present the global statistics on the SSS gradients comparison between gridded products and TSG. In the regions of interest, as it is also the case globally (Figure 4c), satellites products have limited coverage near the coast, while reanalysis products are available up to the coastline. We therefore only estimated the gradients at distance higher than 50 km from the coast.

3.2.1 Global distribution of SSS gradients

Collocating the available TSG SSS gradients computed in the 50-250 km coastal band with those of other products, as described in section 2.2, allows the most direct comparison. Indeed, each TSG SSS gradient is compared with the nearest gradient estimated from a given product within a radius of 50 km and 4 days. However, if several TSG SSS gradients are available

within the collocation radius, their average is used for the comparison. As observed in Figure 4c for coastal SSS, the number of cross-shore sections used to compare with TSG varies from one product to another. All products agree with TSG on SSS gradients with typical order of ± 0.1 pss over 100 km (Figure 10), with a distribution skewed toward negative values. However, Only SMAP JPL and GLORYS reproduce the observed mean SSS gradient. Other products overestimate the observed SSS gradient. In terms of STD of the SSS gradient, all products show lower values than the TSG observations, although SMOS BEC shows weaker difference with the TSG 0.7 pss over 100 km. Other products exhibited differences higher than 1.1 pss over 100 km.

The spatial distribution of the collocated gradients shows that all products reproduce to some extent the sign of the gradients (Figure 11). In northeast Brazil, all products capture the positive SSS gradient observed by TSG (see also Figure 6). In the Amazon River plume region, all products but SMAP RSS also reproduce the negative gradient due to the river discharge, as seen in Figure 5. In the Bay of Bengal, in situ TSG SSS gradient is positive, which seems contradictory with the negative gradient seen in Figure 7. This discrepancy may be because the gradient estimated from TSG corresponds to the mean gradient of several sections and the one corresponding to the case shown in Figure 7 may be flooded in. The seasonal variation of the extension of the RIS due to the mesoscale activity and the negative Indian Ocean dipole may also favor this discrepancy.

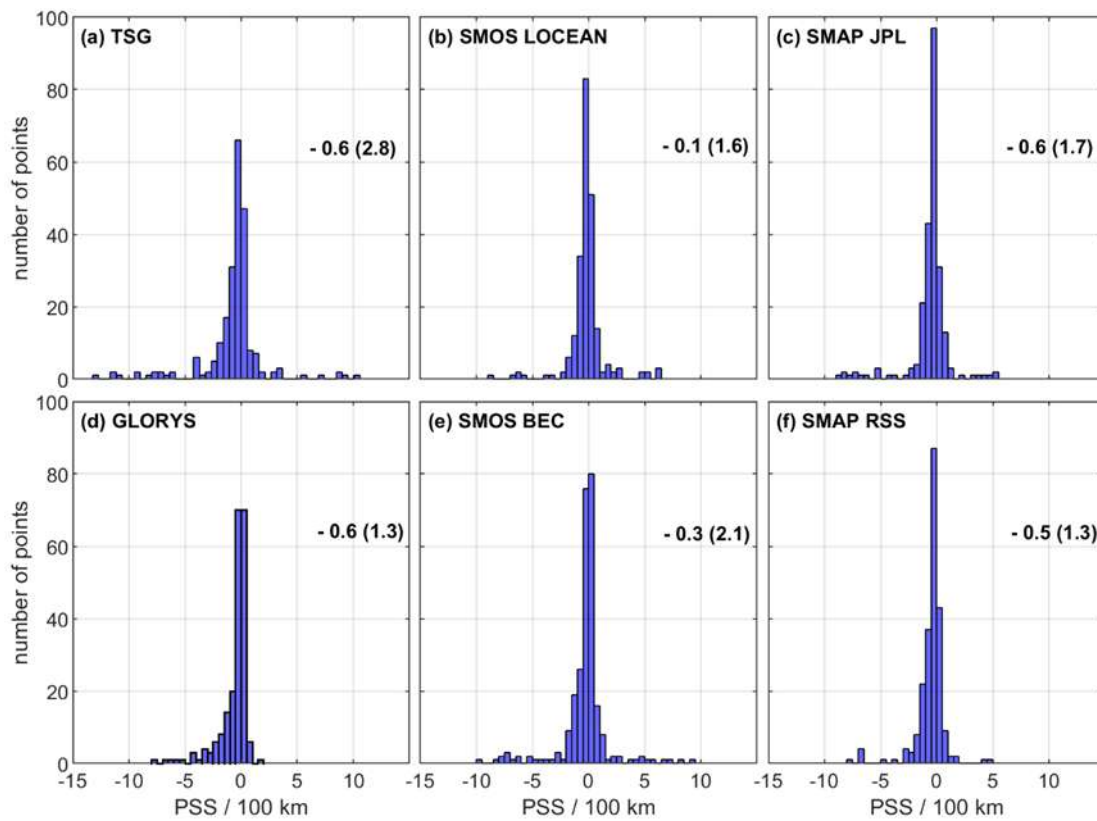


Figure 10. Global map of SSS gradients computed in the 50-250 km coastal band for the April 2015-June 2019 period from (a) TSG; (b) SMOS LOCEAN; (c) SMAP JPL; (d) GLORYS; (e) SMOS BEC and (f) SMAP RSS. Blue indicate negative SSS gradient while red indicate positive SSS gradient.

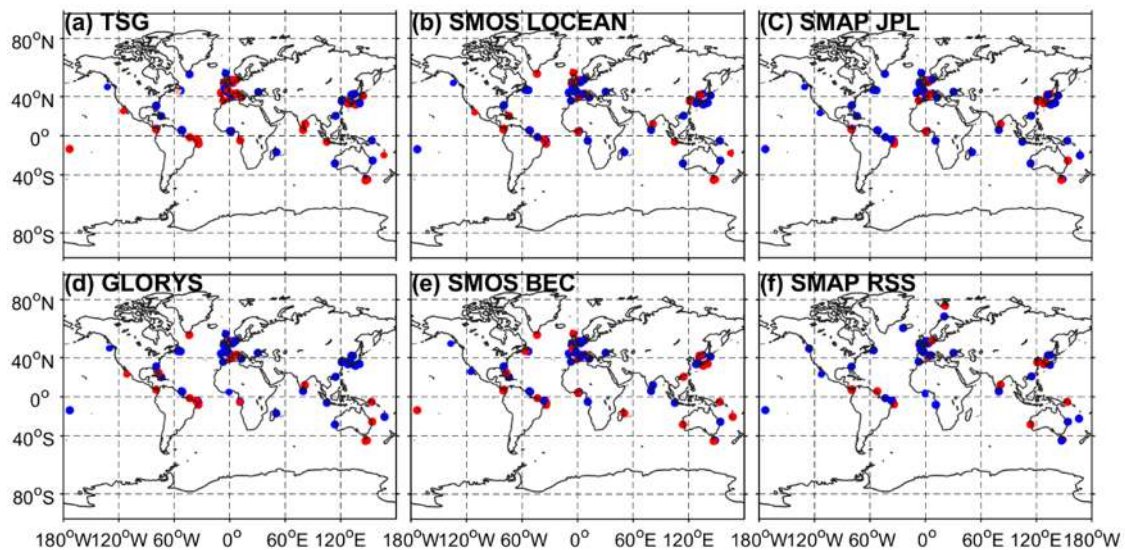


Figure 11. Global map of SSS gradients computed in the 50-250 km coastal band for the April 2015-June 2019 period from (a) TSG; (b) SMOS LOCEAN; (c) SMAP JPL; (d) GLORYS; (e) SMOS BEC and (f) SMAP RSS. Blue indicate negative SSS gradient while red indicate positive SSS gradient.

After collocating the SSS gradients from TSG and gridded products, we now analyze the distribution of all SSS gradients available from TSG, to take advantage of the long period of observations, and all SSS gradients available from gridded products on their common period, to take advantage of their global homogeneous coverage. Note that the SSS gradients shown for satellites and reanalysis products correspond to the temporal average of SSS gradients computed every 4 days, over the satellites common period. The distribution skewness toward negative cross-shore gradients is confirmed for TSG and all products (Figure 12). Although TSG data are relatively sparse in time and space, they display the largest range of gradients, almost reproduced at global scale by GLORYS, which shows a slightly smaller STD. However, the gradient STD is around 3 times smaller for SMAP products, and 5 times smaller for SMOS products, probably due to the lower resolution of satellite products. Among gridded products, GLORYS and SMAP show the most negative mean gradients (-0.35 pss/100 km) while it is less than half for SMOS products (-0.15 pss/100 km).

At global scale, the geographical distribution of SSS gradients reveals a mosaic of negative and positive gradients from all products (Figure 13). TSG data show a relatively balanced occurrence of positive and negative gradients. On the contrary, satellite products are clearly dominated by negative gradients. The SMOS LOCEAN product shows more positive gradients than other satellite products, although they are not found in the regions where we highlighted such occurrence. Compared to the satellite products, GLORYS shows more regions of well-pronounced positive gradients, including the Great Australian Bight, Northeast Brazil and California upwelling regions. Although GLORYS seems to perform better than satellites products on these maps, global statistics based on comparison with collocated TSG data are required to objectively and quantitatively evaluate products performance in the estimation of SSS coastal gradients.

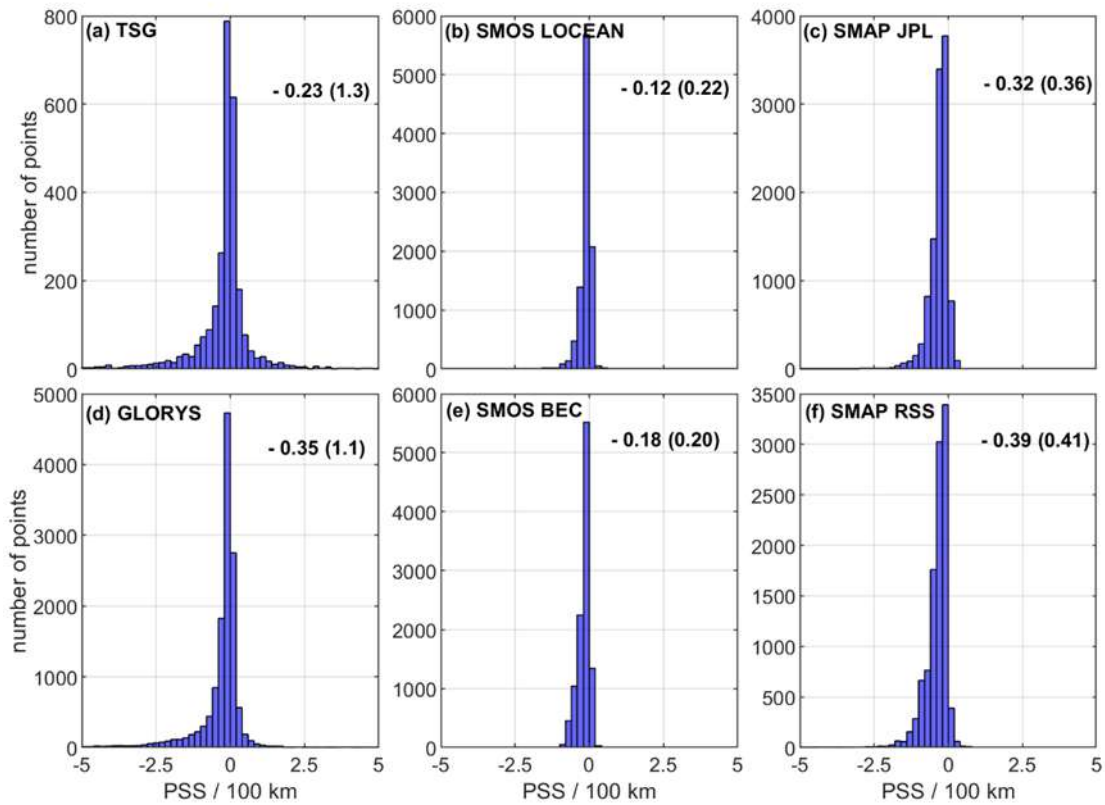


Figure 12. Distribution of SSS gradient computed in 50-250 km coastal band from (a) TSG along the cross-shore ship track on the available period (1993-2019); (b) SMOS LOCEAN; (c) SMAP JPL; (d) GLORYS12V1; (e) SMOS BEC and (f) SMAP RSS on the 2015-2019 period. Values in the distribution and in the bracket correspond respectively to the mean and the standard deviation of the gradient of each dataset.

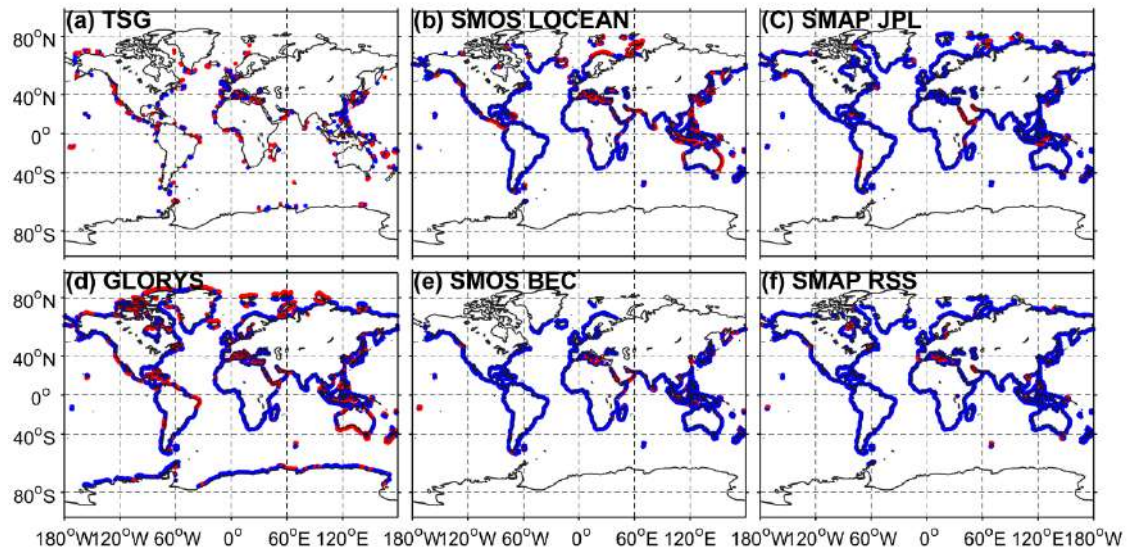


Figure 13. Global map of SSS gradient computed in 50 km and 250 km coastal band. (a) Gradient computed from all TSG along the cross-shore ship track on the available period (1993-2019). (b-f) Mean (2015 -2019) gradient computed respectively from SMOS LOCEAN, SMAP

JPL, GLORYS, SMOS BEC and SMAP RSS. Blue indicate negative SSS gradient while red indicate positive SSS gradient.

3.2.2 Global statistics of SSS gradients comparison

Differences between TSG measurements and satellites or reanalysis SSS products in terms of cross-shore SSS gradient vary according to the product (Figure 14). All products failed in estimating the sign of the gradient in a proportion higher to 30%, whatever the distance from the shelf (Figure 14a). SMOC BEC is the product with the highest error (ranging from 43 to 48%) while SMAC JPL has the lowest error (ranging from 30 to 32%).

When looking at the differences considering only the gradients of the same sign (Figure 14b-c), in the three selected coastal bands, SMOS LOCEAN, SMAP JPL, SMAP RSS and GLORYS overestimate the observed gradients (positive bias) while SMOS BEC underestimates them (negative bias). Overall, all product except GLORYS show a decreasing bias (in absolute value) from largest (50-250 km) to narrow (50-150 km) coastal bands. SMOS products show the highest STD whatever the coastal band. A minimum criterion on STD rather than bias is more relevant to identify the best product, when STD is one order larger than the bias, as is the case here. GLORYS shows an increasing bias and STD from the largest to the narrowest coastal band, which are on average between those found for the SMAP products. SMAP products show on average lower bias (in absolute value) and STD than SMOS products. It must be noted that the number of cross-shore sections also varies according to the product, especially in the 50-150 km band. These variations are consistent with the different numbers of SSS pixels in the coastal zone (Figure 4).

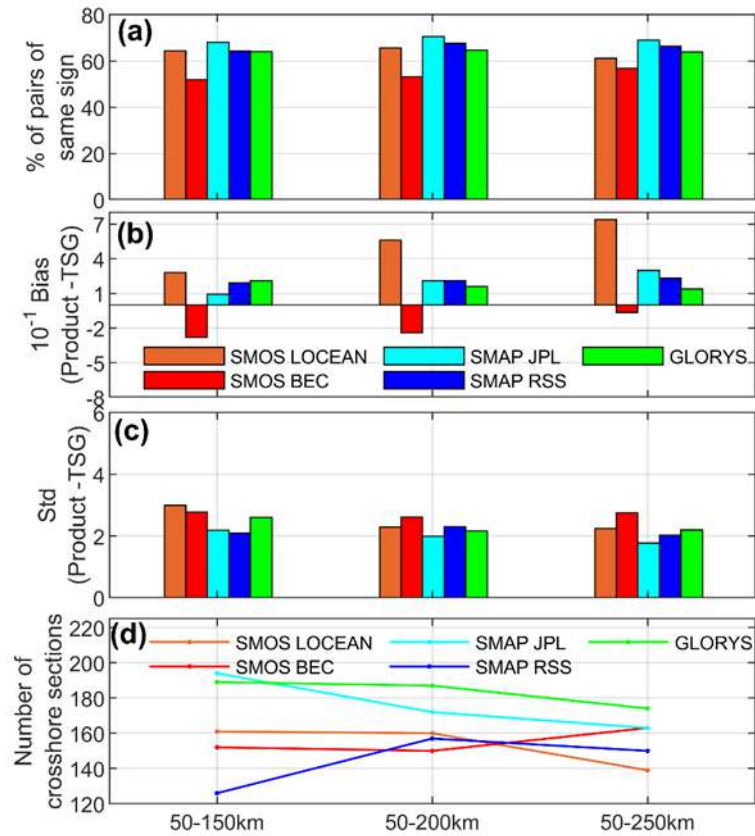


Figure 14. Overall statistics (April 2015- June 2019) of difference between the satellites, the reanalysis products and the TSG cross-shore SSS gradient computed in the 50-250 km coastal band. (a) percentage of pairs of same sign; (b) SSS gradient bias (in pss / 100 km); (c) standard deviation of the SSS gradient bias (in pss / 100 km); (d) number of cross-shore sections used for the comparison.

4. DISCUSSION

In the present study, we investigated the skill of different satellite and reanalysis products at reproducing SSS in the global coastal ocean (< 300 km), as observed with TSG measurements. Four gridded SMOS or SMAP satellite products and a model reanalysis were compared with TSG measurements, in terms of coastal SSS and cross-shore SSS gradient.

Our study evaluated gridded (Level 3 - L3) satellite products rather than along-track (Level 2 - L2) satellite products because of their wider use by the scientific community. In addition, comparing L2 products with TSG measurements would greatly reduce the number of collocated data, which would limit the analyses on a global scale.

Through the global statistics on SSS and SSS gradients, our results revealed that the four SMOS and SMAP L3 gridded products deviated from each other and from the TSG measurement in

the first 300 km from the coast. Several factors can explain the discrepancy between satellites and TSG data. First, spatio-temporal scales are different. At a typical merchant-ship speed of 15 knots, TSG data resolution is about 2-3 km [17] and a 100 km coastal section is sailed along in about 3 hours. The satellite gridded products have a typical 25-km and 8-day resolution [33,36]. The difference in spatial scales is not so much a concern in the cross-shore direction, when averaging SSS in 50-km bands and estimating linear SSS by least square fit applied in 100-km bands. But differences in the temporal and along-shore spatial sampling mean that mesoscale and sub-mesoscale processes, which are particularly strong in coastal regions [34,89], can affect the comparison between satellite and TSG data. Second, there are also differences in vertical levels as satellites estimate salinity in the upper few centimeters, while TSG data are acquired at 5-10 m depth [17,34]. However, given the dominance of coastal freshening (Figure 11), probably due to river discharges or coastal rains, which are associated with strong stratification [54,90–92], the different depth of acquisition would induce a negative bias in satellite SSS at the coast. The fact that we observed the opposite (Figure 4) suggests a small influence of the depth difference. The increasingly positive bias found in most satellite products when approaching the coast may be associated with Radio frequency interference (RFI) pollution. For instance, SMOS is mostly disturbed by RFI over coastal areas of Europe, southern Asia and Middle East [93]. It is also consistent with an earlier study for the SMOS LOCEAN product at global scale [35]. Compared to both bias and standard deviation are larger in our study due to less spatio-temporal filtering of data. However, the increase in STD when approaching the coast may be favored by the increase of SSS variability as observed by [35].

Nevertheless, the bias in coastal SSS absolute value is largely independent from the bias in reproducing coastal SSS gradients. For instance, the SMAP RSS bias in SSS increases of ~ 1 pss toward the coast in the 50-150 km band (Figure 4a). One could expect an induced positive bias in SSS gradient of 0.02 pss km^{-1} (1 pss over 50 km) in this band, whereas it is only $0.002 \text{ pss km}^{-1}$ (Figure 14b). With the same reasoning and still in the 50-150 km band, one could expect an induced bias in SSS gradient that would be negative for SMOS LOCEAN and positive for SMOS BEC, while the opposite is found. The fact that there is no linear relation between SSS bias and SSS gradient bias is probably due to the standard deviation difference (STD) in coastal SSS that is much larger than the bias (Figure 4). Moreover, the cross-shore SSS gradients arguably provide a better monitoring of coastal processes than coastal SSS.

To summarize, satellite SMOS and SMAP gridded products still need to be improved in coastal regions, particularly in the nearest 100 km from the coast for SSS retrievals. Based on the

comparison with collocated TSG data in this coastal band (Figure 4), The SMAP JPL product performs better with a clear minimum in bias and STD, followed by the SMOS LOCEAN, GLORYS reanalysis, SMOS BEC and SMAP RSS products. More SMAP JPL data are also available near the coast. There are fewer differences between products farther than 100 km offshore.

All products failed in estimating the sign of the gradient in more than 30% of cases. SMOC BEC performs while SMAP products perform better (Figure 14a). When considering only the cross-shore SSS gradients of the same sign, from 250, 200 or 150 km until 50 km from the coast (Figure 14b-d), SMAP JPL performs better, followed by SMAP RSS, then (with STD the main criteria) GLORYS, SMOS LOCEAN and SMOS BEC. This seems to re-veal a trade-off between data availability and quality. Indeed, SMAP RSS has the lowest number of cross-shore sections collocated with TSG data, while SMOS BEC has the largest. In this respect, the SMAP JPL product shows the best compromise. It is interesting to note that most satellite products tend to show a positive bias corresponding to an underestimation of coastal freshening. The fact that two satellite products are better than GLORYS means that they globally provide more information in the near-coastal band than a state-of-the-art model fed with Argo profiles, satellite SST and SLA observations.

Despite their differences, all evaluated products agree with the dominance of coastal freshening at global scale (Figures 4.11, 4.13). This was suggested by ship TSG sections (Figures 4.12, 4.14), which are relatively scarce and could be biased due to the frequent location of harbors in estuaries. The satellites and reanalysis products extend this important result globally, thanks to their homogeneous coverage. This can be attributed to river discharges as illustrated here in the Amazon River plume and the Bay of Bengal regions (Figures 4.6, 4.8) and previously documented in regional studies [15,46,47,69,94–97]. More recently, SMOS and SMAP have been shown to reproduce well seasonal and interannual SSS variation in the major rivers mouths [98]. Strong coastal precipitations in the tropics could also induce such freshening [13,45] but their potential contribution could not be quantified here. In-deed, splitting the respective role of river runoff and precipitation on coastal freshwater plumes requires dedicated regional studies (e.g., [91]).

SSS increase at the coast also occurs, as illustrated here in the regions of northeast Brazil, California upwelling system and the Great Australian Bight (Figures 4.7, 4.9, 4.10), and can be induced by different processes. In northeast Brazil, the increase in coastal salinity is induced by

the rise of the salty core of the NBUC that flows along the coast [58,59,61]. In the upwelling system of California, the increase in coastal salinity can be related to the coastal upwelling, which brings higher-salinity waters to the surface [71,72,81]. Finally, the Great Australian Bight, known as inverse estuary, is a region where dominant evapo-ration promotes high salinity along the coast [87,98,99]

In conclusion, the present study shows a great potential of SSS remote sensing to monitor coastal processes, somewhat limited with existing SMOS and SMAP sensors and associated products. The future Surface water and ocean Topography (SWOT) satellite mission will give access to mesoscale geostrophic currents close to the coast [100], which will allow to better understand how coastal SSS anomalies are advected in areas of strong SSS gradient such as river plumes. Ship-drift currents estimated from Automated Information Systems (AIS) data [101] will also be useful for that in the coastal zone. Nevertheless, a more direct and global access to coastal SSS dynamics would require a jump in the resolution of future SSS satellite missions [102].

4.2 ACKNOWLEDGEMENTS.

This work was supported by the CAPES-PRINT (Coordenação de Aperfeiçoamento de Pessoal de Nível Superior) through a PhD internship scholarship grant for A.N.D. This work is a contribution to the International Joint Laboratory TAPIOCA (www.tapioca.ird.fr), to the SMAC project (CAPES/COFECUB n° 88881.142689/2017–01), the CNES TOSCA SMOS project, the PADDLE project (funding by the European Union’s Horizon 2020 research and innovation programme - grant agreement No. 73427), and to the TRIATLAS project, which has also received funding from the European Union’s Horizon 2020 research and innovation program under grant agreement No 817578. SSS data derived from thermosalinograph instruments installed onboard voluntary observing ships were collected, validated, archived, and made freely available by the French Sea Surface Salinity Observation Service (<http://www.legos.obs-mip.fr/observations/sss/>). The authors sincerely thank the data producers who have made satellite SSS datasets available to the public: the SMOS LOCEAN L3 Debiased products (<https://www.catds.fr/Products/Available-products-from-CEC-OS/CEC-Locean-L3-Debiased-v4>), the SMOS BEC global SSS products (<http://bec.icm.csic.es/ocean-global-sss/>), the SMAP JPL and RSS products (<https://podaac.jpl.nasa.gov/SMAP>), and the producers of reanalysis data GLORYS12V1 (<https://resources.marine.copernicus.eu/>)

4.3 REFERENCES

1. Durack, P.J. Ocean salinity and the global water cycle. *Oceanography* **2015**, 28, 20–31, doi:10.5670/oceanog.2015.03.
2. Gordon, A.L.; Giulivi, C.F.; Busecke, J.; Bingham, F.M. Differences among subtropical surface salinity patterns. *Oceanography* **2015**, 28, 32–39, doi:10.5670/oceanog.2015.02.
3. Delcroix, T.; Hénin, C. Seasonal and interannual variations of sea surface salinity in the tropical Pacific Ocean. *J. Geophys. Res.* **1991**, 96, 22135, doi:10.1029/91JC02124.
4. Alexander Haumann, F.; Gruber, N.; Münnich, M.; Frenger, I.; Kern, S. Sea-ice transport driving Southern Ocean salinity and its recent trends. *Nature* **2016**, 537, 89–92, doi:10.1038/nature19101.
5. Hénin, C.; Penhoat, Y. Du; Ioualalen, M. Observations of sea surface salinity in the western Pacific fresh pool: Large-scale changes in 1992–1995. *J. Geophys. Res. C Ocean.* **1998**, 103, 7523–7536, doi:10.1029/97jc01773.
6. Hanawa, K.; Talley, L.D. Mode waters BT - Ocean circulation and Climate. *Ocean Circ. Clim.* **2001**, 373–386.
7. Lukas, R.; Lindstrom, E. The mixed layer of the western equatorial Pacific Ocean. *J. Geophys. Res.* **1991**, 96, 3343, doi:10.1029/90JC01951.
8. Pailler, K.; Bourlès, B.; Gouriou, Y. The barrier layer in the western tropical Atlantic ocean. *Geophys. Res. Lett.* **1999**, 26, 2069–2072, doi:10.1029/1999GL900492.
9. Delcroix, T.; McPhaden, M. Interannual sea surface salinity and temperature changes in the western Pacific warm pool during 1992–2000. *J. Geophys. Res. Ocean.* **2002**, 107, SRF 3-1, doi:10.1029/2001JC000862@10.1002/(ISSN)2169-9291.SURFSL1.
10. Foltz, G.R.; McPhaden, M.J. Impact of barrier layer thickness on SST in the central tropical North Atlantic. *J. Clim.* **2009**, 22, 285–299, doi:10.1175/2008JCLI2308.1.
11. Hopkins, J.; Lucas, M.; Dufau, C.; Sutton, M.; Stum, J.; Lauret, O.; Channelliere, C. Detection and variability of the Congo River plume from satellite derived sea surface temperature, salinity, ocean colour and sea level. *Remote Sens. Environ.* **2013**, 139, 365–385, doi:10.1016/j.rse.2013.08.015.
12. Myers, R.A.; Akenhead, S.A.; Drinkwater, K. The influence of Hudson bay runoff and ice-melt on the salinity of the inner newfoundland shelf. *Atmos. - Ocean* **1990**, 28, 241–256, doi:10.1080/07055900.1990.9649377.
13. Ogino, S.Y.; Yamanaka, M.D.; Mori, S.; Matsumoto, J. Tropical Coastal Dehydrator in Global Atmospheric Water Circulation. *Geophys. Res. Lett.* **2017**, 44, 11,636–11,643, doi:10.1002/2017GL075760.
14. Coles, V.J.; Brooks, M.T.; Hopkins, J.; Stukel, M.R.; Yager, P.L.; Hood, R.R. The pathways and properties of the Amazon river plume in the tropical North Atlantic Ocean. *J. Geophys. Res. Ocean.* **2013**, 118, doi:10.1002/2013JC008981.
15. Chaitanya, A.V.S.; Lengaigne, M.; Vialard, J.; Gopalakrishna, V. V.; Durand, F.; Kranthikumar, C.; Amritash, S.; Suneel, V.; Papa, F.; Ravichandran, M. Salinity measurements

collected by fishermen reveal a ‘river in the sea’ flowing along the eastern coast of India. *Bull. Am. Meteorol. Soc.* **2014**, *95*, 1897–1908, doi:10.1175/BAMS-D-12-00243.1.

16. Chelton, D.B.; Deszoeke, R.A.; Schlax, M.G.; El Naggar, K.; Siwertz, N. Geographical variability of the first baroclinic Rossby radius of deformation. *J. Phys. Oceanogr.* **1998**, *28*, 433–460, doi:10.1175/1520-0485(1998)028<0433:GVOTFB>2.0.CO;2.

17. Alory, G.; Delcroix, T.; Téchiné, P.; Diverres, D.; Varillon, D.; Cravatte, S.; Gouriou, Y.; Grelet, J.; Jacquin, S.; Kestenare, E.; et al. The French contribution to the voluntary observing ships network of sea surface salinity. *Deep Sea Res. Part I Oceanogr. Res. Pap.* **2015**, *105*, 1–18, doi:10.1016/j.dsr.2015.08.005.

18. Smith, S.R.; Alory, G.; Andersson, A.; Asher, W.; Baker, A.; Berry, D.I.; Drushka, K.; Figurskey, D.; Freeman, E.; Holthus, P.; et al. Ship-based contributions to global ocean, weather, and climate observing systems. *Front. Mar. Sci.* **2019**, *6*, 1–26, doi:10.3389/fmars.2019.00434.

19. Kerr, Y.H.; Waldeufel, P.; Wigneron, J.P.; Delwart, S.; Cabot, F.; Boutin, J.; Escorihuela, M.J.; Font, J.; Reul, N.; Gruhier, C.; et al. The SMOS L: New tool for monitoring key elements of the global water cycle. *Proc. IEEE* **2010**, *98*, 666–687, doi:10.1109/JPROC.2010.2043032.

20. Le Vine, D.M.; Lagerloef, G.S.E.; Colomb, F.R.; Yueh, S.H.; Pellerano, F.A. Aquarius: An instrument to monitor sea surface salinity from space. *IEEE Trans. Geosci. Remote Sens.* **2007**, *45*, 2040–2050, doi:10.1109/TGRS.2007.898092.

21. Li, Y.; Wang, F.; Han, W. Interannual sea surface salinity variations observed in the tropical North Pacific Ocean. *Geophys. Res. Lett.* **2013**, *40*, 2194–2199, doi:10.1002/grl.50429.

22. Delcroix, T.; Cravatte, S.; McPhaden, M.J. Decadal variations and trends in tropical Pacific sea surface salinity since 1970. *J. Geophys. Res. Ocean.* **2007**, *112*, 1–15, doi:10.1029/2006JC003801.

23. Foltz, G.R.; McPhaden, M.J. Seasonal mixed layer salinity balance of the tropical North Atlantic Ocean. *J. Geophys. Res. Ocean.* **2008**, *113*, 1–14, doi:10.1029/2007JC004178.

24. Foltz, G.R.; Grodsky, S.A.; Carton, J.A.; McPhaden, M.J. Seasonal salt budget of the northwestern tropical Atlantic Ocean along 38°W. *J. Geophys. Res. C Ocean.* **2004**, *109*, 1–13, doi:10.1029/2003jc002111.

25. Camara, I.; Kolodziejczyk, N.; Mignot, J.; Lazar, A.; Gaye, A.T. On the seasonal variations of salinity of the tropical Atlantic mixed layer. *J. Geophys. Res. Ocean.* **2015**, *120*, 4441–4462, doi:10.1002/2015JC010865.

26. Du, Y.; Zhang, Y. Satellite and Argo observed surface salinity variations in the tropical Indian Ocean and their association with the Indian ocean dipole mode. *J. Clim.* **2015**, *28*, 695–713, doi:10.1175/JCLI-D-14-00435.1.

27. Ratnawati, H.I.; Aldrian, E.; Soepardjo, A.H. Variability of evaporation-precipitation (E-P) and sea surface salinity (SSS) over Indonesian maritime continent seas. *AIP Conf. Proc.* **2018**, *2023*, doi:10.1063/1.5064249.

28. Da-Allada, C.Y.; Gaillard, F.; Kolodziejczyk, N. Mixed-layer salinity budget in the tropical Indian Ocean: seasonal cycle based only on observations. *Ocean Dyn.* **2015**, *65*, 845–857, doi:10.1007/s10236-015-0837-7.

29. Delcroix, T.; Alory, G.; Cravatte, S.; Corrège, T.; McPhaden, M.J. A gridded sea surface salinity data set for the tropical Pacific with sample applications (1950-2008). *Deep. Res. Part I Oceanogr. Res. Pap.* **2011**, *58*, 38–48, doi:10.1016/j.dsr.2010.11.002.
30. Hasson, A.E.A.; Delcroix, T.; Dussin, R. An assessment of the mixed layer salinity budget in the tropical Pacific Ocean. Observations and modelling (1990-2009). *Ocean Dyn.* **2013**, *63*, 179–194, doi:10.1007/s10236-013-0596-2.
31. Alory, G.; Maes, C.; Delcroix, T.; Reul, N.; Illig, S. Seasonal dynamics of sea surface salinity off Panama: The far eastern Pacific Fresh Pool. *J. Geophys. Res. Ocean.* **2012**, *117*, 1–13, doi:10.1029/2011JC007802.
32. Dandapat, S.; Gnanaseelan, C.; Parekh, A. Impact of excess and deficit river runoff on Bay of Bengal upper ocean characteristics using an ocean general circulation model. *Deep. Res. Part II Top. Stud. Oceanogr.* **2020**, *172*, 104714, doi:10.1016/j.dsr2.2019.104714.
33. Kolodziejczyk, N.; Boutin, J.; Vergely, J.-L.; Marchand, S.; Martin, N.; Reverdin, G. Mitigation of systematic errors in SMOS sea surface salinity. *Remote Sens. Environ.* **2016**, *180*, 164–177, doi:10.1016/j.rse.2016.02.061.
34. Boutin, J.; Martin, N.; Kolodziejczyk, N.; Reverdin, G. Interannual anomalies of SMOS sea surface salinity. *Remote Sens. Environ.* **2016**, doi:10.1016/j.rse.2016.02.053.
35. Boutin, J.; Vergely, J.L.; Marchand, S.; D'Amico, F.; Hasson, A.; Kolodziejczyk, N.; Reul, N.; Reverdin, G.; Vialard, J. New SMOS Sea Surface Salinity with reduced systematic errors and improved variability. *Remote Sens. Environ.* **2018**, *214*, 115–134, doi:10.1016/j.rse.2018.05.022.
36. Meissner, T.; Wentz, F.J.; Le Vine, D.M. The salinity retrieval algorithms for the NASA aquarius version 5 and SMAP version 3 releases. *Remote Sens.* **2018**, *10*, doi:10.3390/rs10071121.
37. Gaillard, F.; Diverres, D.; Jacquin, S.; Gouriou, Y.; Grelet, J.; Le Menn, M.; Tassel, J.; Reverdin, G. Sea surface temperature and salinity from French research vessels, 2001-2013. *Sci. Data* **2015**, *2*, 1–9, doi:10.1038/sdata.2015.54.
38. Sea Surface Salinity from Sailing ships : Delayed... - Google Scholar Available online: https://scholar.google.com/scholar?hl=fr&as_sdt=0%2C5&q=Sea+Surface+Salinity+from+Sailing+ships+%3A+Delayed+mode+dataset%2C+annual+release.+&btnG= (accessed on May 4, 2021).
39. Alory, G.; Téchiné, P.; Delcroix, T.; Diverres, D.; Varillon, D.; Donguy, J.; Reverdin, G.; Morrow, R.; Grelet, J.; Gouriou, Y.; et al. Le Service national. **2020**, 1–11.
40. Smith, S.R.; Briggs, K.; Bourassa, M.A.; Elya, J.; Paver, C.R. Shipboard automated meteorological and oceanographic system data archive: 2005–2017. *Geosci. Data J.* **2018**, *5*, 73–86, doi:10.1002/gdj3.59.
41. Olmedo, E.; Martínez, J.; Turiel, A.; Ballabrera-Poy, J.; Portabella, M. Debiased non-Bayesian retrieval: A novel approach to SMOS Sea Surface Salinity. *Remote Sens. Environ.* **2017**, *193*, 103–126, doi:10.1016/j.rse.2017.02.023.
42. Fore, A.; Yueh, S.; Tang, W.; Stiles, B.; Hayashi, A. Combined active / passive retrievals of ocean vector winds and salinities from SMAP. *Int. Geosci. Remote Sens. Symp.* **2016**, *2016-Novem*, 2253–2256, doi:10.1109/IGARSS.2016.7729582.

43. Ferry, N., Parent, L., Garric, G., Barnier, B., & Jourdain, N. C. (2010). Mercator global Eddy permitting ocean reanalysis GLORYS1V1: Description and results. *Mercator-Ocean Quarterly Newsletter*, 36, 15-27.
44. Cabanes, C.; Grouazel, A.; Von Schuckmann, K.; Hamon, M.; Turpin, V.; Coatanoan, C.; Paris, F.; Guinehut, S.; Boone, C.; Ferry, N.; et al. The CORA dataset: Validation and diagnostics of in-situ ocean temperature and salinity measurements. *Ocean Sci.* **2013**, 9, 1–18, doi:10.5194/os-9-1-2013.
45. Dai, A.; Trenberth, K.E. Estimates of Freshwater Discharge from Continents: Latitudinal and Seasonal Variations. *J. Hydrometeorol.* **2002**, 3, 660–687, doi:10.1175/1525-7541(2002)003<0660:EOFDfC>2.0.CO;2.
46. Molleri, G.S.F.; Novo, E.M.L. d. M.; Kampel, M. Space-time variability of the Amazon River plume based on satellite ocean color. *Cont. Shelf Res.* **2010**, 30, 342–352, doi:10.1016/j.csr.2009.11.015.
47. Dag, M.; Benner, R.; Lohrenz, S.; Lawrence, D. Transformation of dissolved and particulate materials on continental shelves influenced by large rivers: Plume processes. *Cont. Shelf Res.* **2004**, 24, 833–858, doi:10.1016/j.csr.2004.02.003.
48. Johns, W.E.; Lee, T.N.; Schott, F.A.; Zantopp, R.J.; Evans, R.H. • EQUATORIAL. **1990**, 95, 103–120.
49. Ffield, A. North Brazil current rings viewed by TRMM Microwave Imager SST and the influence of the Amazon Plume. *Deep. Res. Part I Oceanogr. Res. Pap.* 2005, 52, 137–160.
50. Silva, A.; Araujo, M.; Medeiros, C.; Silva, M.; Bourles, B. *SEASONAL CHANGES IN THE MIXED AND BARRIER LAYERS IN THE WESTERN EQUATORIAL ATLANTIC*; 2005; Vol. 53;.
51. Silva, A.C.; Bourles, B.; Araujo, M. Circulation of the thermocline salinity maximum waters off the Northern Brazil as inferred from in situ measurements and numerical results. *Ann. Geophys.* **2009**, 27, 1861–1873, doi:10.5194/angeo-27-1861-2009.
52. Johns, W.E.; Lee, T.N.; Beardsley, R.C.; Candela, J.; Limeburner, R.; Castro, B. Annual Cycle and Variability of the North Brazil Current. *J. Phys. Oceanogr.* **1998**, 28, 103–128, doi:10.1175/1520-0485(1998)028<0103:ACAVOT>2.0.CO;2.
53. Fratantoni, D.M.; Johns, W.E.; Townsend, T.L. Rings of the North Brazil Current: Their structure and behavior inferred from observations and a numerical simulation. *J. Geophys. Res.* **1995**, 100, 10633, doi:10.1029/95JC00925.
54. Reul, N.; Fournier, S.; Boutin, J.; Hernandez, O.; Maes, C.; Chapron, B.; Alory, G.; Quilfen, Y.; Tenerelli, J.; Morisset, S.; et al. Sea Surface Salinity Observations from Space with the SMOS Satellite: A New Means to Monitor the Marine Branch of the Water Cycle. *Surv. Geophys.* **2014**, 35, 681–722, doi:10.1007/s10712-013-9244-0.
55. Reverdin, G., Olivier, L., Foltz, G. R., Speich, S., Karstensen, J., Horstmann, J., ... & Boutin, J. (2021). Formation and evolution of a freshwater plume in the northwestern tropical Atlantic in February 2020. *Journal of Geophysical Research: Oceans*, e2020JC016981.
56. Grodsky, S.A.; Reul, N.; Lagerloef, G.; Reverdin, G.; Carton, J.A.; Chapron, B.; Quilfen, Y.; Kudryavtsev, V.N.; Kao, H.Y. Haline hurricane wake in the Amazon/Orinoco

plume: AQUARIUS/SACD and SMOS observations. *Geophys. Res. Lett.* **2012**, *39*, 4–11, doi:10.1029/2012GL053335.

57. da Silveira, I.C.A.; de Miranda, L.B.; Brown, W.S. On the origins of the North Brazil Current. *J. Geophys. Res.* **1994**, *99*, 22501, doi:10.1029/94JC01776.

58. Dossa, A.N.; Silva, A.C.; Chaigneau, A.; Eldin, G.; Araujo, M.; Bertrand, A. Near-surface western boundary circulation off Northeast Brazil. *Prog. Oceanogr.* **2021**, *190*, 102475, doi:10.1016/j.pocean.2020.102475.

59. Aubone, N.; Palma, E.D.; Piola, A.R. The surface salinity maximum of the South Atlantic. *Prog. Oceanogr.* **2021**, *191*, 102499, doi:10.1016/j.pocean.2020.102499.

60. Stramma, L.; Fischer, J.; Reppin, J. The North Brazil Undercurrent. *Deep. Res. Part I* **1995**, *42*, 773–795, doi:10.1016/0967-0637(95)00014-W.

61. Assunção, R. V.; Silva, A.C.; Roy, A.; Bourlès, B.; Silva, C.H.S.; TERNON, J.F.; Araujo, M.; Bertrand, A. 3D characterisation of the thermohaline structure in the southwestern tropical Atlantic derived from functional data analysis of in situ profiles. *Prog. Oceanogr.* **2020**, *187*, 102399, doi:10.1016/j.pocean.2020.102399.

62. Danabasoglu, G.; Yeager, S.G.; Bailey, D.; Behrens, E.; Bentsen, M.; Bi, D.; Biastoch, A.; Böning, C.; Bozec, A.; Canuto, V.M.; et al. North Atlantic simulations in Coordinated Ocean-ice Reference Experiments phase II (CORE-II). Part I: Mean states. *Ocean Model.* **2014**, *73*, 76–107, doi:10.1016/j.ocemod.2013.10.005.

63. Prasanna Kumar, S.; Narvekar, J.; Kumar, A.; Shaji, C.; Anand, P.; Sabu, P.; Rijomon, G.; Josia, J.; Jayaraj, K.A.; Radhika, A.; et al. Intrusion of the Bay of Bengal water into the Arabian Sea during winter monsoon and associated chemical and biological response. *Geophys. Res. Lett.* **2004**, *31*, 4–7, doi:10.1029/2004GL020247.

64. Papa, F.; Bala, S.K.; Pandey, R.K.; Durand, F.; Gopalakrishna, V. V.; Rahman, A.; Rossow, W.B. Ganga-Brahmaputra river discharge from Jason-2 radar altimetry: An update to the long-term satellite-derived estimates of continental freshwater forcing flux into the Bay of Bengal. *J. Geophys. Res. Ocean.* **2012**, *117*, 1–13, doi:10.1029/2012JC008158.

65. Durand, F.; Shankar, D.; Birol, F.; Shenoi, S.S.C. Spatiotemporal structure of the East India Coastal Current from satellite altimetry. *J. Geophys. Res. Ocean.* **2009**, *114*, 1–18, doi:10.1029/2008JC004807.

66. Fournier, S.; Vialard, J.; Lengaigne, M.; Lee, T.; Gierach, M.M.; Chaitanya, A.V.S. Modulation of the Ganges-Brahmaputra River Plume by the Indian Ocean Dipole and Eddies Inferred From Satellite Observations. *J. Geophys. Res. Ocean.* **2017**, *122*, 9591–9604, doi:10.1002/2017JC013333.

67. Akhil, V.P.; Lengaigne, M.; Durand, F.; Vialard, J.; Chaitanya, A.V.S.; Keerthi, M.G.; Gopalakrishna, V. V.; Boutin, J.; de Boyer Montégut, C. Assessment of seasonal and year-to-year surface salinity signals retrieved from SMOS and Aquarius missions in the Bay of Bengal. *Int. J. Remote Sens.* **2016**, *37*, 1089–1114, doi:10.1080/01431161.2016.1145362.

68. Akhil, V.P.; Vialard, J.; Lengaigne, M.; Keerthi, M.G.; Boutin, J.; Vergely, J.L.; Papa, F. Bay of Bengal Sea surface salinity variability using a decade of improved SMOS re-processing. *Remote Sens. Environ.* **2020**, *248*, 111964, doi:10.1016/j.rse.2020.111964.

69. Suneel, V.; Alex, M.J.; Antony, T.P.; Gurumoorthi, K.; Trinadha Rao, V.; Harikrishnan, S.; Gopalakrishna, V. V.; Rama Rao, E.P. Impact of Remote Equatorial Winds and Local Mesoscale Eddies on the Existence of “River in the Sea” Along the East Coast of India Inferred From Satellite SMAP. *J. Geophys. Res. Ocean.* **2020**, *125*, doi:10.1029/2020JC016866.
70. Huyer, A.; Kosro, P.M. Mesoscale surveys over the shelf and slope in the upwelling region near point arena, California. *J. Geophys. Res. Ocean.* **1987**, *92*, 1655–1681, doi:10.1029/JC092iC02p01655.
71. Huyer, A. Coastal upwelling in the California current system. *Prog. Oceanogr.* **1983**, *12*, 259–284, doi:10.1016/0079-6611(83)90010-1.
72. Schwing, F.B. Increased coastal upwelling in the California Current System. *J. Geophys. Res. C Ocean.* **1997**, *102*, 3421–3438, doi:10.1029/96JC03591.
73. Lynn, R.J.; Bograd, S.J.; Chereskin, T.K.; Huyer, A. Seasonal renewal of the California Current: The spring transition off California. *J. Geophys. Res. Ocean.* **2003**, *108*, 1–11, doi:10.1029/2003jc001787.
74. Vazquez-Cuervo, J.; Gomez-Valdes, J. SMAP and CalCOFI observe freshening during the 2014-2016 Northeast Pacific Warm Anomaly. *Remote Sens.* **2018**, *10*, 1–16, doi:10.3390/rs10111716.
75. Alory, G.; Da-Allada, C.Y.; Djakouré, S.; Dadou, I.; Jouanno, J.; Loemba, D.P. Coastal Upwelling Limitation by Onshore Geostrophic Flow in the Gulf of Guinea Around the Niger River Plume. *Front. Mar. Sci.* **2021**, *7*, doi:10.3389/fmars.2020.607216.
76. Alory, G.; Vega, A.; Ganachaud, A.; Despinoy, M. Influence of upwelling, subsurface stratification, and heat fluxes on coastal sea surface temperature off southwestern New Caledonia. *J. Geophys. Res. Ocean.* **2006**, *111*, 1–9, doi:10.1029/2005JC003401.
77. Blanco, J.L.; Thomas, A.C.; Carr, M.; Strub, P.T. Seasonal climatology of hydrographic conditions in the upwelling region off northern Chile variance of Marine Sciences , of Maine , • Current system , which supports one of the most. *J. Geophys. Res.* **2001**, *106*, 11451–11467.
78. Chavez, F.P.; Messié, M. A comparison of Eastern Boundary Upwelling Ecosystems. *Prog. Oceanogr.* **2009**, *83*, 80–96, doi:10.1016/j.pocean.2009.07.032.
79. Duncombe Rae, C.M. A demonstration of the hydrographic partition of the Benguela upwelling ecosystem at 26°40'S. *African J. Mar. Sci.* **2005**, *27*, 617–628, doi:10.2989/18142320509504122.
80. Checkley, D.M.; Barth, J.A. Patterns and processes in the California Current System. *Prog. Oceanogr.* **2009**, *83*, 49–64, doi:10.1016/j.pocean.2009.07.028.
81. Takesue, R.K.; van Geen, A.; Carriquiry, J.D.; Ortiz, E.; Godínez-Orta, L.; Granados, I.; Saldívar, M.; Ortlieb, L.; Escribano, R.; Guzman, N.; et al. Influence of coastal upwelling and El Niño-Southern Oscillation on nearshore water along Baja California and Chile: Shore-based monitoring during 1997-2000. *J. Geophys. Res. Ocean.* **2004**, *109*, 1–14, doi:10.1029/2003jc001856.
82. Nunes Vaz, R.A.; Lennon, G.W.; Bowers, D.G. Physical behaviour of a large, negative or inverse estuary. *Cont. Shelf Res.* **1990**, *10*, 277–304, doi:10.1016/0278-4343(90)90023-F.

83. Simier, M.; Blanc, L.; Aliaume, C.; Diouf, P.S.; Albaret, J.J. Spatial and temporal structure of fish assemblages in an 'inverse estuary', the Sine Saloum system (Senegal). *Estuar. Coast. Shelf Sci.* **2004**, *59*, 69–86, doi:10.1016/j.ecss.2003.08.002.
84. Winant, C.D.; De Velasco, G.G. Tidal dynamics and residual circulation in a well-mixed inverse estuary. *J. Phys. Oceanogr.* **2003**, *33*, 1365–1379, doi:10.1175/1520-0485(2003)033<1365:TDARCI>2.0.CO;2.
85. Sadrinasab, M.; Kämpf, J. Three-dimensional flushing times of the Persian Gulf. *Geophys. Res. Lett.* **2004**, *31*, 1–4, doi:10.1029/2004GL020425.
86. Lennon, G.W.; Bowers, D.G.; Nunes, R.A.; Scott, B.D.; Ali, M.; Boyle, J.; Wenju, C.; Herzfeld, M.; Johansson, G.; Nield, S.; et al. Gravity currents and the release of salt from an inverse estuary. *Nature* **1987**, *327*, 695–697, doi:10.1038/327695a0.
87. Middleton, J.F.; Bye, J.A.T. A review of the shelf-slope circulation along Australia's southern shelves: Cape Leeuwin to Portland. *Prog. Oceanogr.* **2007**, *75*, 1–41, doi:10.1016/j.pocean.2007.07.001.
88. Petrushevics, P.; Bye, J.A.T.; Fahlbusch, V.; Hammat, J.; Tippins, D.R.; van Wijk, E. High salinity winter outflow from a mega inverse-estuary-the Great Australian Bight. *Cont. Shelf Res.* **2009**, *29*, 371–380, doi:10.1016/j.csr.2008.10.003.
89. Drushka, K.; Asher, W.E.; Sprintall, J.; Gille, S.T.; Hoang, C. Global patterns of submesoscale surface salinity variability. *J. Phys. Oceanogr.* **2019**, *49*, 1669–1685, doi:10.1175/JPO-D-19-0018.1.
90. Dossa, A.; Da-Allada, C.; Herbert, G.; Bourlès, B. Seasonal cycle of the salinity barrier layer revealed in the northeastern Gulf of Guinea. *African J. Mar. Sci.* **2019**, *41*, 163–175, doi:10.2989/1814232x.2019.1616612.
91. Houndegnonto, O.J.; Kolodziejczyk, N.; Maes, C.; Bourlès, B.; Da-Allada, C.Y.; Reul, N. Seasonal Variability of Freshwater Plumes in the Eastern Gulf of Guinea as Inferred From Satellite Measurements. *J. Geophys. Res. Ocean.* **2021**, *126*, doi:10.1029/2020JC017041.
92. Drushka, K.; Asher, W.E.; Ward, B.; Walesby, K. Understanding the formation and evolution of rain-formed fresh lenses at the ocean surface. *J. Geophys. Res. Ocean.* **2016**, *121*, 2673–2689, doi:10.1002/2015JC011527.
93. Oliva, R.; Daganzo-Eusebio, E.; Kerr, Y.H.; Mecklenburg, S.; Nieto, S.; Richaume, P.; Gruhier, C. SMOS radio frequency interference scenario: Status and actions taken to improve the RFI environment in the 1400-1427-MHZ passive band. *IEEE Trans. Geosci. Remote Sens.* **2012**, *50*, 1427–1439, doi:10.1109/TGRS.2012.2182775.
94. Behara, A.; Vinayachandran, P.N.; Shankar, D. Influence of Rainfall Over Eastern Arabian Sea on Its Salinity. *J. Geophys. Res. Ocean.* **2019**, *124*, 5003–5020, doi:10.1029/2019JC014999.
95. Dai, A.; Qian, T.; Trenberth, K.E.; Milliman, J.D. Changes in continental freshwater discharge from 1948 to 2004. *J. Clim.* **2009**, *22*, 2773–2792, doi:10.1175/2008JCLI2592.1.
96. Gouveia, N.A.; Gherardi, D.F.M.; Wagner, F.H.; Paes, E.T.; Coles, V.J.; Aragão, L.E.O.C. The Salinity Structure of the Amazon River Plume Drives Spatiotemporal Variation of Oceanic Primary Productivity. *J. Geophys. Res. Biogeosciences* **2019**, *124*, 147–165, doi:10.1029/2018JG004665.

97. Fournier, S.; Lee, T. Seasonal and interannual variability of sea surface salinity near major river mouths of the world ocean inferred from gridded satellite and in-situ salinity products. *Remote Sens.* **2021**, *13*, 1–14, doi:10.3390/rs13040728
98. Feng, M.; Meyers, G.; Pearce, A.; Wijffels, S. Annual and interannual variations of the Leeuwin Current at 32°S. *J. Geophys. Res. Ocean.* **2003**, *108*, doi:10.1029/2002jc001763.
99. Grumbine, R.W. A model of the formation of high-salinity shelf water on polar continental shelves. *J. Geophys. Res.* **1991**, *96*, 22049, doi:10.1029/91jc00531.
100. Morrow, R.; Fu, L.L.; Ardhuin, F.; Benkiran, M.; Chapron, B.; Cosme, E.; D'Ovidio, F.; Farrar, J.T.; Gille, S.T.; Lapeyre, G.; et al. Global observations of fine-scale ocean surface topography with the Surface Water and Ocean Topography (SWOT) Mission. *Front. Mar. Sci.* **2019**, *6*, 1–19, doi:10.3389/fmars.2019.00232.
101. Guichoux, Y., Lennon, M., & Thomas, N. (2016, July). Sea surface currents calculation using vessel tracking data. In Proceedings of the Maritime Knowledge Discovery and Anomaly Detection Workshop, (Ispra: Joint Research Centre).
102. Rodriguez-Fernandez, N.J.; Mialon, A.; Merlin, O.; Suere, C.; Cabot, F.; Khazaal, A.; Costeraste, J.; Palacin, B.; Rodriguez-Suquet, R.; Tournier, T.; et al. SMOS-HR: A High Resolution L-Band Passive Radiometer for Earth Science and Applications. *Int. Geosci. Remote Sens. Symp.* **2019**, 8392–8395, doi:10.1109/IGARSS.2019.8897815.

5 CONCLUSIONS AND PERSPECTIVES

5.1 CONCLUSIONS

Ocean circulation plays a key role in the regulation of climate. The study of ocean circulation developed strongly at the end of the 19th century, especially after the Challenger campaign from 1872 to 1876. The general overview of the ocean circulation is now well known, but many questions remain open, especially from a regional point of view, which requires the observation of the areas of interest with high-resolution. In this context, the objectives of this dissertation were to describe and analyze the western boundary circulation off the northeast Brazil region, as well as to analyze the coastal SSS gradients of the global ocean. Our objectives were achieved by using data from *in situ* measurements, satellite data and reanalysis data. The advances made in this dissertation can be summarized in three main points.

- First, we described the near surface off western boundary off Northeast Brazil. According to previous studies, the ocean dynamics off NEB is mainly dominated by the NBUC-NBC current system. This dynamic was globally described by previous studies. The NBUC is formed south of 10°S from the bifurcation of the sSEC (e.g., Silveira et al., 1994; Stramma et al., 1995; Velleda et al., 2012), from where it flows equatorward along the NEB coast. Around ~5°S, it is fed by the cSEC to form the NBC at the surface that flows northwestward (Bourles et al., 1999; Goes et al., 2005). In spite of these numerous studies, the detailed dynamics between 11°S and 5°S remained poorly documented, especially in terms of spatio-temporal variability, and the mechanisms that can induce such variability. In addition, there were a controversial debate about the origin of the South Equatorial Current (SEUC). Bourles et al. (1999a) showed that the NBUC weakens and retroflects to feed the SEUC. On the other hand, Schott et al. (1998) pointed out that the SEUC is not fed by the NBUC, but by the large-scale recirculation of the tropical gyre (the equatorial branch of the South Equatorial Current, eSEC). Moreover, Goes et al. (2005) observed that in addition to recirculation, there was a small contribution from the NBUC to the eSEC. In the present dissertation, we have made progress in this respect, to fill gaps in comprehension of ocean dynamic within the region. Along the Northeast coast between 9.4°S and 6°S, the NBUC flows equatorward over the continental slope of northeast Brazil. However, its mean velocity and transport is stronger in spring than fall. The zonal flow in the region is subject to the orographic effect that deviates it from the northeastward to the northwestward at about 7.5°S. In addition, mesoscale activities influence

this near-surface circulation locally. At $\sim 4.8^\circ\text{S}$, the central branch of the SEC enters to the equatorward flow to form the intense surface current, the NBC. Regarding the NBUC retroflection into the SEUC, it does not seem to retroflect in fall (Dossa et al., 2021). However, in a complementary work, in which I participated, it has been shown that the NBUC can retroflect in spring to feed the SEUC (Silva et al., 2021) (see annex). On the basis of the above presented results, we draw an updated schematic representation of the circulation in the region (see Figure 1 in Chapter 2).

- Second, we further analyzed mesoscale activities off northeast Brazil ($37^\circ\text{--}26^\circ\text{W}$; $13^\circ\text{S--}1^\circ\text{S}$) since the mesoscale activities were poorly documented in the region. From in situ observation and altimetry data, we pointed out local mesoscale activities influence on the near-surface dynamic of the region. Second, we took advantage from 26 years of altimetry data to provide general view of their characteristics as well as their seasonal variation as possible mechanisms that could drive their formation. About 1500 eddies with a lifetime of at least 14 days, an amplitude and a radius of at least 1 cm and 25 km respectively, are formed within the NEB between 1993 and 2018, which 60% (40%) are cyclonic (anticyclonic). These eddies are characterized by a kinetic energy ranging between 10 and 205 $\text{cm}^2 \text{ s}^{-2}$ and are formed mostly in August-October-September. The northern part of the NEB ($36^\circ\text{--}26^\circ\text{W}$; $6^\circ\text{--}2^\circ\text{S}$) is dominated by the occurrence of cyclonic eddies unlike the southern part ($36^\circ\text{--}26^\circ\text{W}$; $6^\circ\text{--}2^\circ\text{S}$), where 44% (56%) of eddies formed are anticyclonic (cyclonic). Applying the Rayleigh (1880) method to the geostrophic currents from the Altimetry data, we revealed that the formation of cyclonic eddies in the northern part of the NEB is favored by the barotropic instabilities and the negative wind stress curl. Meanwhile, in the southern part, the formation of both types of eddies is not only formed by the wind stress curl and barotropic instabilities, but also by the meandering of surface currents.

- Finally, we analyzed the coastal SSS gradients of the global ocean. Salinity is an important parameter for understanding global climate. High SSS values are found in regions where evaporation dominates precipitation (Delcroix and Hénin, 1991; Gordon et al., 2015) while low SSS are found in ITCZs where precipitation dominates evaporation. In coastal regions the distribution of SSS is affected by river discharges (e.g., Hopkins et al. (2013)), ice melt at high latitudes (Myers et al., 1990), coastal upwelling. These different processes can induce coastal SSS anomalies that are in turn transported along the coast through alongshore currents that are intense at the western boundary. Despite various efforts to understand better the spatial distribution of SSS, the patterns of the coastal gradient of SSS remain poorly

documented at the global scale mainly due to the challenging performance of satellites in coastal regions and the need to improve the freshwater forcing in order to strengthen the boundary conditions of numerical models. We provided in the present dissertations, satellites and reanalysis products skills in reproducing coastal SSS gradient in global Ocean. The skills of each product to reproduce coastal SSS, at global scale, varied from one product to another. Most products showed good performance in the 100-300 km coastal band, but near the coast, both satellites and reanalysis performance remains critical. At regional scale, skills very dependent on coastal regions, therefore, we recommend for regional validation between exploitation of satellite products for coastal studies. Furthermore, SSS satellite products outperform GLORYS; provide more coastal band information than the state-of-the-art Argo and SLA/SST satellite model. In terms of coastal SSS gradient, we have shown through our analysis that the bias of coastal SSS and coastal SSS gradients are not related. Furthermore, the satellites reveal a global dominance of coastal cooling, related to river runoff on plateaus and possibly heavy tropical precipitation in the tropics, confirming TSG observations that may be biased due to ports frequently located in estuaries.

5.2 PERSPECTIVES

This dissertation has brought new elements to our knowledge, notably on the near-surface circulation of the western rim, the mesoscale activities off northeast Brazil and on the coastal gradients of SSS at the global scale. However, several aspects would need further investigation.

Tropical regions of the oceans, although oligotrophic because they contain minimal vertical nutrient flux and low biological productivity, are considered to be areas of very high diversity (Hartmann et al., 2012). This oligotrophic character is explained by the existence of a permanent thermocline in the region (e.g., Assunção et al., 2020), which does not allow nutrient-rich deep waters to mix with surface waters. The topographic characteristics of these areas can affect the water flow (Dossa et al., 2021, Silva et al., 2021), and cause physical changes such as elevated isotherms, isopycnals (Genin and Boehlert, 1985), and nutrient isolines (Comeau et al., 1995). This upward deflection of subsurface (nutrient-rich) water masses may generate increased primary production in the euphotic zone where there is sufficient light for photosynthesis (Furuya et al., 1995; Genin & Boehlert, 1985; Odate & Furuya, 1998). Thus, the results of physical parameters could be combined with other abiotic constituents (nutrients) to improve our understanding of the contribution of current transport.

Furthermore, we have partly answered the contradictory debate on the SEUC, by providing elements on its characteristics in austral spring (Silva et al., 2021) and fall (Dossa et al., 2021). However, the physical mechanisms that could lead to its variability need to be studied to better understand the circulation of the western boundary of the tropical Atlantic.

On other hand, mesoscale activities had remained poorly documented in the region until now. Nevertheless, these oceanic structures, which can be cyclonic or anticyclonic, have an effect on the physical properties and consequently on the biological ecosystems. They can affect the entire marine ecosystem (plankton, nekton or seabirds). In this dissertation, we have studied the characteristics of these structures off Northeast Brazil. Further studies should examining the mesoscale eddy influences on the physical properties of the water masses, the transport of particles, and their interaction with the surrounding environment. In this regard, oceanographic surveys could be set up to study the evolution of these eddies and their impact on the biological activity of the region. A monitoring strategy with floats, in parallel with continuous measurements using SADCP and biological measurements could be developed. The different analyses developed to describe the ocean dynamics, identify and track eddies off northeast Brazil could help in the preparation of these surveys.

SSS satellite data were until recently considered limited near the coast, but their extension to the coast has recently been extended with the introduction of a coastal bias correction (Boutin et al., 2018). This allowed us to perform a global analysis of coastal SSS gradients. We highlighted physical processes that can induce a positive or negative gradient in certain specific regions. However, it would be interesting to group them by categories according to the sign and amplitude of the mean coastal SSS gradient and further relate them to physical processes that could drive positive or negative gradient. In addition, the seasonal and the interannual variation of the global coastal SSS could be investigated. Moreover, the sign of the gradient could be related to geographical and climatic conditions (e.g., tropics/extra-tropics, presence or not of rivers, coastal relief, upwelling, width of the continental shelf, prevailing wind, and monsoon). The future SWOT (Surface water and ocean Topography) satellite mission will give access to mesoscale geostrophic currents close to the coast, which will allow a better understanding of how coastal SSS anomalies are transported in areas with strong SSS gradient, such as river plumes.

REFERENCES

- Aguedjou, H. M. A., Dadou, I., Chaigneau, A., Morel, Y., & Alory, G., 2019. Eddies in the Tropical Atlantic Ocean and Their Seasonal Variability. **Geophysical Research Letters**, 46, 156–164.
- Alexander Haumann, F., Gruber, N., Münnich, M., Frenger, I., & Kern, S., 2016. Sea-ice transport driving Southern Ocean salinity and its recent trends. *Nature*, 537(7618), 89–92.
- Arhan, M., Mercier, H., Bourlès, B., & Gouriou, Y. (1998). Hydrographic sections across the Atlantic at 7°30N and 4°30S. *Deep-Sea Research Part I: Oceanographic Research Papers*, 45(6), 829–872.
- Arístegui, J., Tett, P., Hernández-Guerra, A., Basterretxea, G., Montero, M. F., Wild, K., et al. (1997). The influence of island-generated eddies on chlorophyll distribution: A study of mesoscale variation around Gran Canaria. *Deep-Sea Research Part I: Oceanographic Research Papers*, 44(1), 71–96.
- Aroucha, L. C., Velleda, D., Lopes, F. S., Tyaquicã, P., Lefèvre, N., & Araujo, M. (2020). Intra- and Inter-Annual Variability of North Brazil Current Rings Using Angular Momentum Eddy Detection and Tracking Algorithm: Observations From 1993 to 2016. *Journal of Geophysical Research: Oceans*, 125(12), 1–20.
- Arruda, W. Z., Campos, E. J. D., Zharkov, V., Soutelino, R. G., & da Silveira, I. C. A. (2013). Events of equatorward translation of the Vitoria Eddy. *Continental Shelf Research*, 70, 61–73.
- Barton, E. D., Basterretxea, G., Flament, P., Mitchelson-Jacob, E. G., Jones, B., Arístegui, J., & Herrera, F. (2000). Lee region of gran canaria. *Journal of Geophysical Research: Oceans*, 105(C7), 17173–17193.
- Boebel, O., Davis, R. E., Ollitrault, M., Peterson, R. G., Richardson, P. L., Schmid, C., & Zenk, W. (1999). The intermediate depth circulation of the western South Atlantic. *Geophysical Research Letters*, 26(21), 3329–3332.
- Bourles, B., Molinari, R. L., Johns, E., Wilson, W. D., & Leaman, K. D. (1999b). Upper layer currents in the western tropical North Atlantic (1989–1991). *Journal of Geophysical Research: Oceans*, 104, 1361–1375.
- Bourlès, B., Gouriou, Y., & Chuchla, R. (1999a). On the circulation in the upper layer of the western equatorial Atlantic. *Journal of Geophysical Research: Oceans*, 104(C9), 21151–21170.
- Caltabiano, A. C. V., Robinson, I. S., & Pezzi, L. P. (2005). Multi-year satellite observations of instability waves in the Tropical Atlantic Ocean. *Ocean Science Discussions (OSD)*, 2(1), 283–294.
- Campos, E. J. D. (2006). Equatorward translation of the Vitoria Eddy in a numerical simulation. *Geophysical Research Letters*, 33(22), 1–5.
- Chaigneau, A., Eldin, G., & Dewitte, B. (2009). Eddy activity in the four major upwelling systems from satellite altimetry (1992–2007). *Progress in Oceanography*, 83(1–4), 117–123.

- Chelton, D. B., Schlax, M. G., & Samelson, R. M. (2011). Global observations of nonlinear mesoscale eddies. *Progress in Oceanography*, 91(2), 167–216.
- Delcroix, T., & Hénin, C. (1991). Seasonal and interannual variations of sea surface salinity in the tropical Pacific Ocean. *Journal of Geophysical Research*, 96(C12), 22135.
- Deremble, B., Dewar, W. K., & Chassignet, E. P. (2017). Vorticity dynamics near sharp topographic features. *Journal of Marine Research*, 74(6), 249–276.
- Dickey, T. D., Nencioli, F., Kuwahara, V. S., Leonard, C., Black, W., Rii, Y. M., et al. (2008). Physical and bio-optical observations of oceanic cyclones west of the island of Hawai'i. *Deep-Sea Research Part II: Topical Studies in Oceanography*, 55(10–13), 1195–1217.
- Djakouré, S., Penven, P., Bourlès, B., Veitch, J., & Koné, V. (2014). Coastally trapped eddies in the north of the Gulf of Guinea. *Journal of Geophysical Research: Oceans*, 119(10), 6805–6819.
- Doglioli, A. M., Griffo, A., & Magaldi, M. G. (2004). Numerical study of a coastal current on a steep slope in presence of a cape: The case of the Promontorio di Portofino. *Journal of Geophysical Research C: Oceans*, 109(12), 1–19.
- Dossa, A., Da-Allada, C., Herbert, G., & Bourlès, B. (2019). Seasonal cycle of the salinity barrier layer revealed in the northeastern Gulf of Guinea. *African Journal of Marine Science*, 41(2), 163–175.
- Dossa, A. N., Silva, A. C., Chaigneau, A., Eldin, G., Araujo, M., & Bertrand, A. (2021). Near-surface western boundary circulation off Northeast Brazil. **Progress in Oceanography**, 190, 102475.
- Ffield, A. (2005). North Brazil current rings viewed by TRMM Microwave Imager SST and the influence of the Amazon Plume. *Deep-Sea Research Part I: Oceanographic Research Papers*.
- Frenger, I., Gruber, N., Knutti, R., & Münnich, M. (2013). Imprint of Southern Ocean eddies on winds, clouds and rainfall. *Nature Geoscience*, 6(8), 608–612.
- Fu, L. L., Chelton, D. B., Le Traon, P. Y., & Morrow, R. (2010). Eddy dynamics from satellite altimetry. *Oceanography*, 23(4), 15–25.
- Garzoli, S. L. (2004). North Brazil Current retroflection and transports. *Journal of Geophysical Research*, 109(C1), C01013.
- Garzoli, S. L., Ffield, A., & Yao, Q. (2003). North Brazil Current rings and the variability in the latitude of retroflection. *Elsevier Oceanography Series*, 68(C), 357–373.
- Goes, M., Molinari, R., Da Silveira, I., & Wainer, I. (2005). Retroflections of the North Brazil Current during February 2002. *Deep-Sea Research Part I: Oceanographic Research Papers*, 52(4), 647–667.
- Gordon, A. L. (1986). Interocean exchange of thermocline water. *Journal of Geophysical Research*, 91(C4), 5037.

- Harper, S. (2000). Thermocline ventilation and pathways of tropical-subtropical water mass exchange. *Tellus, Series A: Dynamic Meteorology and Oceanography*, 52(3), 330–345.
- Hénin, C., Penhoat, Y. Du, & Ioualalen, M. (1998). Observations of sea surface salinity in the western Pacific fresh pool: Large-scale changes in 1992-1995. *Journal of Geophysical Research C: Oceans*, 103(3334), 7523–7536.
- Hüttl-Kabus, S., & Böning, C. W. (2008). Pathways and variability of the off-equatorial undercurrents in the Atlantic Ocean. *Journal of Geophysical Research: Oceans*, 113(10).
- Jochum, M., & Malanotte-Rizzoli, P. (2004). A new theory for the generation of the equatorial subsurface countercurrents. *Journal of Physical Oceanography*, 34(4), 755–771.
- Johns, W. E., Lee, T. N., Schott, F. A., Zantopp, R. J., & Evans, R. H. (1990). The North Brazil Current retroflection: Seasonal structure and eddy variability. *Journal of Geophysical Research: Oceans*, 95(C12), 22103-22120.
- Lukas, R., & Lindstrom, E. (1991). The mixed layer of the western equatorial Pacific Ocean. *Journal of Geophysical Research*, 96(S01), 3343.
- Lumpkin, R., & Garzoli, S. L. (2005). Near-surface circulation in the Tropical Atlantic Ocean. *Deep-Sea Research Part I: Oceanographic Research Papers*, 52(3), 495–518.
- Magaldi, M. G., Özgökmen, T. M., Griffa, A., & Rixen, M. (2010). On the response of a turbulent coastal buoyant current to wind events: The case of the Western Adriatic Current. *Ocean Dynamics*, 60(1), 93–122.
- Malanotte-Rizzoli, P., Hedstrom, K., Arango, H., & Haidvogel, D. B. (2000). Water mass pathways between the subtropical and tropical ocean in a climatological simulation of the North Atlantic ocean circulation. *Dynamics of Atmospheres and Oceans*, 32(3–4), 331–371.
- Molinari, R.L., 1982. Observations of eastward currents in the tropical South Atlantic Ocean: 1978-1980. *Journal of Geophysical Research*, 87, 9707-9714.
- Morel, Morrow, R., & Le Traon, P. Y. (2006). 15 Years of Satellite Altimetry and Mesoscale Ocean Dynamics. European Space Agency, (Special Publication) ESA SP, (614).
- Morrow, R., Birol, F., Griffin, D., & Sudre, J. (2004). Divergent pathways of cyclonic and anticyclonic ocean eddies. *Geophysical Research Letters*, 31(24), 1–5.
- Ogino, S. Y., Yamanaka, M. D., Mori, S., & Matsumoto, J. (2017). Tropical Coastal Dehydrator in Global Atmospheric Water Circulation. *Geophysical Research Letters*, 44(22), 11,636-11,643.
- Pascual, A., Faugère, Y., Larnicol, G., & Le Traon, P. Y. (2006). Improved description of the ocean mesoscale variability by combining four satellite altimeters. *Geophysical Research Letters*, 33(2), 2–5.
- Pegliasco, C., Chaigneau, A., & Morrow, R. (2015). Main eddy vertical structures observed in the four major Eastern Boundary Upwelling Systems. *Journal of Geophysical Research: Oceans*, 120(9), 6008–6033.

- Peterson, R. G., & Stramma, L. (1991). Upper-level circulation in the South Atlantic Ocean. *Progress in Oceanography*, 26(1), 1–73.
- Rodrigues, R. R., Rothstein, L. M., & Wimbush, M. (2007). Seasonal Variability of the South Equatorial Current Bifurcation in the Atlantic Ocean: A Numerical Study. *Journal of Physical Oceanography*, 37(1), 16–30.
- Schmitz, W. J., & McCartney, M. S. (1993). On the North Atlantic Circulation. *Reviews of Geophysics*, 31(1), 29–49.
- Schott, F. a., Dengler, M., Zantopp, R., Stramma, L., Fischer, J., & Brandt, P. (2005). The Shallow and Deep Western Boundary Circulation of the South Atlantic at 5°–11°S. *Journal of Physical Oceanography*, 35, 2031–2053.
- Schott, F. A., Stramma, L., & Fischer, J. (1995). The warm water inflow into the western tropical Atlantic boundary regime, spring 1994. *Journal of Geophysical Research*, 100(C12).
- Schott, Friedrich A., Stramma, L., & Fischer, J. (1995). The warm water inflow into the western tropical Atlantic boundary regime, spring 1994. *Journal of Geophysical Research*, 100(C12), 24745.
- Schott, Friedrich A., Fischer, J., & Stramma, L. (1998). Transports and Pathways of the Upper-Layer Circulation in the Western Tropical Atlantic. *Journal of Physical Oceanography*, 28(10), 1904–1928.
- Schott, Friedrich A., Stramma, L., & Fischer, J. (2004). The warm water inflow into the western tropical Atlantic boundary regime, spring 1994. *Journal of Geophysical Research*, 100(C12), 24745.
- Silva, A., Araujo, M., Medeiros, C., Silva, M., & Bourles, B. (2005). SEASONAL CHANGES IN THE MIXED AND BARRIER LAYERS IN THE WESTERN EQUATORIAL ATLANTIC. *BRAZILIAN JOURNAL OF OCEANOGRAPHY* (Vol. 53).
- Silva, A. C., Bourles, B., & Araujo, M. (2009). Circulation of the thermocline salinity maximum waters off the Northern Brazil as inferred from in situ measurements and numerical results. *Annales Geophysicae*, 27(5), 1861–1873.
- Silva, M., Araujo, M., Servain, J., Penven, P., & Lentini, C. A. D. (2009). High-resolution regional ocean dynamics simulation in the southwestern tropical Atlantic. *Ocean Modelling*, 30(4), 256–269.
- da Silveira, Ilson C. A., de Miranda, L. B., & Brown, W. S. (1994). On the origins of the North Brazil Current. *Journal of Geophysical Research*, 99(C11), 22501.
- Silveira, Ilson Carlos Almeida da, Schmidt, A. C. K., Campos, E. J. D., Godoi, S. S. de, & Ikeda, Y. (2000). A corrente do Brasil ao largo da costa leste brasileira. *Brazilian Journal of Oceanography*, 48(2).
- Simoës-Sousa, I. T., Silveira, I. C. A., Tandon, A., Flierl, G. R., Ribeiro, C. H. A., & Martins, R. P. (2021). The Barreirinhas Eddies: Stable Energetic Anticyclones in the Near-Equatorial South Atlantic. *Frontiers in Marine Science*, 8(February).

- Sprintall, J., & Tomczak, M. (1992). Evidence of the Barrier Layer in the Surface-Layer of the Tropics. *Journal of Geophysical Research-Oceans*, 97, 7305–7316.
- Stammer, D. (1997). Global characteristics of ocean variability estimated from regional TOPEX/POSEIDON altimeter measurements. *Journal of Physical Oceanography*, 27(8), 1743–1769.
- Stramma, L., & England, M. (1999). On the water masses and mean circulation of the South Atlantic Ocean. *Journal of Geophysical Research: Oceans*, 104(C9), 20863–20883.
- Stramma, L., & Schott, F. (1999). The mean flow field of the tropical Atlantic Ocean. *Deep Sea Research Part II: Topical Studies in Oceanography*, 46(1–2), 279–303.
- Stramma, L., Fischer, J., & Reppin, J. (1995). The North Brazil Undercurrent. *Deep-Sea Research Part I*, 42(5), 773–795.
- Varona, H. L., Veleda, D., Silva, M., Cintra, M., & Araujo, M. (2019). Amazon River plume influence on Western Tropical Atlantic dynamic variability. *Dynamics of Atmospheres and Oceans*, 85(October 2018), 1–15.
- Veleda, D., Araujo, M., Zantopp, R., & Montagne, R. (2012). Intraseasonal variability of the North Brazil Undercurrent forced by remote winds. *Journal of Geophysical Research: Oceans*, 117(11), 1–10.
- Villas Bôas, A. B., Sato, O. T., Chaigneau, A., & Castelão, G. P. (2015). The signature of mesoscale eddies on the air-sea turbulent heat fluxes in the South Atlantic Ocean. *Geophysical Research Letters*, 42(6), 1856–1862.

**APENDIX A – SEASONAL CYCLE OF THE SALINITY BARRIER LAYER
REVEALED IN THE NORTHEASTERN GULF OF GUINEA (14 pages)**

In this section, we present the two collaborative articles we have contributed to



African Journal of Marine Science

ISSN: 1814-232X (Print) 1814-2338 (Online) Journal homepage: <https://www.tandfonline.com/loi/tams20>

Seasonal cycle of the salinity barrier layer revealed in the northeastern Gulf of Guinea

AN Dossa, CY Da-Allada, G Herbert & B Bourlès

To cite this article: AN Dossa, CY Da-Allada, G Herbert & B Bourlès (2019) Seasonal cycle of the salinity barrier layer revealed in the northeastern Gulf of Guinea, African Journal of Marine Science, 41:2, 163-175, DOI: [10.2989/1814232X.2019.1616612](https://doi.org/10.2989/1814232X.2019.1616612)

To link to this article: <https://doi.org/10.2989/1814232X.2019.1616612>



© 2019 The Author(s). Co-published by NISC Pty (Ltd) and Informa UK Limited, trading as Taylor & Francis Group



Published online: 24 Jul 2019.



Submit your article to this journal [↗](#)



View Crossmark data [↗](#)

Seasonal cycle of the salinity barrier layer revealed in the northeastern Gulf of Guinea

AN Dossa^{1,2*}, CY Da-Allada^{1,3,4,5} , G Herbert⁶  and B Bourlès⁶ 

¹ International Chair in Mathematical Physics and Applications (ICPMA-UNESCO Chair), University of Abomey-Calavi, Cotonou, Benin

² Laboratório de Oceanografia Física Estuarina e Costeira, Departamento de Oceanografia, Universidade Federal de Pernambuco (UFPE), Recife-Pernambuco, Brazil

³ Ecole Nationale Supérieure des Travaux Publics (ENSTP)/Université Nationale des Sciences, Technologies, Ingénierie et Mathématiques (UNSTIM), Abomey, Benin

⁴ Laboratoire d'Hydrologie Marine et Côtière/Institut de Recherches Halieutiques et Océanologiques du Bénin (LHMC/IRHOB), Institut de Recherche pour le Développement (IRD), Cotonou, Benin

⁵ Institut de Recherche pour le Développement/Laboratoire d'Océanographie Physique et Spatiale (IRD/LOPS), Institut Français de Recherche pour l'Exploitation de la Mer (IFREMER), Centre National de la Recherche Scientifique (CNRS), Université de Brest, Institut Universitaire Européen de la Mer (IUEM), Brest, France

⁶ Institut de Recherche pour le Développement (IRD), Instrumentation, Moyens Analytiques, Observatoires en Géophysique et Océanographie (IMAGO), Brest, France

* Corresponding author, e-mail: nath2dossa@gmail.com

The region located in the far northeast of the Gulf of Guinea (NEGG), eastern tropical Atlantic, remains poorly documented due to a lack of available *in situ* ocean data. Heavy rainfall and intense river discharges observed in this region induce a strong salinity stratification that may have a significant impact on the mixed layer depth and on sea surface temperatures, through the so-called barrier-layer effect. By using recent *in situ* data and climatological outputs from a numerical simulation, we reveal the existence of a barrier layer in the NEGG and describe its seasonal occurrence. In the NEGG, the barrier layer limits the mixed layer depth. From January to March, significant values for the barrier-layer thickness are observed mostly due to the horizontal advection of fresh water. From April, vertical mixing along with vertical advection increase the sea surface salinity; hence, the barrier-layer thickness decreases and reaches its minimum in July. During the rest of the year, values for the barrier-layer thickness are again high, mostly under the influence of the Niger River discharge and precipitation, with the highest values recorded in October, when the river discharge and precipitation are at a maximum.

Keywords: mixed layer depth, Niger River discharge, numerical model, oceanography, sea surface salinity, tropical Atlantic, vertical stratification

Introduction

In a classically stratified ocean, the surface layer is virtually homogeneous in temperature, salinity and density. Thus, the layer that is homogeneous in density (also called the mixed layer) is determined by the pycnocline, which is at the same depth as both the halocline and the thermocline. However, in some parts of the ocean, particularly in tropical oceans where strong salinity gradients may be present, a salt stratification may be observed within the isothermal layer. When the halocline and the thermocline no longer coincide, the mixed layer depth is then determined by the halocline. The barrier layer (BL) is a layer that is homogeneous in temperature but stratified in density, and is located between the top of the thermocline and the base of the mixed layer (Godfrey and Lindstrom 1989; Sprintall and Tomczak 1992; de Boyer Montégut et al. 2007; Mignot et al. 2007).

The BL is a physical phenomenon observed in the three tropical oceans. De Boyer Montégut et al. (2007) have shown that the BL is almost permanent in tropical/

subtropical regions, such as the western tropical Atlantic and western Pacific oceans, the Bay of Bengal, the equatorial eastern Indian Ocean and subtropical basins, as well as at high latitudes, such as the Labrador Sea and in parts of the Arctic and Southern oceans. Those authors also showed that the BL appears seasonally in northern subtropical basins, the southern Indian Ocean and the Arabian Sea. Strong precipitation and river runoff have been shown to contribute to BL formation in the Bay of Bengal (Shetye et al. 1996; Varkey et al. 1996; Rao and Sivakuma 2003). Ando and McPhaden (1997) have shown that the main mechanism for BL formation in the western part of the tropical Pacific basin is the strong precipitation observed in that region. The contribution of strong precipitation to BL formation was also confirmed in the western tropical Atlantic basin (Tanguy et al. 2010).

Salinity, through the BL process, can modify heat exchange between the mixed layer and the interior ocean. The BL can reduce cooling through the entrainment of

surface water. Salt stratification limits the depth of the mixed layer and therefore the amount of solar flux entering the lower ocean layer (Lukas and Lindström 1991; Maes et al. 2002). Thus, positive sea surface temperature (SST) anomalies can persist for a long time-period in the presence of a BL (e.g. Maes et al. 2002). The BL can also limit nutrient transfer into the euphotic zone, with limiting effects on biological productivity (Prasanna Kumar et al. 2004).

The northeastern Gulf of Guinea (NEGG), eastern tropical Atlantic (1°–5° N, 5°–10° E), remains very poorly documented due to a lack of *in situ* ocean data for the region, where strong precipitation and important river runoff (mostly from the Niger River) are observed. According to Dai and Trenberth (2002), the Niger River's discharge (annual mean $7 \times 10^3 \text{ m}^3 \text{ s}^{-1}$) is the 12th-largest in the world. These freshwater inputs could be expected to lead to a salinity stratification that is likely to generate a BL, similar to that observed off the Amazon River mouth in the western part of the Atlantic basin (Sprintall and Tomczak 1992; Pailler et al. 1999). In the NEGG region, strong precipitation also plays an important role in sea surface salinity (SSS) variability (Berger et al. 2014; Da-Allada et al. 2014a; Camara et al. 2015).

By analysing *in situ* measurements obtained during the French oceanographic cruise EQUALANT, carried out in the boreal summer of 2000, Guiavarc'h (2003) provided evidence of a BL in the NEGG, especially around 3° N, 6° E. More recently, by using the climatology of de Boyer Montégut et al. (2007), Breugem et al. (2008) suggested that the BL does not exist in the NEGG in either the boreal winter (December to February) or boreal summer (June to August). However, very few temperature/salinity data were available for the region (see Figure 2 of de Boyer Montégut et al. 2007). Nonetheless, recent *in situ* data are now available, which, combined with the results of a high-resolution numerical model, allowed a focused study to be conducted in this region. The aim of the present study was thus to verify and confirm the existence of a BL in the NEGG, describe its seasonal cycle, and discuss its potential causes.

Materials and methods

In-situ data

Salinity and temperature data were obtained during the French EQUALANT-2000 and EGEE oceanographic cruises. The EQUALANT-2000 cruise was carried out as a French contribution to the international CLIVAR (CLimate and Ocean – VARIability, Predictability and Change) project (see <http://www.clivar.org>). Based on three meridional sections carried out in the Gulf of Guinea (along 10° W, 0° E and 6° E), this cruise was implemented on board the RV *Thalassa*, from 25 July to 20 August in 2000 (for details see Bourlès et al. 2002). We used data that were collected at 6° E between 0.33° N and 3.5° N. CTD profiles were carried out every 0°30' in latitude (every 0°20' in the equatorial band between 1° S and 1° N) along all three sections, from 12 to 17 August in 2000. The vertical resolution of the CTD data was 1 m.

In the framework of the program 'Etude de la circulation océanique et du climat dans le Golfe de Guinée' (EGEE) (Bourlès et al. 2007), the French oceanographic component of the African Monsoon Multidisciplinary Analysis (AMMA) program (Redelsperger et al. 2006), six oceanographic

surveys were carried out in the Gulf of Guinea from June 2005 to September 2007. We used CTD data that were collected along 6° E every 0°30' of latitude (every 0°20' in the equatorial band between 1° S and 1° N), on 7 and 8 June 2007 during the fifth EGEE cruise (EGEE5) and from 3 to 5 September 2007 during the sixth EGEE cruise (EGEE6). The vertical resolution of the CTD data was 1 m (for details, see Kolodziejczyk et al. 2014).

To investigate the potential causes of the BL, we also used freshwater-input data, namely for precipitation and Niger River runoff. We used precipitation data from ERA-Interim (ERA) (Dee et al. 2011) and from the Global Precipitation Climatology Project (GPCP) (Adler et al. 2003). Both datasets were available monthly from 1979 to present, with a resolution of 0.75° for ERA and 2.5° for GPCP. Niger River runoff was determined from altimetry, using the method developed by Papa et al. (2010).

Sea surface salinity (SSS) data were obtained from the SMOS satellite and from the In-Situ Analysis System (ISAS) (Gaillard et al. 2016). The SSS product derived from the SMOS data was L3_DEBIAS_LOCEAN_V3, with improved adjustment of land–sea biases close to the coast (Boutin et al. 2018) and thus suitable for studies close to river plumes. This product was distributed by the Ocean Salinity Expertise Center (CECOS) of the CNES-IFREMER Centre Aval de Traitement des Données SMOS (CATDS) at IFREMER, Plouzané, France. The datasets were 9-day composites at a spatial resolution of $0.25^\circ \times 0.25^\circ$ and were available for the period 2010–2017 (<https://www.catds.fr/Products/Available-products-from-CEC-OS/CEC-Locean-L3-Debiased-v3>). The ISAS product consisted of climatological gridded fields of temperature and salinity based mainly on autonomous Argo profiling floats and CTD profiles and it was available for the whole period 2002–2016, with a spatial resolution of $0.5^\circ \times 0.5^\circ$ (<https://archimer.ifremer.fr/doc/00309/42030/>).

The NOAA_OI_SST_V2 dataset, also called the Reynolds product, provided by the NOAA/OAR/ESRL PSD, Boulder, Colorado, USA (<https://www.esrl.noaa.gov/psd/>), was also used to compare the model seasonal cycle of SST with observations. It was produced on a grid of $0.25^\circ \times 0.25^\circ$, and was available daily from 1981 to present.

ROMS framework

The numerical simulation results employed were from the Regional Ocean Modeling System (ROMS) framework (Shchepetkin and McWilliams 2005) with a configuration specially adapted to the Gulf of Guinea (Herbert et al. 2016). This model solves the three-dimensional primitive equation of Navier-Stokes following the Boussinesq and hydrostatic approximations. The version of the model used allowed grid refinement (AGRIF code), as follows: a zoom called a 'child' simulation, with a fine mesh (resolution of $1/15^\circ$), was nested in a wider domain, called a 'parent' simulation, that was at a lower resolution ($1/5^\circ$). The wider domain extended from 60° W to 15.3° E, and from 17° S to 8° N, and the finer domain was from 10° W to 14.1° E, and from 17° S to 6° N. The vertical coordinate was discretised into 45 sigma levels, with the vertical S-coordinate surface and bottom-stretching parameters set, respectively, to $\theta_s = 6$ and $\theta_b = 0$, to keep sufficient resolution near the surface (Haidvogel and

Beckmann 1999). In the first 150 m, the model had 23 sigma levels. The vertical S-coordinate H_c parameter, which gives the approximate transition depth between the horizontal surface levels and the bottom terrain-following levels, was set to $H_c = 10$ m (Herbert et al. 2016). The Global Earth Bathymetric Chart of the Oceans (GEBCO) 1-resolution dataset was used for the topography (www.gebco.net). The parent simulation was forced at its borders by monthly fields of salinity and temperature, provided by World Ocean Atlas 2009 (WOA09) climatological fields with a spatial resolution of $1^\circ \times 1^\circ$. Atmospheric forcing on the sea surface (heat, freshwater and wind stress) was provided by Comprehensive Ocean–Atmosphere Data Set (COADS) climatology with a spatial resolution of $1^\circ \times 1^\circ$. The flows of the major rivers (Amazon, Congo, Niger, Ogooué, Sanaga and Volta rivers) were prescribed monthly from the climatology of Dai and Trenberth (2002). In addition, the model used surface-restoring for salinity.

The simulation was integrated for 15 climatological years, with outputs averaged every 2 days. A statistical equilibrium was reached after 6 years of spin-up. Hence, the model analyses were based on the monthly model outputs averaged from year 7 to year 15.

Criteria for determining the barrier-layer thickness (BLT)

Our computation of the barrier-layer thickness (BLT) was based on the following formula: $BLT = ILD - MLD$, where ILD is the isothermal layer depth, and MLD is the mixed layer depth. We defined the ILD as the depth where the temperature was 0.5°C below the SST at the reference depth of 10 m (Monterey and Levitus 1997; Spall et al. 2000; Foltz et al. 2003; de Boyer Montégut et al. 2004; Da-Allada et al. 2015). The MLD was determined using the density (σ) criterion $\Delta\sigma = 0.03 \text{ kg m}^{-3}$ (de Boyer Montégut et al. 2004; Da-Allada et al. 2013); this corresponds to the depth where the density was equal to $\sigma + \Delta\sigma$, where σ is the density at the reference depth of 10 m. The reference depth was chosen at 10 m in order to avoid the strong diurnal cycle that occurs in the first few meters of the ocean (de Boyer Montégut et al. 2004; Da Allada et al. 2015). These criteria for ILD and MLD allowed improved capture of the vertical salinity gradient. Da-Allada et al. (2014a, 2017) used the same criterion for MLD ($\Delta\sigma = 0.03 \text{ kg m}^{-3}$) to compute the MLD in the Gulf of Guinea.

We also performed sensitivity tests on the MLD and BLT computations. As their values depend on the choice of criteria, we computed different values of MLD and BLT based on different criteria of density, temperature and reference depth. The MLD and BLT monthly errors were estimated as the standard errors of the MLD and BLT computations (Appendix).

Results

Model validation

Mean states of sea surface salinity (SSS) and temperature (SST)

The spatial distributions of the annual mean SSS from the ROMS model and from the SMOS and ISAS products are shown in Figure 1. The model and both the SMOS and ISAS products showed very similar patterns, with high SSS (~ 36)

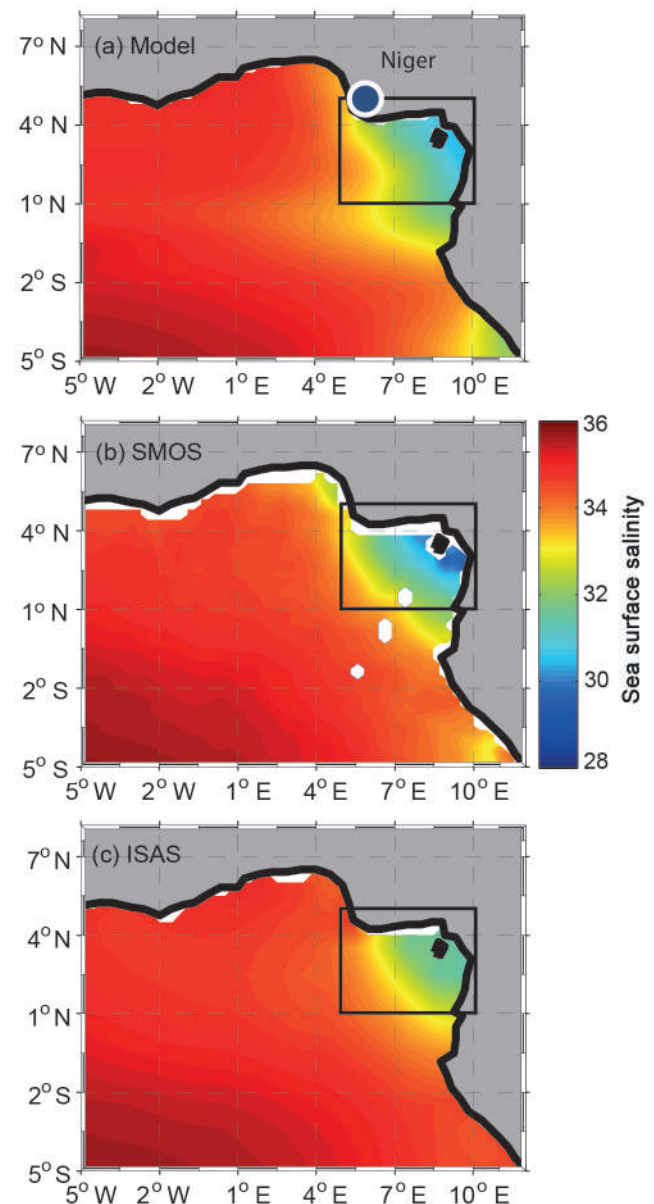


Figure 1: Annual mean sea surface salinity from (a) ROMS model, (b) SMOS product, and (c) ISAS product in the Gulf of Guinea, West Africa. Boxes indicate the focal area of study (defined here as the northeastern Gulf of Guinea [NEGG]). The position of the Niger River mouth is indicated in (a)

found in the southwestern region, and low SSS (~ 31) found in the northeastern region of the Gulf of Guinea, near the African coast. This region is under the influence of the Niger River discharge and high precipitation, enhanced by the presence of Mount Cameroon. The model exhibited another region with a low SSS value in the vicinity of 5°S , close to the coast between 10°E and 12°E , attributable to the Congo River discharge. This region of low SSS was also detected by the SMOS product. In contrast, the ISAS product did not exhibit such low SSS values in this region. Also, the SMOS product captured the low SSS values in the northeastern

region better than the ISAS. This difference may be explained by the low number of *in situ* data available to build the ISAS product (Figure 2 in Gaillard et al. 2016).

The model reproduced the spatial distribution of the observed SST reasonably well (Figure 2). Both the model and the observations exhibited an SST maximum ($>27^{\circ}\text{C}$) north of the equator, from 5°W to the African coast. However, the model seemed to slightly underestimate the SST, as was visible from 5°W to 2°W along the equator. South of the equator, a weaker SST ($<27^{\circ}\text{C}$) was recorded from 5°W to 12°E , both by the model and from observations.

These comparisons showed that the ROMS model produced a satisfactory simulation of spatial distributions of SSS and SST.

Seasonal variability in SSS and SST

Seasonal cycles of SSS and SST in the NEGG area ($1^{\circ}\text{--}5^{\circ}\text{N}$, $5^{\circ}\text{--}10^{\circ}\text{E}$), deduced from the ROMS model and from the observations (SMOS and ISAS for SSS, and Reynolds for SST), are shown in Figure 3. Both SSS and SST exhibited seasonal variation in the NEGG. The SSS seasonality simulated by the model presented maximum values between July and September and minimum values between January and February. The model output

represented an underestimate compared with the ISAS observations from December to September, with a bias of 2.4 in February, but an overestimate from September to November, with a bias of 0.2 in October. When compared with the SMOS observations, the model underestimated SSS from January to July (with a bias of 0.6 in April) and overestimated SSS during the rest of the year (with a bias of 1.8 in November). The lag of ~ 1 month between the model output and the maxima and minima in the observations might be due to uncertainties in freshwater forcing. The model reproduced the seasonality of observed SST reasonably well throughout the year. Maximum SST values ($>27.5^{\circ}\text{C}$) were found from January to April, and minimum values ($<27.4^{\circ}\text{C}$) from May to December. However, the model presented a cold bias (of -0.7°C in April, and -0.9°C in August) throughout the year.

Despite the biases, which were relatively small, the model reproduced the seasonality in SSS and SST adequately and was thus considered to be appropriate for the current study.

Vertical distributions in salinity and temperature

EQUALANT-2000 observations and the ROMS model output at 6°E in August — The vertical distribution of salinity in August is shown from the EQUALANT-2000

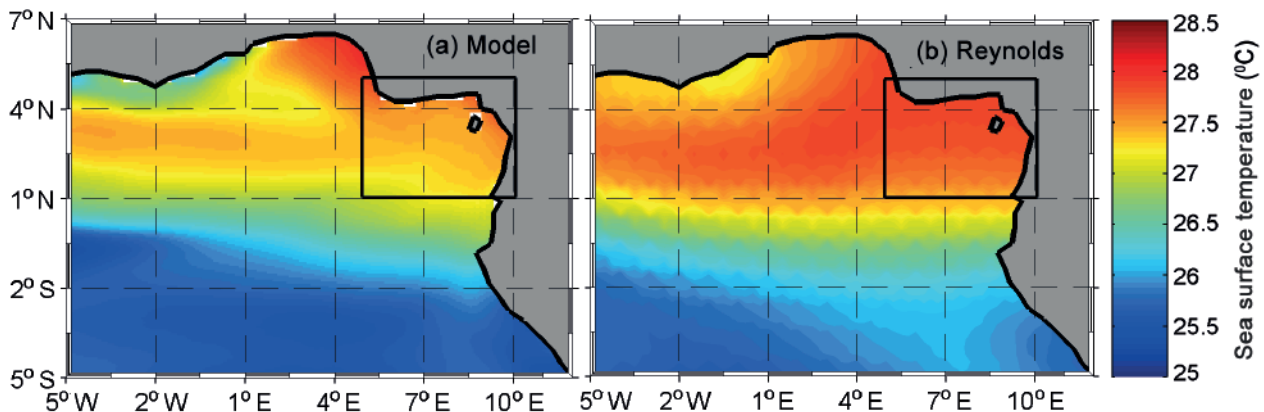


Figure 2: Annual mean sea surface temperature (SST) from (a) the ROMS model and (b) the Reynolds product. Boxes indicate the focal area of study (northeastern Gulf of Guinea, West Africa)

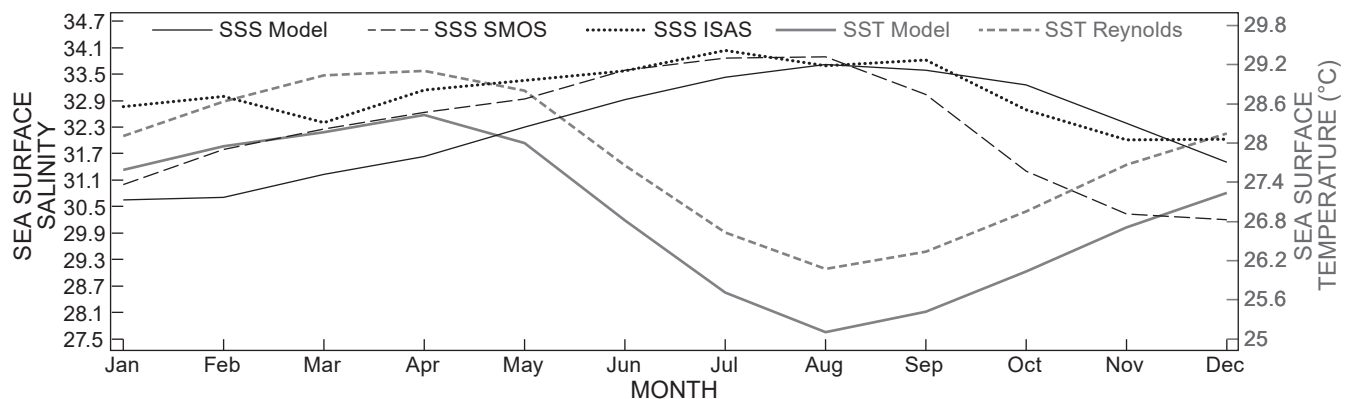


Figure 3: Seasonality of sea surface salinity (SSS) and sea surface temperature (SST) for the SMOS and Reynolds products and for the ISAS product and the ROMS model, in the northeastern Gulf of Guinea, West Africa

cruise (Figure 4a) and from the model (Figure 4b) along 6° E from 0° N to 3.5° N. The EQUALANT-2000 salinity values were obtained from 12 to 17 August 2000, whereas the model salinity was a monthly average for August. The EQUALANT-2000 data exhibited a fresh layer between 0.33° N and 2.5° N, extending from the surface down to a depth of 30 m, with values between 33.5 and 34.5. This fresh layer was also simulated by the model. At 3.5° N, another fresh layer was observed at the surface, with a thickness of 20 m, both in the model output and in the EQUALANT-2000 data, although the *in situ* data revealed saltier conditions (~34.5) than the simulated data (~34). Below 40 m, salinity values were above 35.5 in both the model output and the EQUALANT-2000 data.

A warm surface layer with a thickness of approximately 35 m was present in both the EQUALANT-2000 data and in the model output, with SST values higher than 25 °C, as illustrated on the vertical sections for temperature (Figure 5). The thermocline was apparent at a depth of ~35 m in both the EQUALANT-2000 data and the model output, and the temperature decreased with depths below 40 m.

EGEE5 observations and model output at 6° E in June — In June, both the EGEE5 data (Figure 6a) and the model output (Figure 6b) showed a fresh surface layer with salinity of ~33. Below 40 m depth, the salinity increased strongly and exhibited maximum values of up to 36 at 50–60 m depth. The temperature profiles from the EGEE5 observations (Figure 7a) and the model output (Figure 7b) both exhibited a warm surface layer (>26 °C). Below this layer, the model simulated well the temperature decrease with depth, from 22 °C at ~40 m to 14 °C at ~120 m.

Hence, the ROMS model adequately reproduced the vertical distribution of salinity and temperature in June along 6° E from 0.5° N to 2.5° N.

EGEE6 observations and model output at 6° E in September — Data from EGEE6 were available from 3 to 5 September 2007. The salinity vertical section (Figure 8a) showed an important fresh layer north of 2.5° N from the surface down to a depth of 20 m, with values as low as 32. This local freshwater layer was also present in the model output (Figure 8b). However, the salinity values from the model were higher (~33.5). Also, both the model output and the observations suggested a weak decrease in salinity above ~30 m between 0° N and 1° N.

Both the EGEE6 observations and the model output exhibited a warm surface layer (>25 °C) north of 1° N, extending down to the thermocline (Figure 9). The model simulated a more diffuse and shallower thermocline (i.e. at ~50 m depth) than was reflected in the observations (at ~60 m depth). However, both model and observations exhibited the same thermocline shape, deeper at ~2° N and shallower close to the coast in the north.

Hence, the model adequately reproduced the spatial (horizontal and vertical) distribution of SSS and SST in September along 6° E, and thus its use was considered appropriate to verify the existence of a BL and to analyse its spatial and temporal variations.

Evidence of a barrier layer in the northeastern Gulf of Guinea
Below, we compare the output of the ROMS model to observations that were available in August and September only.

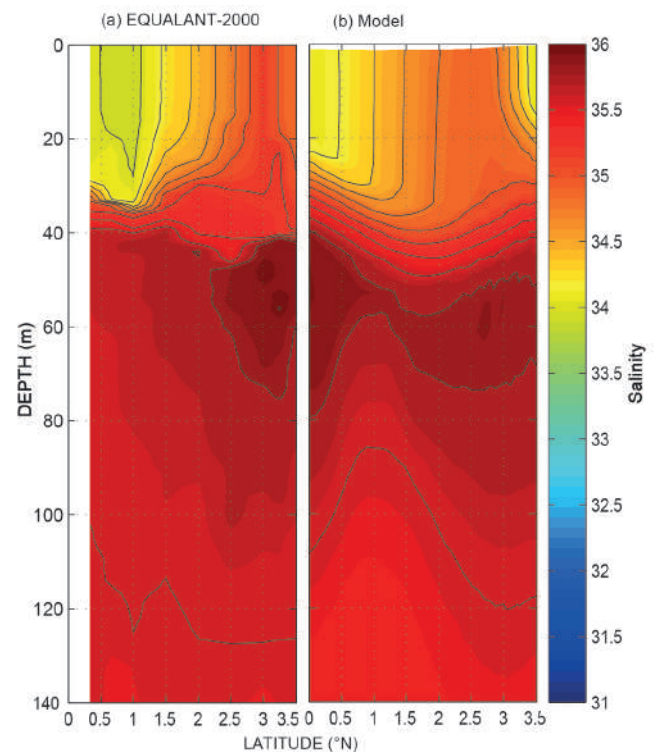


Figure 4: Vertical sections of salinity in August, from (a) the EQUALANT-2000 cruise and (b) the ROMS model, along 6° E between 0° N and 3°50' N, from the surface to a depth of 140 m

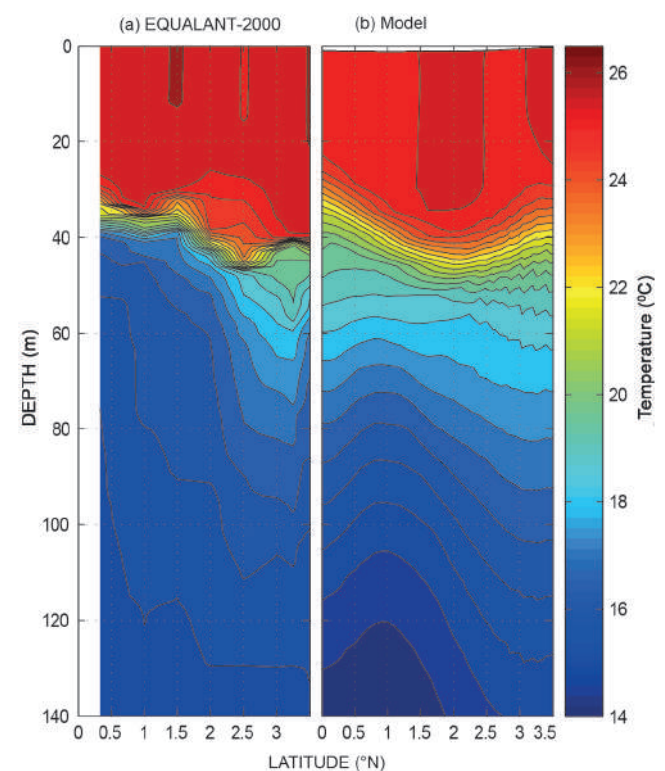


Figure 5: Vertical sections of temperature in August, from (a) the EQUALANT-2000 cruise and (b) the ROMS model, along 6° E between 0° N and 3.5° N, from the surface to a depth of 140 m

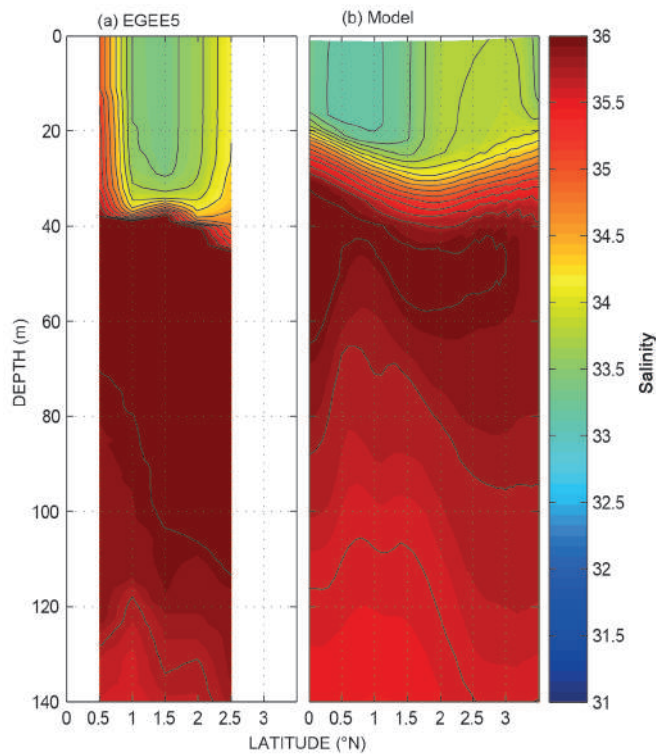


Figure 6: Vertical sections of salinity in June, from (a) the EGEE5 cruise and (b) the ROMS model, along 6° E between 0° N and 3°50' N, from the surface to a depth of 140 m

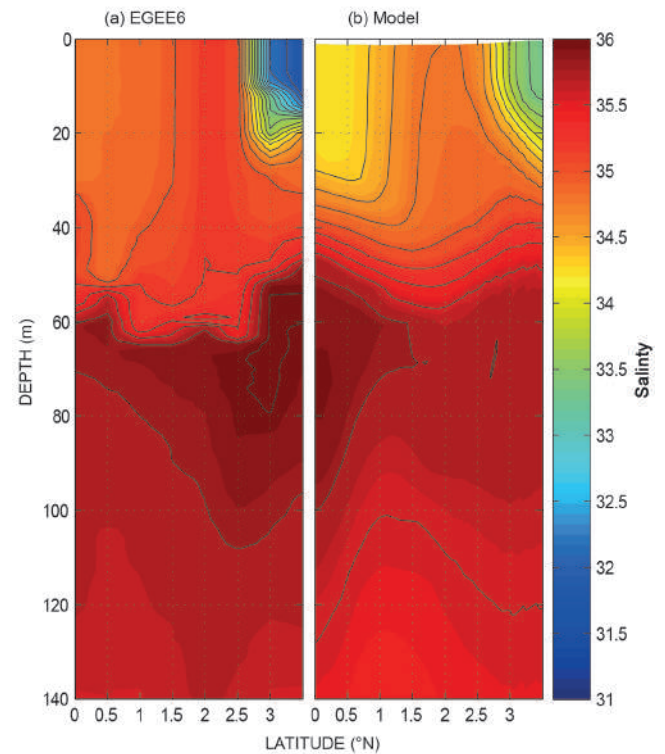


Figure 8: Vertical sections of salinity in September, from (a) the EGEE6 cruise and (b) the ROMS model, along 6° E between 0° N and 3°50' N, from the surface to a depth of 140 m

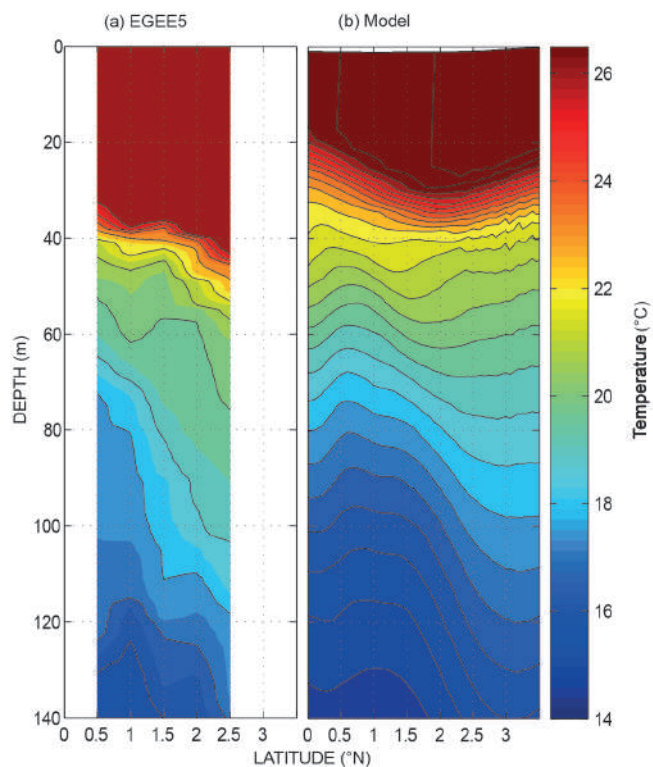


Figure 7: Vertical sections of ocean temperature in June, from (a) the EGEE5 cruise and (b) the ROMS model, along 6° E between 0° N and 3°50' N, from the surface to a depth of 140 m

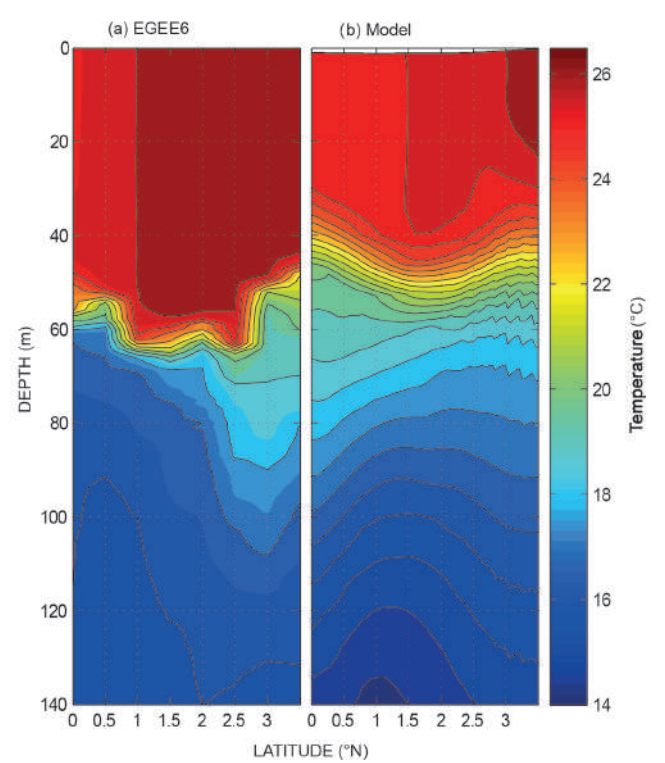


Figure 9: Vertical sections of ocean temperature in September, from (a) the EGEE6 cruise and (b) the ROMS model, along 6° E between 0° N and 3°50' N, from the surface to a depth of 140 m

August profiles

Vertical profiles of temperature, salinity and density are shown from EQUALANT-2000 observations (Figure 10a), the model output (Figure 10b) and from ISAS (Figure 10c). The *in situ* EQUALANT-2000 data were available for 12 August 2000, and the model and ISAS profiles for the month of August across multiple years.

The *in situ* profiles of EQUALANT-2000 exhibited a surface layer of 20-m thickness, homogeneous in salinity, temperature and density (Figure 10a). In the model, this homogeneous surface layer exhibited a thickness of 12 m (Figure 10b). The *in situ* observations showed two clear salinity vertical gradients, at 20 m and 40 m (Figure 10a). At 20 m depth, the observed temperature underwent a slight change from 26° to 25.5 °C. In the same layer, the density profile also presented clear gradients, at the same depths as the salinity gradients. According to the definition of BL (see above), it is apparent that the observations revealed a BL of 20-m thickness, at between 20 and 40 m depth (Figure 10a). In the model, the salinity profile also showed vertical gradients around 15 and 30 m, although less marked than in the EQUALANT-2000 observations. However, these gradients were also apparent in the temperature and density profiles, clearly indicating the presence of a BL of 15-m thickness between 15 and 30 m (Figure 10b). In addition, the monthly mean of the BLT obtained from the model was compared with that obtained from the ISAS at 3.25° N and 6° E in August. ISAS exhibited a BLT of 21 m (Figure 10c), a difference of 6 m when compared with the model.

September profiles

An equivalent comparison as for August, above, was made for September, but with observations from EGEE6 recorded on 3 September 2007. The EGEE6 data provided evidence of a BL of ~32-m thickness (Figure 11a). The monthly average data from the model for September suggested a BL of 14-m thickness (Figure 11b). The important BLT value recorded from the EGEE6 data might be associated with the desalinisation that occurred during the same month around the same position (Figure 8a).

Furthermore, we compared the monthly mean of the BLT obtained from the model with that from the ISAS data at the position 3.5° N, 6° E in September. The BLT from the ISAS data was 10-m thicker than that simulated by the model (Figure 11c). The difference might be linked to the spatial distribution of the BLT in the model, as it might be extended westward during this period of the year.

Mean state and seasonal cycle of the BLT in the NEGG

Here we describe the BLT mean state and its seasonal spatial distribution as computed from the model monthly average output, with a particular focus on the NEGG region.

Annual mean of the BLT

The annual mean of the BLT computed from the model output and the annual mean of the precipitation are presented in Figure 12. The presence of a substantial BLT (>10 m) was evident in the area 1–6° N, 3–10° E, with thicknesses in the NEGG of up to 17 m at around 2° N, 7° E. In the same region the mean precipitation from the ERAI data was at a maximum, with values of up to

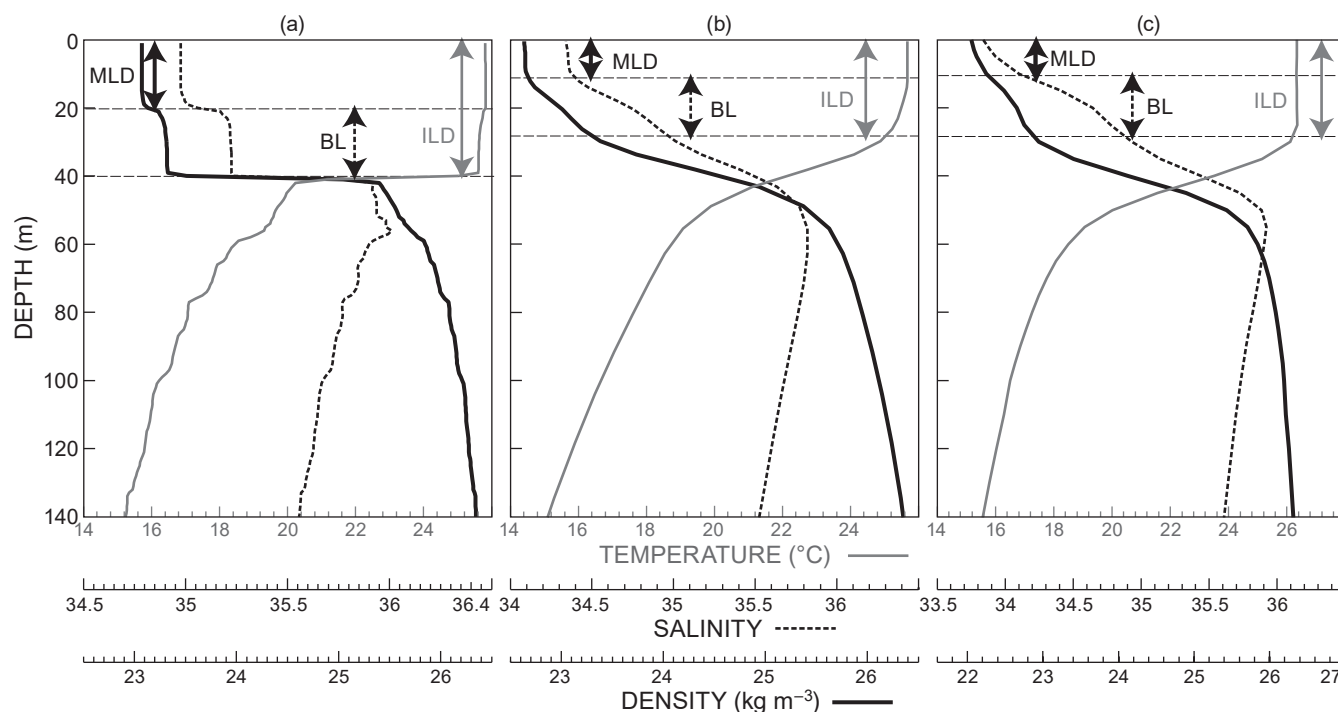


Figure 10: Profiles of ocean temperature, salinity and density at the location 3.25° N, 6° E, as obtained from: (a) observations from the EQUALANT-2000 cruise, recorded on 12 August 2000; (b) the ROMS model; and (c) data from the ISAS product, recorded in August. BL = barrier layer; ILD = isothermal layer depth; MLD = mixed layer depth

10 mm day⁻¹ (Figure 12b). In its mean state, the region where the BL was present corresponded to the region where low SSS values (see Figure 1) and significant precipitation were observed. Just as low values of SSS are related to precipitation and river runoff, so too are BLT values induced by precipitation and river runoff in this region.

Monthly variation in distribution and thickness of the BLT

To analyse the extent and seasonal variations of the BL in the Gulf of Guinea, monthly maps of the BLT, from January to December, over the region 6° N, 5° W–5° S, 12° E, were computed from the ROMS simulation output

(Figure 13). The extent of the BL in the Gulf of Guinea showed considerable variation. From January to April the BL extended over a large part of the Gulf of Guinea, and the highest values of the BLT (>20 m) were observed in the NEGG in February and March. The extent of the BL decreased from May until July and remained in the most northeastern region close to the coast. From August the extent of the BL increased again with the thickness at >22 m, until October when a robust BL extended over the whole NEGG, from around 5° W to 10° E at ~1° N. In October the BL was also observed along the coast south of the equator, with thickness values of ~10 m. In November

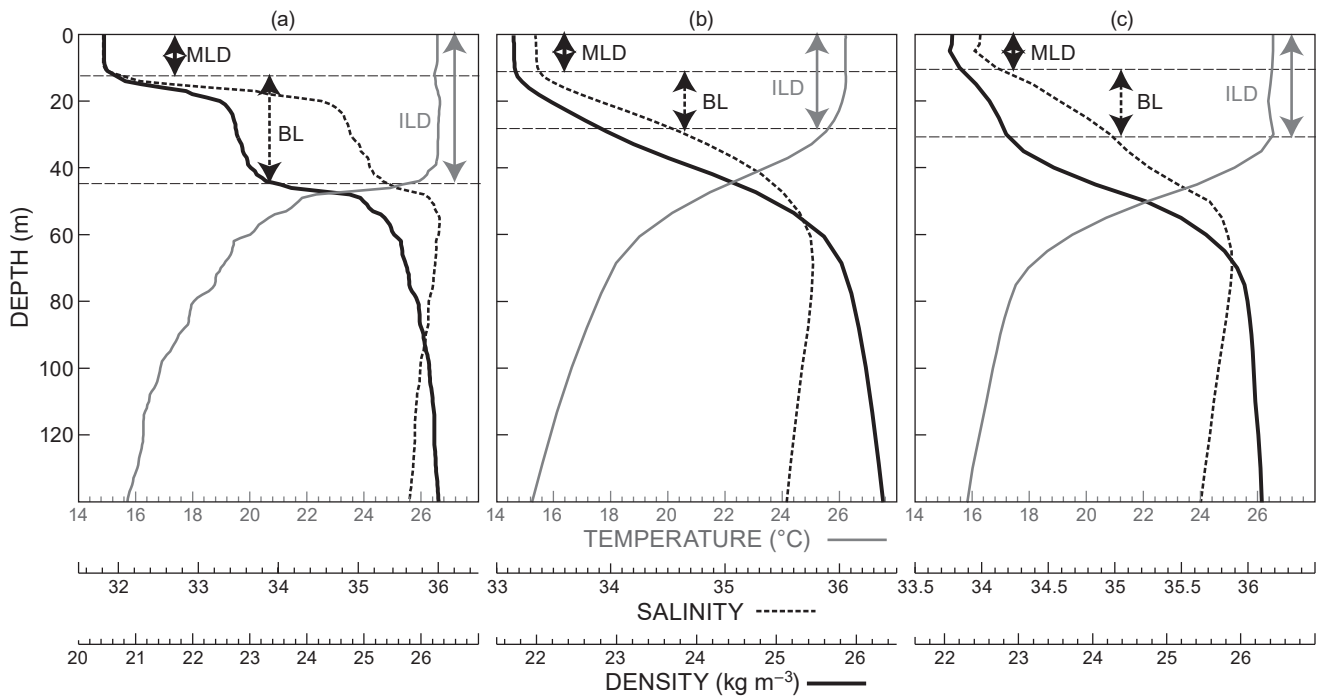


Figure 11: Profiles of ocean temperature, salinity and density at the location 3.5° N, 6° E, as obtained from: (a) observations from the EGEE6 cruise, recorded on 3 September 2007; (b) the ROMS model; and (c) data from the ISAS product, recorded in September. BL = barrier layer; ILD = isothermal layer depth; MLD = mixed layer depth

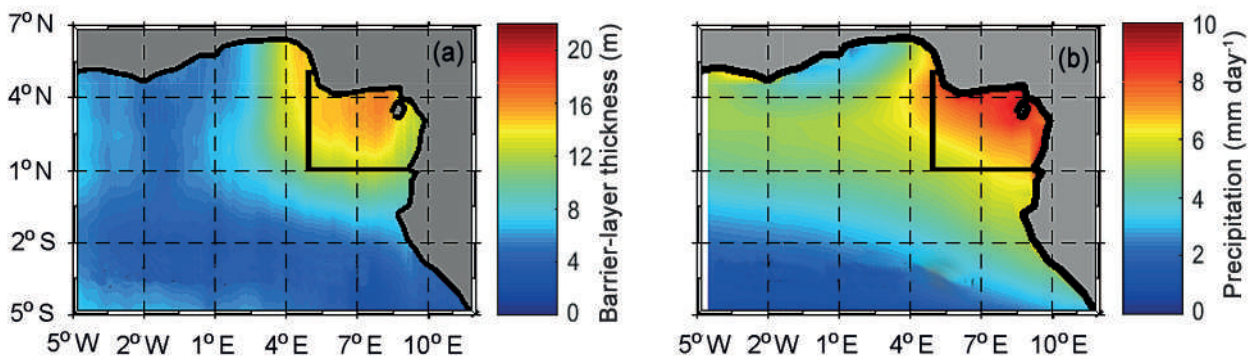


Figure 12: (a) Annual mean of the barrier-layer thickness in the northeastern Gulf of Guinea, West Africa, computed from the ROMS simulation, and (b) annual mean of precipitation computed from the ERA-Interim product. Boxes indicate the focal area of the study

and December the BL still extended over a large part of the NEGG but with decreasing thickness values.

Seasonal cycle of the barrier layer and its impact on the mixed layer depth

Seasonal cycles of the SSS, the MLD (with estimated error) and the BLT (with estimated error) obtained from the ROMS model are shown in Figure 14. SSS, as previously described (Figure 3), exhibited distinct seasonality, with maximum values in August/September (>33.3) and minimum values in January/February (<31). The seasonal occurrence of the BL in the NEGG was analysed in terms of its thickness (i.e. the BLT). The BLT was greater than 10 m from January to March, then decreased until August,

with a minimum in May, June and July (<6 m). The BLT then increased to a maximum of 18 m in October, before decreasing again to 10 m in December. Hence there were two main seasons with regard to the BL: the first from September to March, with relatively high BLT values, and the second from April to August, when the BLT was weaker. The weakest values of the MLD were associated with high values of the BLT, and conversely high values of the MLD were associated with the lowest BLT values. This suggests that the BL affects the MLD by limiting its depth. The inverse relationships between SST and SSS, along the sections at 6° E carried out during the EQUALANT-2000 and EGEE6 cruises, might indicate a potential impact of the BL on SST.

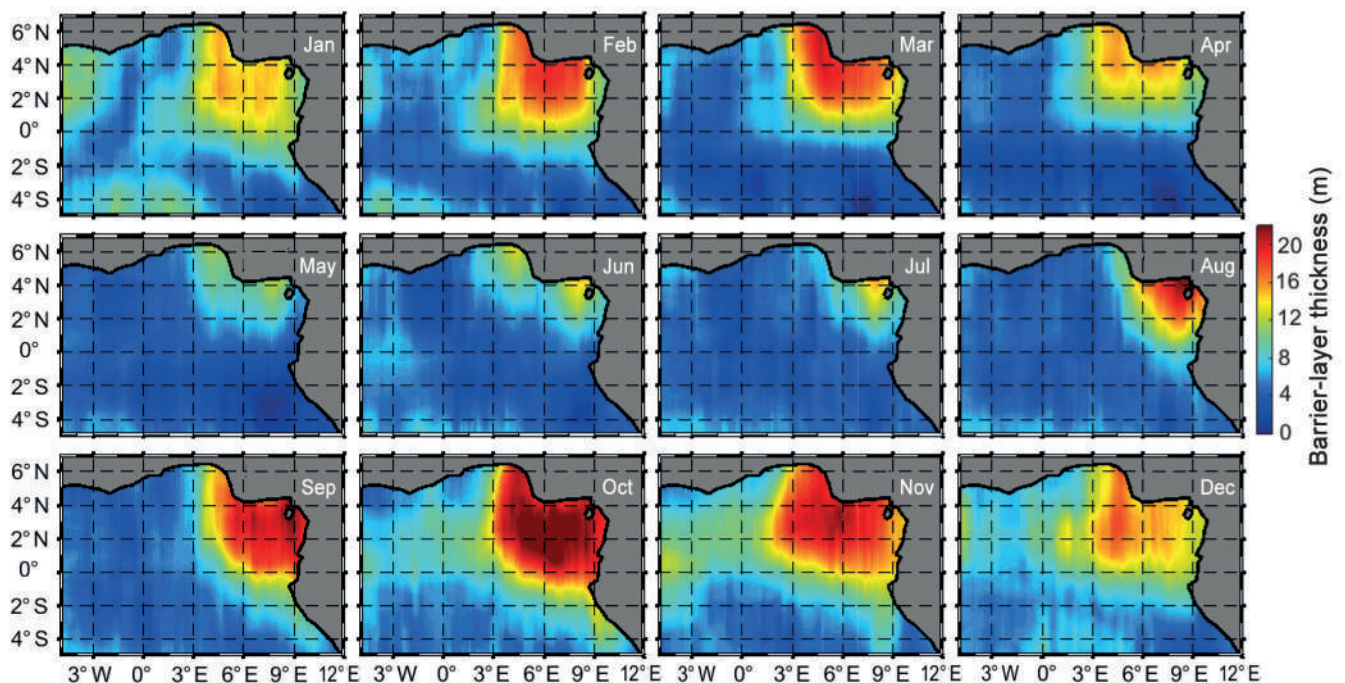


Figure 13: Monthly maps of the barrier-layer thickness in the Gulf of Guinea, West Africa, as computed from the ROMS simulation

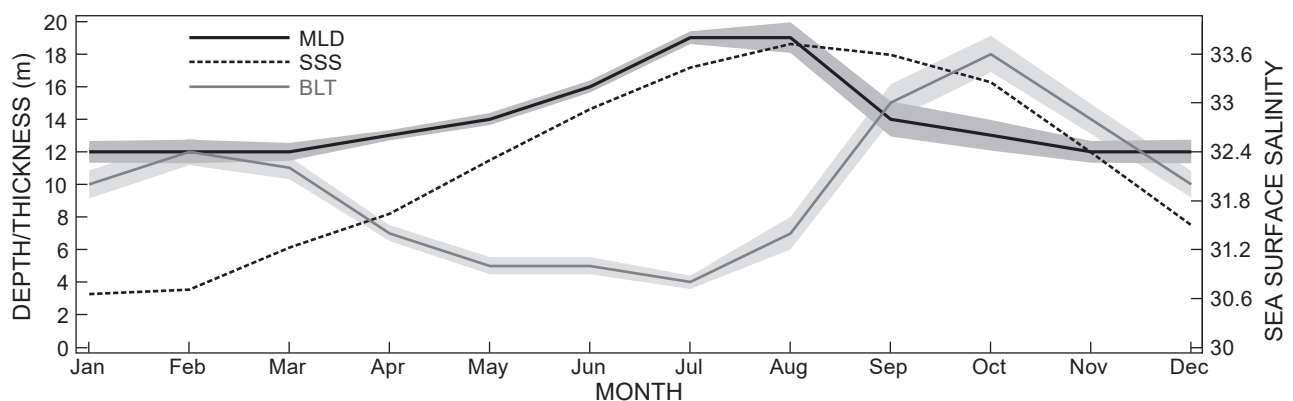


Figure 14: Seasonal cycles in the northeastern Gulf of Guinea and as inferred from the ROMS simulation of sea surface salinity (SSS), barrier-layer thickness (BLT), and mixed layer depth (MLD); shaded areas indicate standard deviations estimated by means of sensitivity tests (see Appendix)

Discussion

To our knowledge, and probably due to the lack of *in situ* data for the region, previous studies have not pointed out the presence and seasonal occurrence of any BL in the NEGG. In this study, we have revealed the existence of the BL and described its seasonal cycle in the NEGG by using a ROMS model and available *in situ* observations. Although Guiavarc'h (2003), using *in situ* data, had suggested the existence of the BL, its formation had not been well documented due to insufficient data. We computed the BLT based on temperature and density criteria, and our computation was performed with a sensitivity test using the criteria $0.5\text{ }^{\circ}\text{C}$ for the ILD and 0.03 kg m^{-3} for the MLD. These criteria had been shown in previous studies to be most suitable for capturing the vertical salinity gradient (Tanguy et al. 2010; Da Allada et al. 2014a, 2017).

Using a ROMS simulation, we have shown that the annual mean BL is present in a large part of the Gulf of Guinea, extending from 5° S to 7° N and from 5° W to 12° E . In particular, the northeastern area ($1^{\circ}\text{--}6^{\circ}\text{ N}$, $3^{\circ}\text{--}10^{\circ}\text{ E}$), bordered by the coast of West Africa, exhibits a robust BL pattern with maximal BLT values. These large BLT values in the NEGG, where the BL is observed throughout the year, are induced mainly by the contributions of river discharge and precipitation. Hence, we focused on the NEGG region.

We have also shown that the BL in the NEGG exhibits a seasonal pattern, with the extent of the BL being at a maximum during February and October and at a minimum in July. The BL seasonally affects the MLD by limiting its depth, and the BLT and the MLD vary in an opposite phase. Also, in August/September, when the BL is confined to the NEGG, the SST is at a maximum and is associated with minimum values of SSS.

Figure 15 shows seasonal cycles of the BLT in the NEGG, the Niger River discharge and precipitation from two products, ERAI and GPCP, which exhibited similar cycles. Here, we diagnose the relative contributions of the

Niger River discharge and precipitation to seasonality in the BL. Precipitation was highest in October ($\sim 10.5\text{ mm day}^{-1}$ from ERAI, and 9 mm day^{-1} from GPCP), and lowest in January/February. This region is under the influence of the Inter-Tropical Convergence Zone (ITCZ) which affects the seasonal variability of rain in the NEGG. The Niger River discharge was low from January to July before increasing to a maximum in October and then decreasing again. The coincident low precipitation and Niger River discharge from January to March indicate that these cannot be responsible for the high BLT levels recorded during these particular months; hence, it appears that other processes influence the BL during this period. Da-Allada et al. (2014b) found that a seasonal decrease in the salinity of the mixed layer in the NEGG was a consequence of both freshwater flux (precipitation plus runoff) and horizontal advection. Therefore, the horizontal advection of fresh water might be the mechanism inducing high BLT values at the beginning of the year. The BLT then decreased from March to a minimum of 4 m in July, which is a period during which high precipitation was recorded (maximum in May and June) before a decrease, but the Niger River discharge remained low. A recorded increase in SSS from May to August in the Bight of Biafra is due to vertical advection and vertical mixing (Berger et al. 2014; Da-Allada et al. 2014b). Consequently, these vertical processes contribute to a decrease in the BLT by increasing salinity of the mixed layer. The BLT in the NEGG increased from August, to a maximum of 18 m in October, and then decreased to 10 m in December, during which period precipitation and the Niger River discharge followed a similar trend. Given the coincident maxima in October in the Niger River discharge, precipitation and the BLT, it can be deduced that the strong BL from August to December is directly induced by precipitation and the Niger River runoff.

It appears that the mechanism that induces the BL is the presence of low-salinity surface water in the region. A similar result was found by Paillet et al. (1999) in the western tropical Atlantic. Using *in situ* and high-resolution

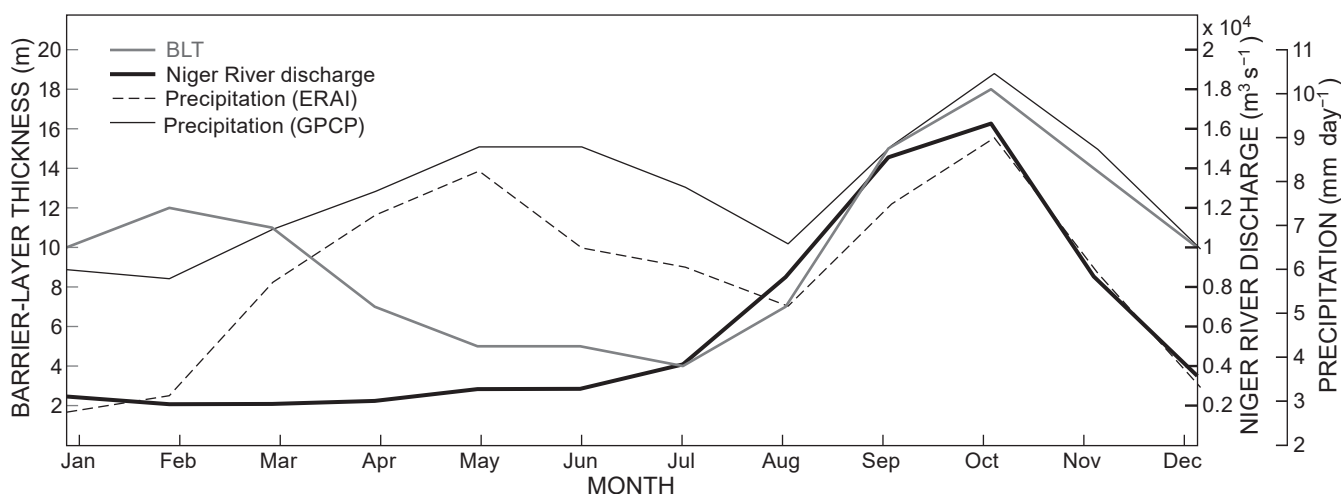


Figure 15: Seasonal cycles of the barrier-layer thickness (BLT) in the northeastern Gulf of Guinea computed from the ROMS simulation, values of Niger River discharge and precipitation, from the ERA-Interim product (ERAI) and the Global Precipitation Climatology Project (GPCP)




CTD data, they suggested that fresh water from the Amazon River may induce a strong halocline that generates a BL. Also, Cronin and McPhaden (2002) noted that a BL can be formed through rainfall which, in the absence of strong mixing and surface heating, can induce BL formation between the fresh lens and the top of the isothermal layer.

Ocean currents might cause a BL to be advected horizontally from its region of formation (Cronin and McPhaden 2002). In the northern Gulf of Guinea, two major currents are present: the Guinea Current and the South Equatorial Current (Hisard 1975; Hisard and Merle 1979). The eastward-flowing Guinea Current is observed between the coast and the northern branch of the South Equatorial Current, between 2° N and 4° N, depending on season (Donguy and Privé 1964). Variations of these currents might be one of the mechanisms responsible for the seasonal extension of the BL into the Gulf of Guinea.

In this study, in agreement with the studies of Guiavarc'h (2003) but contrary to Breugem et al. (2008), we observed a BL in the NEGG with a well-marked seasonal cycle. The BL could not be observed by previous studies due to a lack of *in situ* surface and subsurface data for this region. We combined recently available *in situ* data for the NEGG with climatologic simulation outputs. The ROMS model used surface-restoring for salinity, and it is noted that this could affect the simulated salinity results (e.g. Large et al. 1997; Behrens et al. 2013). Although the model reproduced the vertical salinity distribution well, it would be interesting to revisit our results by using a numerical model without surface-restoring.

Acknowledgements — This work was initiated during a research training period carried out as part of the International Chair in Mathematical Physics and Applications (ICMPA) at the University of Abomey-Calavi (Cotonou, Benin), as part of a degree program entitled Regional Master in Physical Oceanography and Applications. We thank TOTAL SA and the French Institut de Recherche pour le Développement (IRD) for supporting this academic programme and we acknowledge the Laboratório de Oceanografia Física Estuarina e Costeira (LOFEC) (Recife, Brazil), where this work was completed. We thank the two anonymous reviewers for their constructive suggestions that helped improve the manuscript. This work falls within the framework of the Jeunes Equipes Associées à l'IRD (JEA) programme, named 'Variabilité de la salinité et flux d'eau douce à multi-échelles,' which is supported by the IRD. We thank the IRD IMAGO team that ensured works at sea during EQUALANT and EGEE cruises. EQUALANT 2000 and EGEE cruise data are available through their DOI: 10.17600/40060 and 10.18142/95, respectively.

ORCID

Bernard Bourles  <https://orcid.org/0000-0001-6515-4519>
 Casimir Da-Allada  <https://orcid.org/0000-0002-9147-445X>
 Gaëlle Herbert  <https://orcid.org/0000-0001-8911-9697>

References

Adler RF, Huffman GJ, Chang A, Ferraro R, Xie P, Janowiak J et al. 2003. The Version-2 Global Precipitation Climatology Project (GPCP) monthly precipitation analysis (1979–present). *Journal of Hydrometeorology* 4: 1147–1167.

- Ando K, McPhaden MJ. 1997. Variability of surface layer hydrography in the tropical Pacific Ocean. *Journal of Geophysical Research* 102(C10): 23063–23078.
- Behrens E, Biastoch A, Böning CW. 2013. Spurious AMOC trends in global ocean sea-ice models related to subarctic freshwater forcing. *Ocean Modelling* 69: 39–49.
- Berger H, Tréguier A, Perenne N, Talandier C. 2014. Dynamical contribution to sea surface salinity variations in the eastern Gulf of Guinea based on numerical modeling. *Climate Dynamics* 43: 3105–3122.
- Bourlès B, D'Orgeville M, Eldin G, Chuchla R, Gouriou Y, du Penhoat Y, Arnault S. 2002. On the thermocline and subthermocline eastward currents evolution in the Eastern Equatorial Atlantic. *Geophysical Research Letters* 29: 32-1–32-4.
- Bourlès B, Brandt P, Caniaux G, Dengler M, Gouriou Y, Key E et al. 2007. African Monsoon Multidisciplinary Analysis (AMMA): special measurements in the tropical Atlantic. *CLIVAR Exchange* No. 41 (vol. 12). Qingdao, China: Climate Variability and Predictability Programme. pp 7–9.
- Boutin J, Vergely JL, Marchand S, D'Amico F, Hasson A, Kolodziejczyk N et al. 2018. New SMOS sea surface salinity with reduced systematic errors and improved variability. *Remote Sensing of Environment* 214: 115–134.
- Breugem W-P, Chang P, Jang CJ, Mignot J, Hazeleger W. 2008. Barrier layers and tropical Atlantic SST biases in coupled GCMs. *Tellus Series A* 60: 885–897.
- Camara I, Kolodziejczyk N, Mignot J, Lazar A, Gaye AT. 2015. On the seasonal variations of salinity of the tropical Atlantic mixed layer. *Journal of Geophysical Research: Oceans* 120: 4441–4462.
- Cronin MF, McPhaden MJ. 2002. Barrier layer formation during westerly wind bursts. *Journal of Geophysical Research: Oceans* 107(C12): SRF 21-1–SRF 21-12.
- Da-Allada CY, Alory G, du Penhoat Y, Kestenare E, Durand F, Hounkonnou NM. 2013. Seasonal mixed-layer salinity balance in the Tropical Atlantic Ocean: mean state and seasonal cycle. *Journal of Geophysical Research: Oceans* 118: 332–345.
- Da-Allada CY, Alory G, du Penhoat Y, Jouanno J, Hounkonnou NM, Kestanare E. 2014a. Causes for the recent increase in sea surface salinity in the north-eastern Gulf of Guinea. *African Journal of Marine Science* 36: 197–205.
- Da-Allada CY, du Penhoat Y, Jouanno J, Alory G, Hounkonnou NM. 2014b. Modeled mixed-layer salinity balance in the Gulf of Guinea: seasonal and interannual variability. *Ocean Dynamics* 64: 1783–1802.
- Da-Allada CY, Gaillard F, Kolodziejczyk N. 2015. Mixed-layer salinity budget in the tropical Indian Ocean: seasonal cycle based only from observations. *Ocean Dynamics* 65: 845–857.
- Da-Allada CY, Jouanno J, Gaillard F, Kolodziejczyk N, Maes C, Reul N, Bourlès B. 2017. Importance of the Equatorial Undercurrent on the sea surface salinity in the eastern equatorial Atlantic in boreal spring. *Journal of Geophysical Research: Oceans* 122: 521–538.
- Dai A, Trenberth K. 2002. Estimates of freshwater discharge from continents: latitudinal and seasonal variations. *Journal of Hydrometeorology* 3: 660–687.
- de Boyer Montégut CB, Madec G, Fischer AS, Lazar A, Ludicone D. 2004. Mixed layer depth over the global ocean: an examination of profile data and a profile-based climatology. *Journal of Geophysical Research* 109: C12003.
- de Boyer Montégut CB, Mignot J, Lazar A, Cravatte S. 2007. Control of salinity on the mixed layer depth in the world ocean: 1. General description. *Journal of Geophysical Research* 112: C06011.
- Dee DP, Uppala SM, Simmons AJ, Berrisford P, Poli P, Kobayashi S et al. 2011. The ERA-Interim reanalysis: configuration and performance of the data assimilation system. *Quarterly Journal of the Royal Meteorological Society* 137: 553–597.

- Donguy JR, Privé M. 1964. Les conditions de l'Atlantique entre Abidjan et l'équateur – 2e partie. Variations hydrauliques annuelles entre Abidjan et l'Equateur. *Cahiers Océanographiques* 16: 393-398.
- Foltz GR, Grodsky SA, Carton JA. 2003. Seasonal mixed layer heat budget of the tropical Atlantic Ocean. *Journal of Geophysical Research* 108: 3146.
- Gaillard F, Reynaud T, Thierry V, Kolodziejczyk N, von Schuckmann K. 2016. *In situ* based reanalysis of the global ocean temperature and salinity with ISAS: variability of the heat content and steric height. *Journal of Climate* 29: 1305–1323.
- Godfrey JS, Lindstrom EJ. 1989. The heat budget of the equatorial western Pacific surface mixed layer. *Journal of Geophysical Research* 94: 8007–8017.
- Guiavarc'h C. 2003. Analyse de la salinité dans les couches supérieures du Golfe de Guinée. Rapport de stage de DEA Océanologie, Météorologie et Environnement. Brest, France: Université de Bretagne Occidentale.
- Haidvogel DB, Beckmann A. 1999. Numerical ocean circulation modeling. London: Imperial College Press.
- Herbert G, Bourlès B, Penven P, Grelet J. 2016. New insight on the upper layer circulation north of Gulf of Guinea. *Journal of Geophysical Research: Oceans* 121: 6793–6815.
- Hisard P. 1975. La circulation superficielle dans la partie occidentale du Golfe de Guinée. *Documents Scientifiques* No. 6. Abidjan: Centre de Recherches Océanographiques. pp 41–57.
- Hisard P, Merle J. 1979. Onset of summer surface cooling in the Gulf of Guinea during GATE. *Deep-Sea Research* 26 (suppl.): 325–341.
- Kolodziejczyk N, Marin F, Bourlès B, Gouriou Y, Berger H. 2014. Seasonal variability of the Equatorial Undercurrent termination and associated salinity maximum in the Gulf of Guinea. *Climate Dynamics* 43: 3025–3046.
- Large WG, Danabasoglu G, Doney SC, McWilliams JC. 1997. Sensitivity to surface forcing and boundary layer mixing in a global ocean model: annual-mean climatology. *Journal of Physical Oceanography* 27: 2418–2447.
- Lukas R, Lindström EJ. 1991. The mixed layer of the western equatorial Pacific Ocean. *Journal of Geophysical Research* 96 (suppl.): 3343–3357.
- Maes C, Picaut J, Belamari S. 2002. Salinity barrier layer and onset of El Niño in a Pacific coupled model. *Geophysical Research Letters* 29: article 2206.
- Mignot J, de Boyer Montégut C, Lazar A, Cravatte S. 2007. Control of salinity on the mixed layer depth in the world ocean: 2. Tropical areas. *Journal of Geophysical Research* 112: C10010.
- Monterey G, Levitus S. 1997. Seasonal variability of mixed layer depth for the world ocean. *NOAA Atlas NESDIS* No. 14. Washington DC: US Department of Commerce.
- Pailler K, Bourlès B, Gouriou Y. 1999. The barrier layer in the western tropical Atlantic Ocean. *Journal of Geophysical Research* 26: 2069–2072.
- Papa F, Durand F, Rossow WB, Rahman A, Bala SK. 2010. Satellite altimeter-derived monthly discharge of the Ganga-Brahmaputra River and its seasonal to interannual variations from 1993 to 2008. *Journal of Geophysical Research* 115: C12013.
- Prasanna Kumar S, Nuncio M, Narvekar J, Kumar A, Sardesai S, de Souza SN et al. 2004. Are eddies nature's trigger to enhance biological productivity in the Bay of Bengal? *Geophysical Research Letters* 29: 88-1–88-4.
- Rao RR, Sivakumar R. 2003. Seasonal variability of sea surface salinity and salt budget of the mixed layer of the north Indian Ocean. *Journal of Geophysical Research* 108: 3009.
- Redelsperger J-L, Thorncroft CD, Diedhiou A, Lebel T, Parker DJ, Polcher J. 2006. African Monsoon Multidisciplinary Analysis: an international research project and field campaign. *Bulletin of the American Meteorological Society* 87: 1739–1746.
- Shchepetkin AF, McWilliams J-C. 2005. The regional oceanic modeling system (ROMS): a split-explicit, free-surface, topography-following-coordinate oceanic model. *Ocean Modelling* 9: 347–404.
- Shetye SR, Gouveia AD, Shankar D, Shenoi SSC, Vinayachandran P, Sundar N et al. 1996. Hydrography and circulation in the western bay of Bengal during the northeast monsoon. *Journal of Geophysical Research* 101: 14011–14025.
- Spall MA, Weller RA, Furey PW. 2000. Modeling the three-dimensional upper ocean heat budget and subduction rate during the Subduction Experiment. *Journal of Geophysical Research* 105: 26151–26166.
- Sprintall J, Tomczak M. 1992. Evidence of the barrier layer in the surface layer of the tropics. *Journal of Geophysical Research* 97: 7305–7316.
- Tanguy Y, Arnault S, Lattes P. 2010. Isothermal, mixed, and barrier layers in the subtropical and tropical Atlantic Ocean during the ARAMIS experiment. *Deep-Sea Research I* 57: 501–517.
- Varkey MJ, Murty VSN, Suryanarayana A. 1996. Physical oceanography of the Bay of Bengal and Andaman Sea. In: Ansell AD, Gibson RN, Barnes M (eds), *Oceanography and marine biology: an annual review*, vol. 34. London: Allen and Unwin. pp 1–70.

Appendix

Error estimates

Sensitivity tests allowed us to estimate the error on the barrier-layer (BL) computation. We first computed the barrier-layer thickness (BLT) for each month of the year, based on eight different criteria for the mixed layer depth (MLD) and the isothermal layer depth (ILD). We then evaluated the error as the standard deviation of the BL computed from each criterion from January to December. Note that the choice of the criterion was based on three parameters: $\Delta\sigma$ (density), ΔT (temperature), and the associated reference depth Z_0 .



APENDIX B – SURFACE CIRCULATION AND VERTICAL STRUCTURE OF UPPER OCEAN VARIABILITY AROUND FERNANDO DE NORONHA ARCHIPELAGO AND ATOLL ROCAS DURING SPRING 2015 AND FALL 2017 (16 pages)

In this section, we present the two collaborative articles we have contributed to

Surface Circulation and Vertical Structure of Upper Ocean Variability Around Fernando de Noronha Archipelago and Rocas Atoll During Spring 2015 and Fall 2017

Alex Costa da Silva^{1*}, Alexis Chaigneau^{2,3,4}, Alina N. Dossa¹, Gerard Eldin², Moacyr Araujo^{1,5} and Arnaud Bertrand⁶

¹ Departamento de Oceanografia da Universidade Federal de Pernambuco – DOCEAN/UFPE, Recife, Brazil, ² Laboratoire d'Études en Géophysique et Océanographie Spatiale (LEGOS), Université de Toulouse, CNES, CNRD, IRD, UPS, Toulouse, France, ³ Institut de Recherches Halieutiques et Océanologiques du Beinin (IRHOB), Cotonou, Benin, ⁴ International Chair in Mathematical Physics and Applications (ICMPA–UNESCO Chair), Cotonou, Benin, ⁵ Brazilian Research Network on Global Climate Change – Rede CLIMA, São José dos Campos, Brazil, ⁶ Institut de Recherche pour le Développement (IRD), MARBEC, Univ. Montpellier, CNRS, IFREMER, IRD, Sète, France

OPEN ACCESS

Edited by:

Miguel A. C. Teixeira,
University of Reading,
United Kingdom

Reviewed by:

Zhongxiang Zhao,
University of Washington,
United States
Xavier Carton,
Université de Bretagne Occidentale,
France

*Correspondence:

Alex Costa da Silva
alex.csilva@ufpe.br

Specialty section:

This article was submitted to
Physical Oceanography,
a section of the journal
Frontiers in Marine Science

Received: 23 August 2020

Accepted: 30 March 2021

Published: 23 April 2021

Citation:

Costa da Silva A, Chaigneau A, Dossa AN, Eldin G, Araujo M and Bertrand A (2021) Surface Circulation and Vertical Structure of Upper Ocean Variability Around Fernando de Noronha Archipelago and Rocas Atoll During Spring 2015 and Fall 2017. *Front. Mar. Sci.* 8:598101. doi: 10.3389/fmars.2021.598101

Using current, hydrographic and satellite observations collected off Northeast Brazil around the Fernando de Noronha Archipelago and Rocas Atoll during two oceanographic cruises (spring 2015 and fall 2017), we investigated the general oceanic circulation and its modifications induced by the islands. In spring 2015, the area was characterized by lower SST (26.6°C) and deep mixed-layer (~90 m). At this depth, a strong current shear was observed between the central branch of the eastward flowing near-surface South Equatorial Current and the westward flowing South Equatorial Undercurrent. In contrast, in fall 2017, SST was higher (~28.8°C) and the mixed-layer shallower (~50 m). The shear between the central South Equatorial Current and the South Equatorial Undercurrent was weaker during this period. Interestingly, no oxygen-rich water from the south (retroflexion of the North Brazil undercurrent) was observed in the region in fall 2017. In contrast, we revealed the presence of an oxygen-rich water entrained by the South Equatorial Undercurrent reaching Rocas Atoll in spring 2015. Beside these global patterns, island wake effects were noted. The presence of islands, in particular Fernando de Noronha, strongly perturbs central South Equatorial Current and South Equatorial Undercurrent features, with an upstream core splitting and a reorganization of single current core structures downstream of the islands. Near islands, flow disturbances impact the thermohaline structure and biogeochemistry, with a negative anomaly in temperature (−1.3°C) and salinity (−0.15) between 200 and 400 m depth in the southeast side of Fernando Noronha (station 5), where the fluorescence peak (> 1.0 mg m^{−3}) was shallower than at other stations located around Fernando de Noronha, reinforcing the influence of flow-topography. Satellite maps of sea-surface temperature and chlorophyll-a confirmed the presence of several submesoscale features in the study region. Altimetry data suggested the presence of a cyclonic

mesoscale eddy around Rocas Atoll in spring 2015. A cyclonic vortex (radius of 28 km) was actually observed in subsurface (150–350 m depth) southeast of Rocas Atoll. This vortex was associated with topographically induced South Equatorial Undercurrent flow separation. These features are likely key processes providing an enrichment from the subsurface to the euphotic layer near islands, supplying local productivity.

Keywords: mesoscale activity, satellite data, western tropical Atlantic, shipboard measurements, island wake, central South Equatorial Current, South Equatorial Undercurrent

INTRODUCTION

The tropical Atlantic presents a relatively strong static stability with a well-marked thermocline, which is seasonally modulated by the meridional displacement of the Intertropical Convergence Zone (ITCZ), controlling the regime of precipitation and trade winds (Araujo et al., 2011; Nogueira Neto et al., 2018; Assunção et al., 2020). In such regions, vertical mixing, and upwelling are usually restricted to local mechanisms such as divergence of currents, winds and interactions between ocean currents and topography. Interactions between currents and topography, such as oceanic islands and seamounts, can lead to the generation of (sub)mesoscale eddies, changes in current intensity and directions, disturbances of the thermohaline structure, or orographically-induced upwelling [e.g., the special issues dealing with flow encountering abrupt topography (Oceanography, 2019; Vol. 32, No 4) and bio-physical coupling around seamounts (Deep-Sea Research, 2020; Vol. 176)]. This kind of processes is observed in the western tropical Atlantic off northeast Brazil around the oceanic islands of Fernando de Noronha Archipelago (FN) and the Rocas Atoll (RA) (Lessa et al., 1999; Travassos et al., 1999; Chaves et al., 2006; Tchamabi et al., 2017, 2018).

FN and RA, located ~350 km from the mainland (**Figure 1**) encompass oceanic ecosystems classified as “Ecologically or Biologically significant Marine Areas (EBSAs)”¹. Oceanic areas nearby FN and RA are energetic regions subjected to strong seasonally driven features, such as the complex system of zonal equatorial currents and countercurrents, the confluence of water masses, or the trade winds systems (Araujo et al., 2011; Tchamabi et al., 2017, 2018; Foltz et al., 2019). The principal currents of the region are the central branch of the South Equatorial Current (cSEC) located north of the South Equatorial Countercurrent, and the South Equatorial Undercurrent (SEUC) centered at about 4°S (**Figure 1**). These zonal currents flow in opposite direction, with cSEC flowing westwards and SEUC flowing eastwards (Silveira et al., 1994; Stramma and Schott, 1999; Lumpkin and Garzoli, 2005). The near-surface circulation in the region is mostly driven by the meridional migration of the ITCZ. In austral winter (June to August), the ITCZ is located north of the equator and trade winds are stronger. Conversely, in austral fall (March–May), the ITCZ is located close to the equator and the winds are relaxed (Servain et al., 2014; Hounsou-Gbo et al., 2015, 2019). The seasonal ITCZ displacement also influences precipitation regime at FN and RA, with a rainy season extending from March

to July, and a dry season extending from August to January (Assunção et al., 2016).

In the western tropical Atlantic, many complex physical processes around oceanic island wake are not well described because most of survey efforts have focused on broader processes. The main large-scale currents were well identified by several historical programs developed along the western edge of the tropical Atlantic (e.g., the *Global Atmospheric Research Program—GARP*; *Atlantic Tropical Experiment—GATE*; *Francais Océan Climat Atlantique Equatorial—FOCAL*; *Prediction and Research moored Array in the Tropical Atlantic—PIRATA* programs, and the ETAMBOT and CITHER projects). Although numerous, all those previous initiatives focused on a large-scale picture of the tropical Atlantic circulation and knowledge about the interaction of the large-scale currents with RA and FN is still scarce. To provide a detailed picture of the current-island interactions, here we use current, hydrographic, and satellite data collected during the *Acoustic along the BRAZILIAN COaSt* (ABRACOS) cruises in Austral spring 2015 and fall 2017 (Bertrand et al., 2015; 2017). These two periods were found to be representative of canonical spring and fall conditions in the area (Assunção et al., 2020; Dossa et al., 2021). More specifically, we describe the upper-ocean circulation around FN and RA and highlight some mesoscale features observed on currents, thermohaline structure and primary productivity.

DATA AND METHODOLOGY

In situ Observations

In situ data were collected during the two ABRACOS surveys carried out onboard the French R/V Antea in austral spring 2015 (ABRACOS 1, 30 September–08 October 2015) and fall 2017 (ABRACOS 2, 26 April–03 May 2017) (**Figure 2**). The *in situ* datasets described below are publically available (Bertrand et al., 2015, 2017).

Vertical profiles of physical and biogeochemical parameters were collected from the surface to 1,000 m depth using a Seabird SBE911+ conductivity temperature depth (CTD) probe equipped with dissolved oxygen (SBE43) and fluorescence (*Wetlabs*®ECO) sensors. Data were acquired at a frequency of 24 Hz and averaged every 0.1 dbar. All the sensors were laboratory-calibrated before and after each cruise. In the study area, a total of 20 (15, respectively) CTD profiles were acquired during ABRACOS 1 (ABRACOS 2) (**Figure 2**). Conductivity, temperature, pressure, and dissolved oxygen accuracies are of 3 mS/m, 0.001°C, 0.7

¹<http://www.cbd.int/marine/doc/azores-brochure-en.pdf>

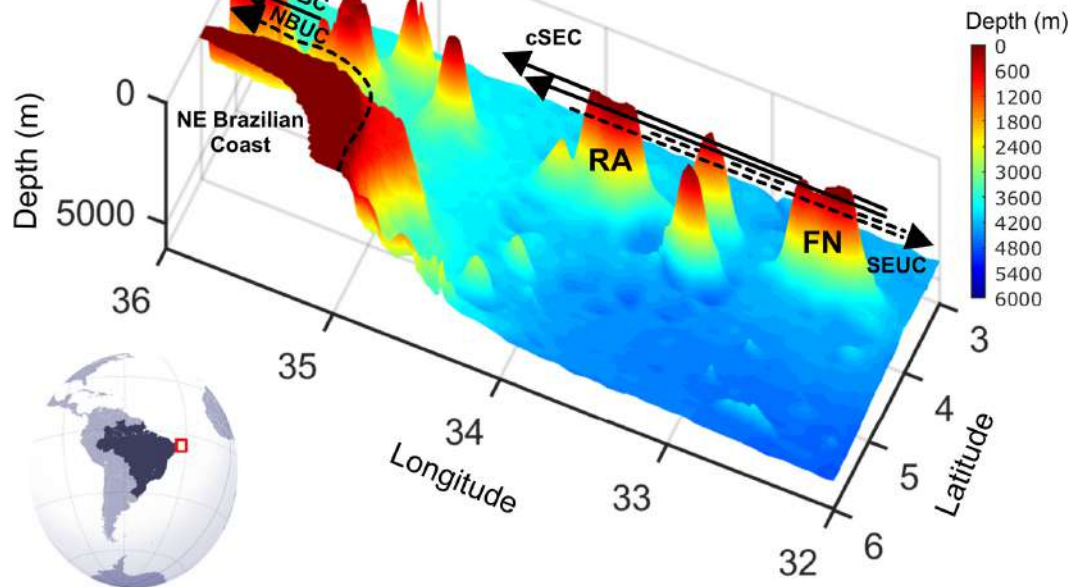


FIGURE 1 | Map of the study area in the western Tropical Atlantic Ocean off northeast Brazil (also indicated by the red box on the globe). General bathymetric (colour scale) is shown at 0–6,000 m depth. Surface and subsurface currents are represented by solid and dashed lines, respectively. RA, Rocas Atoll; FN, Fernando de Noronha Archipelago; cSEC, central branch of the South Equatorial Current, SEUC, South Equatorial Undercurrent, NBC, North Brazil Current; NBUC, North Brazil Undercurrent.

dbar, and 0.09 ml l^{-1} , respectively. The fluorescence sensor measures chlorophyll concentration in the range $0\text{--}125 \text{ mg m}^{-3}$ with a sensitivity of 0.02 mg m^{-3} . A total of 30 water samples (15 for each survey) were collected using Niskin bottles to determine dissolved oxygen (DO) concentrations using the Winkler titration method (Grasshoff et al., 1983).

In order to investigate the stability of the water column, the Brunt-Väisälä (N) frequency was computed from temperature and salinity profiles, using the equation:

$$N = \sqrt{-\frac{g}{\rho_0} \frac{\partial \rho}{\partial z}} \quad (1)$$

where z is depth (in m), g is gravity, ρ is density and $\rho_0 = 1,025 \text{ kg m}^{-3}$ is the reference density. Seawater density was based on the atmosphere International Equation of State of Seawater (UNESCO, 1981).

We use vertical profiles of current velocity and hydrographic data to calculate the Richardson number. The Richardson number (Ri) is a measure of the dynamic stability associated with the competing effects of stratification and shear in the flow. It is expressed as the ratio of the vertical gradient of buoyancy over the vertical shear of horizontal velocity:

$$Ri = \frac{N^2}{\left(\frac{dU}{dz}\right)^2 \left(\frac{dV}{dz}\right)^2} \quad (2)$$

The vortex Rossby Number (Ro) is used to compare the local relative vorticity of the eddy to the planetary vorticity (Eq. 3). Rossby number and Burger number were used to determine the significance of Coriolis acceleration and stratification, respectively, and their impacts on flow dynamics.

$$Ro = \frac{U}{fL} \quad (3)$$

Where f is the Coriolis parameter, U is the maximum velocity and L is the horizontal length scale of the vortex.

The Burger number (Eq. 4) (Pedlosky, 1987) is a dimensionless parameter related to the aspect ratio (H/L), where H is the vertical length scale of the vortex. The Burger number can also be defined as the square of the ratio of the deformation radius to the horizontal scale of the vortex. The Rossby deformation radius is given in Eq. 5.

$$Bu = (NH/fL)^2 \quad (4)$$

$$Rd = \frac{NH}{f} \quad (5)$$

Vertical profiles of current velocity were continuously acquired along the ship track using a ship-mounted Acoustic Doppler Current Profiler (SADCP) from Teledyne-RDI (OS75 instrument). Raw SADCP data were collected every 3 s in deep water (water-depth $< 150 \text{ m}$), and every 1 s in shallow water (water-depth $< 150 \text{ m}$) using a vertical bin length of 8 m, and

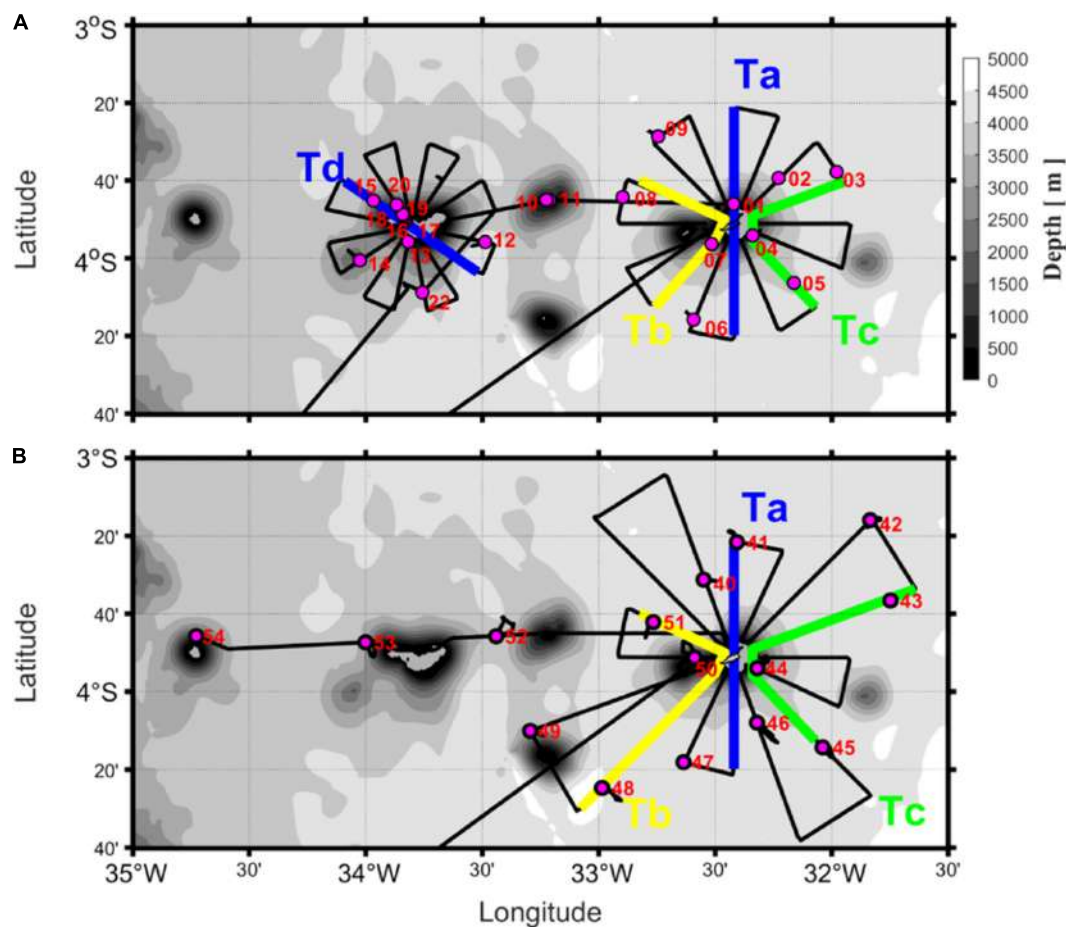


FIGURE 2 | Bathymetric maps of the study area with SADCP sections (black solid lines) acquired during ABRACOS 1 in spring 2015 **(A)** and ABRACOS 2 in fall 2017 **(B)**. The thick blue lines (Ta) indicate the transect detailed in section “Circulation Patterns.” The thick yellow lines (Tb), the thick green lines (Tc) and the thick blue lines (Td) indicate the transects discussed in section “Discussion.” Pink dots show the positions of the CTD profiles.

averaged into 10 min profiles. SADCP data were processed and edited using the Common Ocean Data Access System (CODAS) software package developed by the SOEST, University of Hawaii². The relative velocities were rotated from the transducer to the Earth reference frame using the ship gyrocompass. The global positioning system (GPS) was used to retrieve the absolute current velocities. The orientation of the transducer relative to the gyroscopic compass and an amplitude correction factor for the SADCP were determined by standard calibration procedures (Joyce, 1989; Pollard and Read, 1989). Finally, velocity profiles were averaged hourly, providing profiles in the 19–600 m range.

To better describe the main currents, we separated the data into 2 layers: the surface layer (0–100 m depth), which includes the cSEC, and the subsurface layer (100–400 m depth), where mainly the SEUC is present.

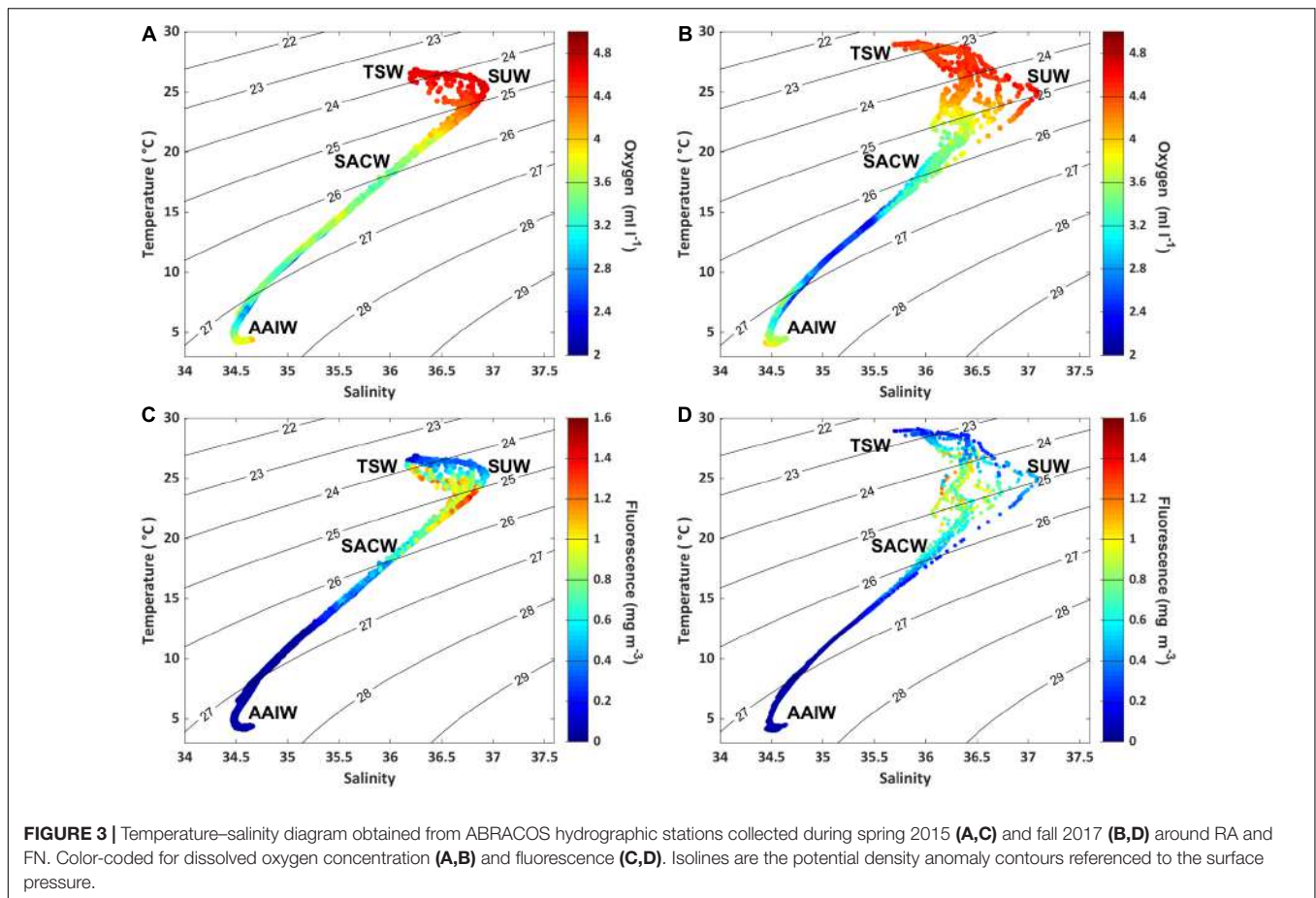
Satellite Data

To provide a more comprehensive image of dynamical processes acting around FN and RA and help the interpretation of

results obtained from *in situ* data, several satellite products distributed by the Copernicus Marine Environment Monitoring Service (CMEMS)³ were extracted in the study region for the periods corresponding to the ABRACOS cruises. The sea surface temperature (SST) product is the so-called OSTIA (Operational SST and Ice Analysis) that combines satellite and *in situ* data. This SST product is daily available from 1 October 1981 to 31 December 2018 on a regular grid of 0.05° resolution (Donlon et al., 2012). Sea-surface chlorophyll-*a* (Chl-*a*) concentration maps were from the Copernicus-GlobColour product provided by the ACRI-ST company. Chl-*a* was obtained from the merging of multi sensors such as SeaWiFS, MODIS, and MERIS. This product is daily available from 2007 to the present with a spatial resolution of 4 km (Garneron, 2013). Wind-stress data were produced by CERSAT/IFREMER and consist on a blended wind dataset based on remotely sensed surface winds derived from scatterometers and radiometers. It spans from 1992 to present and is daily available on a regular grid of 0.25° (Bentamy and Croizé-Fillon, 2011). Altimetry data is the Salto/Duacs gridded

²<http://currents.soest.hawaii.edu>

³<http://marine.copernicus.eu>



product of sea-surface height (SSH) and derived geostrophic currents. This product, available from January 1993 to the present, was computed from several multimissions altimeter measurements of SSH, interpolated daily onto a $0.25^\circ \times 0.25^\circ$ longitude/latitude grid (Ducet et al., 2000; Pujol et al., 2016; Taburet et al., 2019).

RESULTS

Water Masses and Thermohaline Structure

Based on the thermohaline properties observed during spring 2015 (Figures 3A,C) and fall 2017 (Figures 3B,D) and previous works (Schott et al., 1998; Stramma and Schott, 1999) four main water masses were identified in the 0–1,000 m depth-range: the Tropical Surface Water (TSW), the Subtropical Underwater (SUW), the South Atlantic Central Water (SACW), and the Antarctic Intermediate Water (AAIW). The TSW is located on the surface layer above the $\sigma_\theta = 24.5 \text{ kg m}^{-3}$ isopycnal, located at about 100 m depth. During spring 2015 (Figures 3A,C) the TSW was characterized by relatively high values of temperature ($>26^\circ\text{C}$), dissolved oxygen ($4.3\text{--}5.0 \text{ ml l}^{-1}$), and relatively low values of fluorescence ($<1 \text{ mg m}^{-3}$) and salinity (<36.5) in the mixed layer (limited to $\sim 90 \text{ m}$ depth). During fall 2017, the mixed

layer was shallower ($\sim 50 \text{ m}$ depth), and TSW was characterized by temperature higher than 27°C , salinity lower than 36.5 , dissolved oxygen concentrations between 4.3 and 4.7 ml l^{-1} and fluorescence in the range $0\text{--}0.9 \text{ mg m}^{-3}$ (Figures 3B,D). At both seasons, just below the TSW between $\sigma_\theta = 24.5 \text{ kg m}^{-3}$ and $\sigma_\theta = 25.5 \text{ kg m}^{-3}$, lied the SUW characterized by a local maximum in salinity (>36.5) (Figure 3). This water-mass, which was more clearly observed in spring 2015 than in fall 2017, is also characterized by relatively high oxygen ($>4 \text{ ml l}^{-1}$) and fluorescence ($>0.5 \text{ mg m}^{-3}$) values.

Below the SUW, takes place the SACW characterized by a nearly linear temperature-salinity relationship covering wide temperature ($10\text{--}20^\circ\text{C}$) and salinity ($34.9\text{--}36.2$) ranges. This water-mass was associated with a relative oxygen minimum of $3.3\text{--}3.5 \text{ ml l}^{-1}$ ($2.3\text{--}2.7 \text{ ml l}^{-1}$, respectively) during spring 2015 (fall 2017) at $150\text{--}500 \text{ m}$ depth. At these depths, fluorescence values were weak due to light limitation. Finally, the isopycnal $\sigma_\theta = 27.1 \text{ kg m}^{-3}$ (about 500 m) marks the transition between SACW and AAIW. AAIW is characterized by a local salinity minimum of ~ 34.5 and a local oxygen maximum of $\sim 3\text{--}3.5 \text{ ml l}^{-1}$. Fluorescence is almost zero at the depth of the AAIW.

In the surface layer, the mixed-layer containing TSW was spatially very homogeneous and characterized by a mean SST of 26.7°C (28.8°C , respectively) in spring 2015 (fall 2017) (Figures 4A, 5A, 6A). Surface salinity was also higher in spring

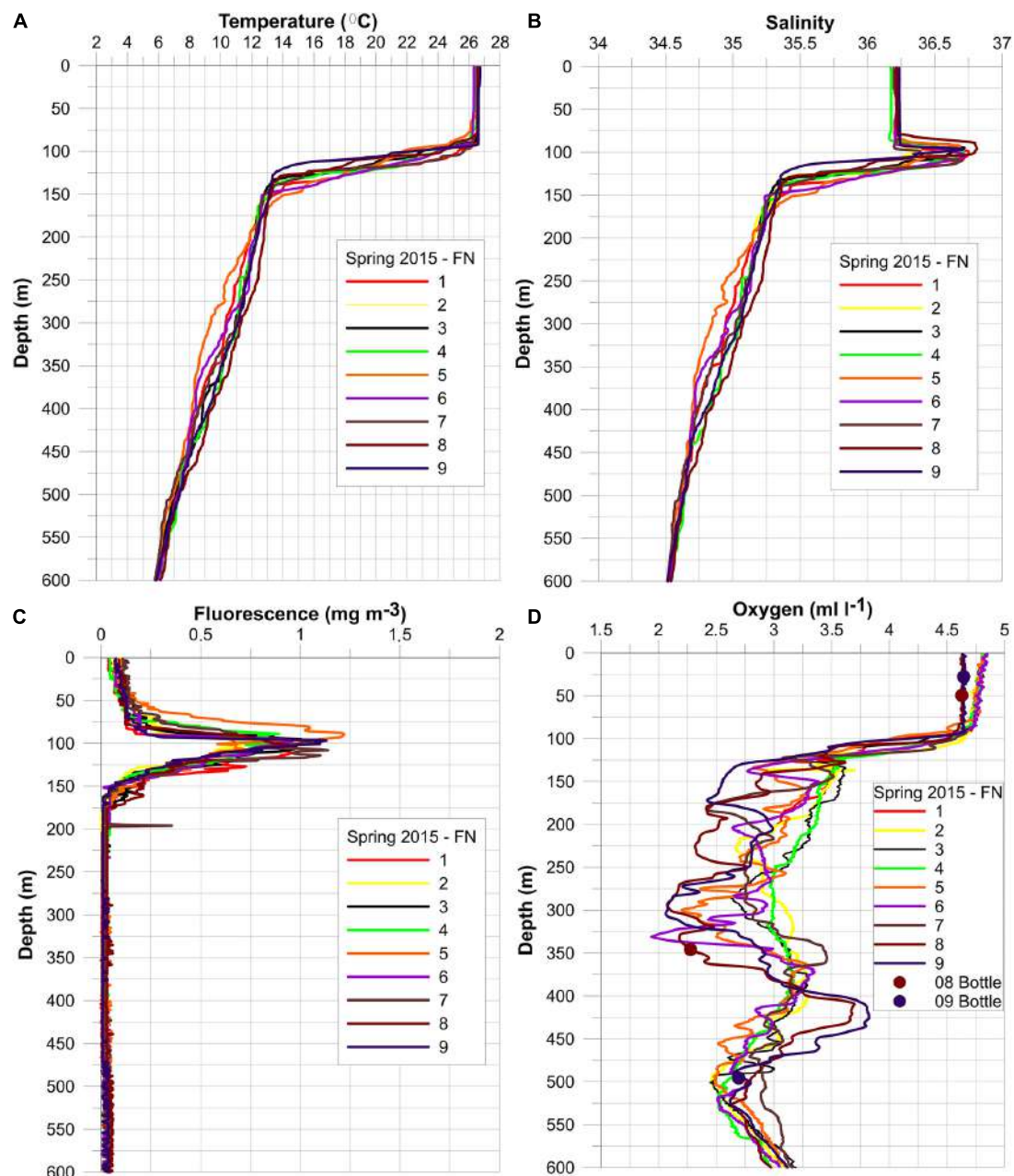


FIGURE 4 | CTD profiles obtained during the ABRACOS surveys in spring 2015 around the Fernando de Noronha Archipelago. Vertical profiles of temperature (A), salinity (B), fluorescence (C), and dissolved oxygen (D).

2015 (~ 36.2) than in fall 2017 (~ 35.9) (Figures 4B, 5B, 6B). Below, a sharp thermocline-halocline was observed with an upper limit at ~ 90 and 50 m in spring 2015 and fall 2017, respectively (Figures 4A, 5A, 6A). The seasonal thermocline extended down to ~ 150 m in spring 2015 and to ~ 100 m depth in fall 2017. During both cruises, a thin layer with maximum salinity (≥ 36.7 and ≥ 36.3) was present at ~ 80 – 120 m and ~ 60 – 90 m, respectively (Figures 4B, 5B, 6B), associated with SUW.

Surface fluorescence concentration of the TSW was twice lower in spring 2015 (average: 0.10 mg m^{-3}) than in fall 2017

(average: 0.20 mg m^{-3}) (Figures 4C, 5C, 6C). Peaks of maximum fluorescence (average: $\sim 1 \text{ mg m}^{-3}$) were observed in the SUW during spring 2015 and fall 2017 (Figures 4C, 5C, 6C).

In the surface layer, DO concentrations were similar and of $\sim 4.5 \text{ ml l}^{-1}$ during both cruises (Figures 4D, 5D, 6D). During spring 2015, CTD stations located north and south of RA also presented higher DO concentrations ($\geq 3.5 \text{ ml l}^{-1}$) below the thermocline layer. During fall 2017 low DO concentrations ($\sim 2.5 \text{ ml l}^{-1}$) were observed in subsurface around FN and RA (Figures 5D, 6D).

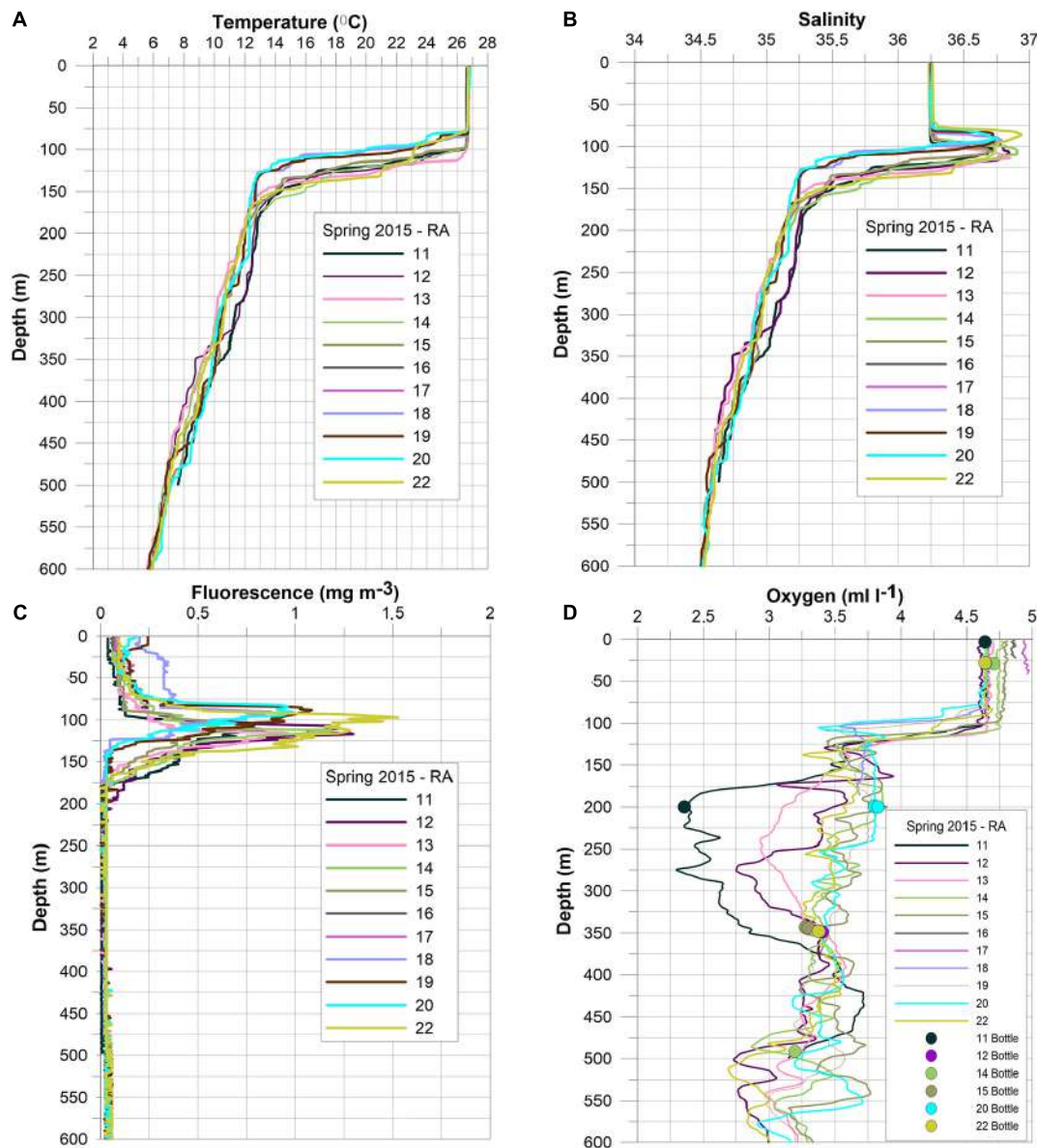


FIGURE 5 | CTD profiles obtained during the ABRACOS surveys in spring 2015 around the Rocas Atoll. Vertical profiles of temperature (A), salinity (B), fluorescence (C), and dissolved oxygen (D).

More specifically, during spring 2015, temperature profiles at stations 11 and 12, close to RA, presented positive temperature ($+1^{\circ}\text{C}$) and salinity ($+0.16$) anomalies in the depth range 200–350 m (Figure 5A). Corresponding DO concentration were lower than 3.5 ml l^{-1} (Figure 5D). Conversely, at station 05 close to FN, a negative anomaly in temperature (-1.3°C) and salinity (-0.15) was observed in the depth range 200–400 m (Figure 4A). At this station, the fluorescence peak was shallower than at other stations located around FN (Figure 4C). In addition, a shallower thermocline and halocline was observed at stations 18, 19, and 20, located north of RA, when compared to the other stations around RA (Figure 5A). In those stations, surface fluorescence concentration was higher ($0.18\text{--}0.24 \text{ mg m}^{-3}$) and

the peaks of maximum fluorescence were shallower (above 100 m) (Figure 5C). Finally, stations 14–22 located north and south of RA did not show a marked DO minimum (Figure 5D).

During fall 2017, at stations 48 and 54, the thermocline and halocline were deeper than at other stations (Figure 6A). In addition, station 42 located north of FN presented a positive temperature ($+1^{\circ}\text{C}$) and salinity ($+0.1$) anomaly between 350 and 450 m depth. At this station, in the depth range 425–600 m, DO concentration was higher ($>3.2 \text{ ml l}^{-1}$) than at other stations.

Finally, the upper thermocline was deeper in spring 2015 ($\sim 90 \text{ m}$) than fall 2017 ($\sim 50 \text{ m}$). Specifically, in spring 2015, stations 05, 09, 12, 20, and 22 (Figures 7A–E) presented deeper

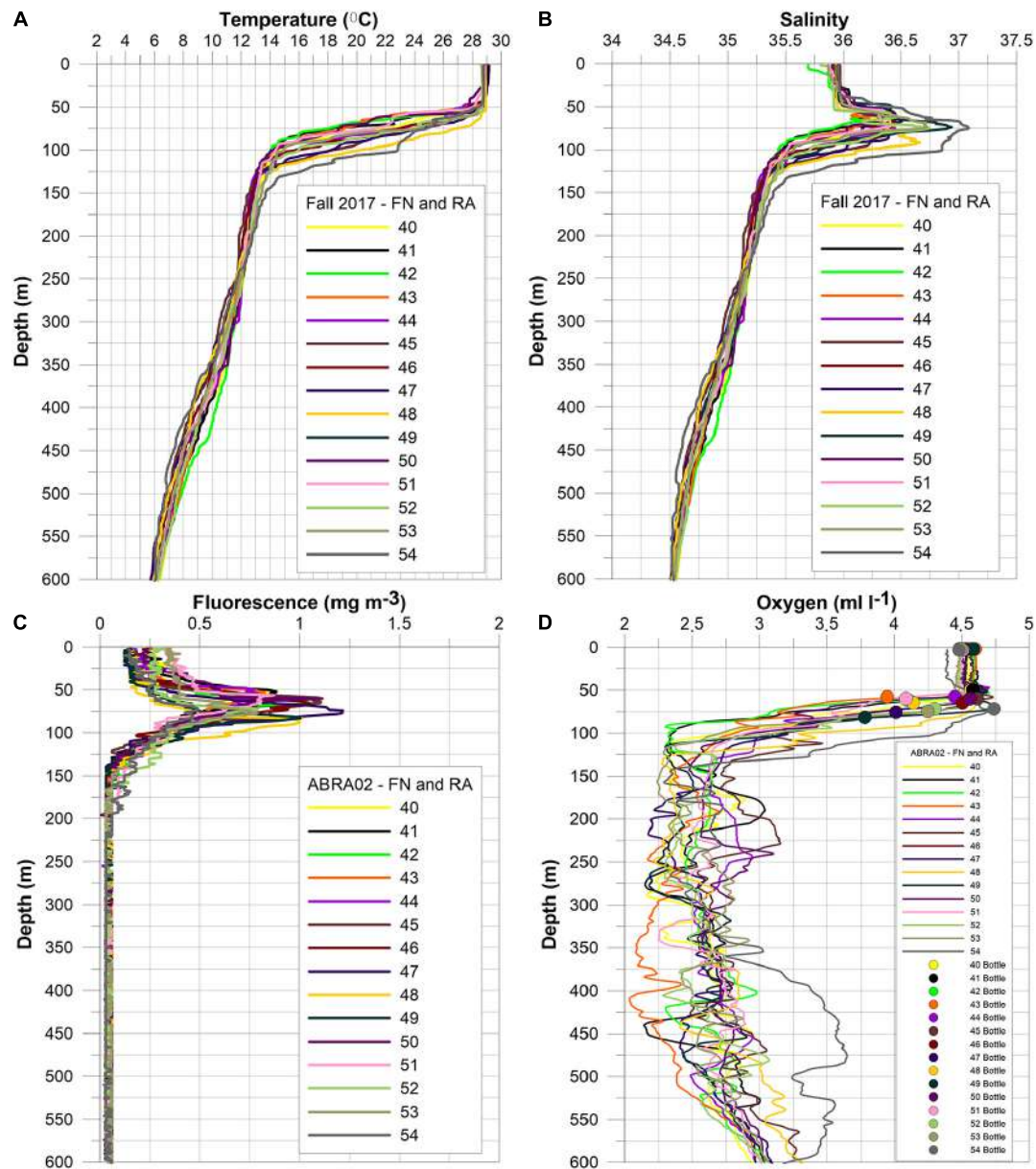


FIGURE 6 | CTD profiles obtained during the ABRACOS surveys in fall 2017 around the Fernando de Noronha Archipelago and Rocas Atoll. Vertical profiles of temperature (A), salinity (B), fluorescence (C), and dissolved oxygen (D).

halocline and thermocline when compared to stations 53 in fall 2017 (Figures 7E,F). The area north of FN and RA (stations 09 and 20; Figures 7B,D) presented stronger vertical gradients at the lower limit of the mixed layer depth than in the southern area (stations 05 and 12, Figures 7A,C). Station 20 located north of RA presented a low Ri between 150 and 250 m depth.

Below the surface layer (near 250 m depth), stations 12 and 22 show low Ri values (<0.5 and <0.3 , respectively) in the southeast side of RA (Figures 7C,E).

During spring 2015, the upper thermocline and maximum salinity depth (between 50 and 100 m depth) presented a higher peak of Brunt-Väisälä frequency near in surface than in fall

2017 (Figure 7F), confirming a stronger vertical stratification and static stability.

Circulation Patterns

cSEC and SEUC Volume Transports Around FN

Although several SADCP sections were performed around FN and RA, we selected a meridional section (crossing FN from North to South (transect Ta in Figure 2) to represent the ocean circulation in the region. In spring 2015, the cSEC flowed westward above 100 m depth on both sides of FN (Figure 8) but was more intense on the northern side ($U \sim -50 \text{ cm s}^{-1}$)

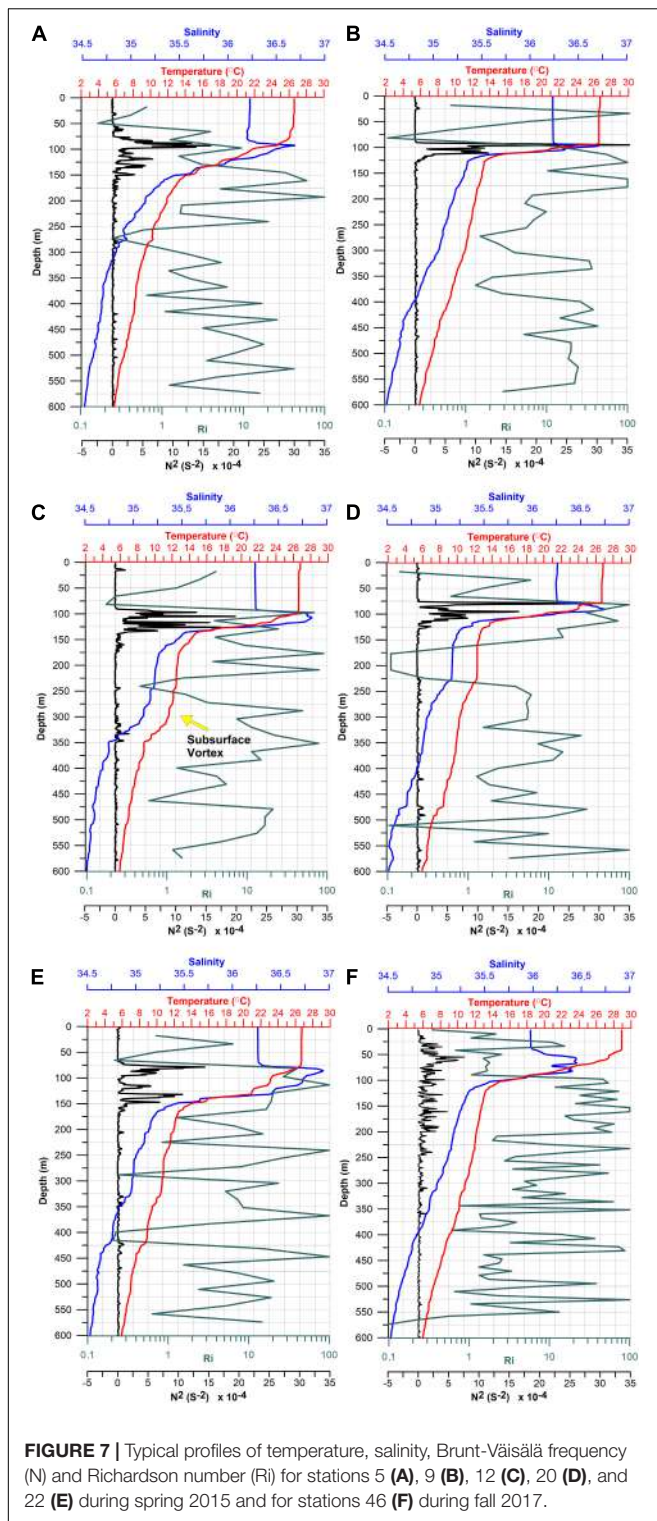


FIGURE 7 | Typical profiles of temperature, salinity, Brunt-Väisälä frequency (N) and Richardson number (Ri) for stations 5 (A), 9 (B), 12 (C), 20 (D), and 22 (E) during spring 2015 and for stations 46 (F) during fall 2017.

than on the southern side ($U \sim -20 \text{ cm s}^{-1}$) (Figure 8A). The cSEC westward transport was estimated to be of $1.2 \pm 0.1 \text{ Sv}$ across this meridional section in spring 2015. In fall 2017, the cSEC was restricted above 70 m (Figure 8B) and its zonal velocity component was higher than in spring 2015, with an average of

$\sim -60 \text{ cm s}^{-1}$ in the surface layer (0–100 m) in both sides of the island (Figure 8B). Corresponding westward transport was estimated to be of $4 \pm 0.2 \text{ Sv}$.

In the subsurface layer, between 100 and 400 m depth, the zonal component of the flow reversed and the current was oriented eastward, as is typical of the SEUC. Therefore, a strong current shear occurred between the near-surface cSEC and the subsurface SEUC. In spring 2015, the SEUC presented a maximum zonal velocity of 70 cm s^{-1} south of FN at $\sim 200 \text{ m}$ depth (Figure 8A). North of FN, the SEUC zonal velocity was weaker ($\leq 40 \text{ cm s}^{-1}$). The SEUC eastward transport, integrated between 100 and 400 m depth along the meridional section, was estimated to $5.6 \pm 0.5 \text{ Sv}$. In fall 2017, the SEUC was weaker than in spring 2015, having a maximum zonal velocity of 30 cm s^{-1} south of FN around 150 m depth (Figure 8B). On the northern side of FN, the SEUC velocity was much weaker ($< 10 \text{ cm s}^{-1}$) (Figure 8B). In fall 2017, the integrated SEUC transport was estimated to $3.8 \pm 0.7 \text{ Sv}$. Finally, below $\sim 450 \text{ m}$, the circulation was weak and not further investigated in this study.

Near-Surface and Subsurface Circulation Around FN and RA

In order to depict the regional circulation around FN and RA, we divided the circulation into two distinct layers: the near-surface layer (0–100 m depth) that includes the cSEC and the subsurface layer (100–400 m depth) mainly associated with the SEUC.

In spring 2015, the near-surface circulation was dominated by the cSEC (Figures 8A, 9A). Around FN, surface currents varied in direction and intensity on both sides (north and south) of the archipelago. On the northern side of the archipelago, surface current was more intense (50 cm s^{-1}) with a prevailing northwestward flow (Figure 9A). A similar northwestward flow was also observed on the northern side of RA. In fall 2017, the cSEC had a prevailing westward direction with mean velocities of 50 cm s^{-1} (Figure 9C). During this period, no clear current-islands interaction was observed.

In the subsurface layer (100–400 m depth), during spring 2015, the SEUC dominated around FN with maximum velocity (30 cm s^{-1}) south of the island. Near RA, currents flowed predominantly south/southeastwards, being more intense on the western side of the atoll. Between FN and RA (about 33°W), the eastward flow was weaker ($< 10 \text{ cm s}^{-1}$). Interestingly, in spring 2015, a small-scale subsurface cyclonic circulation was observed southeast of RA (illustrated by a black circle in Figure 9B). This subsurface cyclonic eddy had an estimated radius of $\sim 28 \text{ km}$ and was probably driven by the topographically induced flow separation (Figure 9B). This eddy-like structure, centered at 33.38°W and 4°S and having a typical swirl velocity of 20 cm s^{-1} , did not have a signature in the near-surface layer dominated by the cSEC. In fall 2017 the influence of the SEUC was observed in the 100–400 m depth layer around FN, with an average current velocity of 20 cm s^{-1} flowing eastward south of FN. Northwest of FN, the northeast flow was weaker ($\leq 10 \text{ cm s}^{-1}$). Finally, west of RA currents moved southwards (Figure 9D).

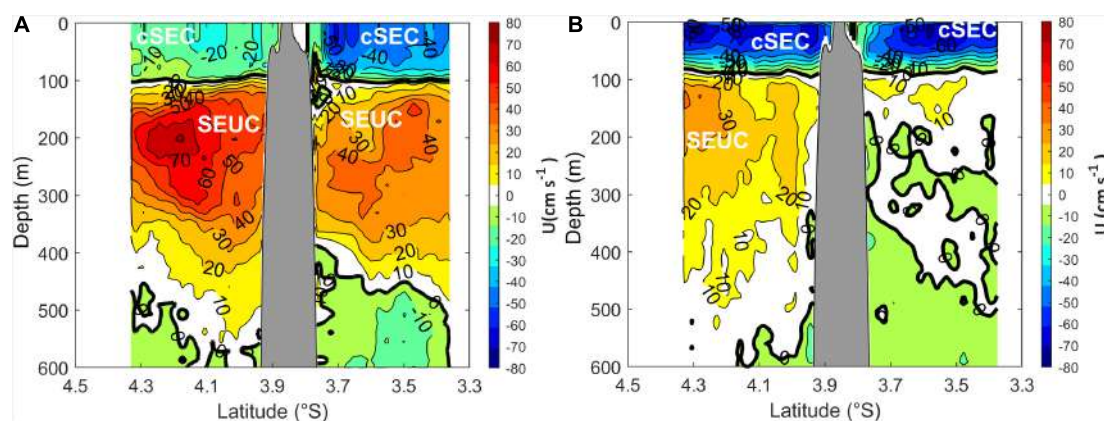


FIGURE 8 | Mean zonal velocity components (in cm s^{-1}) obtained from ABRACOS cruises in spring 2015 (A) and fall 2017 (B) around Fernando de Noronha archipelago (vertical blue transect Ta in **Figure 2**). The contour interval is 10 cm s^{-1} .

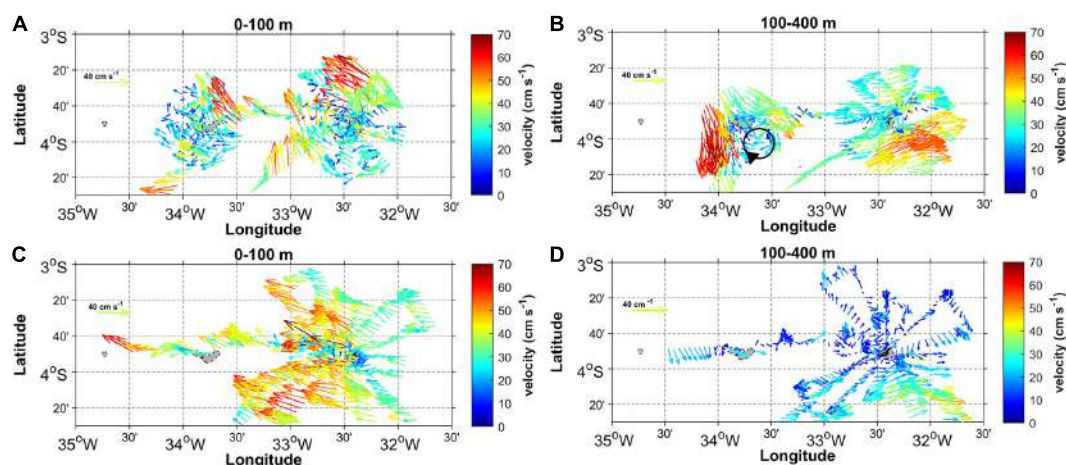


FIGURE 9 | Mean current velocity obtained from ABRACOS cruises at 0–100 m during spring 2015 (A) and fall 2017 (C), and at 100–400 during spring 2015 (B) and fall 2017 (D). Black circle in **Figure 8B** indicates the cyclonic mesoscale circulation.

Regional Surface Characteristics From Satellite Observations

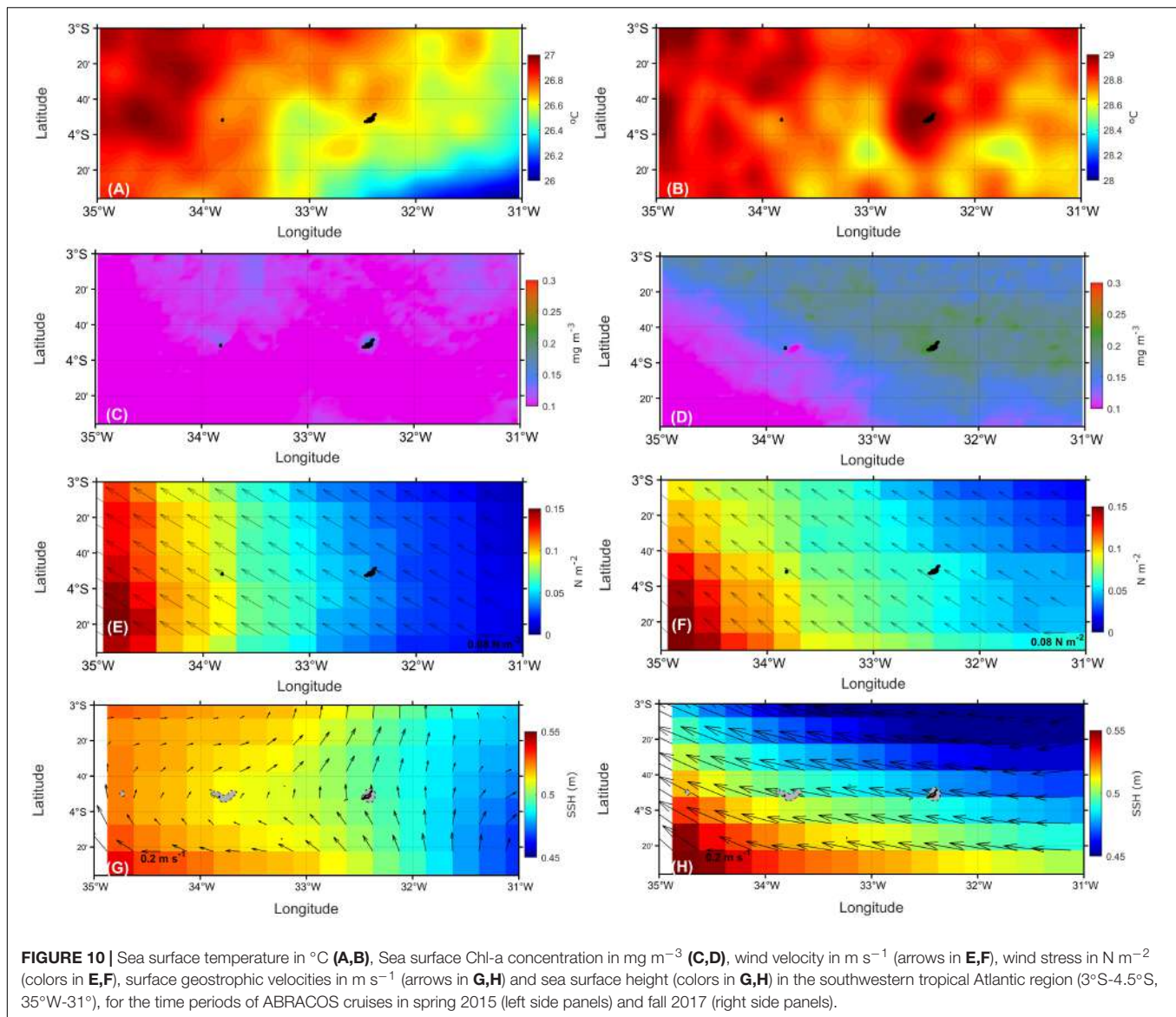
SST was lower in spring 2015 ($<27^{\circ}\text{C}$) than in fall 2017 ($>28^{\circ}\text{C}$) (**Figures 10A,B**), in agreement with the SST values observed from CTD data. In spring 2015, the SST showed a large-scale northwestward gradient, varying from 26°C southeast of FN to 27°C northwest of RA. This SST distribution suggests that the cSEC tended to cool the downstream regions. In fall 2017, the SST was much more homogeneous in the study region and varied by less than 0.4°C . Several mesoscale temperature structures were observed during both seasons (**Figures 10A,B**).

Surface Chl-a concentration was lower in spring 2015 (about 0.1 mg m^{-3}) than in fall 2017 (0.2 mg m^{-3}) (**Figures 10C,D**). Higher surface fluorescence values were also observed in fall 2017 from CTD data. In spring 2015, satellite Chl-a concentrations were higher in the vicinity of FN and RA, suggesting a topographic influence on the primary productivity. In fall 2017, a large-scale northeastward Chl-a gradient was

observed, with mean Chl-a concentrations varying from 0.10 to 0.23 mg m^{-3} .

Surface winds blew northwestwards and intensified westwards (**Figures 10E,F** and **Supplementary Figures 1E,F**). It might be related with coastal effects associated with the proximity of land. This intensification was more pronounced in spring 2015 than in fall 2017. Overall surface winds were higher in spring 2015 ($\geq 0.1 \text{ N m}^{-2}$) than fall 2017 ($\leq 0.1 \text{ N m}^{-2}$).

In spring 2015, some changes were observed in the predominant directions of the surface currents (0–100 m depth) around FN and RA, which was not observed in fall 2017. In spring 2015, SSH and associated geostrophic currents depicted a surface current flowing northward on the northern and eastern sides of FN. On the northern side of RA, a northeastward flow was observed (**Figure 10G**). The presence of a mesoscale cyclonic eddy around RA was depicted. In fall 2017, a clear geostrophic westward flow was observed (**Figure 10H**) around FN and RA and no eddy was observed (**Supplementary Figure 1H**).



DISCUSSION

In situ and satellite data are used to discuss the temporal variability of the oceanic characteristics around FN and RA in spring 2015 and fall 2017 that have been shown to be representative of canonical spring and fall conditions (Assunção et al., 2020; Dossa et al., 2021). We also discuss the impacts of FN and RA on the thermohaline structure, local circulation, including mesoscale features, primary productivity and dissolved oxygen distribution.

Spatiotemporal Variability of Physical and Biogeochemical Parameters

In the southwestern tropical Atlantic, negative ocean-atmosphere heat fluxes and stronger winds are observed in spring, leading to a lower SST and deeper mixed-layer. In contrast, in fall,

positive buoyancy due to positive heat fluxes and the relaxation of southeast trade winds lead to a higher SST and shallower mixed-layer (Araujo et al., 2011; Servain et al., 2014; Nogueira Neto et al., 2018; Assunção et al., 2020). Similarly, *in situ* ABRACOS measurements showed higher SST values in fall 2017 (28.8°C) than in spring 2015 (26.7°C). In fall 2017, during the rainy season, relatively low surface salinity and low wind stress were associated with warmer SST in the western tropical Atlantic (**Supplementary Figure 1**).

Previous studies (Schott et al., 1998, 2003; Stramma and Schott, 1999) described the SEUC characteristics across two meridional sections (35 and 31°W) between 2 and 5°S . These studies underlined the relatively small variability of the SEUC vertical position at 35°W in a depth range of 200 – 500 m between 2.5 and 4°S . However, using the ABRACOS mesoscale cruises, we showed that the SEUC can exhibit important temporal variability. The SEUC flowed eastward with greater intensity in the southern

part of FN during spring 2015, with a weakening in fall 2017. In the northern part of FN, the influence of the SEUC was not observed in fall 2017.

We observed an influence of the cSEC on the southern and northern sides of the island in the surface layer. This strong surface current was also associated with a variation of the mixed layer depth, which was shallower around FN and RA during fall 2017.

In situ and satellite data revealed a relatively strong variability of near surface fluorescence/Chl-a concentrations in the oceanic area around FN and RA among cruise periods with high concentration in fall 2017 when the mixed layer was shallower. In spring 2015, Chl-a was slightly higher in the northern part of the study area (**Figure 10C** and **Supplementary Figure 1C**), along the equatorial region, which may be associated to equatorial wind-driven upwelling. In fall 2017, a clear surface zonal “tongue” of maximum Chl-a was observed at 3°S, involving FN and RA areas, reaching a maximum of about 0.2 mg m^{-3} . This high productivity may be associated to nutrient rich waters transported westward by the cSEC, which is stronger during fall 2017 reaching a maximum of about 0.2 mg m^{-3} (**Figures 10G,H** and **Supplementary Figures 1G,H**). CTD profiles confirm the increase in fluorescence concentrations around FN and RA during fall 2017, with two to fourfold higher concentrations when compared to spring 2015 (**Figures 4C, 5C, 6C**). Note that the Chl-a variability in the equatorial Atlantic can be influenced by several mechanisms, such as the seasonal variations of upwelling driven by the meridional displacement of the ITCZ, the westward advection by the SEC, or the perturbation of the equatorial upwelling by eastward propagating Kelvin waves (Servain et al., 1982; Grodsky et al., 2008). We here highlighted that FN and RA can also locally impact the Chl-a distribution.

Around FN and RA, DO concentration was lower than $\sim 3 \text{ ml l}^{-1}$ in the depth range 150–350 m in fall 2017 (**Figure 6D**). In spring 2015, this pattern was observed around FN but 5 out of 8 profiles around AR presented $\text{DO} > 3 \text{ ml l}^{-1}$ in this depth range (**Figures 4D, 5D**). These oxygen maxima have been reported in the SEUC farther east (Tsuchiya, 1986; Schott et al., 1998). These oxygen signatures are used to diagnose the origin of the SEUC. Our results can provide further insight in a current debate. Indeed, according to Bourlès et al. (1999), in the region where the NBC forms, the NBUC weakens and retroflects to feed the SEUC. On the contrary, Schott et al. (1998) indicated that the SEUC is not supplied by the oxygen-rich and high-salinity NBUC waters, but is mostly made up of low-oxygen interior recirculation waters out of the SEC. This was also supported by Goes et al. (2005), that stated that apart from the gyre recirculation, there is a minor contribution from the NBUC to the SEUC. Finally, recently, Dossa et al. (2021) also showed that the NBUC retroflection does not feed the SEUC, which instead originates from the SEC retroflection, at least in fall. Still, the presence of profiles with higher DO concentration in spring 2015 raise again the question about a potential contribution of the NBUC to the SEUC. The orientation of the subsurface currents in the area of RA in spring 2015 may also indicate the presence of a retroflection. In the same sense, using float trajectories (around 200 m depth), Fischer

et al. (2008) reported that, in austral spring, a float deployed south of the SEUC followed its eastward flow but then drifted westwards. The float was then entrained by the NBUC and re-entered the SEUC northwest of RA. At 23°W, Brandt et al. (2008) observed an oxygen maximum in the deepest part of the SEUC ($\sim 400 \text{ m}$), indicating either a direct connection to the western boundary flow or a recirculation of oxygen-rich water from the south. Around RA, we observed a south/southeastwards flow (100–400 m depth) (**Figure 9B**). It seems therefore that in spring, the NBUC can retroflect to reach RA. However, the contribution of this retroflection to the SEUC remains unclear since the NBUC signature was lost close to RA and no more observable around FN. Therefore, it seems that as proposed by Goes et al. (2005), the NBUC can retroflect, at least in spring, but the contribution of the NBUC to the SEUC is likely negligible. Further studies are needed to quantify such effects and fully explain the mechanisms potentially involved in the NBUC-SEUC connection.

Island Wake Observed From CTDO and SADCP Data

To study possible effects of local flow-topography interactions over the large-scale circulation patterns, in **Figures 11, 12**, we examined the vertical zonal velocity profiles (0–600 m depth) in the western and eastern side of FN (transects Tb and Tc in **Figure 2**) and in the northwestern and southeastern side of RA (transect Td in **Figure 2**). The westward near-surface cSEC and eastward subsurface SEUC dominated at both periods, with stronger cSEC velocities in fall 2017 than spring 2015. On the opposite and, the subsurface SEUC transport was stronger in spring 2015 (**Figure 11**). In addition, a quite different circulation patterns was observed west and east of FN for both periods. In spring 2015, near-surface (0–100 m depth) zonal currents undergo important changes in their direction and intensity between upstream and downstream areas near FN, with maximal values higher in the western ($U \sim 20 \text{ cm s}^{-1}$) than the eastern ($U \sim 10 \text{ cm s}^{-1}$) side of FN (**Figures 11A,B**). The presence of the archipelago also induced strong perturbations of the cSEC, with a splitting of the cSEC core upstream of the archipelago in both periods (**Figure 11A** versus **Figure 11B**, and **Figure 11C** versus **Figure 11D**), although higher currents were observed in fall 2017, with maxima intensity ($\sim 80 \text{ cm s}^{-1}$) measured at the western side of FN (**Figure 11C**).

Below the surface layer, between 100 and 400 m depth, the effects of island wake on the SEUC was also visible. A current core splitting was indeed observed in the eastern side of FN, with maximum velocities occurring north of 3.9°S ($U \sim 30 \text{ cm s}^{-1}$) and a core of 20 cm s^{-1} centered at 3.7°S in spring 2015 (**Figure 11A**). A stronger and single SEUC core was observed downstream of FN, suggesting a reorganization of the eastward subsurface flow in the eastern portion of the archipelago, with eastward velocities higher than 50 cm s^{-1} at 3.9–4.2°S (**Figure 11B**). A similar scenario was observed in fall 2017 west of FN and north of 3.9°S, although with a much less intense and even a reversed transport north of the archipelago ($U \sim -10 \text{ cm s}^{-1}$ at 3.7°S). East of FN, the SEUC presented

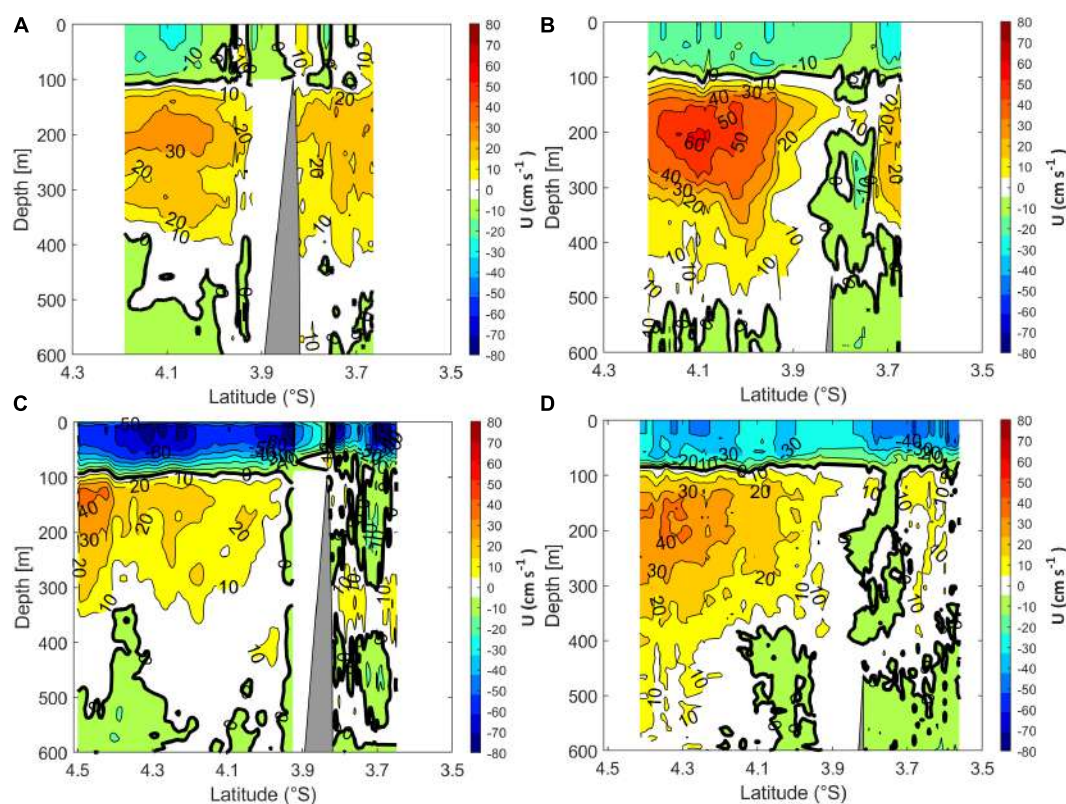


FIGURE 11 | Zonal velocity component (in cm s^{-1} , 0–600 m depth) near FN in the western (left side, see Tb transects in **Figure 2**) and eastern (right side, see Tc transects in **Figure 2**) regions, during spring 2015 (**A,B**) and fall 2017 (**C,D**). The contour interval is 10 cm s^{-1} . The transects (Tb and Tc) are not along a single straight line, but along two non-meridional line segments.

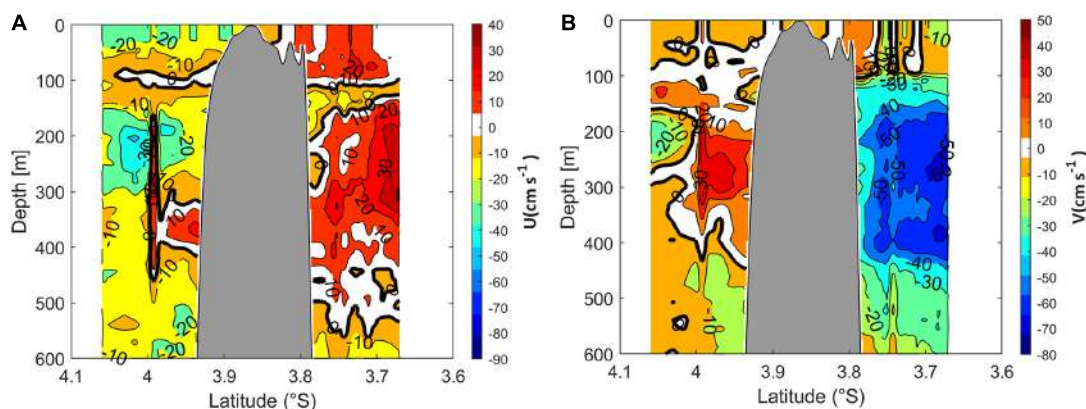


FIGURE 12 | Mean zonal (**A**) and meridional (**B**) velocity components (in cm s^{-1}) during spring 2015 around RA (see Td transect in **Figure 2**). The contour interval is 10 cm s^{-1} . In each panel, the bold black solid line contours represents null value of the velocity.

a maximum intensity of 40 cm s^{-1} at $\sim 4.5^\circ\text{S}$ (**Figure 11C**). In the subsurface layer (100–400 m) SEUC intensity was maximal of 40 cm s^{-1} in the east side of FN at $\sim 200 \text{ m}$ depth (**Figure 11D**).

These changes in the intensity and direction of the currents around the islands can be related to local topography. Cross-sectional vertical profiles of the temperature, salinity, fluorescence/Chl-a and dissolved oxygen concentrations

are presented in **Supplementary Figure 2**. Transects were constructed from CTDO stations 05, 04, 01, and 08 (spring 2015), and 45, 44, 50, and 51 (fall 2017), represented by black triangles (see **Figure 2** for the stations position).

Besides currents (intensity and direction) differences, vertical distributions of temperature and salinity are not the same in both sides of FN (Hydrographic transects in

Supplementary Figures 2C,D). During spring 2015, we notice below 100 m depth a deepening of isotherms (see for example 10°C, **Supplementary Figure 2A**) and isohalines (for example 35.2 and 34.9, **Supplementary Figure 2C**) in the west side of FN, which is associated to observed splitting in SEUC structure due to the presence of the island (**Figure 11A**). Although less intense, this scenario is also observed during fall 2017 for the same isotherms and isohalines (**Supplementary Figures 2B,D**), which seems to be also associated to perturbations in SEUC structure imposed by the island wake (**Figure 11C**).

Indeed numerical simulations (e.g., Tchamabi et al., 2017), showed a subsurface cooling around the FN and RA, which was mainly driven by the interruption of cSEC by the bathymetry, enhancing vertical mixing and mesoscale eddy activity in the thermocline. It suggests that the island wake leads to an enrichment from the subsurface to the euphotic layer near FN and RA, supplying the productivity in these regions. This locally enhanced productivity is also visible on the satellite Chl-a observations (**Figure 10C**).

Another section is carried out on the northwestern and southeastern sides of the atoll (transects Td in **Figure 2**). In the surface layer (0–100 m), there is a predominantly eastward flow ($U > 0$ and $V < 0$) and below the surface layer there is an eastward flow centered at 250 meters in the northwestern part of RA (**Figure 12**). As shown later, in the subsurface layer (around 150–350 m depth), a cyclonic vortex structure was observed downstream (southeast side) of RA (red circle in **Figures 9B, 12**). However, the application of existing Richardson number (station 12 and 22) shows low Ri (< 0.3) values around 200–400 m depth indicating the vortex (**Figures 7D,E**).

The maximal vortex velocity $U_{max} \approx 20 \text{ cm.s}^{-1}$ is reached for the characteristic radius $R_{max} \approx 28 \text{ km}$, resulting in a vortex Rossby number $Ro \approx 0.7$ of this cyclonic vortex. The Rossby radius of deformation (R_d) is 23 km, a value very close to the vortex radius. In the equatorial region, R_d is one order of magnitude larger (Houry et al., 1987; Simoes-Sousa et al., 2021). Strong surface Eddies close to the equator present very small values of the Coriolis parameter f , leading to high Rossby number. Although some of these eddies are also highly circular, most of them have very small amplitudes (Douglass and Richman, 2015). The Burger number of the vortex is about 3. These values are consistent with the processes associated with a cyclonic eddy shedding observed in the Gulf of Guinea (Djakouré et al., 2014).

Corresponding temperature and salinity signatures were observed between 150 and 350 m depth at the same position (station 12 and 22, **Figures 7C,E**). At this depth range, an anomalous (and almost stepwise) increase in temperature and salinity was observed, associated with subsurface mesoscale changes in currents (**Figure 12**) and small Richardson numbers (**Figures 7C,E**). This subsurface vortex structure was also probably generated by the island wake (e.g., Aristegui et al., 1997; Chérubin and Garavelli, 2016). The maximum of subsurface fluorescence was also observed at Station 22, in the edge of the eddy-like feature (**Figure 5A**). Cyclonic and anticyclonic eddies are known to strongly modulate primary production in oligotrophic waters around islands (e.g., Aristegui et al., 1997). Maximum primary productivity is often observed near eddy

edges, where numerous filaments are observed due to enhanced lateral straining, stretching and stirring (e.g., Mahadevan, 2016; Lévy et al., 2018).

CONCLUSION

Based on two regional mesoscale cruises realized off the Northeast Brazilian coast, we described the upper-ocean circulation and how island wake impact the main features around Fernando de Noronha island and Rocas Atoll in two contrasted periods, Austral spring 2015 and fall 2017, considered as representative of the mean spring and fall conditions. In spring, the area was characterized by a lower SST (26.6°C) and deeper mixed-layer (~90 m). At this depth, a strong vertical shear was observed between the surface cSEC and the subsurface SEUC. In contrast, in fall, SST was higher (~28.8°C), the mixed-layer shallower (~50 m), and the vertical shear between the cSEC and the SEUC weaker. Our study suggested that SEUC was fed (not fed, respectively) by the NBUC in spring 2015 (fall 2017). However, from the available datasets, it was not possible to quantify how much this retroflexion fed the SEUC in spring 2015. To unravel the scientific debate on the NBUC-SEUC connection, dedicated oceanographic cruises and numerical modeling approaches would be needed. Beside these global patterns, the physical processes in the wakes of islands were clear with the splitting of the large-scale currents, the presence of mesoscale meanders and a subsurface eddy-like structure. These features are likely key processes providing an enrichment from the subsurface to the euphotic layer near FN and RA, supplying the local productivity. Enhancement of primary production around the archipelago was also observed from satellite data in spring 2015. In addition to the new information described above, this work enables the planning of future cruises to be carried out for a better understanding of mesoscale vortex processes, water mass transport around the islands and in the tropical Atlantic.

DATA AVAILABILITY STATEMENT

The datasets presented in this study can be found in online repositories. The names of the repository/repositories and accession number(s) can be found below: ABRACOS Data (doi: 10.17600/15005600 and doi: 10.17600/17004100).

AUTHOR CONTRIBUTIONS

ACo and AB planned and organized oceanographic surveys. GE, AB, AD, and ACo worked in data processing and QC. All authors wrote and reviewed the manuscript.

FUNDING

This work was a contribution to the LMI TAPIOCA, the SMAC project (CAPES/COFECUB no. 88881.142689/2017–01),

the PADDLE project (funding by the European Union's Horizon 2020 Research and Innovation Programme—Grant Agreement 73427) and EU H2020 TRIATLAS project under Grant Agreement 817578.

ACKNOWLEDGMENTS

We thank the officers and crew of the R/V Antea for their able assistance and cooperation. MA thanks the Brazilian Research Network on Global Climate Change—Rede CLIMA (FINEP-CNPq 437167/2016-0) and the Brazilian National Institute of Science and Technology for Tropical Marine Environments—INCT AmbTropic (CNPq/FAPESB 565054/2010-4 and 8936/2011) for their support.

REFERENCES

- Araujo, M., Limongi, C., Servain, J., Silva, M., Leite, F. S., Veleda, D., et al. (2011). Salinity-induced mixed and barrier layers in the southwestern tropical Atlantic Ocean off the northeast of Brazil. *Ocean Sci.* 7, 63–73. doi: 10.5194/os-7-63-2011
- Aristegui, J., Tett, P., Hernandez-Guerra, A., Basterretxea, G., Montero, M. F., Wild, K., et al. (1997). The influence of island-generated eddies on chlorophyll distribution: a study of mesoscale variation around Gran Canaria. *Deep-Sea Res.* 44, 71–96. doi: 10.1016/S0967-0637(96)00093-3
- Assunção, R. V., Silva, A. C., Amédée, R., Bourlès, B., Silva, C. H. S., Ternon, J. F., et al. (2020). 3D characterisation of the thermohaline structure in the southwestern tropical Atlantic derived from functional data analysis of in situ profiles. *Prog. Oceanogr.* 187:102399. doi: 10.1016/j.pcean.2020.102399
- Assunção, R. V., Silva, A. C., Martins, J., and Flores, M. M. (2016). Spatial-Temporal variability of the thermohaline properties in the coastal region of Fernando de Noronha Archipelago. *Brazil. J. Coast. Res. Special Issue* 75, 512–516. doi: 10.2112/SI75-103.1
- Bentamy, A., and Croizé-Fillon, D. (2011). Gridded surface wind fields from Metop/ASCAT measurements. *Int. J. Remote Sens.* 33, 1729–1754. doi: 10.1080/01431161.2011.600348
- Bertrand, A., Alory, G., Chaigneau, A., Eldin, G., Grelet, J., Devesa, J., et al. (2017). ABRACOS 2 Cruise - Physical Datasets. SEANOE, doi: 10.17882/76352
- Bertrand, A., Costa Da Silva, A., Chaigneau, A., Eldin, G., Roubaut, F., Grelet, J., et al. (2015). ABRACOS Cruise - Physical Datasets. SEANOE, doi: 10.17882/76696
- Bourlès, B., Molinari, R. L., Johns, E., Wilson, W. D., and Leaman, K. D. (1999). Upper layer currents in the western tropical North Atlantic (1989–1991). *J. Geophys. Res.* 104, 1361–1375. doi: 10.1029/1998JC900025
- Brandt, P., Hormann, V., Bourlès, B., Fischer, J., Schott, F. A., Stramma, L., et al. (2008). Oxygen tongues and zonal currents in the equatorial Atlantic. *J. Geophys. Res.* 113:C04012. doi: 10.1029/2007JC004435
- Chaves, T. B. C., Mafalda, J. R. P., Santos, C., Souza, C. S., Moura, G., Sampaio, J., et al. (2006). Planktonic biomass and hydrography in the Exclusive Economic Zone of Brazilian Northeast. *Trop. Oceanogr.* 34, 12–30.
- Chérubin, L. M., and Garavelli, L. (2016). Eastern Caribbean circulation and island mass effect on St. Croix, US Virgin Islands: a mechanism for relatively consistent recruitment patterns. *PLoS One* 11:e0150409. doi: 10.1371/journal.pone.0150409
- Djakouré, S., Penven, P., Bourlès, B., Veitch, J., and Koné, V. (2014). Coastally trapped eddies in the north of the gulf of guinea. *J. Geophys. Res.* 119, 6805–6819. doi: 10.1002/2014JC010243
- Donlon, C. J., Martin, M., Stark, J., Roberts-Jones, J., Fiedler, E., and Wimmer, W. (2012). The Operational Sea Surface Temperature and Sea Ice analysis (OSTIA). *Remote Sens Environ.* 116, 140–158. doi: 10.1016/j.rse.2010.10.017, 2011
- Dossa, A. N., Silva, A. C., Chaigneau, A., Eldin, G., Araujo, M., and Bertrand, A. (2021). Near-surface western boundary circulation off Northeast Brazil. *Prog. Oceanogr.* 80:102475. doi: 10.1016/j.pcean.2020.102475
- Douglass, E. M., and Richman, J. G. (2015). Analysis of ageostrophy in strong surface eddies in the Atlantic Ocean. *J. Geophys. Res.* 120, 1490–1507.
- Ducet, N., Le Traon, P. Y., and Reverdin, G. (2000). Global high-resolution mapping of ocean circulation from TOPEX/Poseidon and ERS-1 and -2. *J. Geophys. Res.* 105, 19477–19498. doi: 10.1029/2000JC900063
- Fischer, J., Hormann, V., Brandt, P., Schott, F. A., Rabe, B., and Funk, A. (2008). South Equatorial 834 Undercurrent in the western to central tropical Atlantic. *Geophys. Res. Lett.* 35:L21601. doi: 10.1029/2008GL035753
- Foltz, G. R., Brandt, P., Richter, I., Rodriguez-Fonseca, B., Hernandez, F., Dengler, M., et al. (2019). The Tropical Atlantic Observing System. *Front. Mar. Sci.* 6:206. doi: 10.3389/fmars.2019.00206
- Garnesson, P. (2013). *Global Ocean Chlorophyll, PP and PFT (Copernicus-GlobColour) From Satellite Observations - Near Real Time*. Available online at: <https://sextant.ifremer.fr/record/bc19d37d-fa0d-4035-b80e-33a15e7e29e4/>
- Goes, M., Molinari, R., Da Silveira, I., and Wainer, I. (2005). Retroreflections of the North Brazil Current during February 2002. *Deep-Sea Res. I* 52, 647–667. doi: 10.1016/j.dsr.2004.10.010
- Grasshoff, K., Ehrhardt, M., and Kremling, K. (1983). *Methods of Seawater Analysis*. Hoboken NJ: Wiley.
- Grodsky, S. A., Carton, J. A., and McClain, C. R. (2008). Variability of upwelling and chlorophyll in the equatorial Atlantic. *Geophys. Res. Lett.* 35:L03610. doi: 10.1029/2007GL032466
- Hounsou-Gbo, G. A., Araujo, M., Bourlès, B., Veleda, D. R. A., and Servain, J. (2015). Tropical Atlantic contributions to strong rainfall variability along the Northeast Brazilian coast. *Adv. Meteorol.* 2015:902084. doi: 10.1155/2015/902084
- Hounsou-Gbo, G. A., Servain, J., Araujo, M., Caniaux, G., Bourlès, B., Fontenele, D., et al. (2019). SST Indexes in the tropical South Atlantic for Forecasting Rainy Seasons in Northeast Brazil. *Atmosphere* 10:335. doi: 10.3390/atmos10060335
- Houry, S., Dombrowsky, E., De Mey, P., and Minster, J. (1987). Brunt-vaiala frequency and rossby radii in the south Atlantic. *J. Phys. Oceanogr.* 17, 1619–1626. doi: 10.1175/1520-04851987017<1619:BVFARR>2.0.CO;2
- Joyce, T. M. (1989). On in situ “calibration” of shipboard ADCPs. *J. Atmos. Oceanic Technol.* 6, 169–172.
- Lessa, R. P. T., Mafalda, P. Jr., Advincula, R., Lucchesi, R. B., Bezerra, J. L. Jr., Vaskejr, T., et al. (1999). Distribution and abundance of ichthyoneuston at seamounts and islands off North-Eastern Brazil. *Arch. Fish. Mar. Res.* 47, 239–252.
- Lévy, M., Franks, P. J. S., and Smith, K. S. (2018). The role of submesoscale currents in structuring marine ecosystems. *Nat. Commun.* 9:4758. doi: 10.1038/s41467-018-07059-3
- Lumpkin, R., and Garzoli, S. L. (2005). Near-surface circulation in the tropical Atlantic Ocean. *Deep Sea Res Part I* 52, 495–518. doi: 10.1016/j.dsr.2004.09.001

SUPPLEMENTARY MATERIAL

The Supplementary Material for this article can be found online at: <https://www.frontiersin.org/articles/10.3389/fmars.2021.598101/full#supplementary-material>

Supplementary Figure 1 | Sea surface temperature, Sea surface Chl-a concentration, Surface winds stress, and Sea surface height/surface geostrophic velocities, obtained from OSTIA product in the southwestern tropical Atlantic region (4°N–8°S, 39.25°W–27°W), involving Fernando de Noronha Archipelago and Rocas Atoll (rectangle), for the same time periods of ABRACOS cruises: spring 2015 (left side panels), and fall 2017 (right side panels).

Supplementary Figure 2 | Vertical distributions of temperature, salinity, fluorescence, dissolved oxygen concentrations and Brunt-Väisälä frequency (N) near FN, during spring 2015 (left panels) and fall 2017 (right panels). Transects were obtained from CTDO stations 05, 04, 01, and 08 (spring 2015), and 44, 50, and 51 (fall 2017), represented by black triangles. See **Figure 2** for CTDO stations positions (pink dots).

- Mahadevan, A. (2016). The impact of submesoscale physics on primary productivity of plankton. *Ann. Rev. Mar. Sci.* 8, 161–184. doi: 10.1146/annurev-marine-010814-015912
- Nogueira Neto, A. V., Giordani, H., Caniaux, G., and Araujo, M. (2018). Seasonal and interannual mixed-layer heat budget variability in the western tropical Atlantic from Argo floats (2007–2012). *J. Geophys. Res. Oceans.* 123, 5298–5322. doi: 10.1029/2017JC013436
- Pedlosky, J. (1987). *Geophysical Fluid Dynamics*, 2 Edn. Berlin: Springer, 728.
- Pollard, R. T., and Read, J. F. (1989). A method for calibrating ship-mounted acoustic doppler profilers and the limitations of gyro compasses. *J. Atmos. Oceanic Technol.* 6, 859–865.
- Pujol, M.-I., Faugère, Y., Taburet, G., Dupuy, S., Pelloquin, C., Ablain, M., et al. (2016). DUACS DT2014: the new multi-mission altimeter data set reprocessed over 20 years. *Ocean Sci.* 12, 1067–1090. doi: 10.5194/os-12-1067-2016
- Schott, F. A., Dengler, M., Brandt, P., Affler, K., Fischer, J., Bourlès, B., et al. (2003). The zonal currents and transports at 35W in the tropical Atlantic. *Geophys. Res. Lett.* 30:1349. doi: 10.1029/2002GL016849
- Schott, F. A., Fischer, J., and Stramma, L. (1998). Transports and pathways of the upper-layer circulation in the western tropical Atlantic. *J. Phys. Oceanogr.* 28, 1904–1928.
- Servain, J., Caniaux, G., Kouadio, Y. K., McPhaden, M. J., and Araujo, M. (2014). Recent climatic trends in the tropical Atlantic. *Clim. Dyn.* 34, 3071–3089. doi: 10.1007/s00382-014-2168-7
- Servain, J., Picaut, J., and Merle, J. (1982). Evidence of remote forcing in the equatorial Atlantic Ocean. *J. Phys. Oceanogr.* 12, 457–463.
- Silveira, I. C. A., Miranda, L. B., and Brown, W. S. (1994). On the origins of the North Brazil Current. *J. Geophys. Res.* 99, 501–522.
- Simoës-Sousa, I. T., Silveira, I. C. A., Tandon, A., Flierl, G. R., Ribeiro, C. H. A., and Martins, R. P. (2021). The Barreirinhas Eddies: Stable Energetic Anticyclones in the Near-Equatorial South Atlantic. *Front. Mar. Sci.* 8:617011. doi: 10.3389/fmars.2021.617011
- Stramma, L., and Schott, F. (1999). The mean flow field of the tropical Atlantic Ocean. *Deep Sea Res II* 46, 279–303.
- Taburet, G., Sanchez-Roman, A., Ballarotta, M., Pujol, M.-I., Legeais, J.-F., Fournier, F., et al. (2019). DUACS DT-2018: 25 years of reprocessed sea level altimeter products. *Ocean Sci.* 15, 1207–1224. doi: 10.5194/os-15-1207-2019
- Tchamabi, C., Araujo, M., Silva, M. A., Bourlès, B., and Travassos, P. (2018). Ichthyoplankton transport around the Brazilian Fernando de Noronha archipelago and Rocas Atoll: are there any connectivity patterns? *Indian J. Geo Mar. Sci.* 47, 812–818.
- Tchamabi, C. C., Araújo, M., Silva, M., and Bourlès, B. (2017). A study of the Brazilian Fernando de Noronha Island and Rocas Atoll wakes in the tropical Atlantic. *Ocean Model* 111, 9–18. doi: 10.1016/j.ocemod.2016.12.009
- Travassos, P. E. P. F., Hazin, F. H. V., Zagaglia, J. R., Rocha, R. A., and Schober, J. (1999). Thermohaline structure around seamounts and islands off Northeast Brazilian coast. *Arch. Fish. Mar. Res.* 47, 211–222.
- Tsuchiya, M. (1986). Thermostads and circulation in the upper layer of the Atlantic Ocean. *Prog. Oceanogr.* 16, 235–267.
- UNESCO (1981). *Background Papers and Supporting Data on the International Equation of State of Seawater 1980* (No. 38), UNESCO Technical Papers in Marine Science. Paris: UNESCO.

Conflict of Interest: The authors declare that the research was conducted in the absence of any commercial or financial relationships that could be construed as a potential conflict of interest.

Copyright © 2021 Costa da Silva, Chaigneau, Dossa, Eldin, Araujo and Bertrand. This is an open-access article distributed under the terms of the Creative Commons Attribution License (CC BY). The use, distribution or reproduction in other forums is permitted, provided the original author(s) and the copyright owner(s) are credited and that the original publication in this journal is cited, in accordance with accepted academic practice. No use, distribution or reproduction is permitted which does not comply with these terms.